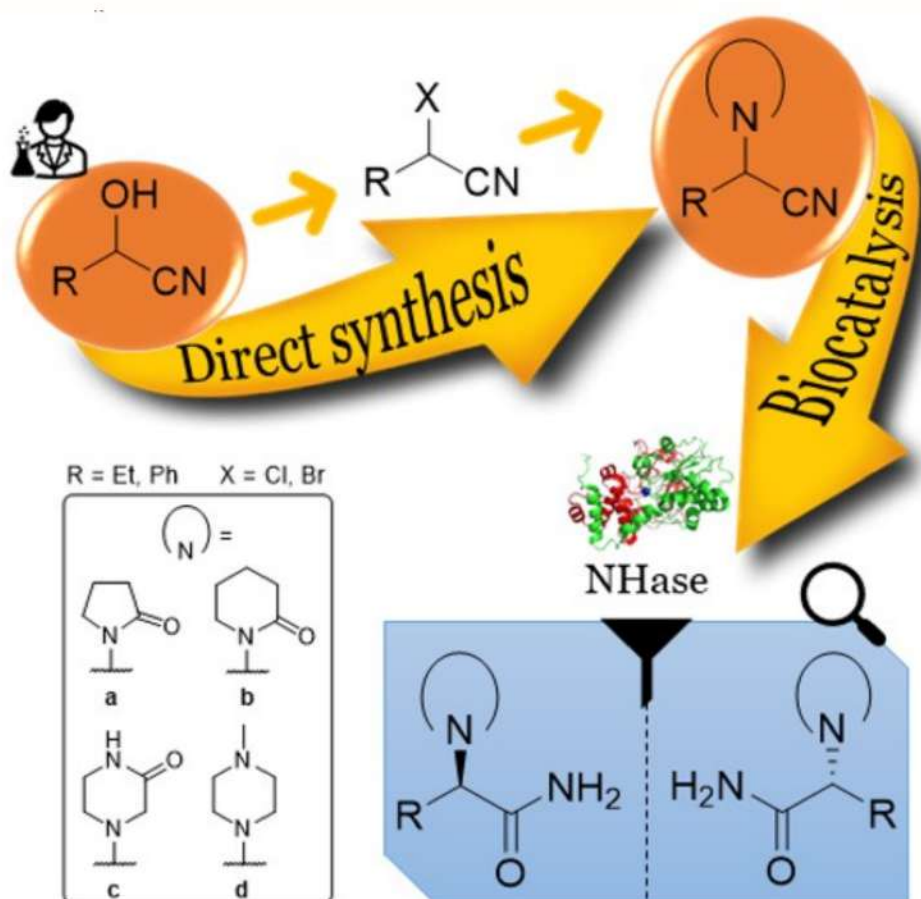


Eclética Química Journal

Volume 47 • number 2 • year 2022



Chemoenzymatic synthesis

Levetiracetam analogs:
chemoenzymatic synthesis,
absolute configuration
assignment and evaluation

Sugarcane bagasse biochar

Sugarcane bagasse biochar
pellets for removal of
caffeine, norfloxacin, and
ciprofloxacin in aqueous
samples

Lactic acid

Separation of lactic acid and
by-products obtained by
catalytic conversion of glycerol
using high-performance liquid

Metastable phase

Ni-Nb-Zr metastable
phases formation, a
thermodynamic and
chemical approach



UNIVERSIDADE ESTADUAL PAULISTA

Reitor

Pasqual Barretti

Vice-Reitora

Maysa Furlan

Pró-Reitora de Graduação

Celia Maria Giacheti

Pró-Reitora de Pós-Graduação

Maria Valnice Boldrin

Pró-Reitor de Pesquisa

Edson Cocchieri Botelho

Pró-Reitor de Extensão Universitária e Cultura

Raul Borges Guimarães

Pró-Reitor de Planejamento Estratégico e Gestão

Estevão Tomomitsu Kimpara



INSTITUTO DE QUÍMICA

Diretor

Sidney José Lima Ribeiro

Vice-Diretora

Denise Bevilaqua

Editorial Team

Editor-in-Chief

Prof. Assis Vicente Benedetti, São Paulo State University, Institute of Chemistry, Araraquara, Brazil

Editors

Prof. Antonio Eduardo Mauro, São Paulo State University, Institute of Chemistry, Araraquara, Brazil

Prof. Horacio Heinzen, University of the Republic, Faculty of Chemistry, Montevideo, Uruguay

Prof. Marcos Carlos de Mattos, Federal University of Ceará, Center of Sciences, Fortaleza, Brazil

Prof. Maria Célia Bertolini, São Paulo State University, Institute of Chemistry, Araraquara, Brazil

Prof. Patrícia Hatsue Suegama, Federal University of Grande Dourados, Faculty of Exact and Technological Sciences, Dourados, Brazil

Prof. Paulo Clairmont Feitosa Lima Gomes, São Paulo State University, Institute of Chemistry, Araraquara, Brazil

Editorial Board

Prof. Bayardo Baptista Torres, University of São Paulo, Institute of Chemistry, São Paulo, Brazil

Prof. Enric Brillas, University of Barcelona, Faculty of Chemistry, Barcelona, Spain

Prof. Francisco de Assis Leone, University of São Paulo, Faculty of Philosophy, Sciences and Literature, Ribeirão Preto, Brazil

Prof. Ivano Gerardt Rolf Gutz, University of São Paulo, Institute of Chemistry, São Paulo, Brazil

Prof. Jairton Dupont, Federal University of Rio Grande do Sul, Institute of Chemistry, Porto Alegre, Brazil

Prof. José Antônio Maia Rodrigues, University of Porto, Faculty of Sciences, Porto, Portugal

Prof. Lauro Kubota, University of Campinas, Institute of Chemistry, São Paulo, Brazil

Prof. Massuo Jorge Kato, University of São Paulo, Institute of Chemistry, São Paulo, Brazil

Prof. Roberto Santana da Silva, University of São Paulo, Faculty of Pharmaceutical Sciences, Ribeirão Preto, Brazil

Prof. Verónica Cortés de Zea Bermudez, University of Trás-os-Montes and Alto Douro, School of Life and Environmental Sciences, Vila Real, Portugal

EDITORIAL PRODUCTION

Ctrl K Produção Editorial – Araraquara, Brazil

digite@ctrlk.com.br

Editorial

The Editor of Eclética Química Journal proudly announces the second issue of 2022. In this issue the readers find a first article describing a chemoenzymatic approach for the synthesis of eight α -*N*-heterocyclic ethyl- and phenylacetamides and screening of twenty nitrile hydratases. The authors evaluated different proportions of ionic liquids and polyethylene glycol as potential green solvents to substitute aqueous buffered solutions to avoid a retro-Strecker reaction of α -aminonitriles and the effect of temperature to optimize the process. The use of unconventional reaction media and low temperatures reduced the nitrile hydratases activity. The absolute configuration of the compounds was determined by electronic circular dichroism spectroscopy and the racemic levetiracetam derivatives showed non inhibitory effect on cholinesterase. Follow, it is presented a quick and straightforward methodology to separate lactic acid and glycerol by high-performance liquid chromatography (HPLC). Glycerol is a by-product of biodiesel obtention and its conversion to lactic acid makes the glycerol industry more profitable, since lactic acid is applied in the textile, cosmetic and food industries, in the synthesis of polylactic acid and as precursor of solvents in green chemistry. A central composite design (CCD) was proposed to study the influence of experimental variables on glycerolysis reaction and HPLC was used to separate and quantify lactic acid. The next article describes the adsorbent efficiency of sugarcane bagasse biochar for removal of caffeine, ciprofloxacin, and norfloxacin from wastewater. The biochar, without chemical and physical activation, was obtained from sugarcane by torrefaction at different temperatures from 260 to 290 °C and characterized by different spectroscopic, microscopic and thermal analysis techniques besides point of zero charge, pH, elemental composition, and surface area determination. The biochar prepared at 280 °C showed the best stability and higher performance in the adsorption of pharmaceutical compounds. Complete this issue, considerations to elucidate some understanding about two metastable phases found in a rapid quenched alloy from Ni-Nb-Zr system during the solidification process. Metastable phases are formed when materials are produced out of the equilibrium conditions, and there is no universal knowledge related to the formation of these phases, but the understanding of metastable phases formation can produce and improve promising technological materials. The hypothesis discussed consider free energies of formation among phases which compete to nucleate, stability of crystalline phases at nanoscale and atomic pair preferences during the nucleation.

The Editor and his team wish to express their sincere thanks to the authors and reviewers for their outstanding collaboration and kindly invite you to submit your manuscript to **Eclética Química Journal**.

Assis Vicente Benedetti
Editor-in-Chief of EQJ

Citation databases: Ecletica Quim. J. is indexed



*Click on the images to follow the links.

EBSCO has no link available. The address is for subscribers only.

INSTRUCTIONS FOR AUTHORS

BEFORE YOU SUBMIT

1. Check [Eclét. Quim. J.'s focus and scope](#)

Eclética Química Journal is a peer-reviewed quarterly publication of the Institute of Chemistry of São Paulo State University (UNESP). It publishes original researches as articles, reviews and short reviews in **all areas of Chemistry**.

2. Types of papers

- a. Original articles
- b. Reviews
- c. Short reviews
- d. Communications
- e. Technical notes
- f. Articles in education in chemistry and chemistry-related areas

Manuscripts submitted for publication as full articles and communications must contain original and unpublished results and should not have been submitted elsewhere either partially or whole.

a. Original articles

The manuscript must be organized in sections as follows:

1. Introduction
 2. Experimental
 3. Results and Discussion
 4. Conclusions
- References

Sections titles must be written in bold and sequentially numbered; only the first letter should be in uppercase letter. Subsections, numbered as exemplified, should be written in normal and italic letters; only the first letter should be in uppercase letter.

Example:

1. Introduction

1.1 History

2. Experimental

2.1 Surface characterization

2.1.1 Morphological analysis

b. Reviews

Review articles should be original and present state-of-the-art overviews in a coherent and concise form covering the

most relevant aspects of the topic that is being revised and indicate the likely future directions of the field. Therefore, before beginning the preparation of a Review manuscript, send a letter (one page maximum) to the Editor with the subject of interest and the main topics that would be covered in the Review manuscript. The Editor will communicate his decision in two weeks. Receiving this type of manuscript does not imply acceptance to be published in **Eclét. Quím. J.** It will be peer-reviewed.

c. Short reviews

Short reviews should present an overview of the state-of-the-art in a specific topic within the scope of the Journal and limited to 5,000 words. Consider a table or image as corresponding to 100 words. Before beginning the preparation of a Short Review manuscript, send a letter (one page maximum) to the Editor with the subject of interest and the main topics that would be covered in the Short Review manuscript.

d. Communications

Communications should cover relevant scientific results and are limited to 1,500 words or three pages of the Journal, not including the title, authors' names, figures, tables and references. However, Communications suggesting fragmentation of complete contributions are strongly discouraged by Editors.

e. Technical notes

Descriptions of methods, techniques, equipment or accessories developed in the authors' laboratory, as long as they present chemical content of interest. They should follow the usual form of presentation, according to the peculiarities of each work. They should have a maximum of 25 pages, including figures, tables, diagrams, etc.

f. Articles in education in chemistry and chemistry-correlated areas

Research manuscript related to undergraduate teaching in Chemistry and innovative experiences in undergraduate and graduate education. They should have a maximum of 25 pages, including figures, tables, diagrams, and other elements.

3. Special issues

Special issues with complete articles dedicated to Symposia and Congresses and to special themes or in honor of scientists with relevant contributions in Chemistry and correlate areas can be published by **Eclét. Quím. J.** under the condition that a previous agreement with Editors is established. All the guides of the journal must be followed by the authors.

4. Approval

Ensure all authors have seen and approved the final version of the article prior to submission. All authors must also approve the journal you are submitting to.

ETHICAL GUIDELINES

Before starting the submission process, please be sure that **all ethical aspects mentioned below were followed.** Violation of these ethical aspects may preclude authors from submitting or publishing articles in **Eclét. Quím. J.**

a. Coauthorship: The corresponding author is responsible for listing as coauthors only researchers who have really taken part in the work, for informing them about the entire manuscript content and for obtaining their permission to submit and publish it.

b. Nonauthors: Explicit permission of a nonauthor who has collaborated with personal communication or discussion to the manuscript being submitted to **Eclet. Quím. J.** must be obtained before being cited.

c. Unbiased research: Authors are responsible for carefully searching for all the scientific work relevant to their reasoning irrespective of whether they agree or not with the presented information.

d. Citation: Authors are responsible for correctly citing and crediting all data taken from other sources. This requirement is not necessary only when the information is a result of the research presented in the manuscript being submitted to **Eclet. Chem. J.**

e. Direct quotations: The word-for-word reproduction of data or sentences as long as placed between quotation marks and correctly cited is not considered ethical deviation when indispensable for the discussion of a specific set of data or a hypothesis.

f. Do not cite: Master's Degree dissertations and PhD theses are not accepted; instead, you must cite the publications resulted from them.

g. Plagiarism: Plagiarism, self-plagiarism, and the suggestion of novelty when the material was already published are unaccepted by **Eclet. Quím. J.** Before reviewing a manuscript, the **Turnitin antiplagiarism software** will be used to detect any ethical deviation.

h. Simultaneous submissions of the same manuscript to more than one journal is considered an ethical deviation and is conflicted to the declaration has been done below by the authors.

i. Studies with humans or other animals: Before submitting manuscripts involving human beings, materials from human or animals, the authors need to confirm that the procedures established, respectively, by the institutional committee on human experimentation and Helsinki's declaration, and the recommendations of the animal care institutional committee were followed. Editors may request complementary information on ethical aspects.

COPYRIGHT NOTICE

The corresponding author transfers the copyright of the submitted manuscript and all its versions to **Eclet. Quím. J.**, after having the consent of all authors, which ceases if the manuscript is rejected or withdrawn during the review process.

When a published manuscript in **Eclet. Quím. J.** is also published in other Journal, it will be immediately withdrawn from **Eclet. Quím. J.** and the authors informed of the Editor decision.

Self-archive to institutional, thematic repositories or personal webpage is permitted just after publication. The articles published by **Eclet. Quím. J.** are licensed under the [Creative Commons Attribution 4.0 International License](#).

PUBLICATION CHARGES

Eclética Química Journal is supported by the Institute of Chemistry/UNESP and publication is free of charge for authors.

MANUSCRIPT PREPARATION

COVER LETTER

We provide a template to help you prepare your cover letter. To download it, click [here](#).

The cover letter **MUST** include:

1. Identification of authors

- a. The authors' full names (they must be written in full and complete, separated by comma)

João M. José	Incorrect
J. M. José	Incorrect
João Maria José	Correct!

- b. E-mail addresses and affiliations (**neither more nor less than two instances**) of all authors;
- c. ORCID ID links;
- d. A plus sign (+) indicating the corresponding author.

Example:

Author Full Name¹⁺, Author Full Name²

1. University, Faculty or Institute, City, Country.
2. Company, Division or Sector or Laboratory, City, Country.

+ Author 1: address@mail.com, ORCID: <https://orcid.org/xxxx-xxxx-xxxx-xxxx>

Author 2: address@mail.com, ORCID: <https://orcid.org/xxxx-xxxx-xxxx-xxxx>

2. Authors' contribution

We request authors to include author contributions according to CRediT taxonomy standardized contribution descriptions. **CRediT (Contributor Roles Taxonomy)** is a high-level taxonomy, including 14 roles, that can be used to represent the roles typically played by contributors to scientific scholarly output. The roles describe each contributor's specific contribution to the scholarly output.

- a. Please, visit this link (<https://casrai.org/credit/>) to find out which role(s) the authors fit into;
- b. Do not modify the role names; do not write "all authors" in any role. Do not combine two or more roles in one line.**
- c. If there are any roles that no author has engaged in (such as funding in papers that were not funded), write "Not applicable" in front of the name of the role;
- d. Write the authors' names according to the **American Chemistry Society (ACS) citation style**.

Example:

Conceptualization: Foster, J. C.; O'Reilly, R. K.

Data curation: Varlas, S.; Couturaud, B.; Coe, J.; O'Reilly, R. K.

Formal Analysis: Foster, J. C.; Varlas, S.

Funding acquisition: Not applicable.

Investigation: Foster, J. C.; O'Reilly, R. K.

Methodology: Coe, J.; O'Reilly, R. K.

Project administration: O'Reilly, R. K.

Resources: Coe, J.

Software: Not applicable.

Supervision: O'Reilly, R. K.

Validation: Varlas, S.; Couturaud, B.

Visualization: Foster, J. C.

Writing – original draft: Foster, J. C.; Varlas, S.; Couturaud, B.; Coe, J.; O'Reilly, R. K.

Writing – review & editing: Foster, J. C.; Varlas, S.; Couturaud, B.; Coe, J.; O'Reilly, R. K.

4. Indication of reviewers

We kindly ask the authors to suggest **five** suitable reviewers, providing full name, affiliation, and email.

5. Other information

- a. The authors must write one paragraph remarking the novelty and relevance of the work;
- b. The corresponding author must declare, on behalf of the other authors, that the manuscript being submitted is original and its content has not been published previously and is not under consideration for publication elsewhere;
- c. The authors must inform if there is any conflict of interest.

6. Acknowledgements and funding

Acknowledgements and funding information will be requested after the article is accepted for publication.

7. Data availability statement

A data availability statement informs the reader where the data associated with your published work is available, and under what conditions they can be accessed. Therefore, authors must inform if:

Data will be available upon request;

All dataset were generated or analyzed in the current study; or

Data sharing is not applicable.

MANUSCRIPT

We provide a template to help you prepare your manuscript. To download it, click [here](#).

1. General rules

Only manuscripts written in English will be accepted. British or American usage is acceptable, but they should not be mixed. Non-native English speakers are encouraged to have their manuscripts professionally revised before submission.

Manuscripts must be sent in editable files as *.doc, *.docx or *.odt. The text must be typed using font style Times New Roman and size 12. Space between lines should be 1.5 mm and paper size A4, top and bottom margins 2.5 cm, left and right margins 2.0 cm.

All contributions must include an **abstract** (170 words maximum), **three to five keywords** and a **graphical abstract** (8 cm wide × 8 cm high).

Supplementary information: all type of articles accepts supplementary information (SI) that aims at complementing the main text with material that, for any reason, cannot be included in the article.

TITLE

The title should be concise, explanatory and represent the content of the work. The title must have only the first letter of the sentence in uppercase. The following are not allowed: acronyms, abbreviations, geographical location of the research, en or em dashes (which must be replaced by a colon). Titles do not have full point.

ABSTRACT

Abstract is the summary of the article. The abstract must be written as a running text not as structured topics, but its content should present background, objectives, methods, results, and conclusion. It cannot contain citations. The text should be written in a single paragraph with a **maximum of 170 words**.

KEYWORDS

Keywords are intended to make it easier for readers to find the content of your text. As fundamental tools for database indexing, they act as a gateway to the text. The correct selection of keywords significantly increases the chances that a document will be found by researchers on the topic, and consequently helps to promote the visibility of an article within a myriad of publications.

FIGURES, TABLES AND EQUATIONS

Figures, tables and equations must be written with initial capital letter followed by their respective number and period, in bold, without adding zero “**Table 1**”, preceding an explanatory title. Tables, Figures and Equations should appear after the first citation and should be numbered according to the ascending order of appearance in the text (1, 2, 3...).

Figures, tables, schemes and photographs already published by the same or different authors in other publications may be reproduced in manuscripts of **Eclét. Quim. J.** only with permission from the editor house that holds the copyright.

Nomenclature, abbreviations, and symbols should follow IUPAC recommendations.

DATA AVAILABILITY STATEMENT

The data availability statement informs the reader where the data associated with your work is available, and under what conditions they can be accessed. They also include links (where applicable) to the data set.

- a. The data are available in a data repository (cite repository and the DOI of the deposited data);
- b. The data will be available upon request;
- c. All data sets were generated or analyzed in the current study;
- d. Data sharing is not applicable (in cases where no data sets have been generated or analyzed during the current study, it should be declared).

GRAPHICAL ABSTRACT

The graphical abstract must summarize the manuscript in an interesting way to catch the attention of the readers. As already stated, it must be designed with 8 cm wide × 8 cm high, and a 900-dpi resolution is mandatory for this journal. It must be submitted as *.jpg, *.jpeg, *.tif or *.ppt files as supplementary file.

We provide a template to help you prepare your GA. To download it, click [here](#).

SUPPLEMENTARY INFORMATION

When appropriate, important data to complement and a better comprehension of the article can be submitted as Supplementary File, which will be published online and will be made available as links in the original article. This might include additional figures, tables, text, equations, videos or other materials that are necessary to fully document the research contained in the paper or to facilitate the readers' ability to understand the work.

Supplementary material should be presented in appropriate .docx file for text, tables, figures and graphics. All supplementary figures, tables and videos should be referred in the manuscript body as "Table S1, S2...", "Fig. S1, S2..." and "Video S1, S2 ...".

At the end of the main text the authors must inform: This article has supplementary information.

Supplementary information will be located following the article with a different DOI number from that of the article, but easily related to it.

CITATION STYLE GUIDE

From 2021 on, the **Eclet. Quim. J.** will follow the [ACS citation style](#).

Indication of the sources is made by authorship and date. So, the reference list is organized alphabetically by author.

Each citation consists of two parts: the in-text citation, which provides brief identifying information within the text, and the reference list, a list of sources that provides full bibliographic information.

We encourage the citation of primary research over review articles, where appropriate, in order to give credit to those who first reported a finding. Find out more about our commitments to the principles of [San Francisco Declaration on Research Assessment \(DORA\)](#).

What information you must cite?

- a. Exact wording taken from any source, including freely available websites;
- b. Paraphrases of passages;
- c. Summaries of another person's work;
- d. Indebtedness to another person for an idea;
- e. Use of another researchers' work;
- f. Use of your own previous work.

You do not need to cite **common knowledge**.

Example:

Water is a tasteless and odorless liquid at room temperature (common knowledge, no citation needed)

In-text citations

You can choose to cite your references within or at the end of the phrase, as showed below.

Within the cited information:

One author: Finnegan states that the primary structure of this enzyme has also been determined (2004).

Two authors: Finnegan and Roman state that the structure of this enzyme has also been determined (2004).

Three or more authors: Finnegan *et al.* state that the structure of this enzyme has also been determined (2004).

At the end of the cited information:

One author: The primary structure of this enzyme has also been determined (Finnegan, 2004).

Two authors: The primary structure of this enzyme has also been determined (Finnegan and Roman, 2004).

Three or more authors: The primary structure of this enzyme has also been determined (Finnegan *et al.*, 2004).

If you need to cite more than one reference in the same brackets, separate them with semicolon and write them in alphabetic order:

The primary structure of this enzyme was determined (Abel *et al.*, 2011; Borges, 2004; Castro *et al.*, 2021).

Bibliographic references

Article from scientific journals

Foster, J. C.; Varlas, S.; Couturaud, B.; Coe, J.; O'Reilly, R. K. Getting into Shape: Reflections on a New Generation of Cylindrical Nanostructures' Self-Assembly Using Polymer Building Block. *J. Am. Chem. Soc.* **2019**, *141* (7), 2742–2753. <https://doi/10.1021/jacs.8b08648>

Book

Hammond, C. *The Basics of Crystallography and Diffraction*, 4th ed.; International Union of Crystallography Texts on Crystallography, Vol. 21; Oxford University Press, 2015.

Book chapter

Hammond, C. Crystal Symmetry. In *The Basics of Crystallography and Diffraction*, 4th ed.; International Union of Crystallography Texts on Crystallography, Vol. 21; Oxford University Press, 2015; pp 99–134.

Book with editors

Mom the Chemistry Professor: Personal Accounts and Advice from Chemistry Professors Who Are Mothers, 2nd ed.; Woznack, K., Charlebois, A., Cole, R. S., Marzabadi, C. H., Webster, G., Eds.; Springer, 2018.

Website

ACS Publications Home Page. <https://pubs.acs.org/> (accessed 2019-02-21).

Document from a website

American Chemical Society, Committee on Chemical Safety, Task Force for Safety Education Guidelines. *Guidelines for Chemical Laboratory Safety in Academic Institutions*. American Chemical Society, 2016. <https://www.acs.org/content/dam/acsorg/about/governance/committees/chemicalsafety/publications/acs-safety-guidelines-academic.pdf> (accessed 2019-02-21).

Conference proceedings

Nilsson, A.; Petersson, F.; Persson, H. W.; Jönsson, H. Manipulation of Suspended Particles in a Laminar Flow. In *Micro Total Analysis Systems 2002, Proceedings of the μ TAS 2002 Symposium*, Nara, Japan, November 3–7, 2002; The Netherlands, 2002; pp 751–753. https://doi.org/10.1007/978-94-010-0504-3_50

Governmental and legislation information

Department of Commerce, United States Patent and Trademark Office. Section 706.02 Rejection of Prior Art [R-

07.2015]. *Manual of Patent Examining Procedure (MPEP)*, 9th ed., rev. 08.2017, last revised January 2018. <https://www.uspto.gov/web/offices/pac/mpep/s706.html#d0e58220> (accessed 2019-03-20).

Patent

Lois-Caballe, C.; Baltimore, D.; Qin, X.-F. Method for Expression of Small RNA Molecules within a Cell. US 7 732 193 B2, 2010.

Streaming data

American Chemical Society. Game of Thrones Science: Sword Making and Valyrian Steel. *Reactions*. YouTube, April 15, 2015. <https://www.youtube.com/watch?v=cHRcGoje4j4> (accessed 2019-02-28).

For more information, you can access the [ACS Style Quick Guide](#) and the [Williams College LibGuides](#).

SUBMITTING YOUR MANUSCRIPT

The corresponding author should submit the manuscript online by clicking [here](#). If you are a user, register by clicking [here](#).

At the **User home** page, click in **New submission**.

In Step 1, select a section for your manuscript, verify one more time if you followed all these rules in **Submission checklist**, add Comments for the Editor if you want to, and click Save and continue.

In Step 2, you will **upload your manuscript**. Remember it will pass through a double-blind review process. So, do not provide any information on the authorship.

In Step 3, enter **submission's metadata**: authors' full names, valid e-mail addresses and ORCID ID links (with "http" not "https"). Add title, abstract, contributors and supporting agencies, and the list of references.

In Step 4, upload the **cover letter**, the **graphical abstract** and other **supplementary material** you want to include in your manuscript.

In Step 5, you will be able to check all submitted documents in the **File summary**. If you are certain that you have followed all the rules until here, click in **Finish submission**.

REVIEW PROCESS

The time elapsed between the submission and the first response of the reviewers is around three months. The average time elapsed between submission and publication is around seven months.

Resubmission (manuscripts "rejected in the present form" or subjected to "revision") must contain a letter with the responses to the comments/criticism and suggestions of reviewers/editors should accompany the revised manuscript. All modifications made to the original manuscript must be highlighted.

If you want to check our Editorial process, click [here](#).

EDITOR'S REQUIREMENTS

Authors who have a manuscript accepted in **Eclet. Quim. J.** may be invited to act as reviewers.

Only the authors are responsible for the correctness of all information, data and content of the manuscript submitted to **Eclet. Quim. J.** Thus, the Editors and the Editorial Board cannot accept responsibility for the correctness of the material published in **Eclet. Quim. J.**

Proofs

After accepting the manuscript, **Eclet. Quim. J.** technical assistants will contact you regarding your manuscript page proofs to correct printing errors only, i.e., other corrections or content improvement are not permitted. The proofs shall be returned in three working days (72 h) via email.

Appeal

Authors may only appeal once about the decision regarding a manuscript. To appeal against the Editorial decision on your manuscript, the corresponding author can send a rebuttal letter to the editor, including a detailed response to any comments made by the reviewers/editor. The editor will consider the rebuttal letter, and if deemed appropriate, the manuscript will be sent to a new reviewer. The Editor decision is final.

Contact

If you have any question, please contact our team:

Prof. Assis Vicente Benedetti
Editor-in-Chief
ecletica.iq@unesp.br

Letícia Amanda Miguel and Jéssica Odoni
Technical support
ecletica@ctrlk.com.br

SUMMARY

EDITORIAL BOARD	3
EDITORIAL	4
DATABASE	5
INSTRUCTIONS FOR AUTHORS.....	6

ORIGINAL ARTICLES

Levetiracetam analogs: chemoenzymatic synthesis, absolute configuration assignment and evaluation of cholinesterase inhibitory activities 17
Cintia Duarte de Freitas Milagre, Bruno Sergio do Amaral, João Marcos Batista Junior, Adriana Ferreira Lopes Vilela, Carmen Lúcia Cardoso, Humberto Marcio Santos Milagre

Separation of lactic acid and by-products obtained by catalytic conversion of glycerol using high-performance liquid chromatography 74
Andreza de Faria Alves Cruz, Gabriella Pinho Dias, Flávia de Rezende Bittencourt, Donato Alexandre Gomes Aranda

Sugarcane bagasse biochar pellets for removal of caffeine, norfloxacin, and ciprofloxacin in aqueous samples..... 82
Mateus Cottorello Fonsêca, César Augusto Marasco Júnior, Diógenes dos Santos Dias, João Pedro da Silva, Rafaela Silva Lamarca, Clóvis Augusto Ribeiro, Lorena Oliveira Pires, Paulo Clairmont Feitosa de Lima Gomes

Ni-Nb-Zr metastable phases formation, a thermodynamic and chemical approach..... 97
Leonardo Pratavieira Deo

Levetiracetam analogs: chemoenzymatic synthesis, absolute configuration assignment and evaluation of cholinesterase inhibitory activities

Cintia Duarte de Freitas Milagre^{1+✉}, Bruno Sergio do Amaral^{1✉}, João Marcos Batista Junior^{2,3✉}, Adriana Ferreira Lopes Vilela^{4✉}, Carmen Lúcia Cardoso^{4✉}, Humberto Marcio Santos Milagre^{1✉}

1. São Paulo State University, Institute of Chemistry, Araraquara, Brazil.
2. Federal University of São Carlos, Department of Chemistry, São Carlos, Brazil.
3. Federal University of São Paulo, Institute of Science and Technology, São José dos Campos, Brazil.
4. University of São Paulo, Faculty of Philosophy, Sciences and Letters, Ribeirão Preto, Brazil.

+Corresponding author: Cintia Duarte de Freitas Milagre, **Phone:** +55 16 33019668, **Email address:** cintia.milagre@unesp.br

ARTICLE INFO

Article history:

Received: July 19, 2021

Accepted: September 14, 2021

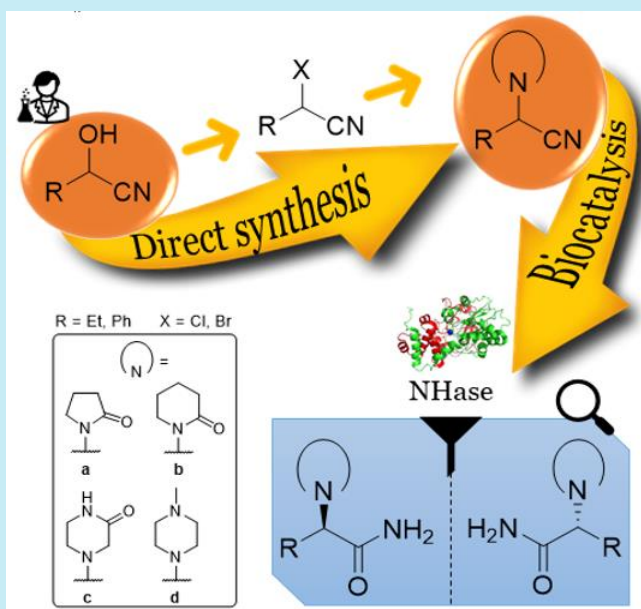
Published: April 01, 2022

Keywords

1. *N*-heterocycles
2. *N*-alkylation
3. biocatalysis
4. electronic circular dichroism (ECD)

Section Editor: Assis Vicente Benedetti

ABSTRACT: A chemoenzymatic approach for the synthesis of α -*N*-heterocyclic ethyl- and phenylacetamides, levetiracetam analogs, is described. Eight nitrile substrates were prepared through the *N*-alkylation of heterocycles (2-pyrrolidinone, 2-piperidinone, 2-oxopiperazine and 1-methylpiperazine) directly from hydroxyl group of ethyl and phenyl α -hydroxynitriles with yield of 35–71% after 12 h. Twenty nitrile hydratases (NHases) were screened and showed that the *N*-derivatives lactam substrates led to their correspondent amides by Co-type NHase with conversion and enantiomeric excess of up to 47.5 and 52.3% for (*S*)-enantiomer, while the piperazine substrates underwent spontaneous decomposition by retro-Strecker reaction. In order to avoid a retro-Strecker reaction of α -aminonitriles, ionic liquids and polyethylene glycol (PEG₄₀₀) were evaluated as alternative green solvents to aqueous buffered solutions in different proportions. Temperature was another parameter investigated during reaction-medium engineering for process optimization. However, unconventional reaction media and low temperature significantly reduced the NHase activity. The absolute configuration of α -*N*-heterocyclic ethyl- and phenylacetamides, some of which were new compounds, was determined using electronic circular dichroism (ECD) spectroscopy. Additionally, their potential as cholinesterase's inhibitors was evaluated.



1. Introduction

N-heterocycles are a key structural unit, which are vastly distributed among natural products and biomolecules, such as DNA and RNA, and correspond to more than 70% of all pharmaceuticals and agrochemicals (Liu *et al.*, 2019; Saini *et al.*, 2013). In addition, they play an important role in materials science, photonics, supramolecular and polymer chemistry (Chen *et al.*, 2019; Hong *et al.*, 2016). Therefore, given their importance, there is an increasing interest in synthesizing compounds bearing an *N*-heterocyclic scaffold. An interesting example in pharmaceuticals is levetiracetam (((2*S*)-2-oxopyrrolidin-1-yl)butanamide, Keppra) (Fig. 1), an antiepileptic drug that contains a pyrrolidinone unit and is commercialized by UCB Pharma, with sales over € 790 million in 2018, where € 221 million corresponded to the US market, € 216 million to the European market and € 352 million to international markets. Its patent in Japan expired in 2020, which impacted the US sales net by generic competition (UCB, 2019). In 2020, the continued generic erosion in the US has been compensated by recovery from a local, one-time rebate adjustment in Europe and continued growth in international markets, where in Japan the UCB team took over distribution of E Keppra from their former partner, reporting net sales of € 788 million. The incorporation of levetiracetam in the Brazilian public health care system (Sistema Único de Saúde, SUS) was approved in December of 2017 (Brazil, 2017).

During levetiracetam discovery and development, a structure-activity-based study by Kenda *et al.* (2004) showed that the amide moiety, as well as the C4-aliphatic chain, is essential for its pharmacological activity. Moreover, the asymmetric center should have (*S*) absolute configuration and pyrrolidinone is preferable over piperazine or *N*-aliphatic derivatives. To this end, several synthetic routes to levetiracetam have been described in the literature (Anuradha and Preeti, 2013; Chaudhry *et al.*, 2014; Krasowski and McMillin, 2014; Lyseng-Williamson, 2011a; 2011b; Narczyk *et al.*, 2019; Tucker *et al.*, 2009; Uges and Vecht, 2010). However, many of these are long, require an excess of chemicals and solvents that commonly results in the loss of material and use hazardous reagents. It may also involve extreme temperatures (from -78 to 200 °C), protection/deprotection steps and the need of either chromatographic separation or chemical resolution leading to low-efficiency processes from economic and environmental perspectives.

Nowadays, complementary catalytic alternatives to stoichiometric reagents for chemical transformations, such as chemoenzymatic synthetic strategies, are mature and widely adopted in the industrial manufacturing of fine chemicals and active pharmaceutical ingredients, with the aim of making organic synthesis greener (Bisogno *et al.*, 2017; Hönig *et al.*, 2017; Sheldon and Pereira, 2017; Souza *et al.*, 2017). Commercially, levetiracetam is currently produced via a chemoenzymatic process, where the biocatalytic step corresponds to the kinetic resolution of a racemic 2-pyrrolidinonylnitrile catalyzed by an engineered nitrile hydratase (94% enantiomeric excess [*ee*], 43% yield), followed by enantiomeric enrichment (> 99% *ee*) through recrystallization and recycling of the undesired (*R*)-enantiomer by base-mediated racemization (Fig. 1) (Tucker *et al.*, 2009).

Nitrile hydratases (NHase, EC 4.2.1.84) are metalloproteins that contain either non-heme iron(III) or non-corrin cobalt(III) centers in their active site—or zinc in the case of NHases from *Myrothecium verrucaria*—and catalyze the hydration of nitrile into the corresponding amide, without formation of carboxylic acid as a coproduct. The enzyme consists of α - and β -subunits, with the active site being located at the interface of the two subunits (D'Antona and Morrone, 2010). The metal cofactor is bound to the α -subunit, and although the substrate is linked to this subunit, the individual subunit has no catalytic activity (Nelp *et al.*, 2014). The Fe-type NHase exhibits photoreactivity regulated by nitric oxide (NO), while the Co-type NHase does not. Empirical observations relate preferential substrate affinity of Fe-type NHase for small aliphatic nitriles, while Co-type NHase displays preferential affinity for aromatic nitriles due to the differences in their substrate binding pockets (Miyanaga *et al.*, 2004; van Pelt *et al.*, 2011). Initial studies indicated a low stereoselectivity for NHases, where the stereoselective conversion of a nitrile to the corresponding carboxylic acid was conducted by amidases (EC 3.2.1.4) or nitrilases (EC 3.5.5.1), which are other important enzymes in the pathways of nitrile metabolism in nature (Shen *et al.*, 2012). However, even if a poor stereoselectivity is detected for an NHase, it can be engineered through directed evolution, rational design, or combined approaches to generate enzymes with higher stereoselectivity. In addition, the enantioselectivity can be further improved by medium engineering (Tao *et al.*, 2010). The opportunities, as well as many of the challenges, come together in the hydration of bulky nitriles.

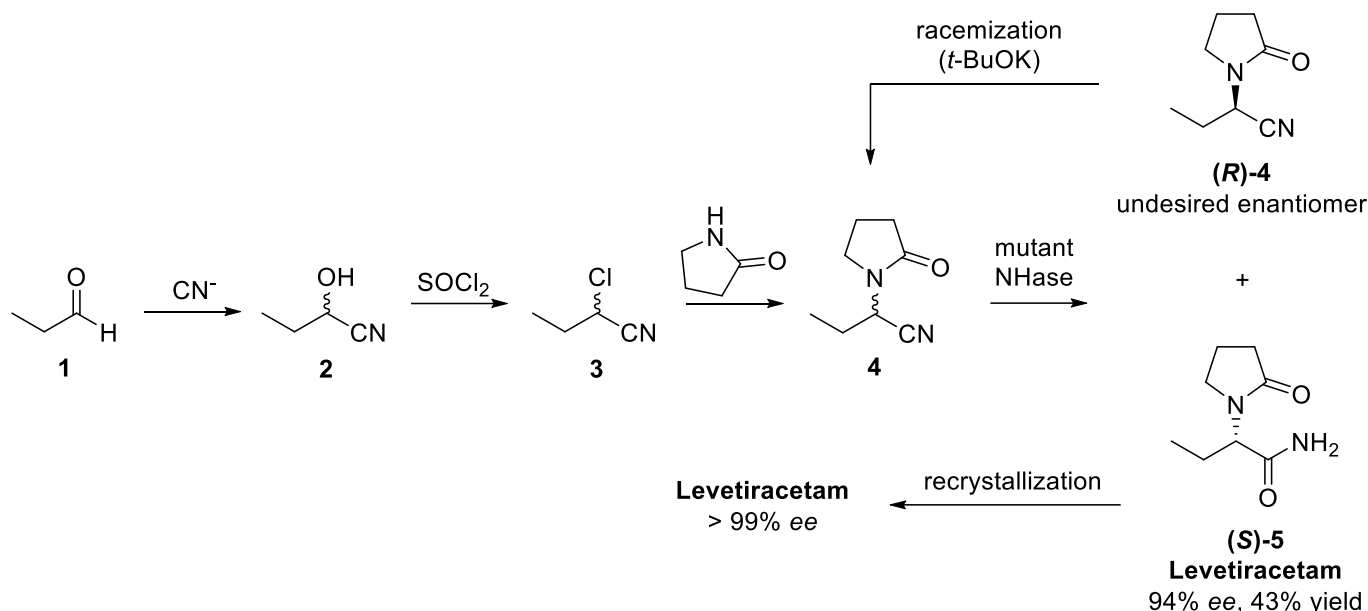


Figure 1. Chemoenzymatic route to levetiracetam using nitrile hydratase (NHase).

Source: Elaborated by the authors using data from [Tucker et al. \(2009\)](#).

In this work, a set of 20 commercially available NHases had their substrate scope and enantioselectivity evaluated towards an ethyl and phenylacetone nitrile series of α -*N*-substituted heterocycles to assess potential biological activities. Initially, the synthetic route used inexpensive aldehydes (propionaldehyde and benzaldehyde) to build α -hydroxynitriles, which had their hydroxyl group substituted by a better leaving group, such as chlorine, with subsequent substitution of chlorine by *N*-heterocycles (2-pyrrolidinone, 2-piperidinone, 2-oxopiperazine and 1-methylpiperazine). However, it was found that the direct *N*-alkylation of these heterocycles could be achieved in high yields directly from the α -hydroxynitriles, thus shortening the route in one step. In addition to the Co-type and Fe-type NHases screening, medium engineering focusing on evaluation of solvent systems to avoid a retro-Strecker reaction in aqueous buffered media, as well as the temperature influence, was investigated. The absolute configuration of α -*N*-heterocyclic ethyl- and phenylacetamides, some of which were new compounds, was determined using electronic circular dichroism (ECD) spectroscopy. Finally, an inhibition assay for acetylcholinesterase was carried out using the freshly prepared α -*N*-heterocyclic ethyl- and phenylacetamides.

2. Experimental

Unless otherwise noted, all reagents and solvents obtained from commercial suppliers were used without

further purification. The 20 nitrile hydratases were obtained from Prozomix Limited ([Prozomix, 2020](#)). Macherey-Nagel Gel 60 F₂₅₄ plates were used for analytical thin layer chromatography (TLC) and visualization under UV light (254 nm) for aromatic compounds or spray reagents (phosphomolybdic acid ethanol solution or *p*-anisaldehyde–sulfuric acid solution) for aliphatic compounds. Dry-column flash chromatography was performed on silica Gel (230–400 mesh) ([Casey et al., 1990](#)). ¹H and ¹³C nuclear magnetic resonance (NMR) spectra were recorded on a Bruker–Fourier 300 operating in 300.19 and 75.48 Hz, respectively, in deuterated chloroform (CDCl₃) or deuterated dimethylsulfoxide (DMSO-*d*₆). ¹⁹F NMR spectra were recorded on a Bruker Avance 400 operating in 376.48 Hz in DMSO-*d*₆. All NMR chemical shifts were expressed in ppm and coupling constants (*J*) in Hertz (Hz), using the solvent signal as internal standard. Fourier transform infrared (FT-IR) were recorded in Thermo Scientific Nicolet iS5 and the scan range was from 4000 to 500 cm⁻¹ in KBr pellet. Melting points (MPs) were measured on a digital device Microquímica MQAPF-302, with a resolution of 0.1 °C in coverslips.

Enzymatic reactions conversions were determined by Shimadzu GC-2010 Plus gas chromatography (GC) equipped with an auto-injector AOC-20i, fitted with a flame ionization detector (FID) and a fused silica capillary column Rtx-5 RESTEK 30 m × 0.25 mm × 0.25 μm. Temperature program: 80 °C (3 min), gradient 30 °C min⁻¹ to 280 °C (5 min). T_{injector} = 260 °C,

$T_{\text{detector}} = 300\text{ }^{\circ}\text{C}$. H_2 was used as carrier gas at a column flow rate of 1.22 mL min^{-1} . Gas chromatography-mass spectrometry analysis (GC-MS) was performed on a Shimadzu GC-2010 plus GC coupled to a Shimadzu MSQP 2010 Plus mass-selective detector in electron ionization (EI, 70 eV) mode. The GC-MS oven was fitted with a fused silica capillary column DB-5 J&W Scientific $30\text{ m} \times 0.25\text{ mm} \times 0.25\text{ }\mu\text{m}$. The same gas chromatography-flame ionization detector (GC-FID) analysis conditions were employed for GC-MS analysis, but with helium as carrier gas.

Enantiomeric excesses (*ees*) were determined by high-performance liquid chromatography (HPLC). Jasco analytical instruments modular HPLC system contained Jasco PU-2089 pump, a Jasco AS-2055 injector, a Jasco MD-2010 diode array detector and a Jasco CD-2095 circular dichroism. Enantiomeric separation of **5a**, **5b** and **9b** were performed using the Chiralcel OD-H column ($250 \times 4.6\text{ mm}$, $5\text{ }\mu\text{m}$, Daicel) in isocratic elution mode with a mixture of *n*-hexane/propan-2-ol 90:10 (v/v) as mobile phase. The enantiomeric separation of **9a** was performed using the Chiralcel IC column ($250 \times 4.6\text{ mm}$, $5\text{ }\mu\text{m}$, Daicel) in isocratic elution with a mixture of hexane/propan-2-ol 70:30 (v/v) as mobile phase. Flow rate was 1.0 mL min^{-1} and circular dichroism operating in 220 nm. Retention times were: (+)-(*R*)-**5a** 18.0 min; (-)-(*S*)-**5a** 24.3 min, (*R*)-**5b** 18.7 min; (*S*)-**5b** 30.0 min, (*R*)-**9a** 31.9 min; (*S*)-**9a** 42.2 min, (*S*)-**9b** 19.8 min; (*R*)-**9b** 24.7 min. The compound (-)-(*S*)-**5a** was confirmed with authentic standard levetiracetam $\geq 98\%$ (Sigma-Aldrich, Saint, Louis, MO, USA) by high-performance liquid chromatography/diode array detector coupled with circular dichroism detection (HPLC-DAD-CD) analysis. The ECD spectra of each enantiomer of **5b**, **9a** and **9b** eluting from the chiral HPLC were measured in the Jasco CD-2095 detector by trapping in a 3.0 cm quartz cell through a switching valve. The spectra were average computed over three instrumental scans, and the intensities are presented in terms of ellipticity values (mdeg). The ECD spectra were baseline corrected by subtraction from a measurement obtained for the same solvent used, as described above.

2.1 General procedure for the synthesis of 2-hydroxybutanenitrile (2)

The aliphatic α -hydroxynitrile **2** was synthesized from propionaldehyde **1** (1 mmol), sodium cyanide (1 mmol) and NaHSO_3 (1 mmol) according to the Young *et al.* (2003) procedure. The crude product was purified by dry-column flash chromatography

(heptane/EtOAc gradient), furnishing **2** as a colorless liquid (70% yield). Infrared (KBr) ν/cm^{-1} 3431, 2976, 2941, 2883, 2248, 1463, 1123, 1104, 1059, 1025, 982; MS (EI 70 eV) m/z (%): 59 (30), 58 (30), 57 (100), 56 (30); ^1H NMR (300.19 MHz, CDCl_3) δ 4.44 (t, 1H, J 6.6 Hz, CH), 1.96–1.80 (m, 2H, CH_2), 1.10 (t, 3H, J 7.4 Hz, CH_3); ^{13}C NMR (75.48 MHz, CDCl_3) δ 119.93 (C_0), 62.48 (CH), 28.49 (CH_2), 8.91 (CH_3).

Caution: all procedures involving sodium cyanide were performed in a well-ventilated lab-hood equipped with a calibrated HCN detector. NeutraliMass spectrometry of HCN-containing waste was performed with commercial bleach (14% sodium hypochlorite solution). The wastes were then stored over a large excess of bleach for disposal.

2.2 Procedure for the synthesis of α -halonitriles (3 and 7)

Based on Choi *et al.* (2016), 0.335 mg of phosphoryl bromide (1.17 mmol) was weighed in a round bottom flask and closed with a rubber septum. With a glass syringe, 450 μL of anhydrous benzene, 195 μL of pyridine (2.4 mmol) and 85 mg of **2** (1 mmol) were added. The reaction mixture was stirred at room temperature for 24 h and the solvent was evaporated under reduced pressure. The residue was diluted in 10 mL of EtOAc and the crude mixture was washed with water ($3 \times 10\text{ mL}$). The organic phase was dried over anhydrous MgSO_4 and the solvent was evaporated, furnishing **3** as a purple liquid (15% yield). Mass spectrometry analysis (EI 70 eV) m/z (%): 121 (12), 119 (12), 81 (13), 79 (13), 68 (83), 52 (16), 41 (100), 39 (57).

The 2-chloro-2-phenylacetonitrile **7** was synthesized from mandelonitrile **6** (1 mmol), pyridine (1.1 mmol) and SOCl_2 (1.1 mmol) in chloroform, according to the Zhang *et al.* (2013) procedure. The crude product was purified by dry-column flash chromatography (hexane/EtOAc gradient), furnishing **7** as a yellow oil (63% yield). Mass spectrometry analysis (EI 70 eV) m/z (%): 59 (30), 58 (30), 57 (100), 56 (30); ^1H NMR (300.19 MHz, CDCl_3) δ 7.58–7.53 (m, 2H, Ar-H), 7.48–7.45 (m, 3H, Ar-H), 5.56 (s, 1H, CH).

2.3 General procedure for the synthesis of α -substituted *N*-heterocyclic nitriles (4a–b and 8a–b)

The reactions were carried out using Teflon-lined stainless-steel autoclave and equipped with a magnetic stirrer, based on the method described by Jenner (1989).

In a typical experiment, $\text{RuCl}_3 \cdot x\text{H}_2\text{O}$ (3.5 mol%) dissolved in 1 mmol of α -hydroxynitrile (2-hydroxybutanenitrile **2** or mandelonitrile **6**) and 5 mmol of nucleophile 2-pyrrolidinone **a** or 2-piperidinone **b** were introduced into the polytetrafluoroethylene (PTFE)-lined stainless steel synthesis autoclave. The autoclave was closed and heated up to 150 °C for 12 h with magnetic stirring and endogenous pressure. The reaction mixture was cooled down to room temperature followed by addition of 5 mL of EtOAc, filtration through filter paper and washing with water basified with NaOH at pH 10 (2×3 mL). The organic phase was dried over anhydrous MgSO_4 and the solvent was evaporated under reduced pressure to give a crude mixture (brown oil), which was purified by dry-column flash chromatography (heptane/EtOAc gradient).

2-(2-oxopyrrolidin-1-yl)butanenitrile (**4a**): orange oil, 38% yield. Purification by dry silica chromatography, 100% EtOAc, IR (KBr) ν/cm^{-1} 3515, 2976, 2938, 2881, 2243, 1690, 1417, 1281, 1216, 933, 814, 642, 567; MS (EI 70 eV) m/z (%): 152 (M^+), 124 (21), 123(100), 112 (37), 84 (17), 69 (66), 68 (35), 41 (50); ^1H NMR (300.19 MHz, CDCl_3) δ 5.01 (t, 1H, J 8.1 Hz, CH), 3.58–3.36 (m, 2H, CH_2^*), 2.43 (t, 2H, J 8.0 Hz, CH_2^*), 2.23–2.00 (m, 2H, CH_2^*), 2.00–1.84 (m, 1H, CH_2), 1.84–1.67 (m, 1H, CH_2), 1.03 (t, 3H, J 7.4 Hz, CH_3); ^{13}C NMR (75.48 MHz, CDCl_3) δ 174.88 (C_0^*), 117.12 (C_0), 44.32 (CH), 43.56 (CH_2^*), 30.47 (CH_2^*), 24.97 (CH_2^*), 17.92 (CH_2), 10.23 (CH_3); *2-oxopyrrolidin-1-yl hydrogens and carbons.

2-(2-oxopiperidin-1-yl)butanenitrile (**4b**): orange oil, 39% yield. Purification by dry silica chromatography, heptane/EtOAc 1:9, IR (KBr) ν/cm^{-1} 3527, 2936, 2878, 2240, 1651, 1487, 1348, 1289, 1178, 1069, 980, 930, 554; MS (EI 70 eV) m/z (%): 166 (M^+), 151 (35), 138 (32), 137 (36), 109 (100), 99 (72), 98 (79), 82 (34), 67 (32), 55 (75), 41 (39); ^1H NMR (300.19 MHz, CDCl_3) δ 5.67 (t, 1H, J 8.2 Hz, CH), 3.54–3.52 (m, 1H, CH_2^*), 3.35–3.25 (m, 1H, CH_2^*), 2.46 (t, 2H, J 6.5 Hz, CH_2^*), 1.93–1.70 (m, 6H, 2CH_2^* and CH_2), 1.03 (t, 3H, J 7.4 Hz, CH_3); ^{13}C NMR (75.48 MHz, CDCl_3) δ 169.87 (C_0^*), 117.77 (C_0), 46.04 (CH), 43.98 (CH_2^*), 32.31 (CH_2^*), 24.25 (CH_2^*), 23.04 (CH_2), 21.05 (CH_2^*), 10.20 (CH_3); *2-oxopiperidin-1-yl hydrogens and carbons.

2-(2-oxopyrrolidin-1-yl)-2-phenylacetonitrile (**8a**): brown oil, 42% yield. Purification by dry silica chromatography, heptane/EtOAc 2:8, IR (KBr) ν/cm^{-1} 3426, 2923, 2243, 1687, 1493, 1455, 1411 1263, 947, 743, 701; MS (EI 70 eV) m/z (%): 200 (M^+), 145 (51), 144 (57), 117 (74), 116 (64), 104 (25), 89 (34), 77 (11); ^1H NMR (300.19 MHz, CDCl_3) δ 7.46–7.38 (m, 5H, Ar-H), 6.47 (s, 1H, CH), 3.56–3.44 (m, 1H, CH_2^*),

3.14–3.04 (m, 1H, CH_2^*), 2.58–2.36 (m, 2H, CH_2^*), 2.20–1.91 (m, 2H, CH_2^*); ^{13}C NMR (75.48 MHz, CDCl_3) δ 174.69 (C_0^*), 131.67 (C_0 , Ar-C), 129.54 (Ar-CH, 3C), 127.27 (Ar-CH, 2C), 115.75 (C_0 , CN), 46.66 (CH), 43.23 (CH_2^*), 30.40 (CH_2^*), 17.65 (CH_2^*); *2-oxopyrrolidin-1-yl hydrogens and carbons.

2-(2-oxopiperidin-1-yl)-2-phenylacetonitrile (**8b**): brown oil, 45% yield. Purification by dry silica chromatography, heptane/EtOAc 3:7, IR (KBr) ν/cm^{-1} 3520, 2939, 2244, 1641, 1485, 1273, 1171, 1076, 981, 921, 821, 725, 695, 651, 544; MS (EI 70 eV) m/z (%): 214 (M^+), 170 (47), 158 (46), 116 (61), 104 (29), 89 (33), 55 (43); ^1H NMR (300.19 MHz, CDCl_3) δ 7.50–7.32 (m, 5H, Ar-H), 7.21 (s, 1H, CH), 3.48–3.36 (m, 1H, CH_2^*), 3.03–2.90 (m, 1H, CH_2^*), 2.64–2.42 (m, 2H, CH_2^*), 1.92–1.72 (m, 4H, CH_2^*); ^{13}C NMR (75.48 MHz, CDCl_3) δ 169.93 (C_0^*), 132.04 (C_0 , Ar-C), 129.36 (Ar-CH, 3C), 127.38 (Ar-CH, 2C), 116.30 (C_0 , CN), 47.99 (CH), 43.81 (CH_2^*), 32.46 (CH_2^*), 22.99 (CH_2^*), 21.12 (CH_2^*); *2-oxopiperidin-1-yl hydrogens and carbons.

2.4 General procedure for the synthesis of α -substituted *N*-heterocyclic nitriles (**4c–d** and **8c–d**)

Based on [Altenkämper et al. \(2009\)](#), 1 mmol of 2-hydroxybutanenitrile **2** or mandelonitrile **6** was dissolved in 0.5 mL acetonitrile (HPLC grade) and 3 mmol of 2-oxopiperazine **c** or 1-methylpiperazine **d** were added. The mixture was heated under reflux for 5–8 h (for reactions with 2-hydroxybutanenitrile) and 20–24 h (for reactions with mandelonitrile). After removing the acetonitrile under reduced pressure, 5 mL EtOAc was added, and the crude mixture was washed with a saturated solution of K_2CO_3 (3×3 mL). The organic phase was dried over anhydrous MgSO_4 , and the solvent was evaporated to yield the expected product.

2-(3-oxopiperazin-1-yl)butanenitrile (**4c**): white solid, 20% yield. Melting point 114–115 °C; IR (KBr) ν/cm^{-1} 3266, 2975, 2940, 2883, 2798, 2227, 1664, 1347, 1170, 1077, 855, 753, 622; MS (EI 70 eV) m/z (%): 167 (M^+), 138 (98), 110 (100), 99 (31), 97 (27), 42 (82), 41 (35); ^1H NMR (300.19 MHz, CDCl_3) δ 6.37 (bs, 1H, NH), 3.56–3.12 (m, 5H, CH and 2CH_2^*), 2.96–2.84 (m, 1H, CH_2^*), 2.75–2.58 (m, 1H, CH_2^*), 1.94–1.75 (m, 2H, CH_2), 1.08 (t, 3H, J 7.4 Hz, CH_3); ^{13}C NMR (75.48 MHz, CDCl_3) δ 168.31 (C_0^*), 116.21 (C_0 , CN), 58.76 (CH), 53.28 (CH_2^*), 46.39 (CH_2^*), 41.18 (CH_2^*), 24.43 (CH_2), 10.64 (CH_3); *3-oxopiperazin-1-yl hydrogens and carbons.

2-(4-methylpiperazin-1-yl)butanenitrile (**4d**): yellow oil, 38% yield. Infrared (KBr) ν/cm^{-1} 2937, 2878, 2797, 2222, 1456, 1377, 1285, 1167, 1010, 859, 809; MS (EI 70 eV) m/z (%): 167 (M^+), 141 (3), 140 (4), 111 (13), 99 (100), 70 (31), 56 (66); ^1H NMR (300.19 MHz, CDCl_3) δ 3.39 (dd, 1H, J 8.6, 7.1 Hz, CH), 2.82–2.67 (m, 2H, CH_2^*), 2.64–2.40 (m, 6H, CH_2^*), 2.32 (s, 3H, CH_3^*), 1.91–1.66 (m, 2H, CH_2), 1.06 (t, 3H, J 7.4 Hz, CH_3); ^{13}C NMR (75.48 MHz, CDCl_3) δ 117.02 (C_0), 59.55 (CH), 54.82 (CH_2^* , 4C), 45.85 (CH_3^*), 24.47 (CH_2), 10.76 (CH_3); *4-methylpiperazin-1-yl hydrogens and carbons.

2-(3-oxopiperazin-1-yl)-2-phenylacetoneitrile (**8c**): white solid, 22% yield. Melting point 173–175 °C; IR (KBr) ν/cm^{-1} 3439, 3208, 2972, 2893, 2849, 2231, 1666, 1497, 1334, 1156, 1069, 758, 710, 521; MS (EI 70 eV) m/z (%): 215 (M^+), 186 (7), 171 (9), 145 (16), 116 (73), 99 (100), 89 (25), 43 (29), 42 (64); ^1H NMR (300.19 MHz, $\text{DMSO}-d_6$) δ 7.91 (s, 1H, NH), 7.51–7.39 (m, 5H, Ar-H), 5.52 (s, 1H, CH), 3.26–3.05 (m, 3H, CH_2^*), 2.85 (d, 1H, J 15.9 Hz, CH_2^*), 2.74–2.62 (m, 1H, CH_2^*), 2.62–2.53 (m, 1H, CH_2^*); ^{13}C NMR (75.48 MHz, $\text{DMSO}-d_6$) δ 166.42 (C_0^*), 132.54 (C_0 , Ar-C), 128.96 (Ar-CH, 3C), 127.75 (Ar-CH, 2C), 115.48 (C_0 , CN), 59.57 (CH), 53.16 (CH_2^*), 45.42 (CH_2^*), 40.02 (CH_2^*); *3-oxopiperazin-1-yl hydrogens and carbons.

2-(4-methylpiperazin-1-yl)-2-phenylacetoneitrile (**8d**): yellow solid, 71% yield. Melting point 63–64 °C; IR (KBr) ν/cm^{-1} 3442, 3064, 2946, 2827, 2792, 2223, 1450, 1285, 1144, 1010, 914, 812, 736, 700; MS (EI 70 eV) m/z (%): 215 (M^+), 116 (10), 99 (100), 70 (19), 56 (60), 44 (37), 42 (26); HRMS (ESI) m/z , observed: 216.1489; $\text{C}_{13}\text{H}_{17}\text{N}_3$ [$M+\text{H}$] $^+$ requires: 216.1495; ^1H NMR (300.19 MHz, CDCl_3) δ 7.56–7.47 (m, 2H, Ar-H), 7.45–7.33 (m, 3H, Ar-H), 4.82 (s, 1H, CH), 2.63 (m, 4H, CH_2^*), 2.47 (m, 4H, CH_2^*), 2.31 (s, 3H, CH_3^*); ^{13}C NMR (75.48 MHz, CDCl_3) δ 133.10 (C_0 , Ar-C), 129.01 (Ar-CH, 3C), 128.09 (Ar-CH, 2C), 115.45 (C_0 , CN), 62.14 (CH), 54.87 (CH_2^* , 4C), 45.89 (CH_3^*); *4-methylpiperazin-1-yl hydrogens and carbons.

2.5 General procedure for the synthesis of racemic amides (5a–b, 5d, 9a–b and 9d)

Based on González-Vera *et al.* (2005), 1 mmol of the corresponding α -substituted *N*-heterocyclic nitriles (**4a–b**, **4d** and **8a–b** and **8d**) were dissolved in 4 mL CH_2Cl_2 and followed by addition of 1.7 mL concentrated H_2SO_4 . The mixture was stirred at room temperature (at different reaction times according to each compound, as shown below). After that, the reaction mixture was taken to an ice bath, neutralized

with NaOH and extracted with EtOAc (3×10 mL). The organic phases were combined, dried over anhydrous MgSO_4 and the solvent was evaporated under vacuum. Further purification was not necessary.

2-(2-oxopyrrolidin-1-yl)butanamide (**5a**): reaction time 4 h, white solid, 80% yield. Melting point 116–117 °C; IR (KBr) ν/cm^{-1} 3392, 3320, 3255, 3204, 2966, 2922, 2871, 1677, 1271, 1442, 694, 629; MS (EI 70 eV) m/z (%): 170 (M^+), 126 (100), 98 (12), 69 (28), 58 (13), 41 (26); ^1H NMR (300.19 MHz, CDCl_3) δ 6.33 (bs, 1H, CONH_2), 5.46 (bs, 1H, CONH_2), 4.45 (dd, 1H, J 8.8, 6.9 Hz, CH), 3.49–3.35 (m, 2H, CH_2^*), 2.54–2.35 (m, 2H, CH_2^*), 2.12–1.89 (m, 3H, CH_2^* and CH_2), 1.78–1.61 (m, 1H, CH_2), 0.91 (t, 3H, J 7.4 Hz, CH_3); ^{13}C NMR (75.48 MHz, CDCl_3) δ 176.26 (C_0^*), 172.41 (C_0), 56.30 (CH), 44.07 (CH_2^*), 31.20 (CH_2^*), 21.15 (CH_2^*), 18.28 (CH_2), 10.62 (CH_3); *2-oxopyrrolidin-1-yl hydrogens and carbons.

2-(2-oxopiperidin-1-yl)butanamide (**5b**): reaction time 60 h, brown solid, 21% yield. Melting point 106–108 °C; IR (KBr) ν/cm^{-1} 3351, 3204, 2947, 2872, 1675, 1626, 1465, 1419, 1288, 1181, 976, 668; MS (EI 70 eV) m/z (%): 184 (M^+), 167 (7), 141 (10), 140 (100), 112 (25), 70 (12), 55 (24), 41 (13); ^1H NMR (300.19 MHz, CDCl_3) δ 6.33 (bs, 1H, CONH_2), 5.33 (bs, 1H, CONH_2), 5.00 (dd, 1H, J 8.5, 7.3 Hz, CH), 3.32–3.17 (m, 2H, CH_2^*), 2.59–2.30 (m, 2H, CH_2^*), 2.00–1.65 (m, 6H, 2CH_2^* and CH_2), 0.91 (t, 3H, J 7.4 Hz, CH_3); ^{13}C NMR (75.48 MHz, CDCl_3) δ 172.74 (C_0^*), 171.48 (C_0), 57.37 (CH), 43.40 (CH_2^*), 32.64 (CH_2^*), 23.25 (CH_2^*), 20.94 (CH_2^*), 20.13 (CH_2), 10.58 (CH_3); *2-oxopiperidin-1-yl hydrogens and carbons.

2-(4-methylpiperazin-1-yl)butanamide (**5d**): Reaction time 22 h, orange oil, 28% yield. Infrared (KBr) ν/cm^{-1} 3357, 2962, 2798, 1671, 1459, 1284, 1172, 1010, 866, 640; MS (EI 70 eV) m/z (%): 185 (M^+), 142 (10), 141 (100), 98 (50), 70 (65), 56 (21), 42 (29); ^1H NMR (300.19 MHz, CDCl_3) δ 6.77 (bs, 1H, CONH_2), 5.57 (bs, 1H, CONH_2), 2.82 (dd, 1H, J 7.4, 5.2, CH), 2.76–2.48 (m, 8H, 4CH_2^*), 2.36 (s, 3H, CH_3^*), 1.83–1.65 (m, 2H, CH_2), 0.99 (t, J 7.5, CH_3); ^{13}C NMR (75.48 MHz, CDCl_3) δ 175.86 (C_0), 70.62 (CH), 55.48 (4CH_2^*), 45.88 (CH_3^*), 21.56 (CH_2), 11.03 (CH_3); *4-methylpiperazin-1-yl hydrogens and carbons.

2-(2-oxopyrrolidin-1-yl)-2-phenylacetamide (**9a**): reaction time 20 h, white solid, 96% yield. Melting point 156–157 °C; IR (KBr) ν/cm^{-1} 3383, 3314, 3257, 3201, 2964, 2924, 2872, 1674, 1423, 1270, 702, 619, 549; MS (EI 70 eV) m/z (%): 174 (100), 131 (36), 106 (18), 91 (19), 77 (9), 70 (1); ^1H NMR (300.19 MHz, CDCl_3) δ 7.41–7.35 (m, 5H, Ar-H), 5.94 (bs, 1H, CONH_2), 5.89 (s, 1H, CH), 5.75 (bs, 1H, CONH_2), 3.78–3.65 (m, 1H, H-12), 3.10–2.98 (m, 1H, CH_2^*),

2.56–2.30 (m, 2H, CH₂*), 2.09–1.99 (m, 1H, CH₂*), 1.971.82 (m, 1H, CH₂*); ¹³C NMR (75.48 MHz, CDCl₃) δ 175.82 (C₀*), 171.44 (C₀), 134.33 (C₀, Ar-C), 129.30 (Ar-CH, 2C), 129.12 (Ar-CH, 2C), 128.88 (Ar-CH, 1C), 58.74 (CH), 45.02 (CH₂*), 31.08 (CH₂*), 18.19 (CH₂*); *2-oxopyrrolidin-1-yl hydrogens and carbons.

2-(2-oxopiperidin-1-yl)-2-phenylacetamide (**9b**): reaction time 60 h, brown solid, 58% yield. Melting point 154–155 °C; IR (KBr) ν/cm^{-1} 3313, 3161, 2960, 2869, 1697, 1613, 1484, 1412, 1296, 1178, 740, 701, 516; MS (EI 70 eV) m/z (%): 232 (M⁺), 215 (12), 189 (17), 188 (100), 91 (45), 82 (20), 55 (18); ¹H NMR (300.19 MHz, CDCl₃) δ 7.47–7.30 (m, 5H, Ar-H), 6.34 (s, 1H, CH), 5.92 (bs, 1H, CONH₂), 5.64 (bs, 1H, CONH₂), 3.52–3.38 (m, 1H, CH₂*), 2.96–2.84 (m, 1H, CH₂*), 2.60–2.39 (m, 2H, CH₂*), 1.90–1.60 (m, 4H, 2CH₂*); ¹³C NMR (75.48 MHz, CDCl₃) δ 171.70 (C₀*), 171.10 (C₀), 134.52 (C₀, Ar-C), 129.70 (Ar-CH, 2C), 128.96 (Ar-CH, 2C), 128.65 (Ar-CH, 1C), 60.34 (CH), 45.27 (CH₂*), 32.57 (CH₂*), 23.30 (CH₂*), 21.04 (CH₂*); *2-oxopiperidin-1-yl hydrogens and carbons.

2-(4-methylpiperazin-1-yl)-2-phenylacetamide (**9d**): reaction time 23 h, brown solid, 85% yield. Melting point 163–165 °C; IR (KBr) ν/cm^{-1} 3405, 3176, 2949, 2795, 1655, 1449, 1291, 1157, 1011, 854, 692, 663; MS (EI 70 eV) m/z (%): 233 (M⁺), 190 (14), 189 (100), 146 (13), 91 (37), 70 (35), 56 (16), 42 (22); ¹H NMR (300.19 MHz, CDCl₃) δ 7.39–7.28 (m, 5H, Ar-H), 6.85 (bs, 1H, CONH₂), 5.62 (bs, 1H, CONH₂), 3.86 (s, 1H, CH), 2.57 (m, 8H, 4CH₂*), 2.35 (s, 3H, CH₃*); ¹³C NMR (75.48 MHz, CDCl₃) δ 174.02 (C₀), 135.55 (C₀, Ar-C), 128.94 (Ar-CH, 2C), 128.85 (Ar-CH, 2C), 128.59 (Ar-CH, 1C), 75.75 (CH), 55.10 (4CH₂*), 45.54 (CH₃*); *4-methylpiperazin-1-yl hydrogens and carbons.

2.6 Enzymatic activity assay

Five microliters of NHases were suspended in 1 mL of Na-phosphate buffer (0.1 mol L⁻¹, pH 7.00) in an Eppendorf tube followed by addition of *n*-butanenitrile (1 mg, 14.5 μmol). The reaction was allowed to proceed for 1 min at 25 °C and 1000 rpm. After this period, the reaction was interrupted by the addition of 500 μL of EtOAc and the organic phase was analyzed by GC-FID. The enzymatic activity was measured by monitoring the *n*-butanenitrile consumption through the analytical curve ($y = 20972x + 7121.9$, $R^2 = 0.990$). All enzymatic assays were performed in Na-phosphate buffer enriched with 0.8 μg L⁻¹ of CoCl₃·6H₂O and 0.8 μg L⁻¹ FeCl₃·6H₂O. Before performing the enzymatic assays

with Fe-type NHases, the enzymes were light reactivated by incubating them in Na-phosphate buffer (0.1 mol L⁻¹, pH 7.0) on ice bath under sunlight for 1.5 h.

2.7 General procedure for NHase-catalyzed synthesis of amides in buffered aqueous medium

In an Eppendorf tube, 1 mL of Na-phosphate buffer (0.1 mol L⁻¹, pH 7.00), 10 μL of NHases, and 5 μmol of substrate (**4a–d** and **8a–d**) were added. The reactions were allowed to proceed for 48 h at 25 °C and 1000 rpm. After that, 500 μL EtOAc was added and the mixture vortexed and centrifuged at 5000 rpm for 1 min. The organic phase was analyzed by GC-FID to determine the conversion rates. Enantiomeric excesses were determined by HPLC-DAD-CD (EtOAc was eliminated under mild heating, 35 °C, and samples were dissolved in propan-2-ol). Control assays were carried out under the same experimental conditions; however, in the absence of the NHases.

2.8 General procedure for ionic liquids synthesis

Ionic liquids have been synthesized in two steps. Firstly 1-butyl-3-methylimidazolium chloride (BMIM.Cl) was prepared. Then, a metathesis reaction between the salt containing the corresponding anion and an alkali metal cation gave the ionic liquid (IL) of interest.

2.8.1 Synthesis of 1-butyl-3-methylimidazolium chloride

N-methylimidazole and 1-chlorobutane were refluxed in acetonitrile following the same procedure described by Dupont *et al.* (2002) furnishing BMIM.Cl. The white solid highly hygroscopic was obtained in 88% yield and stored under N₂. ¹H NMR (300.19 MHz, DMSO-*d*₆) δ 9.14 (s, 1H, CH*), 7.73 (dt, 2H, *J* 20.3, 1.7 Hz, CH*), 4.15 (t, 2H, *J* 7.2 Hz, CH₂), 3.84 (s, 3H, CH₃*), 1.84–1.67 (m, 2H, CH₂), 1.33–1.13 (m, 2H, CH₂), 0.90 (t, 3H, *J* 7.3 Hz, CH₃); ¹³C NMR (75.48 MHz, DMSO-*d*₆) δ 136.70 (CH*), 123.60 (CH*), 122.28 (CH*), 48.42 (CH₂), 35.73 (CH₃*), 31.39 (CH₂), 18.78 (CH₂), 13.30 (CH₃); *3-methylimidazolium hydrogens and carbons.

2.8.2 General procedure for the synthesis of the ionic liquids of interest

An equimolar mixture of salt (NaBF_4 , KPF_6 or LiNTf_2) and BMIM.Cl was vigorously stirred at room temperature for 24 h in excess of acetone. The reaction mixture was filtered in celite column and concentrated under reduced pressure and mild heating (30 °C). The obtained viscous liquid was dissolved in CH_2Cl_2 and washed with water (3×). The organic phase was dried over anhydrous MgSO_4 under stirring for 1 h, followed by solvent evaporation under reduced pressure giving the IL.

1-butyl-3-methylimidazolium tetrafluoroborate (BMIM.BF_4): ^1H NMR (300.19 MHz, $\text{DMSO-}d_6$) δ 9.06 (s, 1H, CH^*), 7.74 (t, 1H, J 1.8 Hz, CH^*), 7.67 (t, 1H, J 1.7 Hz, CH^*), 4.13 (t, 2H, J 7.2 Hz, CH_2), 3.82 (s, 3H, CH_3^*), 1.82–1.67 (m, 2H, CH_2), 1.23 (dq, 2H, J 14.5, 7.3 Hz, CH_2), 0.88 (t, 3H, J 7.3 Hz, CH_3); ^{13}C NMR (75.48 MHz, $\text{DMSO-}d_6$) δ 136.51 (CH^*), 123.65 (CH^*), 122.30 (CH^*), 48.54 (CH_2), 35.76 (CH_3^*), 31.38 (CH_2), 18.81 (CH_2), 13.30 (CH_3). ^{19}F NMR (376.48 MHz, $\text{DMSO-}d_6$) δ -148.29, -148.34; DSC -67 °C (T_g , crystallization temperature) and -74 °C (T_m , melting temperature); *3-methylimidazolium hydrogens and carbons.

1-butyl-3-methylimidazolium hexafluorophosphate (BMIM.PF_6): ^1H NMR (300.19 MHz, $\text{DMSO-}d_6$) δ 9.07 (s, 1H, CH^*), 7.74 (t, 1H, J 1.8 Hz, CH^*), 7.67 (t, 1H, J 1.7 Hz, CH^*), 4.13 (t, 2H, J 7.2 Hz, CH_2), 3.82 (s, 3H, CH_3^*), 1.84–1.63 (m, 2H, CH_2), 1.23 (m, 2H, CH_2), 0.88 (t, 3H, J 7.3 Hz, CH_3); ^{13}C NMR (75.48 MHz, $\text{DMSO-}d_6$) δ 136.52 (CH^*), 123.65 (CH^*), 122.29 (CH^*), 48.54 (CH_2), 35.76 (CH_3^*), 31.37 (CH_2), 18.80 (CH_2), 13.29 (CH_3). ^{19}F NMR (376.48 MHz, $\text{DMSO-}d_6$) δ -70.20 (d, J 711.4 Hz); DSC -64 °C (T_g) and 6 °C (T_m); *3-methylimidazolium hydrogens and carbons.

1-butyl-3-methylimidazolium bis(trifluoromethylsulfonyl)imide (BMIM.NTf_2): ^1H NMR (300.19 MHz, $\text{DMSO-}d_6$) δ 9.07 (s, 1H, CH^*), 7.74 (t, 1H, J 1.8 Hz, CH^*), 7.67 (t, 1H, J 1.7 Hz, CH^*), 4.13 (t, 2H, J 7.2 Hz, CH_2), 3.82 (s, 3H, CH_3^*), 1.81–1.66 (m, 2H, CH_2), 1.32–1.15 (m, 2H, CH_2), 0.88 (t, 3H, J 7.3 Hz, CH_3); ^{13}C NMR (75.48 MHz, $\text{DMSO-}d_6$) δ 136.53 (CH^*), 123.65 (CH^*), 122.30 (CF_3), 121.65 (CH^*), 117.36 (CF_3), 48.54 (CH_2), 35.77 (CH_3^*), 31.38 (CH_2), 18.80 (CH_2), 13.29 (CH_3); ^{19}F NMR (376.48 MHz, $\text{DMSO-}d_6$) δ -78.73 (s); DSC -85 °C (T_g) and -2.5 °C (T_m); *3-methylimidazolium hydrogens and carbons.

2.9 General procedure for NHase-catalyzed synthesis of amides in nonconventional media

The reactions were carried out under monophasic system (buffer: PEG400 and BMIM.BF_4) or biphasic system (buffer: BMIM.PF_6 and BMIM.NTf_2). The final volume of all reactions was 1 mL. The ratios of buffer: ionic liquids were 10, 20, 40 and 80% (v/v) and buffer PEG400 were 10, 25, 50, 95 and 100% (v/v).

In an Eppendorf tube 1 mL of buffer: nonconventional media solution was added, followed by 10 μL of PRO-NHASE(001) or PRO-NHASE(015) and 5 μmol of substrate (**4a–d** and **8a–d**). The reactions were allowed to proceed for 48 h at 25 °C and 1500 rpm. After that 500 μL of Et_2O was added to BMIM.BF_4 , BMIM.PF_6 and PEG400 reactions, and 500 μL EtOAc to BMIM.NTf_2 reactions. The mixture was vortexed and centrifuged at 5000 rpm for 1 min. The organic phase was analyzed by GC-FID for conversion measurements.

2.10 Electronic circular dichroism calculations

All density functional theory (DFT) and time-dependent-DFT (TDDFT) calculations were carried out at 298 K in the gas phase with the Gaussian 09 (2016) software. Calculations were performed for the arbitrarily chosen *S*-configuration for **5b** and **9a–9b**. The conformational searches were carried out at the molecular mechanics level of theory with the Monte Carlo algorithm employing the MM+ force field, incorporated in HyperChem 8.0.10 software. Initially, for compound (*S*)-**5b**, ten conformers with a relative energy (rel E.) within 6 kcal mol⁻¹ were selected and geometry optimized at the B3LYP/6-31G(d) level. The six conformers with rel E. < 1.8 kcal mol⁻¹ were selected for UV and ECD spectral calculations. Regarding (*S*)-**9a** and (*S*)-**9b**, the conformational searches resulted in six conformers for both compounds, with rel E. within 6 kcal mol⁻¹, which were geometry optimized at the B3LYP/6-31G(d) level. The four and two conformers, respectively, with rel E. < 2.0 kcal mol⁻¹ were selected for UV and ECD spectral calculations. Vibrational analysis at the B3LYP/6-31G(d) level resulted in no imaginary frequencies for all conformers, confirming them as real minima. The TDDFT was employed to calculate the excitation energy (in nm) and rotatory strength *R* in the dipole velocity (R_{vel} in cgs units: 10⁻⁴⁰ esu² cm²) form, at the CAM-B3LYP/TZVP level. The calculated rotatory strengths from the first 30 singlet → singlet electronic transitions were simulated into an ECD curve using

Gaussian bands with a bandwidth of σ 0.25 eV. The predicted wavelength transitions were multiplied with a scaling factor of 0.99, determined by the best agreement between experimental and calculated UV spectra. The Boltzmann factor for each conformer was calculated based on Gibbs free energies.

2.11 Cholinesterase inhibition screening assays

The *N*-heterocycles compounds (**5a**, **5b**, **9a** and **9b**) were submitted to cholinesterases inhibition screening assay using the simultaneous on-flow dual parallel enzyme assay system (Seidl *et al.*, 2019). Acetylcholinesterase from *Electrophorus electricus* (eeAChE) and butyrylcholinesterase from *human serum* (BChE) were immobilized independently onto fused silica capillary (0.1 mm I.D \times 0.375 mm \times 30 cm), as previously described elsewhere (Vilela *et al.*, 2018), formed the capillary bioreactors AChE-ICER) and BChE-ICER, where ICER means immobilized capillary enzyme reactor.

The on-flow dual parallel enzyme assay was carried out on a LC system (Nexera Shimadzu) consisting of three LC 20AD pumps, a SIL-20A auto-sampler, a DGU-20A degasser, a CTO-20A oven, and a CBM-20A system controller. The LC system was coupled with an AmaZon speed ion trap (IT) mass spectrometry (MS) instrument (Bruker Daltonics) equipped with an electrospray ionization (ESI) interface source, operating in a positive mode (scan *m/z* 50–250).

The two ICER and the MS instrument were interfaced through two 10-port two-position high-pressure switching valves (Valco Instruments Co. Inc.) (Seidl *et al.*, 2019).

The dual system assay consisted of three steps. Briefly, after sample injection, valves (A and B) in position 1, the reactive content of each ICER was transferred to the storage (step 1). In step 2, with both valves (A and B) in position 2, pump B directed the enzymatic reaction of eeAChE-ICER for analysis in the MS. Meanwhile, the reactive content of huBChE-ICER was held in storage. In step 3, while valve A was switched to position 1 again, valve B was kept in position 2. In this position, the huBChE-ICER enzymatic reaction content held in storage was flushed by pump B and finally analyzed in the MS. Detailed system configuration description, MS parameters, assay inhibition are described in Seidl *et al.* (2019).

Data acquisition was carried out using the Bruker Data Analysis Software (version 4.3). All analyses were performed at room temperature (21 °C). The enzymatic reaction was monitored by direct quantification of

acetylcholine hydrolysis product, choline (Ch) $[M + H]^+$ *m/z* 104 (Seidl *et al.*, 2019; Vilela *et al.*, 2018).

N-heterocycles samples were solubilized in methanol to a stock solution of 1.00 mmol L⁻¹ for each compound. Tacrine was used as standard cholinesterase inhibitor.

The assay inhibition was prepared with 10 μ L of each stock solution (100 μ mol L⁻¹ final concentration), 20 μ L of acetylcholine (ACh) solution (70 μ mol L⁻¹ final concentration) and 70 μ L of ammonium acetate solution (15.0 mmol L⁻¹, pH 8.0). Solutions were prepared in duplicate and 20 μ L aliquots were used for injection. Negative (absence of ACh) and positive (presence of ACh and absence of ligand) controls were analyzed between each sample. Percentage inhibition displayed by each sample was calculated by comparison between the area of enzymatic activity in the presence of the inhibitor (P_i) and absence (P_0), according to the following Eq. 1:

$$\% \text{ inhibition} = \left[1 - \left(\frac{P_i - S_b}{P_0 - S_b} \right) \right] \times 100 \quad (1)$$

where P is the attained peak area of Ch produced: (P_i) in the presence of the tested compound; (P_0) in the absence of the tested compound, and S_b is Ch quantified during spontaneous ACh hydrolysis. S_b was determined by injecting the reaction mixture into an empty open tubular silica capillary (blank analysis to quantify spontaneous ACh hydrolysis).

3. Results and discussion

3.1 Synthesis of α -substituted *N*-heterocyclic nitriles

The first proposed retrosynthetic analysis of the target α -substituted *N*-heterocyclic nitriles (**4a–d** and **8a–d**) is outlined in Fig. 2. However, it was found that **4a–d** and **8a–d** could be obtained directly from the corresponding α -hydroxynitriles (**2** and **6**) via *N*-alkylation.

Whereas α -hydroxynitrile **6** is inexpensive and commercially available, the α -hydroxynitrile **2** was readily prepared from propanaldehyde **1** and a cyanide donor. Aiming at a safer and greener cyanide donor for the synthesis of **2**, the reaction proposed by Wen *et al.* (2012) was evaluated, which uses trimethylsilyl cyanide (TMSCN) and a quaternary ammonium as a phase transfer catalyst. However, the obtained yield of 49% was not sufficient for the first synthetic step (data not shown). Thus, the classical approach by addition of

sodium cyanide in the presence of sodium bisulfite was used, with yield of 70% for **2** (Young *et al.*, 2003).

It is well known that hydroxyl group is a poor leaving group (LG) and is usually replaced by a better one, such as tosyl, mesyl, or halogens. However, in order to avoid a functional group manipulation step, a direct alkylation of the following *N*-heterocycles was

attempted: **a**, 2-pyrrolidinone; **b**, 2-piperidinone; **c**, 2-oxopiperazine; and **d**, 1-methylpiperazine with α -hydroxynitriles (Altenkämper *et al.*, 2009; Jenner, 1989). The results are shown in Tab. 1. The main advantages of the direct *N*-alkylation strategy are the reduction in the number of reaction steps and the generation of fewer residues.

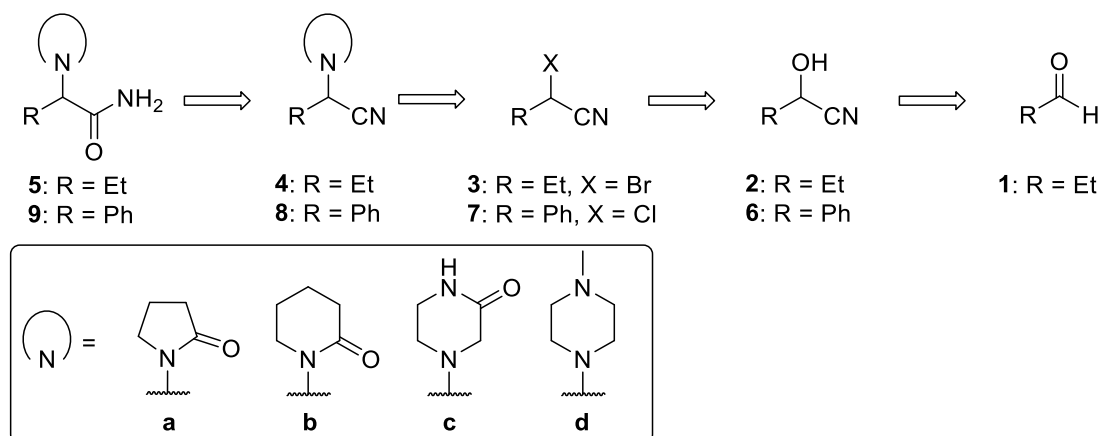


Figure 2. Retrosynthetic route to α -substituted *N*-heterocyclic amides.

Table 1. *N*-heterocyclic alkylation with α -hydroxynitrile and α -halonitrile.

Entry	α -Substituted nitrile	<i>N</i> -heterocycle	Product	Reaction time (h)	Yield (%) ^c
1	2	a , 2-pyrrolidinone ^a	4a	12	50
2	2	b , 2-piperidinone ^a	4b	12	52
3	2	c , 2-oxopiperazine ^b	4c	12	40
4	2	d , 1-methylpiperazine ^b	4d	12	60
5	6	a , 2-pyrrolidinone ^a	8a	12	42
6	6	b , 2-piperidinone ^a	8b	12	48
7	6	c , 2-oxopiperazine ^b	8c	12	35
8	6	d , 1-methylpiperazine ^b	8d	12	71
9	3	d , 1-methylpiperazine ^b	4d	10	59
10	7	c , 2-oxopiperazine ^b	8c	24	27
11	7	d , 1-methylpiperazine ^b	8d	20	75

^aGeneral conditions: α -hydroxynitrile (1 mmol), *N*-heterocycle (5 mmol) and $\text{RuCl}_3 \cdot x\text{H}_2\text{O}$ (3.5 mol%) at 150 °C (autoclave);

^bgeneral conditions: α -hydroxynitriles (1 mmol, 0.5 mL ACN solution), *N*-heterocycle (3 mmol) and heating under reflux;

^cisolated yields.

The *N*-alkylation of both piperazine derivatives, 2-oxopiperazine and 1-methylpiperazine, with α -hydroxynitriles **2** and **6**, proceeded smoothly in the presence of acetonitrile (ACN) under reflux, with yields of 35–71%, after 12 h (Tab. 1, entries 3, 4, 7, and 8).

However, under the same conditions no alkylation was observed for 2-pyrrolidinone and 2-piperidinone, and the starting materials were quantitatively recovered after 24 h. These results could be rationalized by the fact that lactams are less basic than amines, as it can be

seen for the heterocycle **c** in which the *N*-alkylation occurred through the amine moiety and not in the amide moiety. Also, reactions with **d** showed better yields than **c**, since the first one is more basic. To circumvent the lack of *N*-alkylation with the lactam heterocycles **a** and **b**, a reaction using RuCl₃ as catalyst in an autoclave was studied. By carrying out the reaction under 3.5 mol% of catalyst load and 150 °C, moderate yields (42–52%, Tab. 1, entries 1, 2, 5, and 6) of the desired products were obtained after 12 h.

To compare the efficiency of *N*-alkylation of α -hydroxynitriles and α -halonitriles, the chlorination of mandelonitrile **6** was performed using thionyl chloride and pyridine as catalyst (Zhang *et al.*, 2013) under reflux and obtained the 2-chloro-2-phenylacetonitrile **7** in 63% yield. The *N*-alkylation of **7** was carried out under the same reaction conditions previously described for the α -hydroxynitriles. Again, in the absence of ruthenium catalyst, the reaction proceeded only for the piperazine derivatives **c** and **d**, with yields in the same range of the ones obtained with the directly *N*-alkylation of **6** (Tab. 1, entries 10 and 11). Even with a better LG, the lactams **a** and **b** nucleophilicity were not sufficient and the ruthenium catalyst was necessary to afford the correspondent pyrrolidinone and piperidinone derivatives, **8a** and **8b**, in moderate yields. The chlorination of aliphatic α -hydroxynitrile **2** failed after

many attempts using thionyl chloride under different reaction conditions. Then, the bromination of **2** was performed with phosphoryl bromide and pyridine as catalyst (Choi *et al.*, 2016) at room temperature and the 2-bromobutanenitrile **3** in 15% yield was obtained. The *N*-alkylation of **3** was carried out only with piperazine **d** due to the low yield in the halogenation step (Tab. 1, entry 9). The comparison between the *N*-alkylation of α -hydroxynitriles and α -halonitriles stress the better performance of the shorter route leading to a better overall yield and generating fewer residues.

With the α -substituted *N*-heterocyclic nitriles successfully synthesized by directly replacement of α -hydroxynitriles, the scope of enzymatic nitrile hydration was then investigated with a series of Fe-type and Co-type nitrile hydratases.

3.2 Synthesis of α -substituted *N*-heterocyclic amides

The racemic amides were synthesized via classical acid catalysis (H₂SO₄) in dichloromethane (González-Vera *et al.*, 2005) and used as standards for the development of chiral chromatographic methods. The results are shown in Tab. 2.

Table 2. Hydration of α -substituted *N*-heterocyclic nitriles to corresponding amides^a.

Entry	α -Substituted nitrile	Product	Reaction time (h)	Yield (%) ^b
1	4a	5a	4	80
2	4b	5b	60	21
3	4c	5c	60	n.r.
4	4d	5d	22	28
5	8a	9a	20	96
6	8b	9b	60	58
7	8c	9c	60	n.r.
8	8d	9d	23	85

^aGeneral conditions: α -substituted *N*-heterocyclic nitriles (1 mmol), dichloromethane (4 mL) and concentrated sulfuric acid (30 equivalents, 1.7 mL) at room temperature and over magnetic agitation; ^bisolated yields; n.r. = no reaction.

In all cases, no further purification step was necessary after extraction of the products. The nitriles **4c** and **8c** did not lead to the formation of the desired products **5c** and **9c**, respectively. Both compounds are

insoluble in the reaction medium and, even when the reactions were carried out in the presence of DMSO as a cosolvent, there was no product formation.

Except for levetiracetam **5a**, to the best of authors knowledge this is the first time that the α -substituted-*N*-heterocyclic amides **5b**, **5d**, **9a**, **9b**, and **9d** have been synthesized and characterized, as well as their respective α -substituted-*N*-heterocyclic nitriles **4b–d**, **8a–d**.

3.3 Enzymatic reactions with NHases

3.3.1 Nitrile hydratase activity

Twenty NHases commercially available from Prozomix Ltd (Prozomix, 2020) were purchased. For characterization, their activities were monitored by GC-

FID using *n*-butanenitrile as a substrate. One unit of enzymatic activity was defined as the amount (μmol) of *n*-butanamide formed from *n*-butanenitrile, per minute, per milliliter of enzyme solution in 0.1 mol L^{-1} phosphate buffer containing $0.8 \mu\text{g L}^{-1}$ of Co(III) or Fe(III), pH 7.0, at $25 \text{ }^\circ\text{C}$. The results are shown in Tab. 3.

All enzymes were active for *n*-butanenitrile as a substrate (scaffold of aliphatic substrates **4a–d**) which revealed that all commercial NHases show catalytic activity under the reaction conditions (pH, temperature, agitation, buffer and cofactors).

Table 3. Units of enzyme activity of NHases^a from *n*-butanenitrile^b.

Entry	Nitrile hydratase	Type	U mL ^{-1c}
1	PRO-E256	Fe	881
2	PRO-E257	Co	530
3	PRO-E258	Co	554
4	PRO-E259	Co	687
5	PRO-NHASE(001)	Fe	1878
6	PRO-NHASE(002)	Co	450
7	PRO-NHASE(003)	Co	701
8	PRO-NHASE(004)	Co	1
9	PRO-NHASE(007)	Co	111
10	PRO-NHASE(008)	Co	2052
11	PRO-NHASE(009)	Fe	1338
12	PRO-NHASE(010)	Co	14
13	PRO-NHASE(011)	Co	302
14	PRO-NHASE(012)	Fe	3
15	PRO-NHASE(013)	Co	534
16	PRO-NHASE(014)	Co	1
17	PRO-NHASE(015)	Co	348
18	PRO-NHASE(016)	Co	443
19	PRO-NHASE(017)	Co	284
20	PRO-NHASE(018)	Co	>2895

^aProzomix (Prozomix, 2020); ^bgeneral conditions: *n*-butanenitrile ($14.5 \mu\text{mol}$) and $5 \mu\text{L}$ of NHase in a final volume of 1 mL with Na-phosphate buffer (0.1 mol L^{-1} , pH 7.00, containing $0.8 \mu\text{g L}^{-1}$ of Co(III) or Fe(III)) at $25 \text{ }^\circ\text{C}$, 1 min and 1000 rpm ; ^cone unit (U) was defined as the amount of the enzyme that catalyzes the conversion of $1 \mu\text{mol}$ of substrate per minute.

3.3.2 Screening of commercial NHase

All enzymatic experiments were carried out in phosphate buffered aqueous solution, using $10 \mu\text{L}$ of commercial enzyme preparation and 0.25 mmol of substrate and analyzed by GC-FID. It was observed that for *N*-derivatives of 2-oxopiperazine (substrates **4c** and **8c**) and 1-methylpiperazine (substrates **4d** and **8d**), the expected products were not formed. Moreover, the

substrate control experiment (reaction in absence of the enzyme) revealed that these substrates undergo a rapid and spontaneous decomposition by retro-Strecker reaction, leading to the formation of aldehyde and cyanide, which is an inhibitor of NHases (Yasukawa *et al.*, 2011). The results for *N*-derivatives of 2-pyrrolidinone (substrates **4a** and **8a**) and 2-piperidinone (substrates **4b** and **8b**) are shown in Tab. 4.

Table 4. Substrate conversion (**4a–b** and **8a–b**) and enantioselectivity of the commercial NHases in the hydration to **5a–b** and **9a–b**^a.

4a: R = Et, n = 1 4b: R = Et, n = 2
8a: R = Ph, n = 1 8b: R = Ph, n = 2

5a: R = Et, n = 1 5b: R = Et, n = 2
9a: R = Ph, n = 1 9b: R = Ph, n = 2

Entry	Nitrile hydratase		4a		4b		8a		8b	
	Identification	Type	Conversion ^a (%)	<i>ee</i> ^b (%)	Conversion ^a (%)	<i>ee</i> ^b (%)	Conversion ^a (%)	<i>ee</i> ^b (%)	Conversion ^a (%)	<i>ee</i> ^b (%)
1	PRO-E256	Fe	n.r.	-	n.r.	-	n.r.	-	n.r.	-
2	PRO-E257	Co	1.0	n.d.	1.0	n.d.	5.2	1.0 (R)	2.2	5.2 (R)
3	PRO-E258	Co	1.2	n.d.	1.1	n.d.	10.4	2.4 (R)	5.4	7.0 (R)
4	PRO-E259	Co	4.8	17.5 (S)	1.2	n.d.	4.7	1.2 (R)	1.0	n.d.
5	PRO-NHASE(001)	Fe	n.r.	-	n.r.	-	n.r.	-	n.r.	-
6	PRO-NHASE(002)	Co	1.9	n.d.	2.4	n.d.	28.0	3.9 (R)	8.6	14.7 (R)
7	PRO-NHASE(003)	Co	1.1	n.d.	1.0	n.d.	5.2	4.3 (R)	3.0	14.5 (R)
8	PRO-NHASE(004)	Co	1.1	n.d.	1.0	n.d.	2.4	n.d.	2.3	n.d.
9	PRO-NHASE(007)	Co	n.r.	-	n.r.	-	1.4	n.d.	n.r.	-
10	PRO-NHASE(008)	Co	n.r.	-	n.r.	-	1.2	n.d.	n.r.	-
11	PRO-NHASE(009)	Fe	n.r.	-	n.r.	-	n.r.	-	n.r.	-
12	PRO-NHASE(010)	Co	32.0	1.8 (S)	n.r.	-	n.r.	-	n.r.	-
13	PRO-NHASE(011)	Co	14.2	20.6 (S)	7.1	7.9 (S)	13.5	4.9 (R)	13.4	0
14	PRO-NHASE(012)	Fe	n.r.	-	n.r.	-	n.r.	-	n.r.	-
15	PRO-NHASE(013)	Co	5.0	38.9 (S)	1.4	n.d.	3.3	2.4 (R)	4.1	n.d.
16	PRO-NHASE(014)	Co	2.4	n.d.	1.1	n.d.	14.9	8.0 (R)	18.0	3.7 (S)
17	PRO-NHASE(015)	Co	37.4	52.3 (S)	8.4	13.7 (S)	35.9	9.6 (R)	47.5	51.2 (R)
18	PRO-NHASE(016)	Co	n.r.	-	n.r.	-	3.8	n.d.	2.1	n.d.
19	PRO-NHASE(017)	Co	n.r.	-	n.r.	-	6.4	4.5 (R)	2.4	17.3 (R)
20	PRO-NHASE(018)	Co	5.6	0	2.0	n.d.	n.r.	-	1.9	n.d.

General conditions: substrate (5 μmol) and 10 μL of NHase (Prozomix, 2020) in a final volume of 1 mL with Na-phosphate buffer (0.1 mol L⁻¹, pH 7.00, containing 0.8 μg L⁻¹ of Co(III) or Fe(III)) at 25 °C, 48 h and 1000 rpm; n.r. = no reaction was observed; n.d. = not determined; ^aconversion of substrate analyzed by GC-FID; ^benantiomeric excess of product analyzed by LC-UV-CD. The *ee* and conversion are relative measurements and only chromatographic bands with a signal-to-noise ratio higher than 5:1 were considered.

The Co-type enzyme PRO-NHASE(015) showed the best performance for the conversion of all 2-pyrrolidinone and 2-piperidinone nitrile derivatives to

the corresponding amides, with highest conversion and *ee* observed for **5a**. Despite the low conversions observed, PRO-NHASE(011) and PRO-NHASE(013) accepted both aliphatic and aromatic substrates, while

PRO-NHASE(010) was selective to **4a**. On the other hand, no conversion was observed for substrates **4a**, **4b**, **8a**, and **8b**, with all four evaluated Fe-type NHases (Tab. 4, entries 1, 5, 11 and 14). These results are in accordance with the literature in which Co-type NHase has a broader substrate scope and greater activity than Fe-type NHase (Prasad and Bhalla, 2010). These differences occur because a tryptophan residue in Co-type is substituted by a tyrosine residue in Fe-type, near the active site (Kumar and Grapperhaus, 2014; Mitra and Holz, 2007). Still, Fe-type preferentially hydrate aliphatic nitriles and Co-type shows preference to aromatic nitriles (Prasad and Bhalla, 2010) and the four Fe-type used in this work indeed hydrated *n*-butanenitrile (Tab. 3).

These results from the enzymatic reactions using NHases are weak from a synthetic point of view. Although NHase is largely employed for the industrial production of acrylamide and nicotinamide (Jiao *et al.*, 2020; Wang, 2015), the application of the wild-type enzyme can be limited by its narrow substrate specificity, low enantioselectivity, unsatisfactory catalytic activity, inhibition at a high concentration of substrate and low thermostability (Bhalla *et al.*, 2018; Gong *et al.*, 2017; Prasad and Bhalla, 2010; Supreetha *et al.*, 2019; Wang, 2009). To address these issues, protein engineering is the major tool to improve nitrile hydratase features for application in organic synthesis (Wang, 2015). The biocatalytic process to produce levetiracetam **5a** is a good example. A screening was performed with approximately 30 NHases that showed low enantioselectivity and moderate conversions. The best result was obtained with the NHase from *Bradyrhizobium japonicum*, in which 20% conversion and 60% *ee* were observed. This enzyme was engineered to improve its enantioselectivity. Then, the reaction medium engineering was carried out, leading to 43% yield and 94% *ee* which was increased to > 99% *ee* upon recrystallization (Tao *et al.*, 2010).

Regarding non-engineered NHases, a recent work has studied the substrates scope of Co-type NHase from *Rhodococcus rhodochrous* ATCC BAA 870. The authors evaluated 67 substrates that differ in size from small (90 Da) to large (325 Da), in which 32 showed 50 to 100% conversion, 9 showed 16 to 50%, 5 showed 5 to 15% and 21 showed 0 to 5%. The nitrile conversion was influenced by overall size of the substrate and steric hindrance around the cyano group (Mashweu *et al.*, 2020). Other report prepared three sugar nitriles derivatives from 2-acetamido-2-deoxy- β -D-glucopyranosides and none of them was hydrated to the corresponding amide by NHase from *Rhododoccus equi* A4 (Carmona *et al.*, 2006).

Although the observed *ee* values obtained herein are still not satisfactory, all evaluated NHase showed a clear preference for (*S*) aliphatic substrates and (*R*) aromatic ones. This is a good starting point for further biocatalyst engineering (van Pelt *et al.*, 2011).

The stereoselectivity of the enzymatic conversions of compounds **4a–4b** and **8a–8b** was determined using chiral chromatography coupled with an ECD detector. The absolute configurations of the eluting enantiomers of **5b** and **9a–9b** were determined by comparing the ECD spectra obtained after trapping them in the detector with TDDFT calculations at the CAM-B3LYP/TZVP level. The calculations were carried out in order to investigate the influence of both ethyl and phenyl sidechains, as well as that of the *N*-heterocyclic substituents, on their chiroptical properties. All calculations performed for the (*S*)-configuration of **5b** and **9a–9b** resulted in a negative cotton effect at around 240 nm, which is in accordance with the literature data for levetiracetam (**5a**) (Fig. S73–S75) (Li and Si, 2011). Regarding compound **5a**, no ECD spectra were recorded, and the elution order was determined by comparing the retention times of each enantiomer with that of a commercial standard.

The PRO-NHASE(015) was selected for further investigation of medium engineering based on its best results of conversion and enantioselectivity.

3.3.3 Effect of temperature

It is well known that some NHase catalyzed reactions operate at low temperatures. The balance between reactivity and enantioselectivity for engineering the NHase from *Bradyrhizobium japonicum* conducted the final process at 4 °C, for example, in levetiracetam bioanalytical production (Tao *et al.*, 2010).

Table 5. Influence of temperature in the conversion of **4a–b** and **8a–b** into the respective amides catalyzed by PRO-NHASE(015) NHase.

Substrate	Conversion (%)	
	15 °C	25 °C
4a	5.5	37.4
4b	1.5	8.4
8a	8.0	35.9
8b	4.5	47.5

In order to explore the effect of temperature, reactions at both 15 and 25 °C were carried out in parallel and in the same experimental conditions for **4a–b** and **8a–b**. The decrease of 10 °C in the reaction temperature drastically reduced the conversion rates, as

shown in [Tab. 5](#). Therefore, for the additional evaluated parameter, solvent effect, reactions were performed at 25 °C.

3.3.4 Effect of solvent

The control reactions experiments revealed that **4c–d** and **8c–d** undergo spontaneous decomposition by retro-Strecker reaction (section 3.3.2). As an attempt to prevent this undesired and competitive reaction, two solvent systems, which are also environmentally friendly systems, were explored—ionic liquids (IL) and polyethylene glycol (PEG).

The 1-butyl-3-methylimidazolium (BMIM) ionic liquids are the most widely used for biocatalysis and, therefore, the ILs BMIM.BF₄ (water-miscible), BMIM.PF₆ (water-immiscible) and BMIM.NTf₂ (water-immiscible) were chosen for these experiments ([Cantone et al., 2007](#)). The IL system was composed of a combination of phosphate buffered solutions and increasing concentrations of the ILs BMIM.BF₄, BMIM.PF₆, and BMIM.NTf₂ in a range of 10–80% for each one. In a control experiment using substrates **4a–b** and **8a–b** and PRO-NHASE(015), no amide formation was observed and suggests that the ILs could be inhibiting the NHase activity. Interestingly, the substrates **4c–d** and **8c–d** were not decomposed in any reaction media containing ionic liquids.

The second solvent system evaluated was aqueous buffered solution with increasing concentrations of PEG₄₀₀ 10–100%. The reactions performed with substrate **4a** showed that, unlike the IL systems, the PRO-NHASE(015) was active in all proportions of PEG, even at 100%. However, the PEG significantly reduced the activity of this enzyme, with conversion decreasing from 38 to 20% in PEG₄₀₀ concentrations of 0–10%, and declining to 2% with PEG₄₀₀ concentrations higher than 50% (data not shown). In contrast to the ionic liquid system, the substrates **4c–d** and **8c–d** were decomposed in all proportions of buffer: PEG₄₀₀ and the retro-Strecker products were observed. No amide formation was detected for **4c–d** and **8c–d**.

3.4 Cholinesterases inhibition screening assays

The enzymes acetylcholinesterase (AChE) and butyrylcholinesterase (BChE) are omnipresent cholinesterases (ChE) among animals and have gained attention due to its important role in central and peripheral cholinergic neurotransmission, reducing cholinergic neuron activity, one of the event features of Alzheimer's disease (AD) ([Kuca et al., 2016](#)). Epilepsy

and AD are frequently associated with neurological disorders, and both can appear simultaneously in the patient. In addition, a study reported the ameliorating of epileptic patients with nootropic effect by AChE inhibitors ([Ahmad et al., 2019](#)). Similarly, brivaracetam (an analogue of levetiracetam) epilepsy drug is effective in treatment of memory impairment in AD mice ([Ahmad et al., 2019](#)). Also, was demonstrated that carbamazepine, a classical antiepileptic drug, inhibited 39% AChE of brain from zebrafish ([Siebel et al., 2010](#)).

The use of levetiracetam **5a** has been studied to control seizures in people with AD ([Giorgi et al., 2017](#); [U.S Department of Health and Human Services, 2014](#)). [Sola et al. \(2015\)](#) evaluated the AChE and BChE inhibitory activity of (*S*)-**5a** and it was found to be potent human acetylcholinesterase (hAChE) and human butyrylcholinesterase (hBChE) inhibitor, exhibiting IC₅₀ values of 76 and 241 nmol L⁻¹ for hAChE and hBChE, respectively, which were indirectly determined based on colorimetric assay using Ellman's reagent and thiocholine-derivatives as substrate.

In the light of this interesting dual AChE/BChE inhibitory activity, the anticholinesterase potential of the synthesized compounds **5b** and **9a–9b** were verified using the simultaneous on-flow dual parallel enzyme assay system ([Seidl et al., 2019](#)). A label-free assay based on immobilized capillary enzyme reactor (ICER) allowed the direct monitoring of substrate consumption and product formation in real-time by LC-MS, employing the natural substrate of AChE, acetylcholine. [Table 6](#) presents the inhibition percentage of all compounds tested at a concentration of 100 μmol L⁻¹, using tacrine as a positive control.

Table 6. Inhibition of eeAChE-ICER and huBChE-ICER activities by tacrine (positive control; 100 μmol L⁻¹) and *N*-heterocycles samples (100 μmol L⁻¹).

Samples	% inhibition	
	eeAChE-ICER ± SEM ^b	hBChE-ICER ± SEM ^b
Tacrine ^a	100	100
5a	10 ± 2	32 ± 2
5b	0	0
9a	5 ± 1	0
9b	10 ± 1	0

^aReference for AChE and BChE inhibition; ^bMean ± standard error of the mean (SEM, n = 2).

The racemic amides indicated low inhibitory effect when compared to tacrine, with emphasis only on **5a** that presented in increasing selectivity and potency to BChE, with 31.9% inhibition and 9.5 % for AChE.

4. Conclusions

The attempt of stereoselective synthesis of α -substituted-*N*-heterocyclic amides was demonstrated and their absolute configurations were assigned using ECD. The *N*-alkylation of 2-pyrrolidinone, 2-piperidinone, 2-oxopiperazine and 1-methylpiperazine was achieved directly from α -hydroxynitriles, which are usually either commercially available or easily prepared, thus reducing the number of synthetic steps, and minimizing the product waste. As expected, the substrate specificity varied greatly among the nitrile hydratases, highlighting the importance of the initial screening assays. The importance of amides as end products and chiral building blocks instigates the development and optimization of better biocatalysts through protein engineering to satisfactory applications in greener organic synthesis. Although the stereoselectivity was low, the products of enzymatic reactions showed a clear preference of NHases for (*S*)-aliphatic substrates and (*R*)-aromatic ones. The use of unconventional reaction media (ILs and PEG₄₀₀) that have been used successfully for many enzymes proved to be impractical for the commercial NHases used in this work. None of the racemic levetiracetam derivatives exhibit inhibitory effect on acetylcholinesterase, exemplifying the role of stereochemistry in biological activities.

Supplementary Information

Spectra (¹H NMR, ¹³C NMR, MS and IR) of all characterized compounds **2**, **3**, **4a–d**, **5a–b**, **5d**, **7**, **8a–d**, **9a–b**, and **9d**, spectra (¹H, ¹³C, ¹⁹F NMR) of the synthesized ionic liquids and the ECD figures and the lower energy conformers are available in supplementary information.

Authors' contribution

Conceptualization: Milagre, C. D. F.; Milagre, H. M. S.; Cardoso, C. L.; Batista Junior, J. M.

Data curation: Not applicable

Formal Analysis: do Amaral, B. S.; Milagre, C. D. F.; Milagre, H. M. S.; Batista Junior, J. M.; Vilela, A. F. L.; Cardoso, C. L.

Funding acquisition: Milagre, C. D. F.; Milagre, H. M. S.; Cardoso, C. L.; Batista Junior, J. M.

Investigation: do Amaral, B. S.; Vilela, A. F. L.

Methodology: Not applicable

Project administration: Milagre, C. D. F.; Milagre, H. M. S.; Cardoso, C. L.; Batista Junior, J. M.

Resources: Milagre, C. D. F.; Milagre, H. M. S.; Cardoso, C. L.; Batista Junior, J. M.

Software: Not applicable

Supervision: Milagre, C. D. F.; Milagre, H. M. S.; Cardoso, C. L.; Batista Junior, J. M.

Validation: Not applicable

Visualization: Not applicable

Writing – original draft: do Amaral, B. S.; Milagre, C. D. F.; Milagre, H. M. S.; Cardoso, C. L.; Batista Junior, J. M.

Writing – review & editing: do Amaral, B. S.; Milagre, C. D. F.; Milagre, H. M. S.

Data availability statement

All data sets were generated or analyzed in the current study.

Funding

Fundação de Amparo à Pesquisa do Estado de São Paulo (FAPESP). Grant No: 2014/50249-8; 2010/02305-5; 2013/16636-1; 2014/50926-0; 2014/25222-9; 2019/22319-5; 2019/15230-8.

Instituto Nacional de Ciência e Tecnologia INCT BioNat: Conselho Nacional de Desenvolvimento Científico e Tecnológico (CNPq). Grant No: 465637/2014-0.

Coordenação de Aperfeiçoamento de Pessoal de Nível Superior (CAPES). Finance Code 001.

Núcleo de Computação Científica (NCC/GridUNESP).

GlaxoSmithKline (GSK).

Acknowledgments

Not applicable.

References

Ahmad, G.; Rasool, N.; Rizwan, K.; Imran, I.; Zahoor, A. F.; Zubair, M.; Sadiq, A.; Rashid, U. Synthesis, *in-Vitro* Cholinesterase Inhibition, *In-Vivo* Anticonvulsant Activity And *In-Silico* Exploration of *N*-(4-methylpyridin-2-yl)thiophene-2-carboxamide analogs. *Bioorg. Chem.* **2019**, *92*, 103216. <https://doi.org/10.1016/j.bioorg.2019.103216>

Altenkämper, M.; Bechem, B.; Perruchon, J.; Heinrich, S.; Mädél, A.; Ortmann, R.; Dahse, H.-M.; Freunschdt, E.; Wang, Y.; Rath, J.; Stich, A.; Hitzler, M.; Chiba, P.; Lanzer, M.;

- Schlitzer, M. Antimalarial and antitrypanosomal activity of a series of amide and sulfonamide derivatives of a 2,5-diaminobenzophenone. *Bioorg. Med. Chem.* **2009**, *17* (22), 7690–7697. <https://doi.org/10.1016/j.bmc.2009.09.043>
- Anuradha, S.; Preeti, K. Levetiracetam with its therapeutic potentials. *Int. J. Univers. Pharm. Bio Sci.* **2013**, *2* (5), 45–58.
- Bhalla, T. C.; Kumar, V.; Kumar, V.; Thakur, N.; Savitri. Nitrile metabolizing enzymes in biocatalysis and biotransformation. *Appl. Biochem. Biotechnol.* **2018**, *185* (4), 925–946. <https://doi.org/10.1007/s12010-018-2705-7>
- Bisogno, F. R.; López-Vidal, M. G.; de Gonzalo, G. Organocatalysis and biocatalysis hand in hand: Combining catalysts in one-pot procedures. *Adv. Synth. Catal.* **2017**, *359* (12), 2026–2049. <https://doi.org/10.1002/adsc.201700158>
- Brazil. Ministério da Saúde. Portaria nº 56, de 1 de dezembro de 2017. Fica incorporado o levetiracetam para o tratamento da epilepsia, no âmbito do Sistema Único de Saúde – SUS. Brasília: Diário Oficial da União, 2017. https://bvsmms.saude.gov.br/bvs/saudelegis/sctie/2017/prt0056_05_12_2017.html (accessed 2021-07-19).
- Cantone, S.; Hanefeld, U.; Basso, A. Biocatalysis in non-conventional media—ionic liquids, supercritical fluids and the gas phase. *Green Chem.* **2007**, *9* (9), 954–971. <https://doi.org/10.1039/b618893a>
- Carmona, A. T.; Fialová, P.; Křen, V.; Ettrich, R.; Martínková, L.; Moreno-Vargas, A. J.; González, C.; Robina, I. Cyanodeoxy-glycosyl derivatives as substrates for enzymatic reactions. *Eur. J. Org. Chem.* **2006**, *2006* (8), 1876–1885. <https://doi.org/10.1002/ejoc.200500755>
- Casey, M.; Leonard, J.; Lygo, B.; Procter, G. Working up the reaction. In *Advanced practical organic chemistry*; Springer, 1990; pp 141–187. <https://doi.org/10.1007/978-1-4899-6643-8>
- Chaudhry, S. A.; Jong, G.; Koren, G. The fetal safety of Levetiracetam: A systematic review. *Reprod. Toxicol.* **2014**, *46*, 40–45. <https://doi.org/10.1016/j.reprotox.2014.02.004>
- Chen, Z.; Meng, L.; Ding, Z.; Hu, J. Construction of versatile *N*-heterocycles from in situ generated 1,2-Diaza-1,3-dienes. *Curr. Org. Chem.* **2019**, *23* (2), 164–187. <https://doi.org/10.2174/1385272823666190227162840>
- Choi, I.; Chung, H.; Park, J. W.; Chung, Y. K. Active and recyclable catalytic synthesis of indoles by reductive cyclization of 2-(2-Nitroaryl)acetonitriles in the presence of Co-Rh heterobimetallic nanoparticles with atmospheric hydrogen under mild conditions. *Org. Lett.* **2016**, *18* (21), 5508–5511. <https://doi.org/10.1021/acs.orglett.6b02659>
- D’Antona, N.; Morrone, R. Biocatalysis: Green transformations of nitrile function. In *Green chemistry for environmental sustainability*; Sanjay, K., Sharma, A. M., Eds.; CRC Press - Taylor and Francis, 2010.
- Dupont, J.; Consorti, C. S.; Suarez, P. A. Z.; Souza, R. F. Preparation of 1-Butyl-3-Methyl Imidazolium-Based room temperature ionic liquids. *Org. Synth.* **2002**, *79*, 236. <https://doi.org/10.15227/orgsyn.079.0236>
- Gaussian 09*. Revision A.02; Gaussian, Inc.: Wallingford, 2016.
- Giorgi, F. S.; Guida, M.; Vergallo, A.; Bonuccelli, U.; Zaccara, G. Treatment of epilepsy in patients with Alzheimer’s disease. *Expert Rev. Neurother.* **2017**, *17* (3), 309–318. <https://doi.org/10.1080/14737175.2017.1243469>
- Gong, J.-S.; Shi, J.-S.; Lu, Z.-M.; Li, H.; Zhou, Z.-M.; Xu, Z.-H. Nitrile-converting enzymes as a tool to improve biocatalysis in organic synthesis: Recent insights and promises. *Crit. Rev. Biotechnol.* **2017**, *37* (1), 69–81. <https://doi.org/10.3109/07388551.2015.1120704>
- González-Vera, J. A.; García-López, M. T.; Herranz, R. Molecular diversity via amino acid derived α -amino nitriles: Synthesis of spirocyclic 2,6-Dioxopiperazine Derivatives. *J. Org. Chem.* **2005**, *70* (9), 3660–3666. <https://doi.org/10.1021/jo050146m>
- Hong, F.; Xia, Z.; Zhu, D.; Wu, H.; Liu, J.; Zeng, Z. *N*-terminal strategy (N1-N4) toward high performance liquid crystal materials. *Tetrahedron* **2016**, *72* (10), 1285–1292. <https://doi.org/10.1016/j.tet.2015.11.013>
- Hönig, M.; Sonderrmann, P.; Turner, N. J.; Carreira, E. M. Enantioselective chemo- and biocatalysis: Partners in retrosynthesis. *Angew. Chem. Int. Ed.* **2017**, *56* (31), 8942–8973. <https://doi.org/10.1002/anie.201612462>
- Jenner, G. Homogeneous ruthenium catalysis of *N*-alkylation of amides and lactams. *J. Mol. Catal.* **1989**, *55* (1), 241–246. [https://doi.org/10.1016/0304-5102\(89\)80257-3](https://doi.org/10.1016/0304-5102(89)80257-3)
- Jiao, S.; Li, F.; Yu, H.; Shen, Z. Advances in acrylamide bioproduction catalyzed with *Rhodococcus* cells harboring nitrile hydratase. *Appl. Microbiol. Biotechnol.* **2020**, *104*, 1001–1012. <https://doi.org/10.1007/s00253-019-10284-5>
- Kenda, B. M.; Matagne, A. C.; Talaga, P. E.; Pasau, P. M.; Differding, E.; Lallemand, B. I.; Frycia, A. M.; Moureau, F. G.; Klitgaard, H. V.; Gillard, M. R.; Fuks, B.; Michel, P. Discovery of 4-substituted pyrrolidone butanamides as new agents with significant antiepileptic activity. *J. Med. Chem.* **2004**, *47* (3), 530–549. <https://doi.org/10.1021/jm030913e>
- Krasowski, M. D.; McMillin, G. A. Advances in anti-epileptic drug testing. *Clin. Chim. Acta* **2014**, *436*, 224–236. <https://doi.org/10.1016/j.cca.2014.06.002>

- Kuca, K.; Soukup, O.; Maresova, P.; Korabecny, J.; Nepovimova, E.; Klimova, B.; Honegr, J.; Ramalho, T. C.; França, T. C. C. Current approaches against Alzheimer's disease in clinical trials. *J. Braz. Chem. Soc.* **2016**, *27* (4), 641–649. <https://doi.org/10.5935/0103-5053.20160048>
- Kumar, D.; Grapperhaus, C. A. Sulfur-oxygenation and functional models of nitrile hydratase. In *Bioinspired catalysis*; Weigand, W., Schollhammer, P., Eds.; Wiley-VCH Verlag GmbH & Co. KGaA, 2014. <https://doi.org/10.1002/9783527664160.ch12>
- Li, L.; Si, Y.-K. Study on the absolute configuration of Levetiracetam via density functional theory calculations of electronic circular dichroism and optical rotatory dispersion. *J. Pharm. Biomed. Anal.* **2011**, *56* (3), 465–470. <https://doi.org/10.1016/j.jpba.2011.07.002>
- Liu, S.; Zhao, Z.; Wang, Y. Construction of *N*-heterocycles through cyclization of tertiary amines. *Chem. Eur. J.* **2019**, *25* (10), 2423–2441 <https://doi.org/10.1002/chem.201803960>
- Lyseng-Williamson, K. A. Spotlight on Levetiracetam in epilepsy. *CNS Drugs* **2011a**, *25*, 901–905. <https://doi.org/10.2165/11208340-000000000-00000>
- Lyseng-Williamson, K. A. Levetiracetam: A review of its use in epilepsy. *Drugs* **2011b**, *71* (4), 489–514.
- Mashweu, A. R.; Chhiba-Govindjee, V. P.; Bode, M. L.; Brady, D. Substrate profiling of the cobalt nitrile hydratase from *Rhodococcus rhodochrous* ATCC BAA 870. *Molecules* **2020**, *25* (1), 238. <https://doi.org/10.3390/molecules25010238>
- Mitra, S.; Holz, R. C. Unraveling the catalytic mechanism of nitrile hydratases. *J. Biol. Chem.* **2007**, *282* (10), 7397–7404. <https://doi.org/10.1074/jbc.M604117200>
- Miyana, A.; Fushinobu, S.; Ito, K.; Shoun, H.; Wakagi, T. Mutational and structural analysis of cobalt-containing nitrile hydratase on substrate and metal binding. *Eur. J. Biochem.* **2004**, *271* (2), 429–438. <https://doi.org/10.1046/j.1432-1033.2003.03943.x>
- Narczyk, A.; Mrozowicz, M.; Stecko, S. Total synthesis of Levetiracetam. *Org. Biomol. Chem.* **2019**, *17* (10), 2770–2775. <https://doi.org/10.1039/C9OB00111E>
- Nelp, M. T.; Astashkin, A. V.; Brecci, L. A.; McCarty, R. M.; Bandarian, V. The alpha subunit of nitrile hydratase is sufficient for catalytic activity and post-translational modification. *Biochemistry* **2014**, *53* (24), 3990–3994. <https://doi.org/10.1021/bi500260j>
- Prasad, S.; Bhalla, T. C. Nitrile hydratases (NHases): At the interface of academia and industry. *Biotechnol. Adv.* **2010**, *28* (6), 725–741. <https://doi.org/10.1016/j.biotechadv.2010.05.020>
- Prozomix. *Enzyme Catalogue*. 2020. http://www.prozomix.com/products/listing?searchby=name&searchby_name=Nitrile+hydratase&category=21&x=53&y=3 (accessed 2020-01-27).
- Saini, M. S.; Kumar, A.; Dwivedi, J.; Singh, R. A review: Biological significances of heterocyclic compounds. *Int. J. Pharm. Sci. Res.* **2013**, *4* (3), 66–77.
- Seidl, C.; Vilela, A. F. L.; Lima, J. M.; Leme, G. M.; Cardoso, C. L. A novel on-flow mass spectrometry-based dual enzyme assay. *Anal. Chim. Acta* **2019**, *1072*, 81–86. <https://doi.org/10.1016/j.aca.2019.04.057>
- Sheldon, R. A.; Pereira, P. C. Biocatalysis engineering: The big picture. *Chem. Soc. Rev.* **2017**, *46* (10), 2678–2691. <https://doi.org/10.1039/C6CS00854B>
- Shen, Y.; Du, F.; Gao, W.; Wang, A.; Chen, C. Stereoselective nitrile hydratase. *Afr. J. Microbiol. Res.* **2012**, *6* (32), 6114–6121. <https://doi.org/10.5897/AJMR12.101>
- Siebel, A. M.; Rico, E. P.; Capiotti, K. M.; Piato, A. L.; Cusinato, C. T.; Franco, T. M. A.; Bogo, M. R.; Bonan, C. D. *In vitro* effects of antiepileptic drugs on acetylcholinesterase and ectonucleotidase activities in zebrafish (*Danio rerio*) brain. *Toxicol. Vitro* **2010**, *24* (4), 1279–1284. <https://doi.org/10.1016/j.tiv.2010.03.018>
- Sola, I.; Aso, E.; Frattini, D.; López-González, I.; Espargaró, A.; Sabaté, R.; Di Pietro, O.; Luque, F. J.; Clos, M. V.; Ferrer, I.; Muñoz-Torrero, D. Novel Levetiracetam derivatives that are effective against the alzheimer-like phenotype in mice: Synthesis, *in vitro*, *ex vivo*, and *in vivo* efficacy studies. *J. Med. Chem.* **2015**, *58* (15), 6018–6032. <https://doi.org/10.1021/acs.jmedchem.5b00624>
- Souza, R. O. M. A.; Miranda, L. S. M.; Bornscheuer, U. T. A retrosynthesis approach for biocatalysis in organic synthesis. *Chem. Eur. J.* **2017**, *23* (50), 12040–12063. <https://doi.org/10.1002/chem.201702235>
- Supreetha, K.; Rao, S. N.; Srividya, D.; Anil, H. S.; Kiran, S. Advances in cloning, structural and bioremediation aspects of nitrile hydratases. *Mol. Biol. Rep.* **2019**, *46*, 4661–4673. <https://doi.org/10.1007/s11033-019-04811-w>
- Tao, J.; Liu, J.; Chen, Z. Some recent examples in developing biocatalytic pharmaceutical processes. In *Asymmetric catalysis on industrial scale: Challenges, approaches and solutions*; Hans-Ulrich, B., Hans-Jürgen, F., Eds.; Wiley-VCH Verlag GmbH & Co. KGaA, 2010. <https://doi.org/10.1002/9783527630639.ch1>
- Tucker, J. L.; Xu, L.; Yu, W.; Scott, R. W.; Zhao, L.; Ran, N. Chemoenzymatic processes for preparation of Levetiracetam. US WO2009009117, 2009.

U.S Department of Health and Human Services, 2014. Levetiracetam for Alzheimer's disease-associated epileptiform activity. <https://www.nia.nih.gov/alzheimers/clinical-trials/levetiracetam-alzheimers-disease-associated-epileptiform-activity> (accessed 2020-04-29).

UCB. 2018 Full Year Results. UCB https://www.ucb.com/_up/ucb_com_ir/documents/2018_FY_results_presentation_-_final.pdf (accessed 2020-01-17).

Uges, J. W. F.; Vecht, C, J. Levetiracetam. In *Atlas of Epilepsies*; Panayiotopoulos, C. P., Ed.; Springer London, 2010. https://doi.org/10.1007/978-1-84882-128-6_271

van Pelt, S.; Zhang, M.; Otten, L. G.; Holt, J.; Sorokin, D. Y.; van Rantwijk, F.; Black, G. W.; Perry, J. J.; Sheldon, R. A. Probing the enantioselectivity of a diverse group of purified cobalt-centred nitrile hydratases. *Org. Biomol. Chem.* **2011**, *9* (8), 3011–3019. <https://doi.org/10.1039/c0ob01067g>

Vilela, A. F. L.; Seidl, C.; Lima, J. M.; Cardoso, C. L. An improved immobilized enzyme reactor-mass spectrometry-based label free assay for butyrylcholinesterase ligand screening. *Anal. Biochem.* **2018**, *549*, 53–57. <https://doi.org/10.1016/j.ab.2018.03.012>

Wang, M.-X. Progress of enantioselective nitrile biotransformations in organic synthesis. *CHIMIA International Journal for Chemistry* **2009**, *63* (6), 331–333. <https://doi.org/10.2533/chimia.2009.331>

Wang, M.-X. Enantioselective biotransformations of nitriles in organic synthesis. *Acc. Chem. Res.* **2015**, *48* (3), 602–611. <https://doi.org/10.1021/ar500406s>

Wen, Y.; Liang, M.; Wang, Y.; Ren, W.; Lü, X. Perfectly green organocatalysis: Quaternary ammonium base triggered cyanosilylation of aldehydes. *Chinese J. Chem.* **2012**, *30* (9), 2109–2114. <https://doi.org/10.1002/cjoc.201200598>

Yasukawa, K.; Hasemi, R.; Asano, Y. Dynamic kinetic resolution of α -aminonitriles to form chiral α -amino acids. *Adv. Synth. Catal.* **2011**, *353* (13), 2328–2332. <https://doi.org/10.1002/adsc.201100360>.

Young, S. D.; Buse, C. T.; Heathcock, C. H. 2-Methyl-2-(Trimethylsiloxy)Pentan-3-one. In *Organic Syntheses*; John Wiley & Sons, 2003. <https://doi.org/10.1002/0471264180.os063.09>

Zhang, J.; Wang, H.; Ma, Y.; Wang, Y.; Zhou, Z.; Tang, C. CaF₂ Catalyzed S_N2 type chlorodehydroxylation of chiral secondary alcohols with thionyl chloride: A practical and convenient approach for the preparation of optically active chloroalkanes. *Tetrahedron Lett.* **2013**, *54* (18), 2261–2263. <https://doi.org/10.1016/j.tetlet.2013.02.079>

Levetiracetam analogs: chemoenzymatic synthesis, absolute configuration assignment and evaluation of cholinesterase inhibitory activities

Cintia Duarte de Freitas Milagre^{1+*}, Bruno Sergio do Amaral¹, João Marcos Batista Junior^{2,3}, Adriana Ferreira Lopes Vilela⁴, Carmen Lúcia Cardoso⁴, Humberto Marcio Santos Milagre¹

1. São Paulo State University, Institute of Chemistry, Araraquara, Brazil.
2. Federal University of São Carlos, Department of Chemistry, São Carlos, Brazil.
3. Federal University of São Paulo, Institute of Science and Technology, São José dos Campos, Brazil.
4. University of São Paulo, Faculty of Philosophy, Sciences and Letters, Ribeirão Preto, Brazil.

*Corresponding author: Cintia Duarte de Freitas Milagre, Phone: +55 16 33019668, Email address: cintia.milagre@unesp.br

ARTICLE INFO

Article history:

Received: July 19, 2021

Accepted: September 14, 2021

Published: April 01, 2022

Keywords

1. *N*-heterocycles
2. *N*-alkylation
3. biocatalysis
4. electronic circular dichroism (ECD)

Section Editor: Assis Vicente Benedetti

Spectra (¹H NMR, ¹³C NMR, MS and IR) of all characterized compounds **2**, **3**, **4a–d**, **5a–b**, **5d**, **7**, **8a–d**, **9a–b** and **9d**, spectra (¹H, ¹³C, ¹⁹F NMR) of the synthesized ionic liquids and the ECD figures and the lower energy conformers.

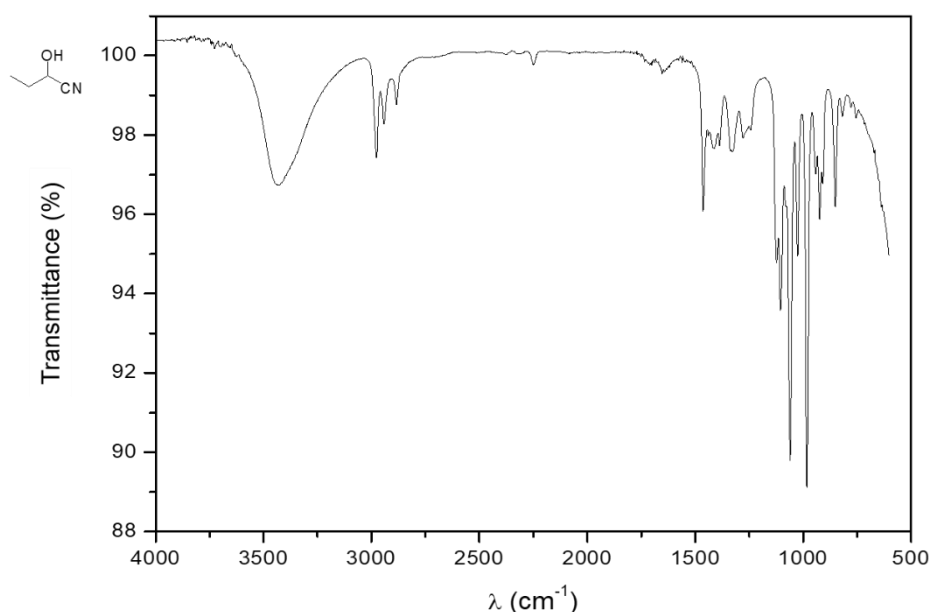


Figure S1. IR spectrum of compound **2**.

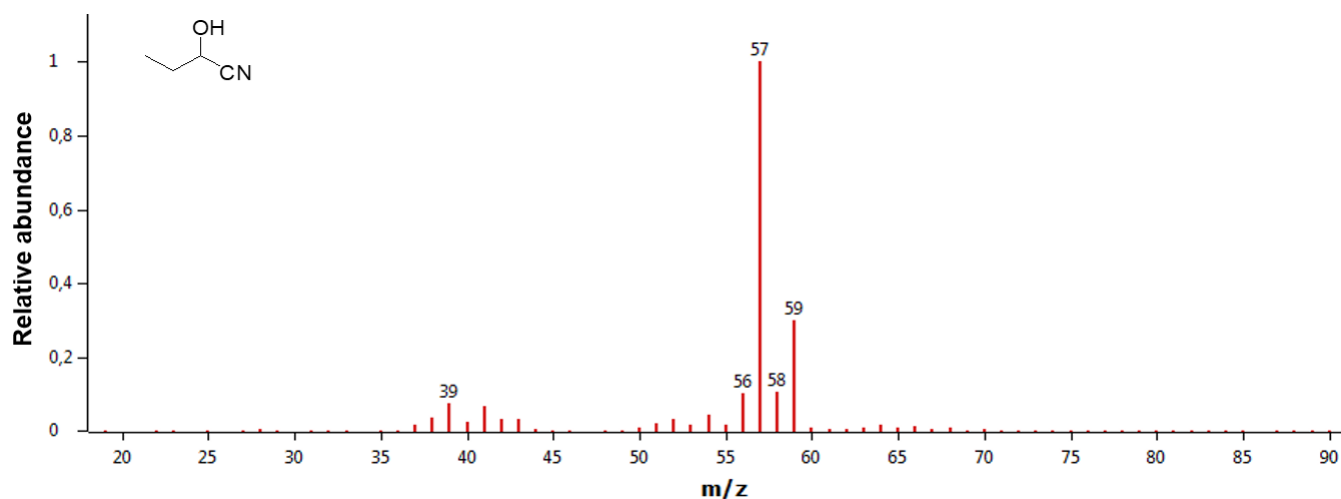


Figure S2. MS (EI, 70 eV) spectrum of compound 2.

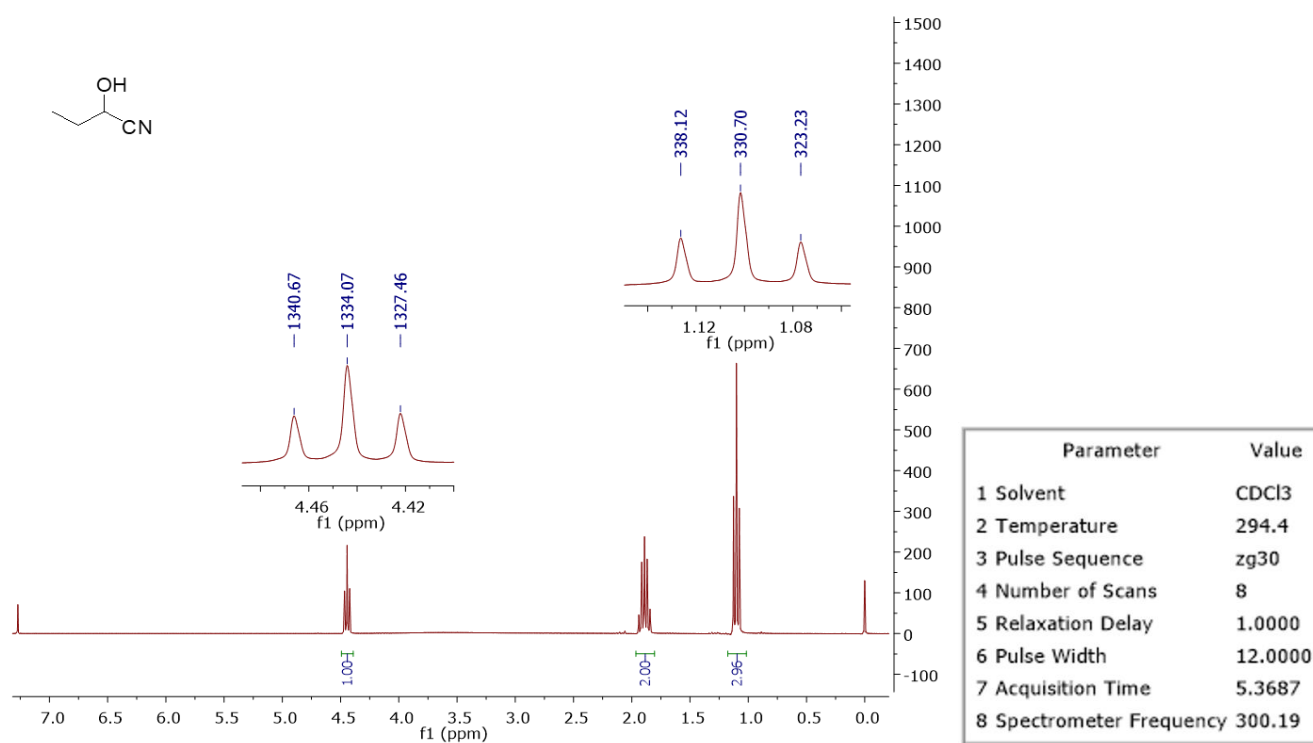


Figure S3. ¹H NMR (300.19 MHz, CDCl₃) spectrum of compound 2.

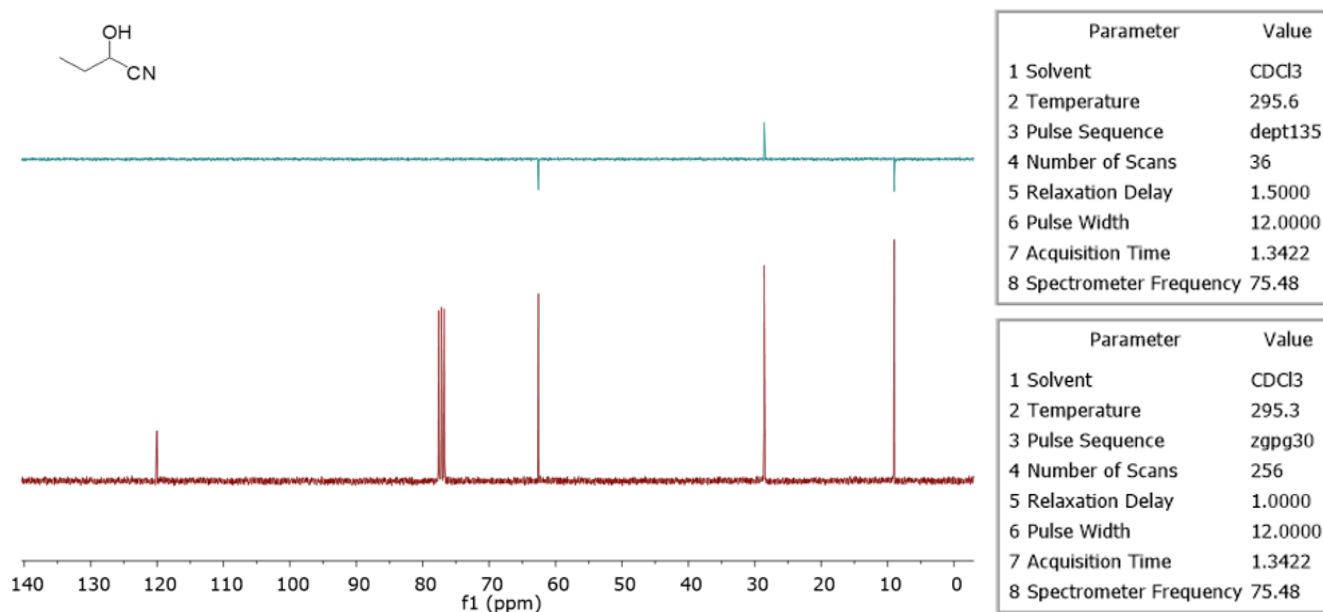


Figure S4. ^{13}C NMR (75.48 MHz, CDCl_3) spectrum and DEPT-135 experiment of compound **2**.

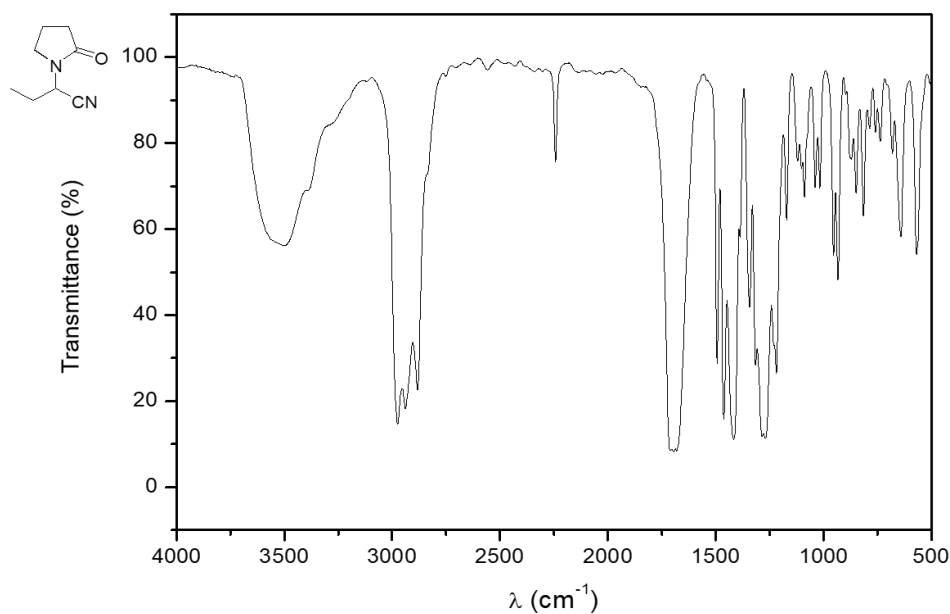


Figure S5. IR spectrum of compound **4a**.

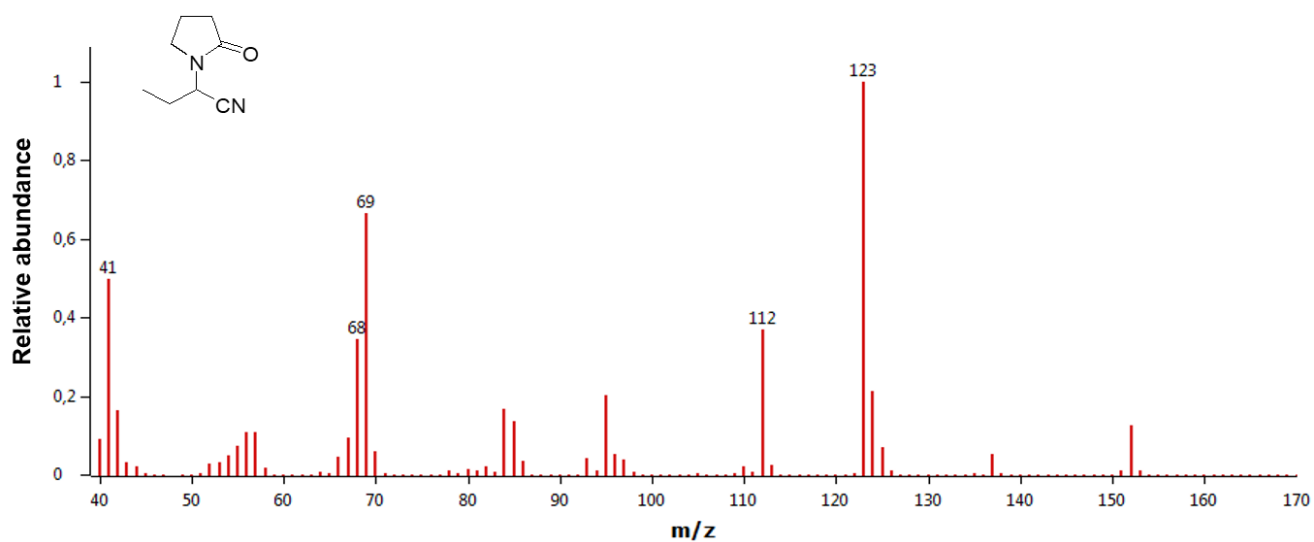


Figure S6. MS (EI, 70 eV) spectrum of compound 4a.

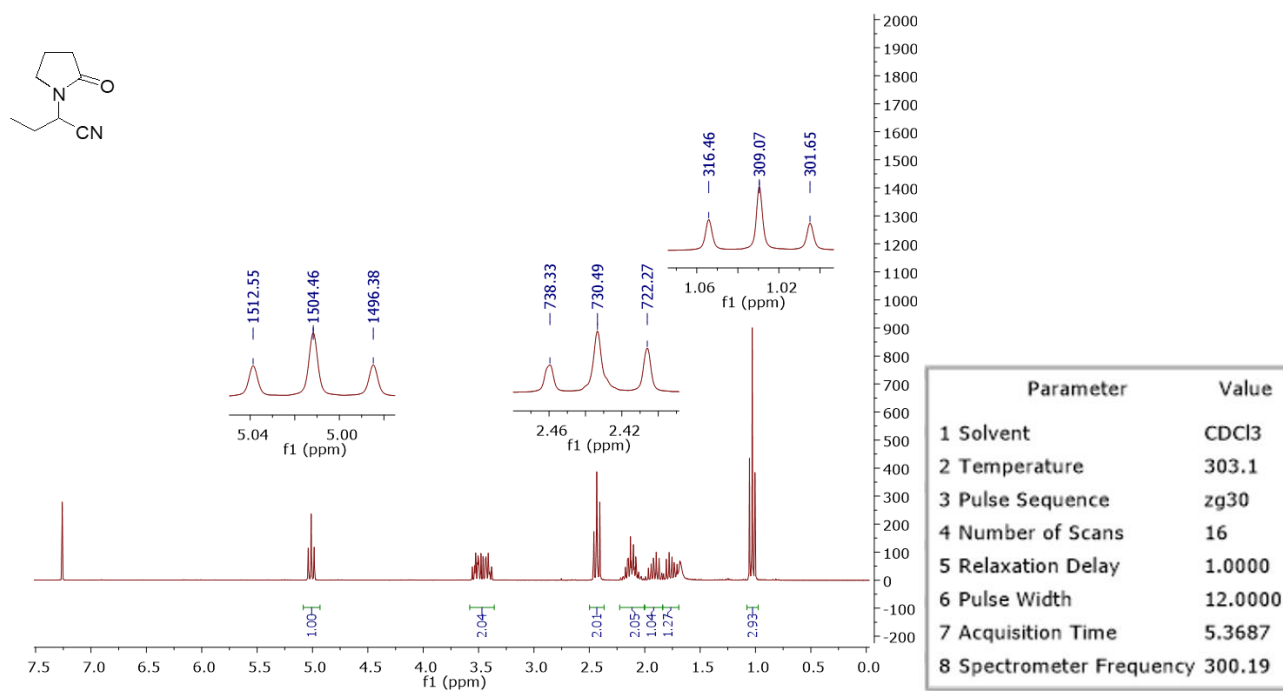


Figure S7. ¹H NMR (300.19 MHz, CDCl₃) spectrum of compound 4a.

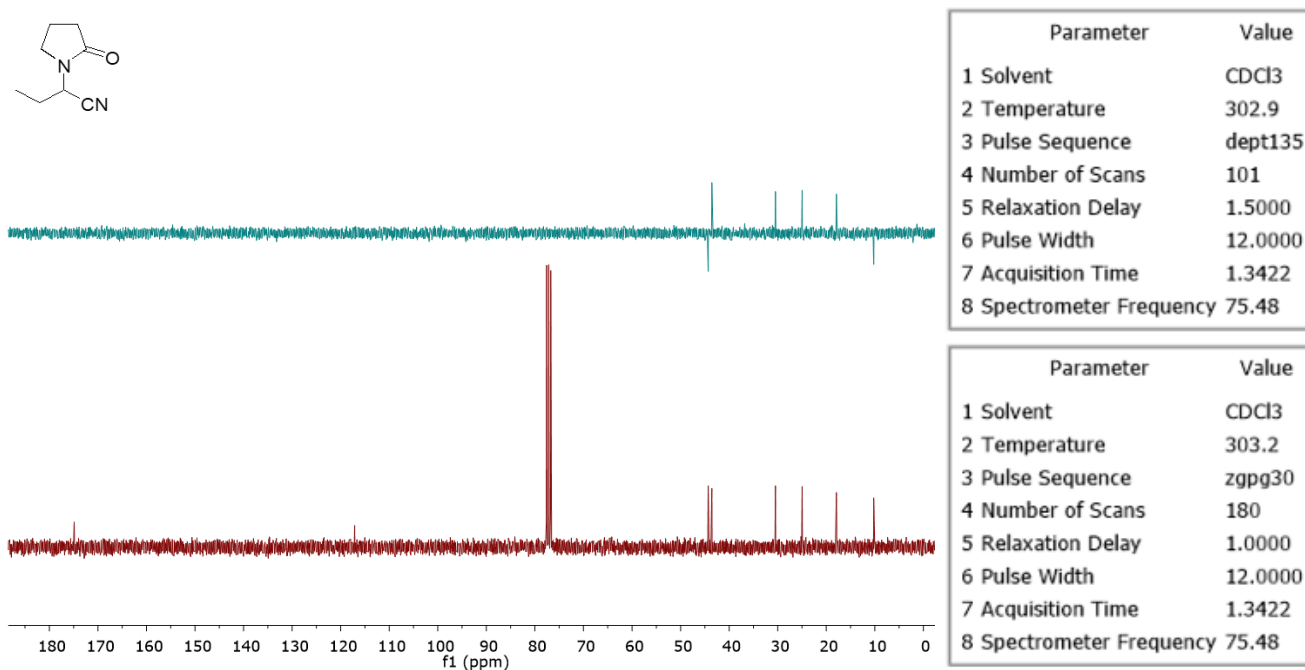


Figure S8. ^{13}C NMR (75.48 MHz, CDCl_3) spectrum and DEPT-135 experiment of compound **4a**.

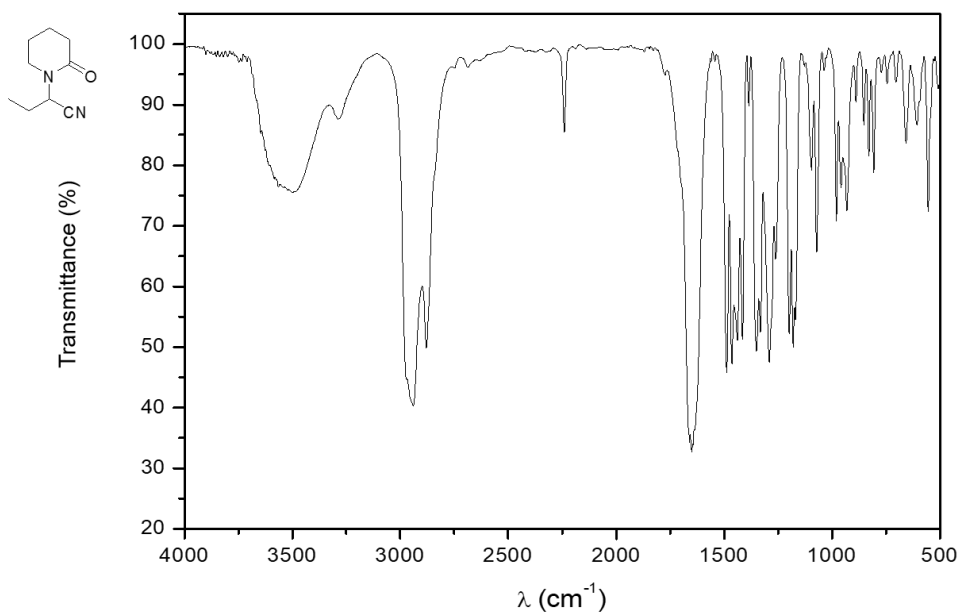


Figure S9. IR spectrum of compound **4b**.

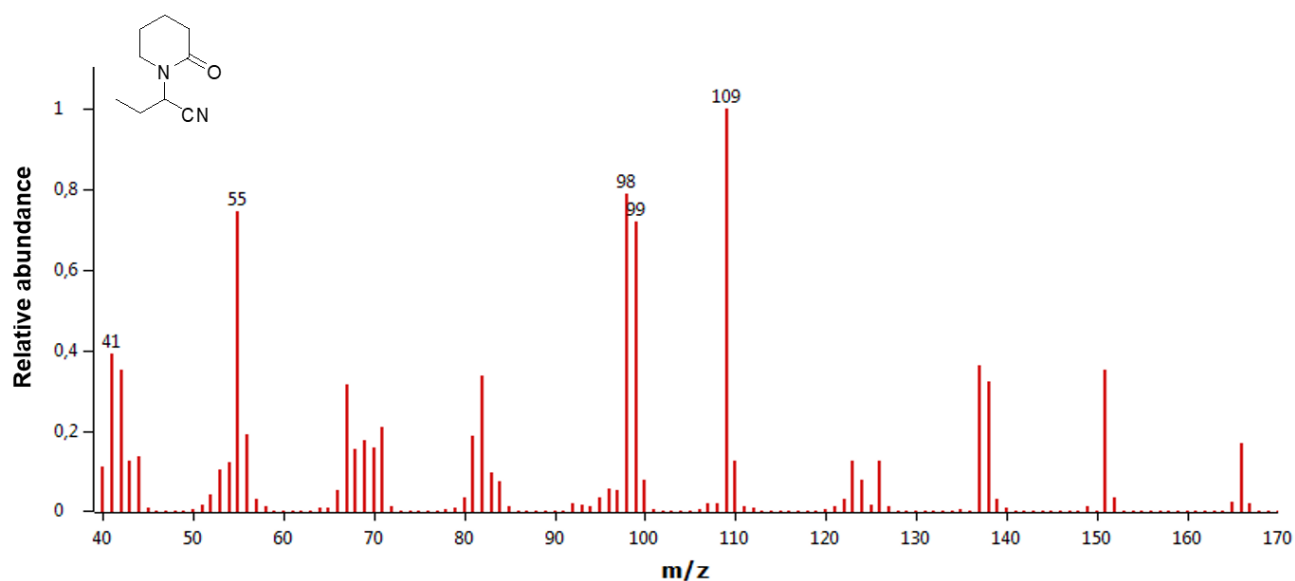
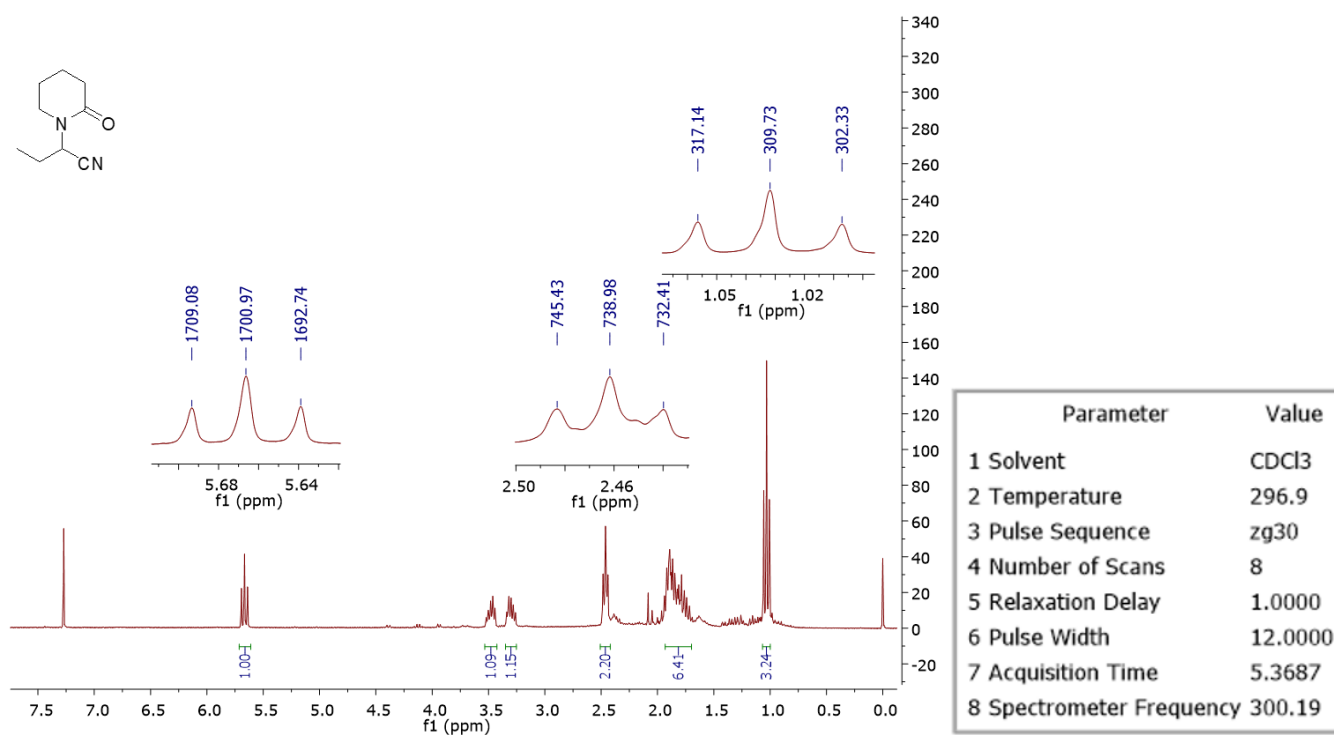


Figure S10. MS (EI, 70 eV) spectrum of compound 4b.

Figure S11. ¹H NMR (300.19 MHz, CDCl₃) spectrum of compound 4b.

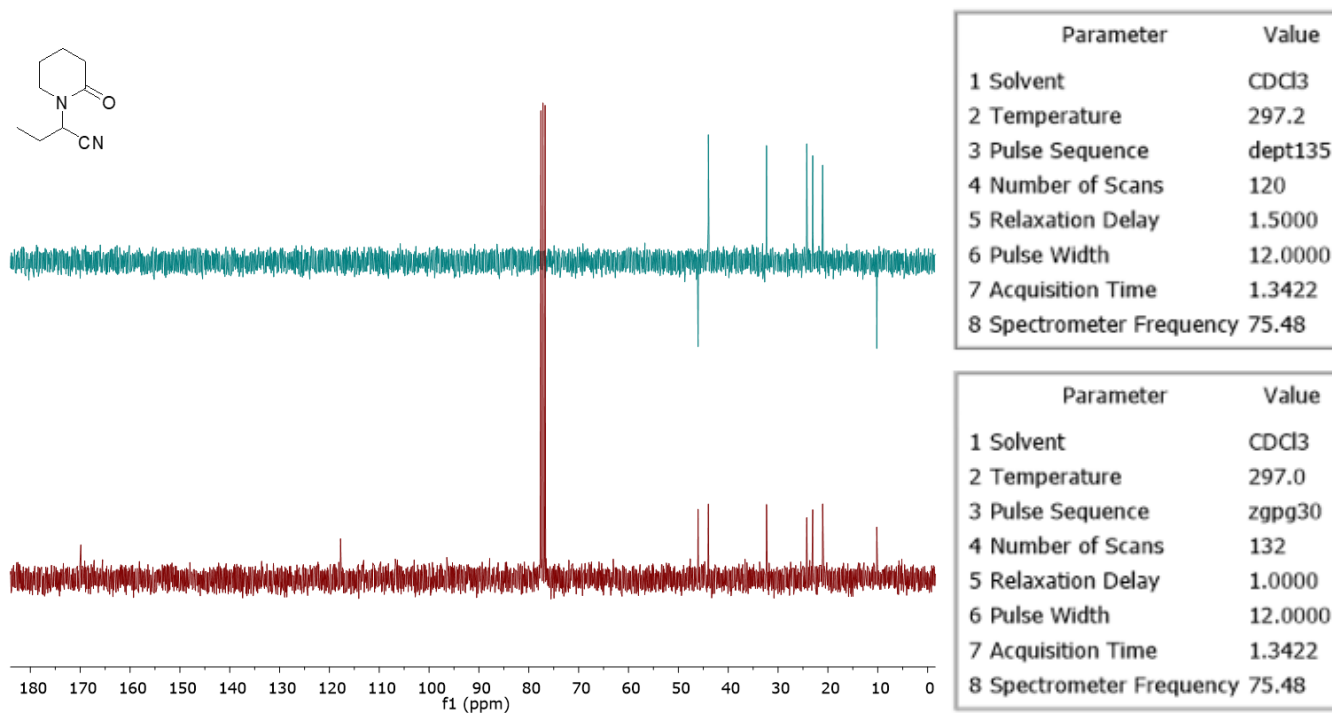


Figure S12. ^{13}C NMR (75.48 MHz, CDCl_3) spectrum and DEPT-135 experiment of compound **4b**.

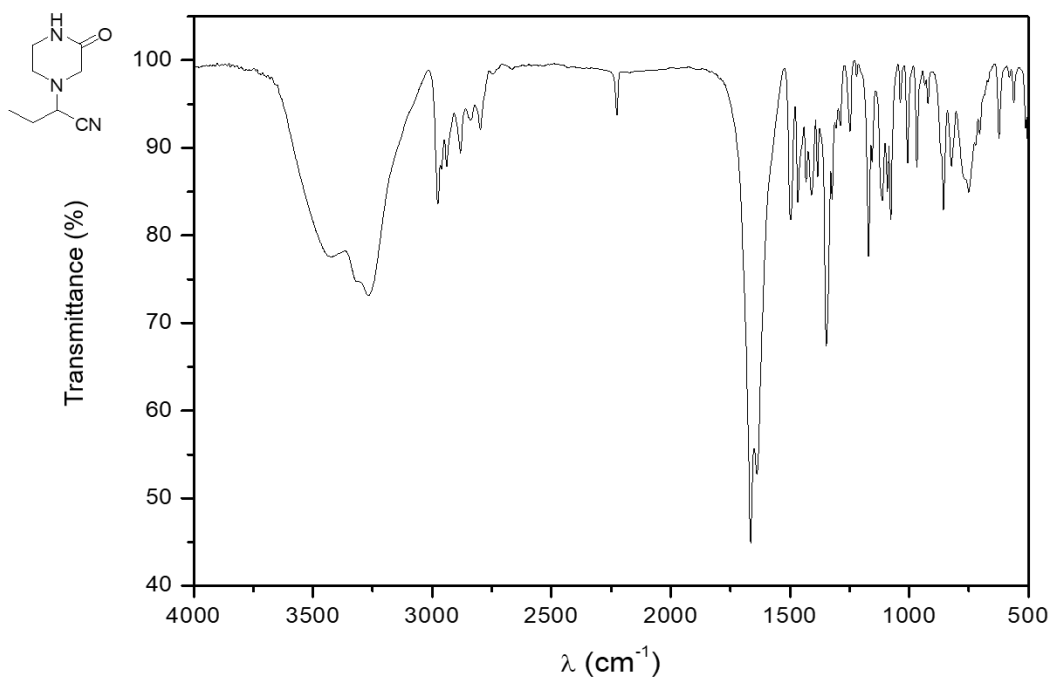


Figure S13. IR spectrum of compound **4c**.

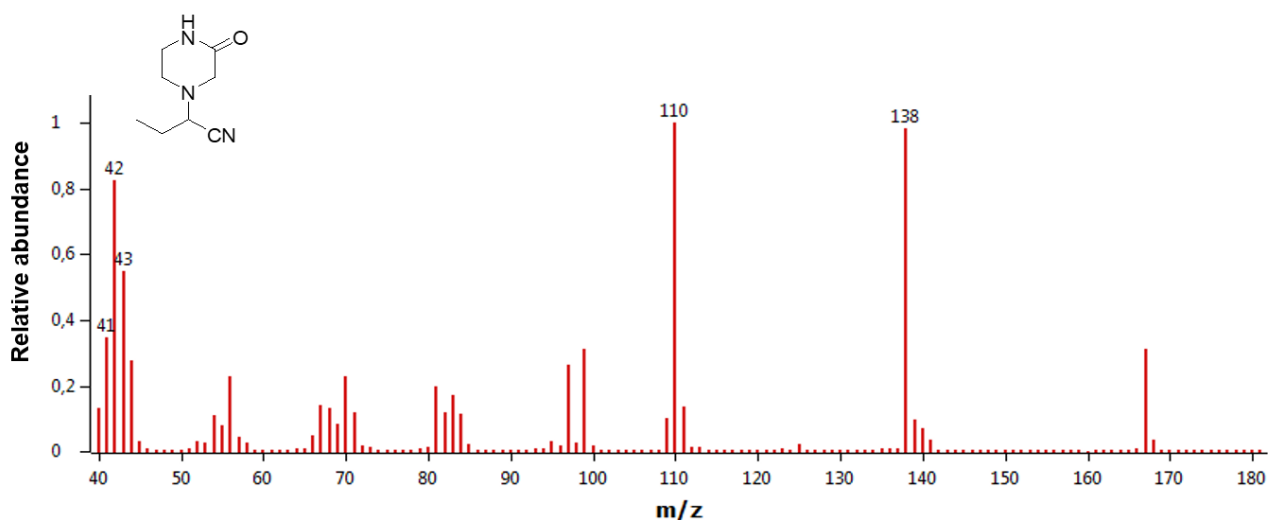


Figure S14. MS (EI, 70 eV) spectrum of compound **4c**.

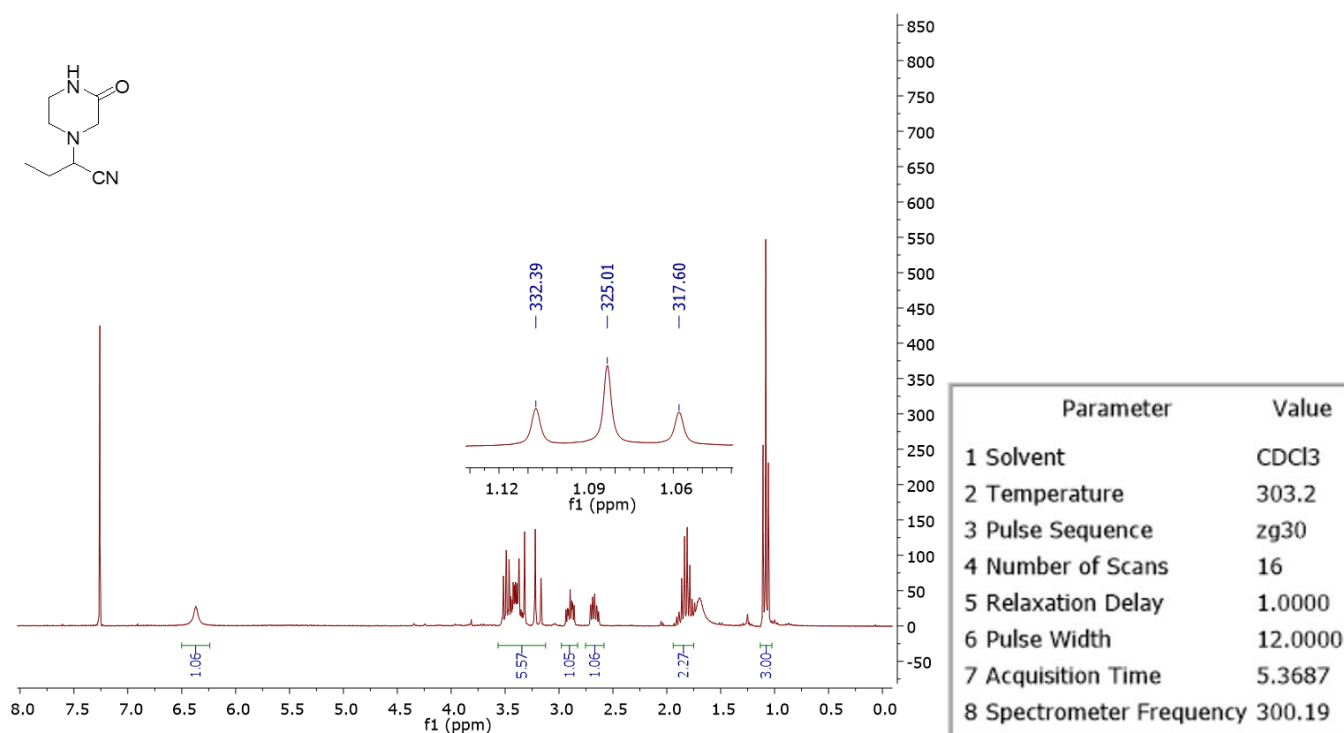


Figure S15. ^1H NMR (300.19 MHz, CDCl_3) spectrum of compound **4c**.

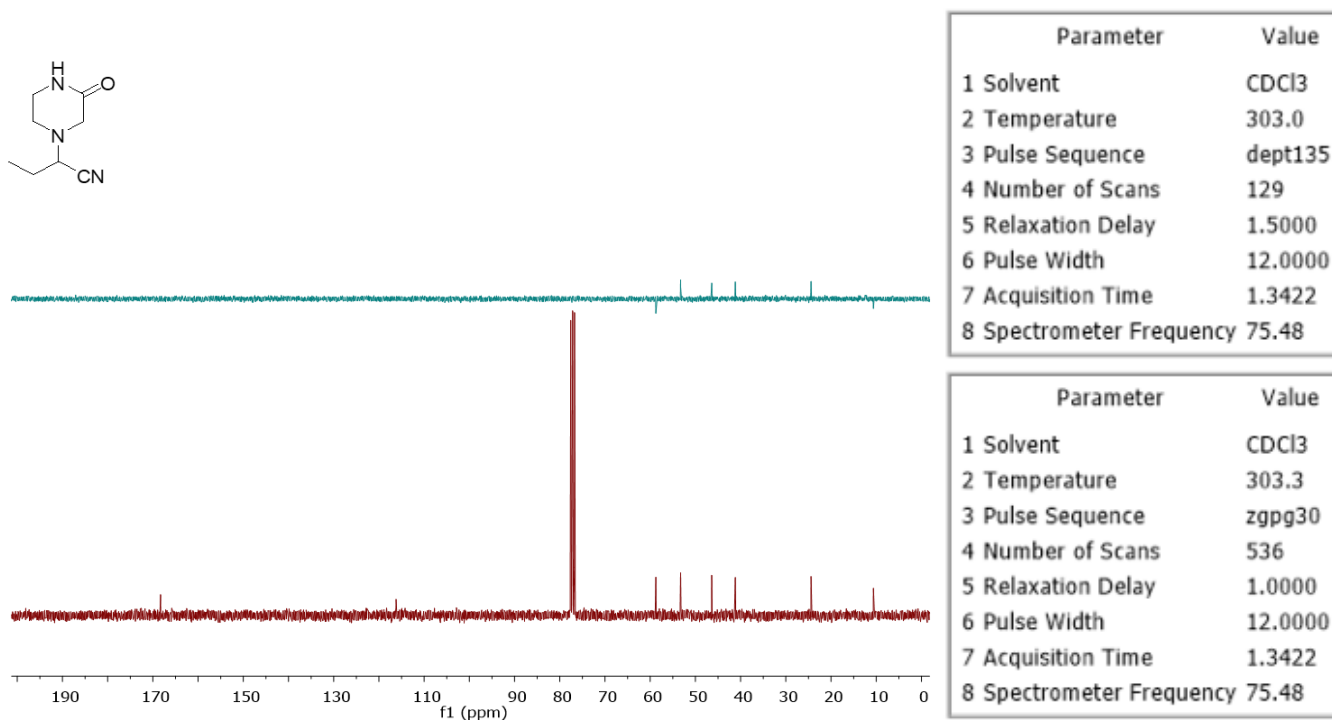


Figure S16. ¹³C NMR (75.48 MHz, CDCl₃) spectrum and DEPT-135 experiment of compound 4c.

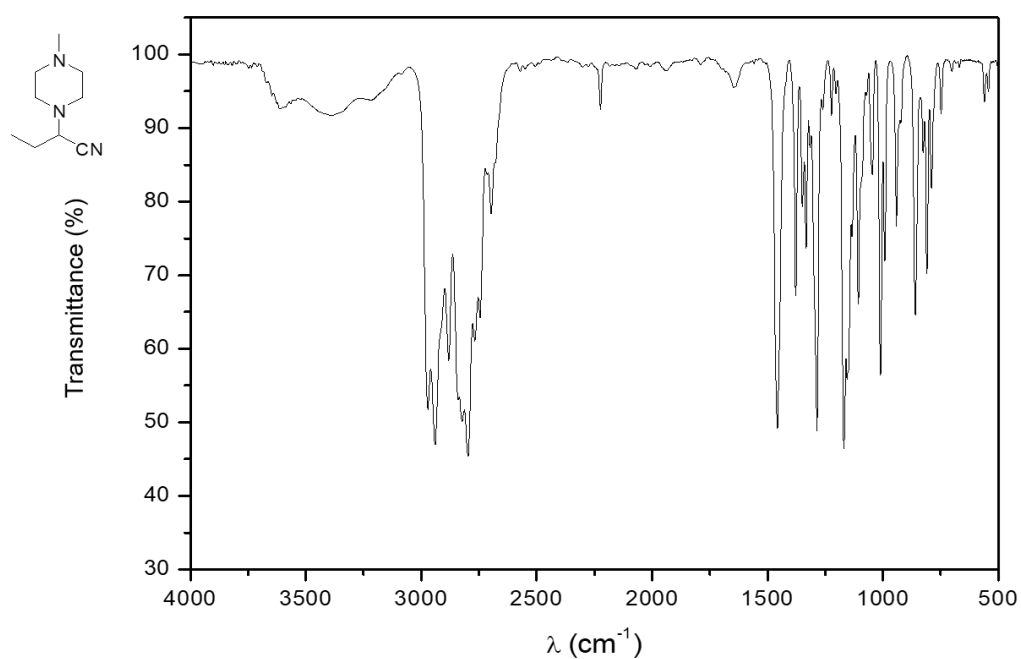


Figure S17. IR spectrum of compound 4d.

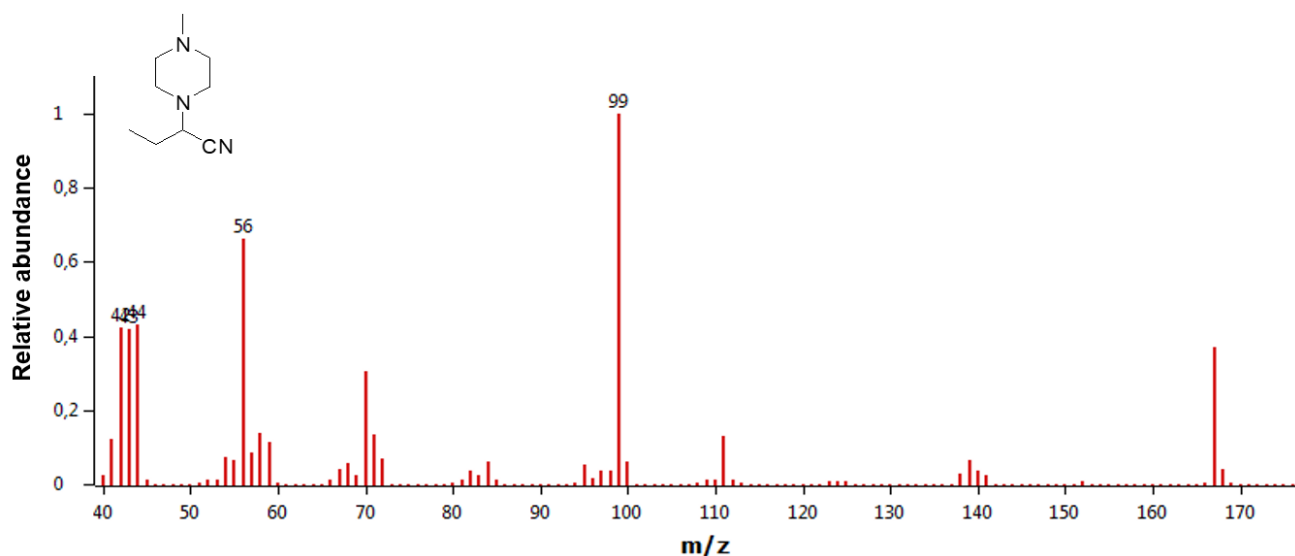


Figure S18. MS (EI, 70 eV) spectrum of compound 4d.

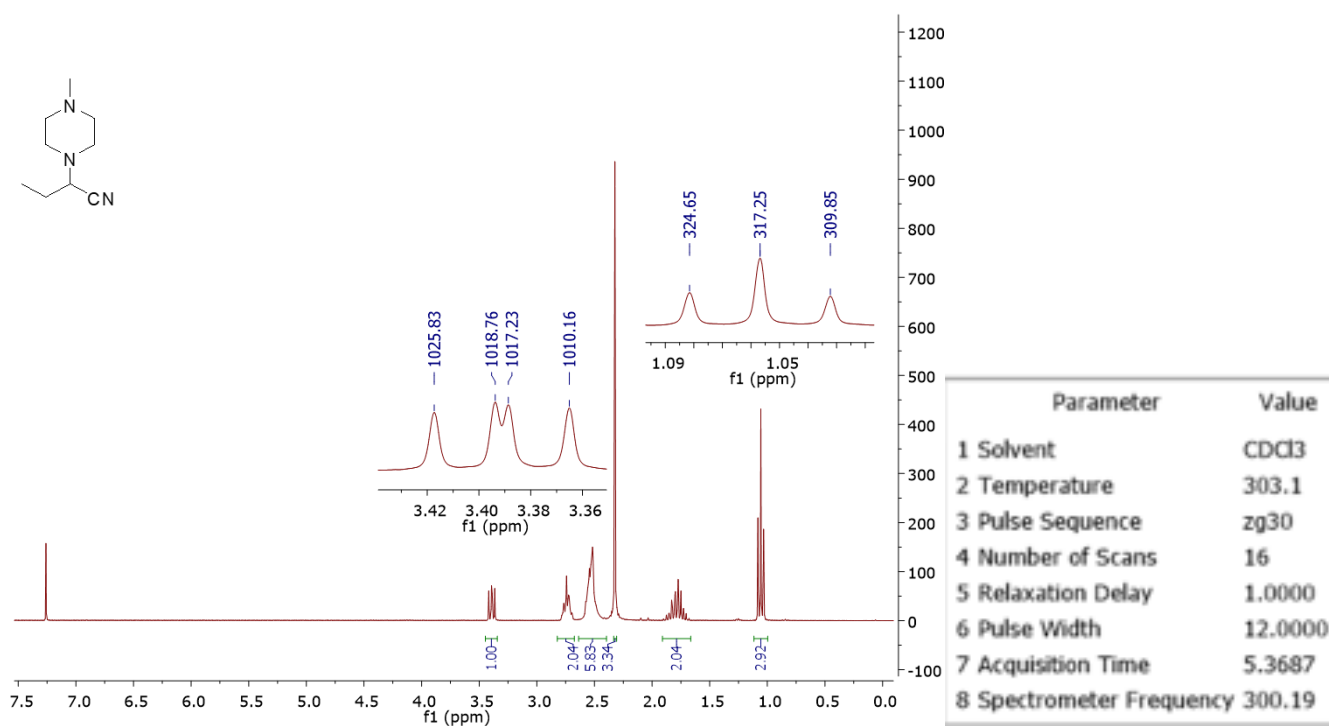
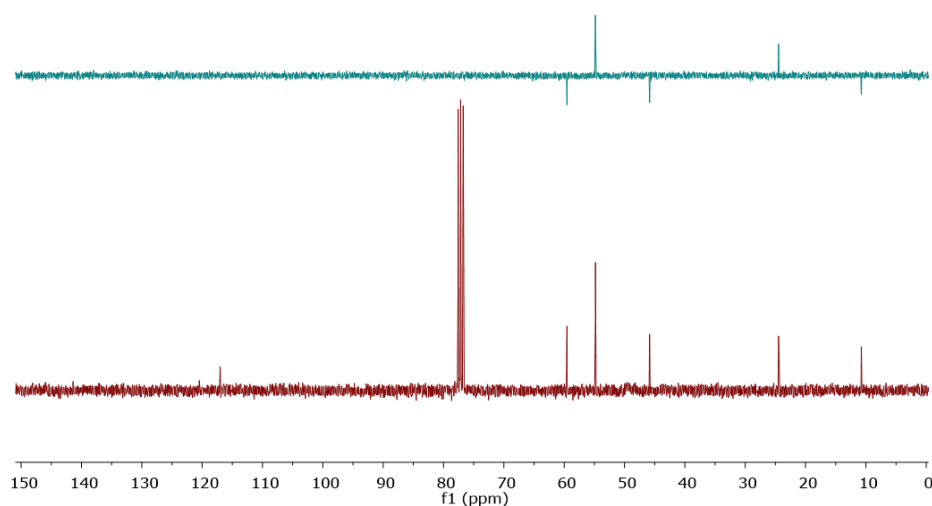
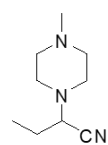


Figure S19. ¹H NMR (300.19 MHz, CDCl₃) spectrum of compound 4d.



Parameter	Value
1 Solvent	CDCl ₃
2 Temperature	303.0
3 Pulse Sequence	dept135
4 Number of Scans	101
5 Relaxation Delay	1.5000
6 Pulse Width	12.0000
7 Acquisition Time	1.3422
8 Spectrometer Frequency	75.48

Parameter	Value
1 Solvent	CDCl ₃
2 Temperature	303.2
3 Pulse Sequence	zgpg30
4 Number of Scans	307
5 Relaxation Delay	1.0000
6 Pulse Width	12.0000
7 Acquisition Time	1.3422
8 Spectrometer Frequency	75.48

Figure S20. ¹³C NMR (75.48 MHz, CDCl₃) spectrum and DEPT-135 experiment of compound **4d**.

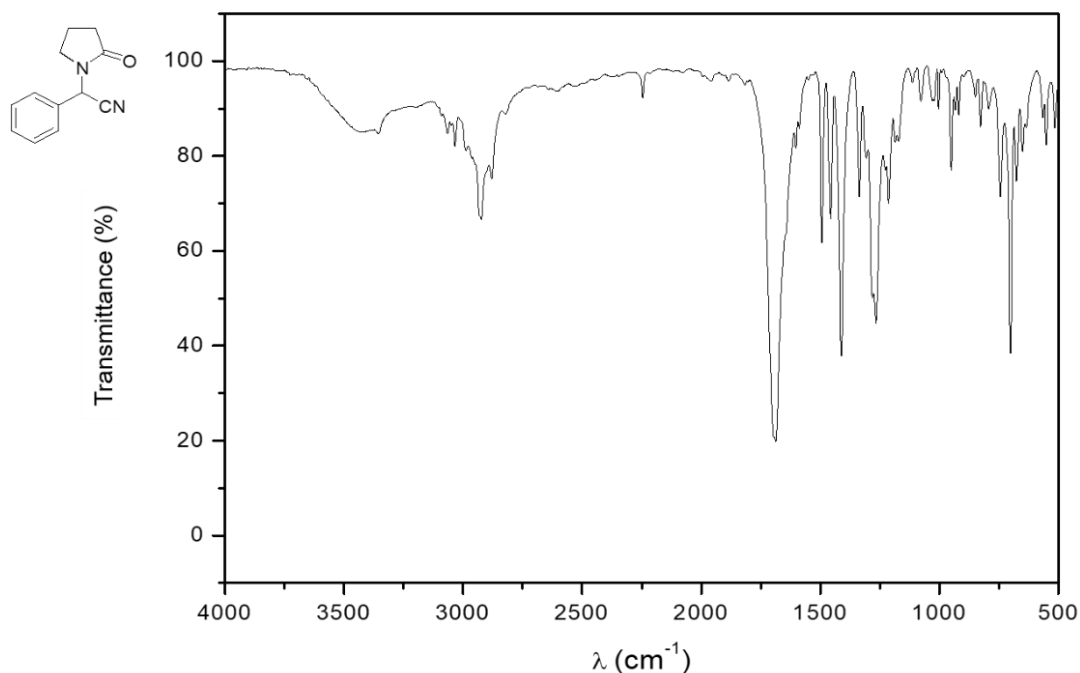
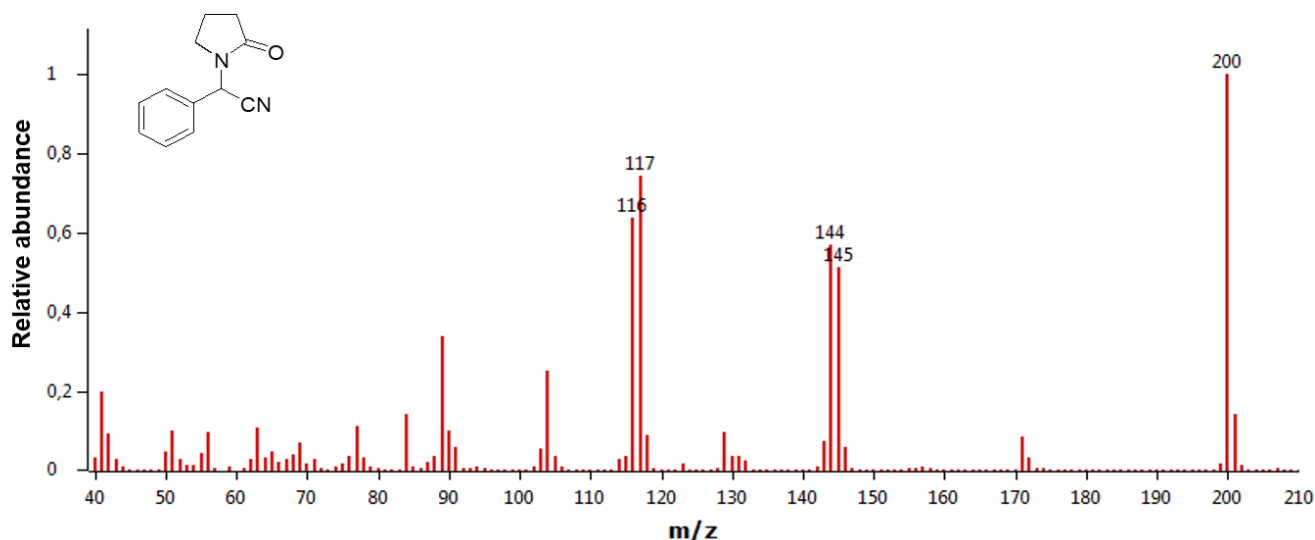
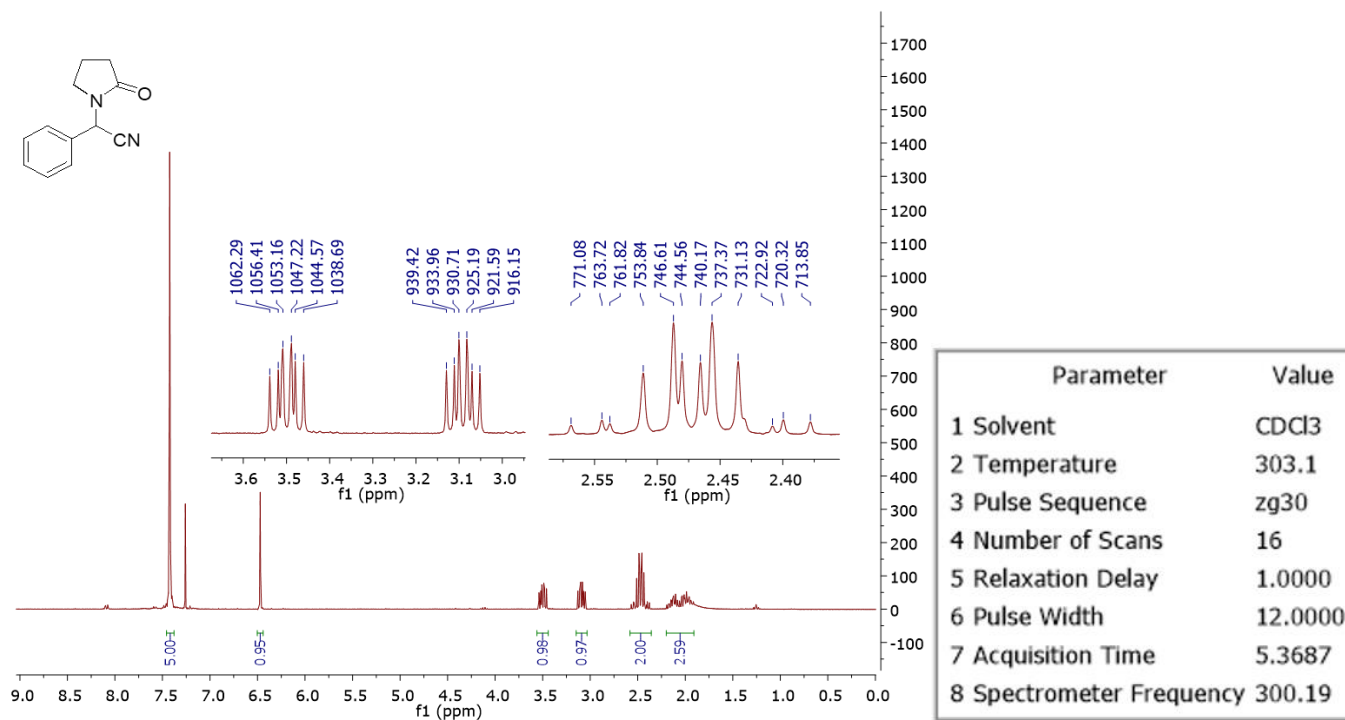


Figure S21. IR spectrum of compound **8a**.

Figure S22. MS (EI, 70 eV) spectrum of compound **8a**.Figure S23. ¹H NMR (300.19 MHz, CDCl₃) spectrum of compound **8a**.

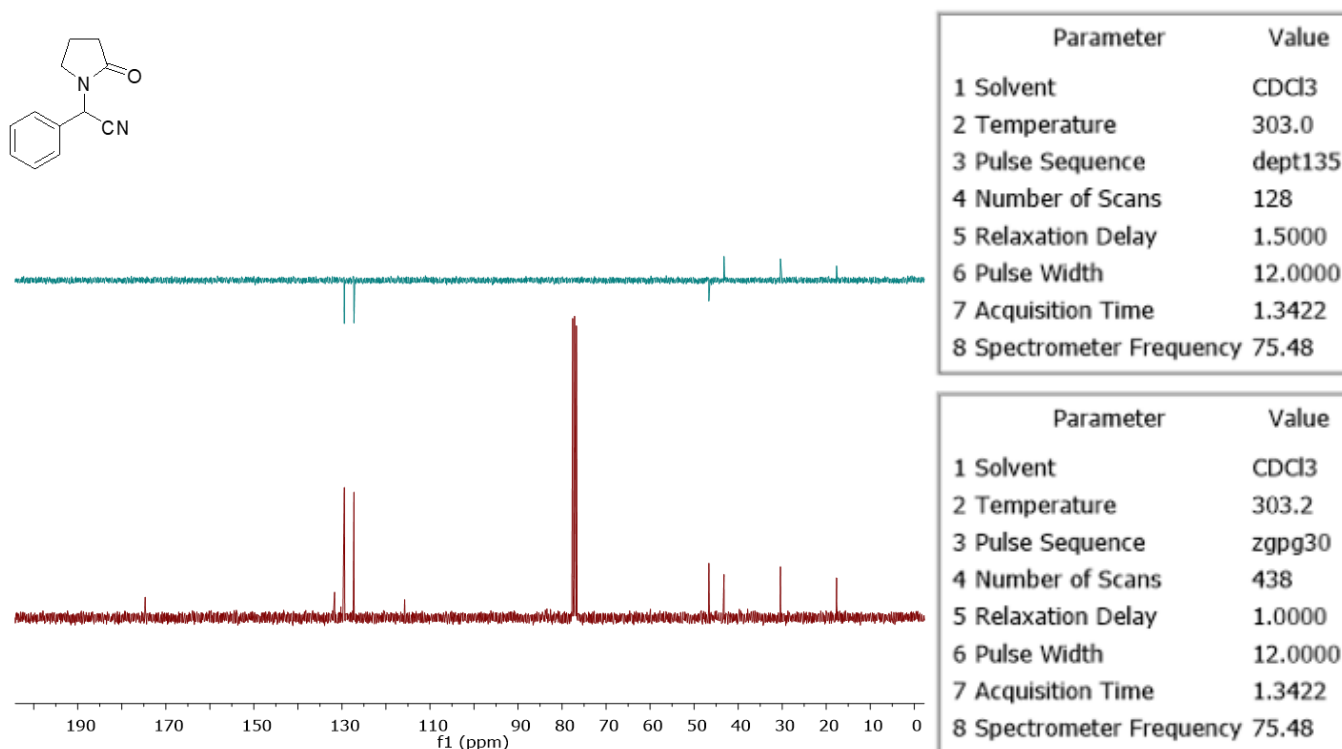


Figure S24. ¹³C NMR (75.48 MHz, CDCl₃) spectrum and DEPT-135 experiment of compound **8a**.

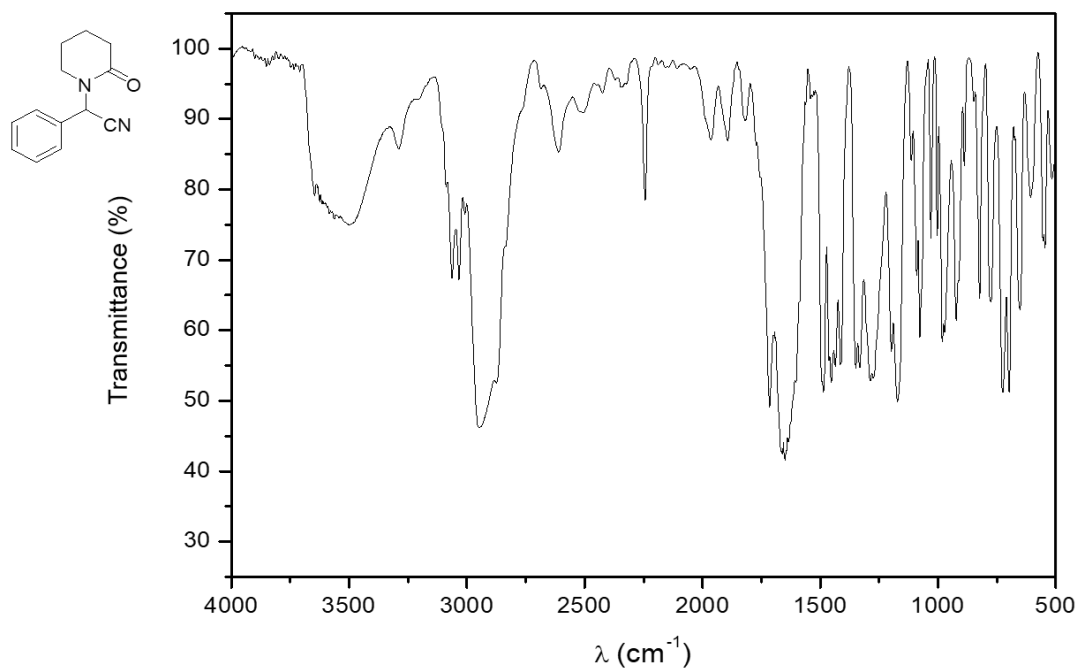


Figure S25. IR spectrum of compound **8b**.

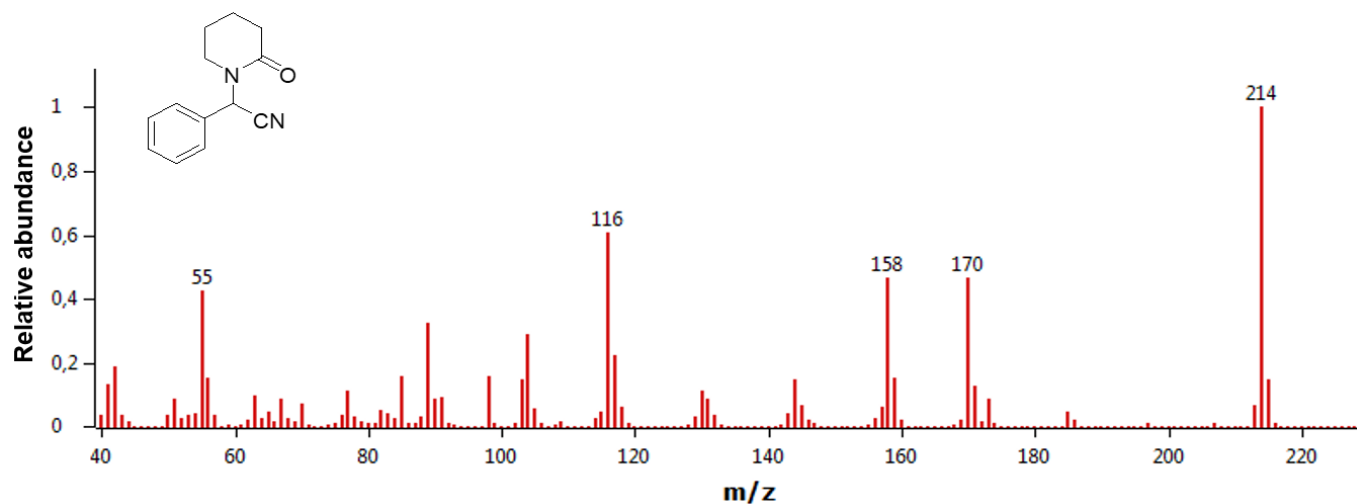


Figure S26. MS (EI, 70 eV) spectrum of compound **8b**.

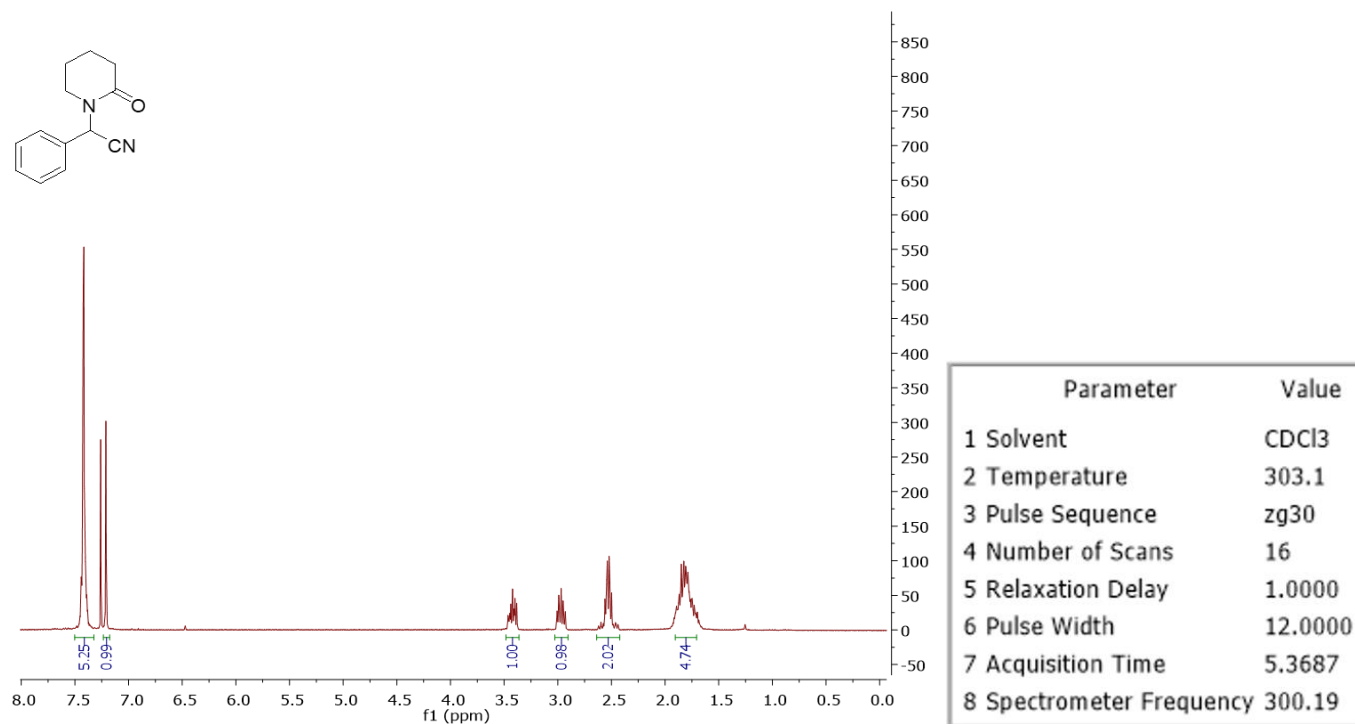


Figure S27. ^1H NMR (300.19 MHz, CDCl_3) spectrum of compound **8b**.

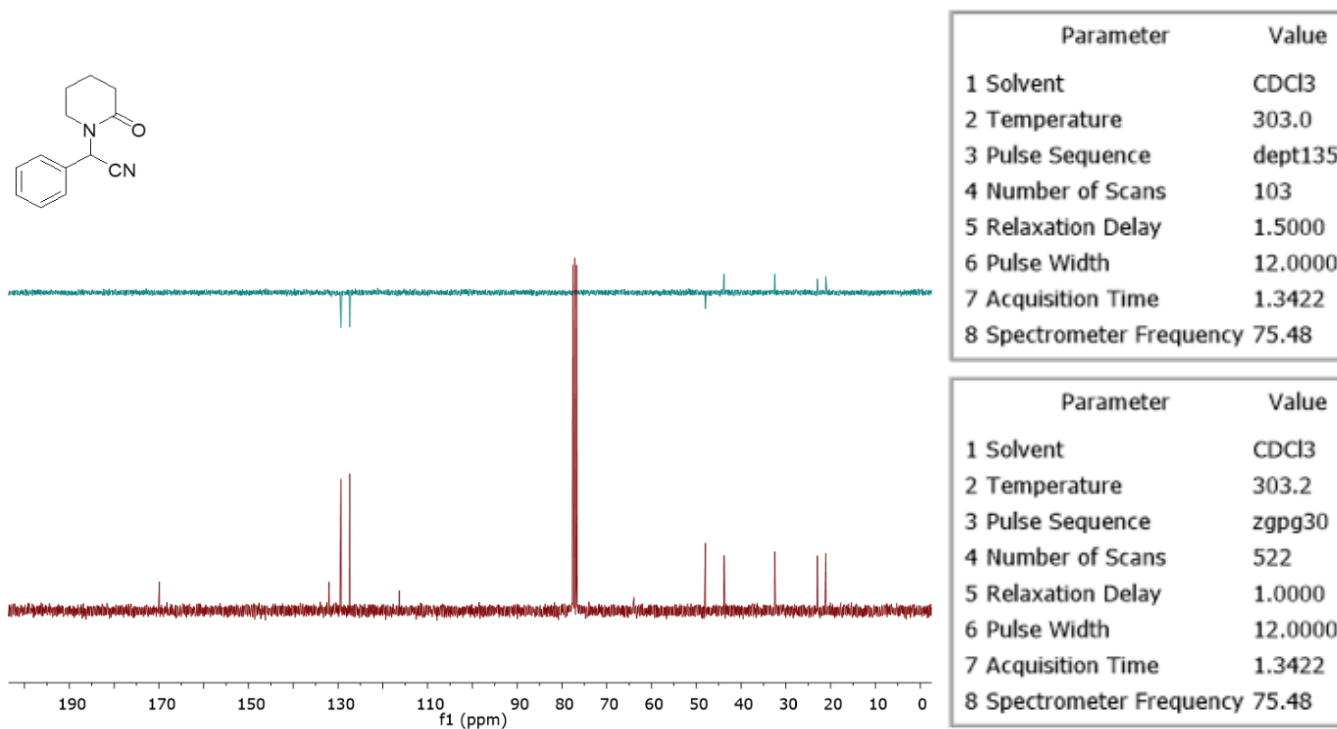


Figure S28. ^{13}C NMR (75.48 MHz, CDCl_3) spectrum and DEPT-135 experiment of compound **8b**.

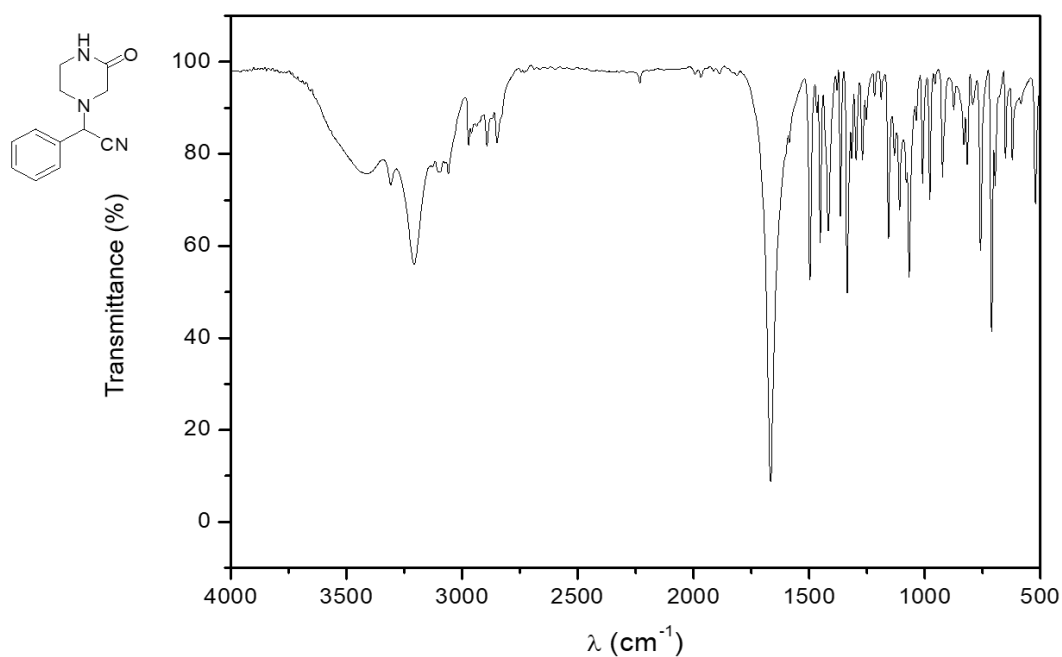


Figure S29. IR spectrum of compound **8c**.

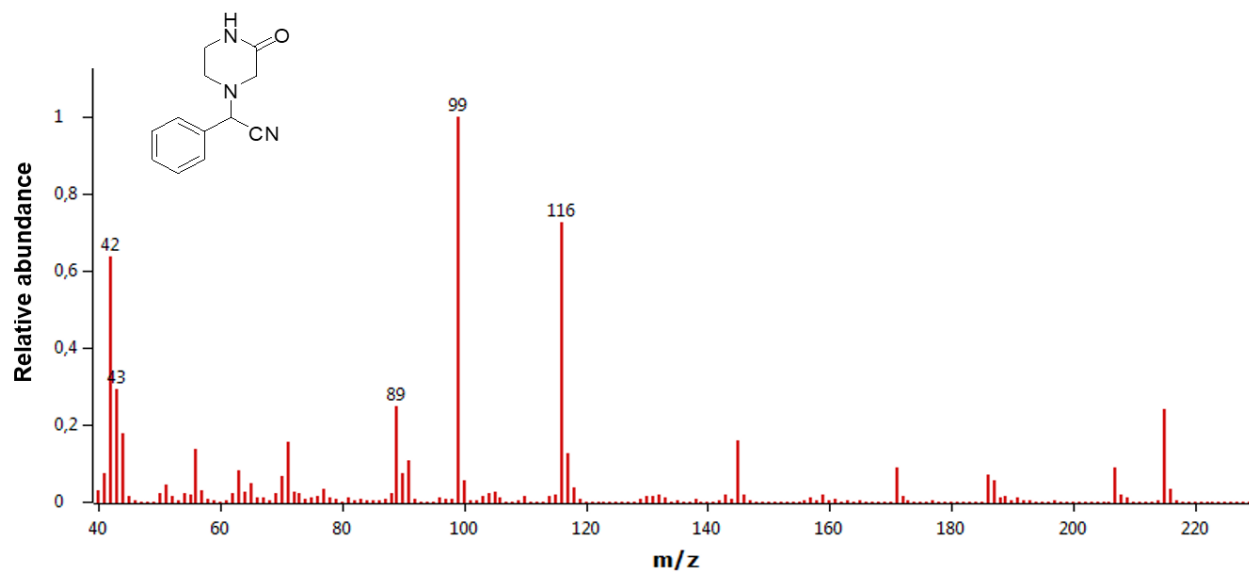


Figure S30. MS (EI, 70 eV) spectrum of compound 8c.

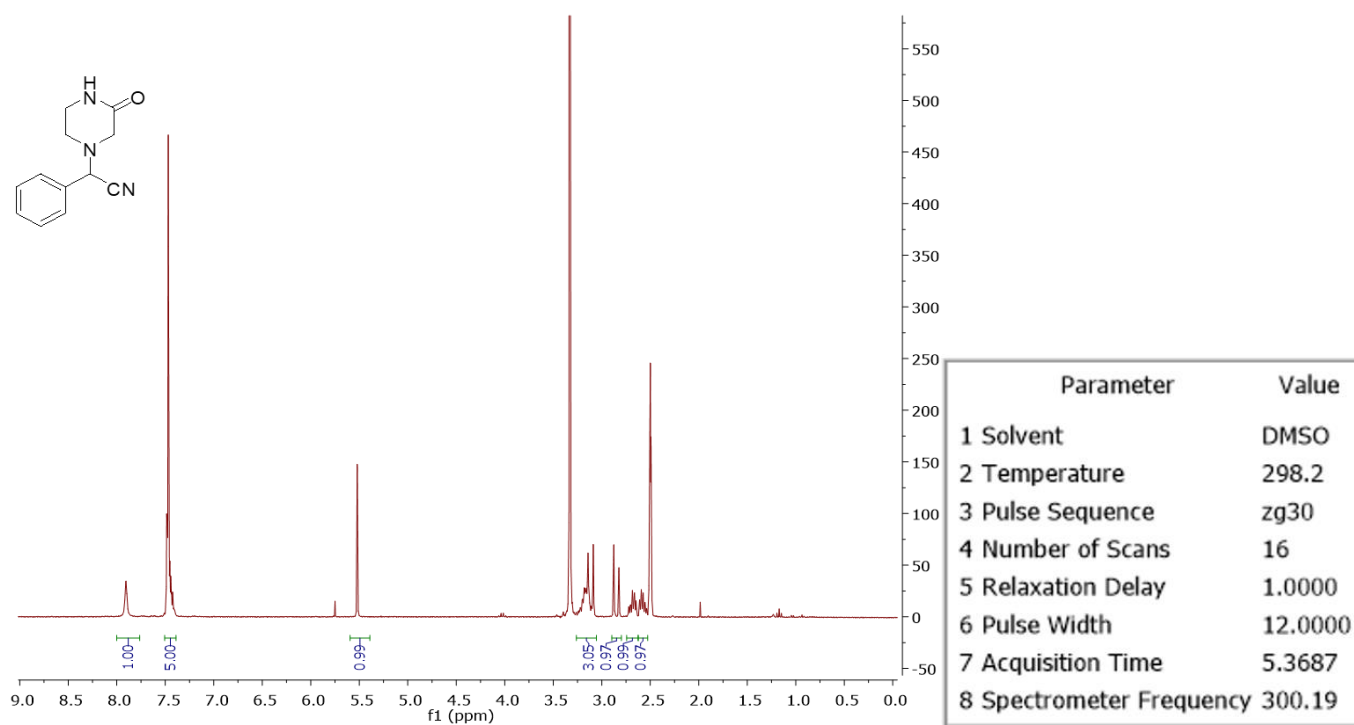
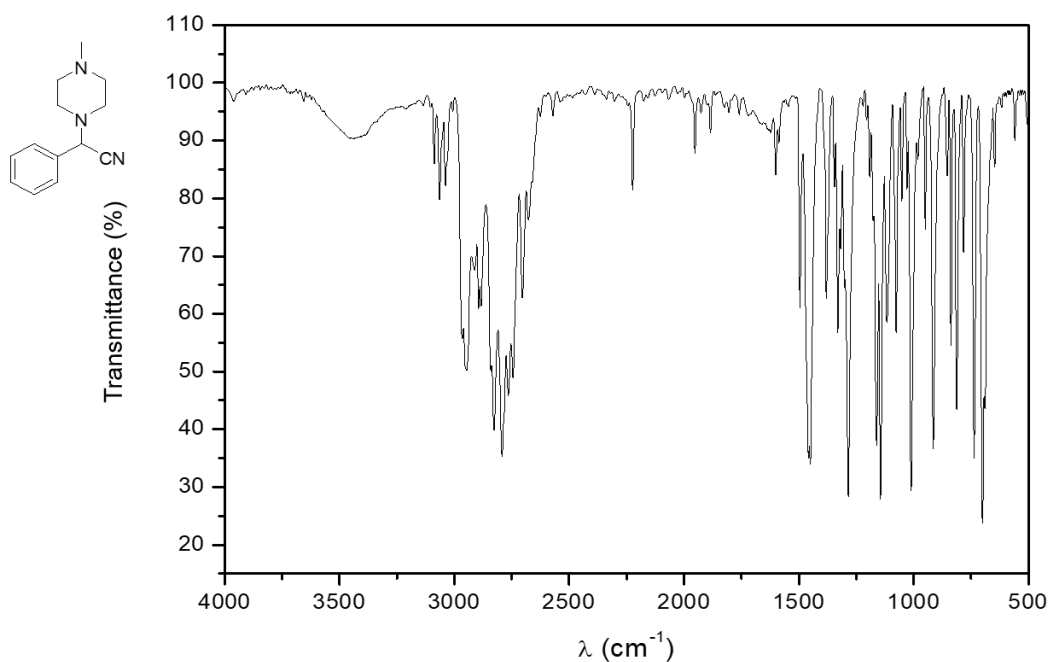
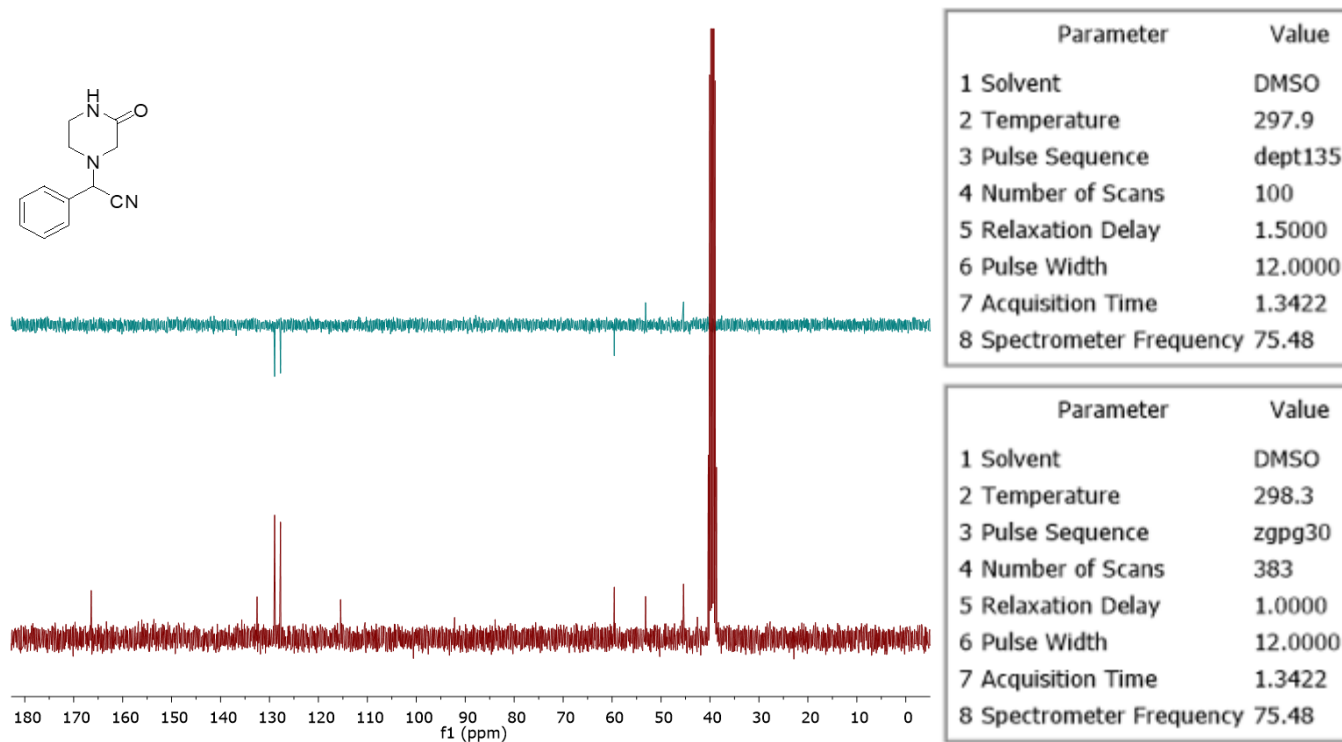


Figure S31. ^1H NMR (300.19 MHz, $\text{DMSO-}d_6$) spectrum of compound 8c.



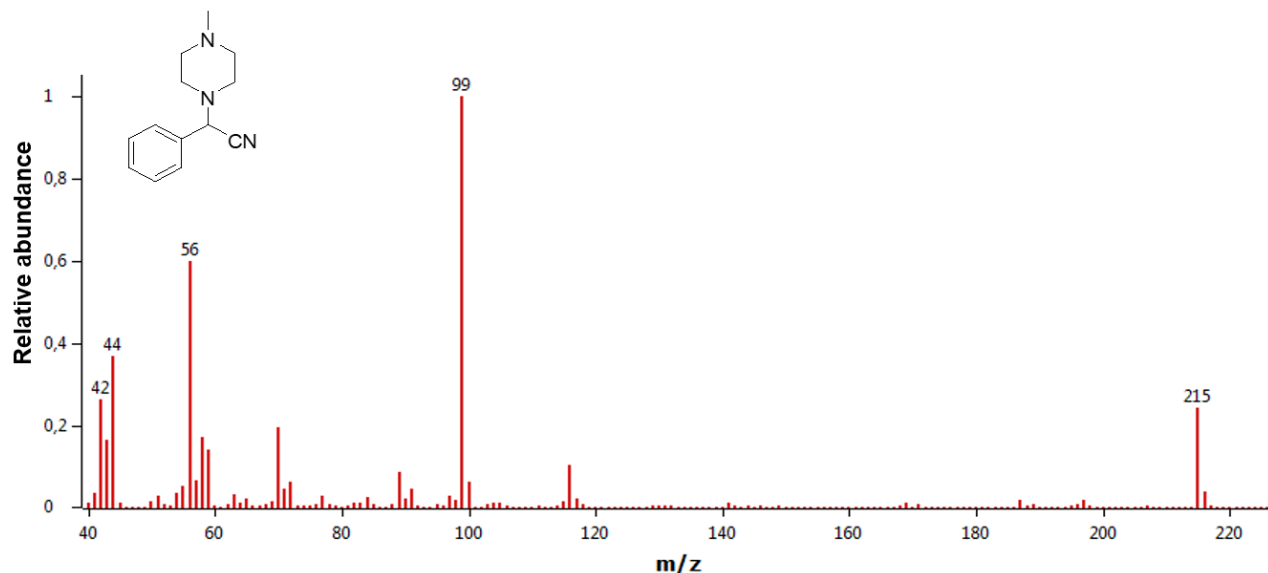


Figure S34. MS (EI, 70 eV) spectrum of compound 8d.

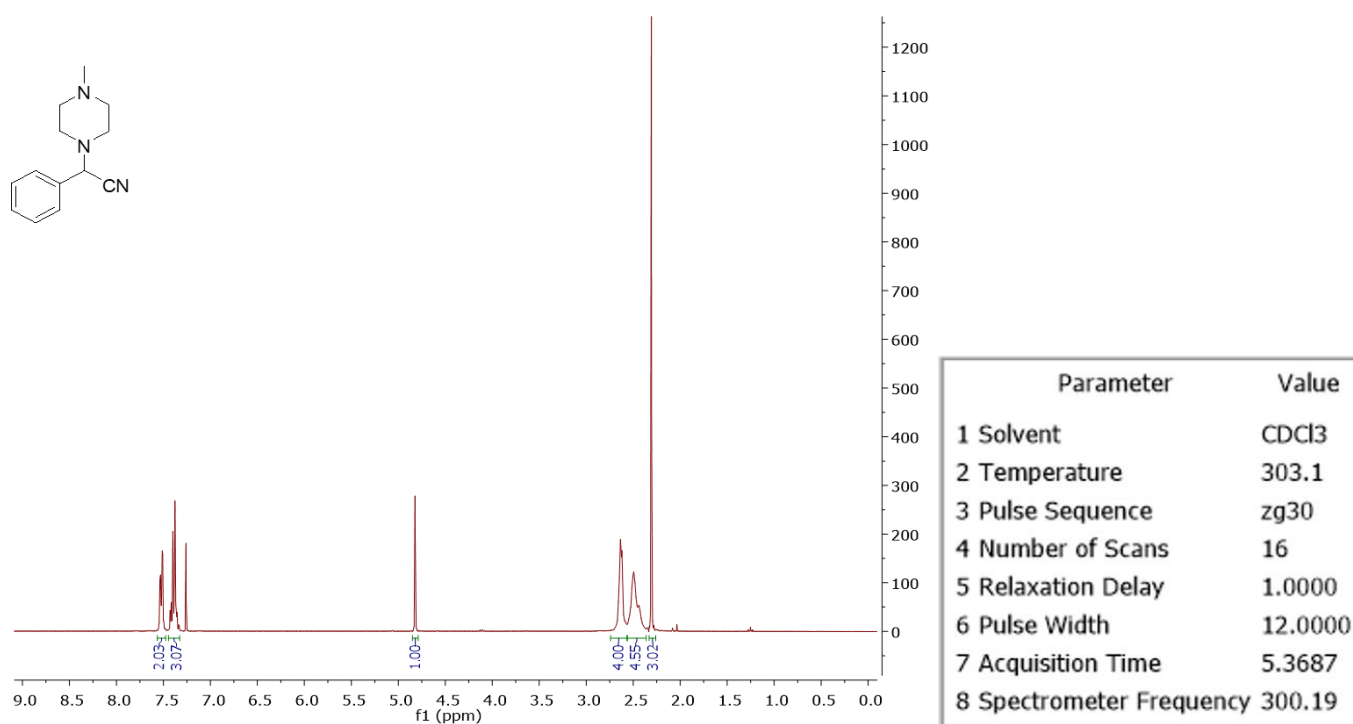


Figure S35. ¹H NMR (300.19 MHz, CDCl₃) spectrum of compound 8d.

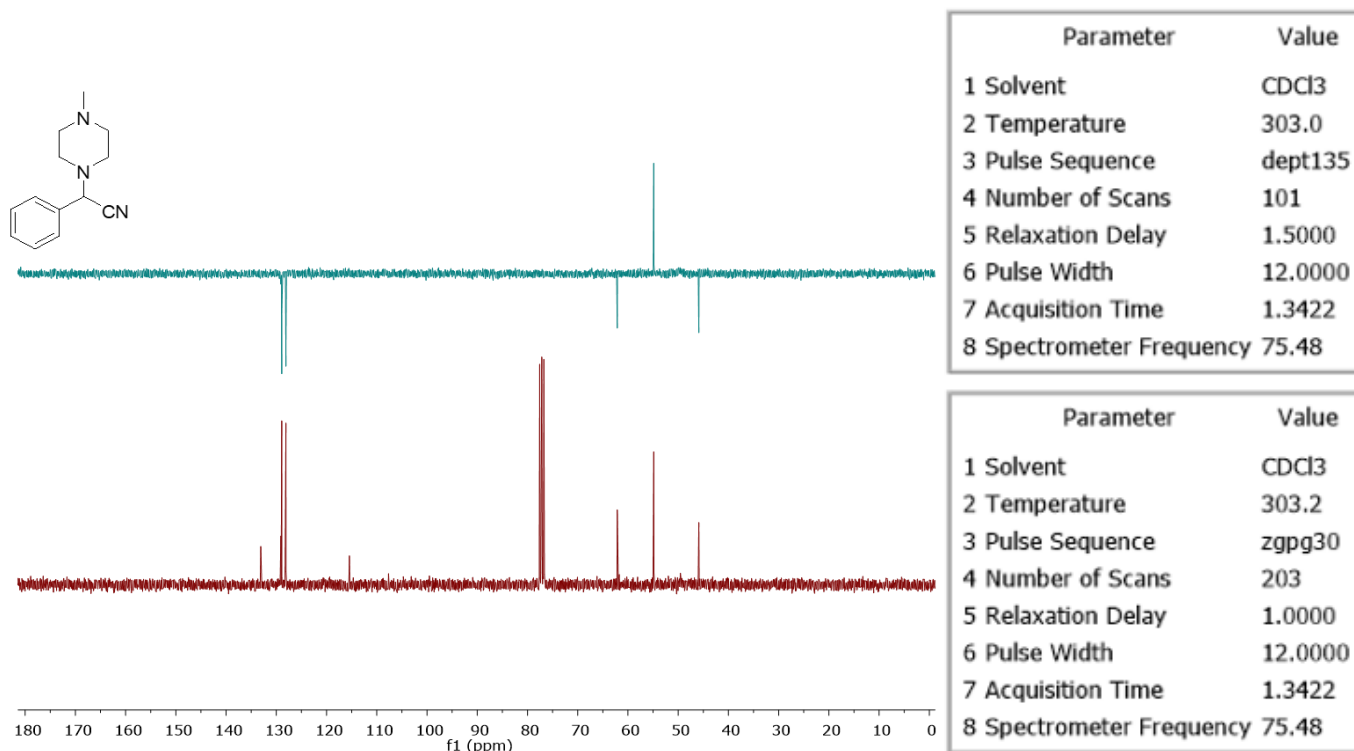


Figure S36. ¹³C NMR (75.48 MHz, CDCl₃) spectrum and DEPT-135 experiment of compound **8d**.

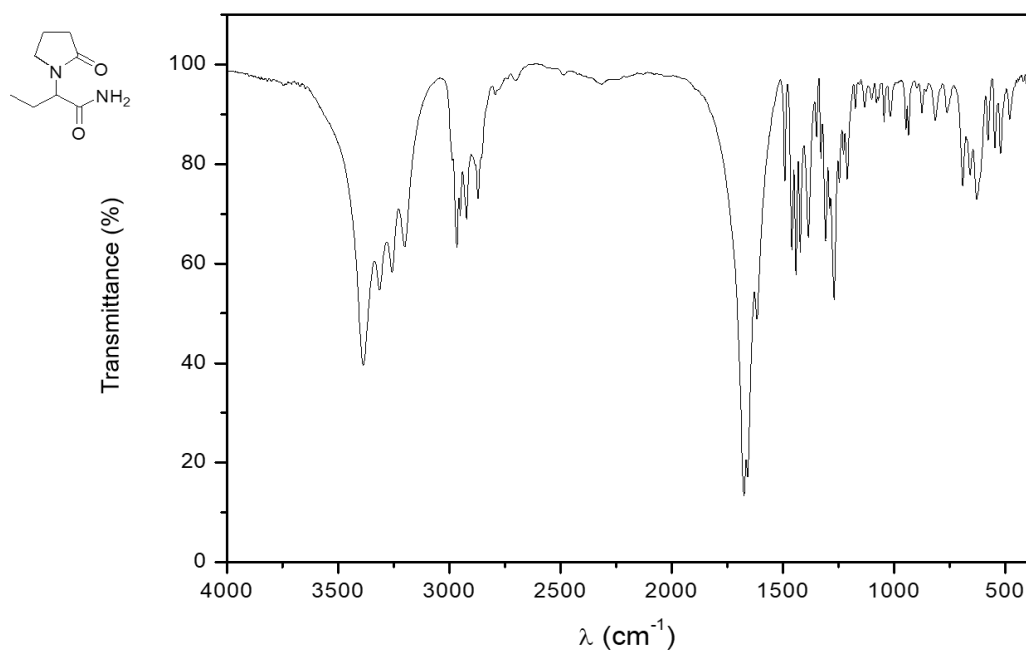


Figure S37. IR spectrum of compound **5a**.

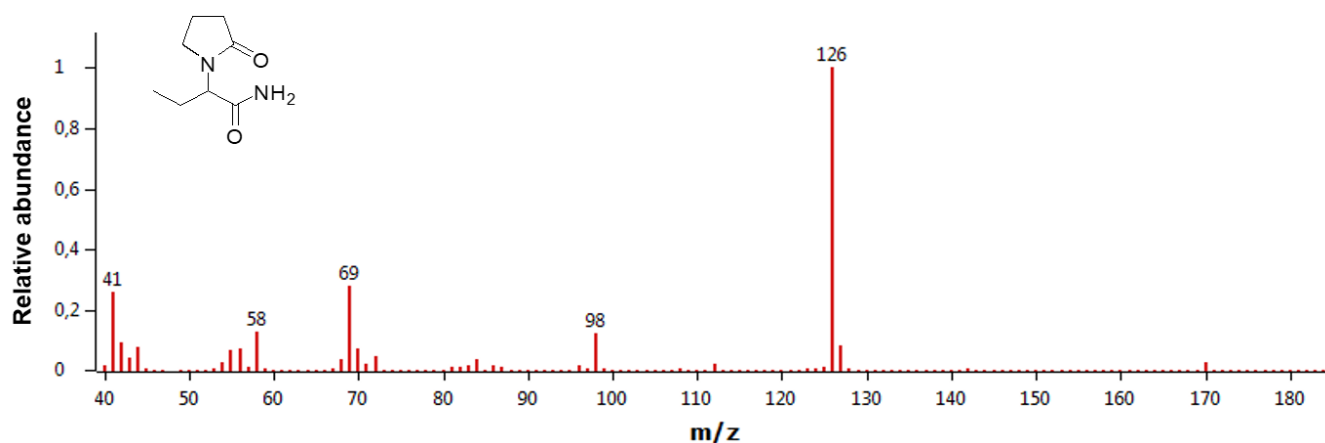


Figure S38. MS (EI, 70 eV) spectrum of compound **5a**.

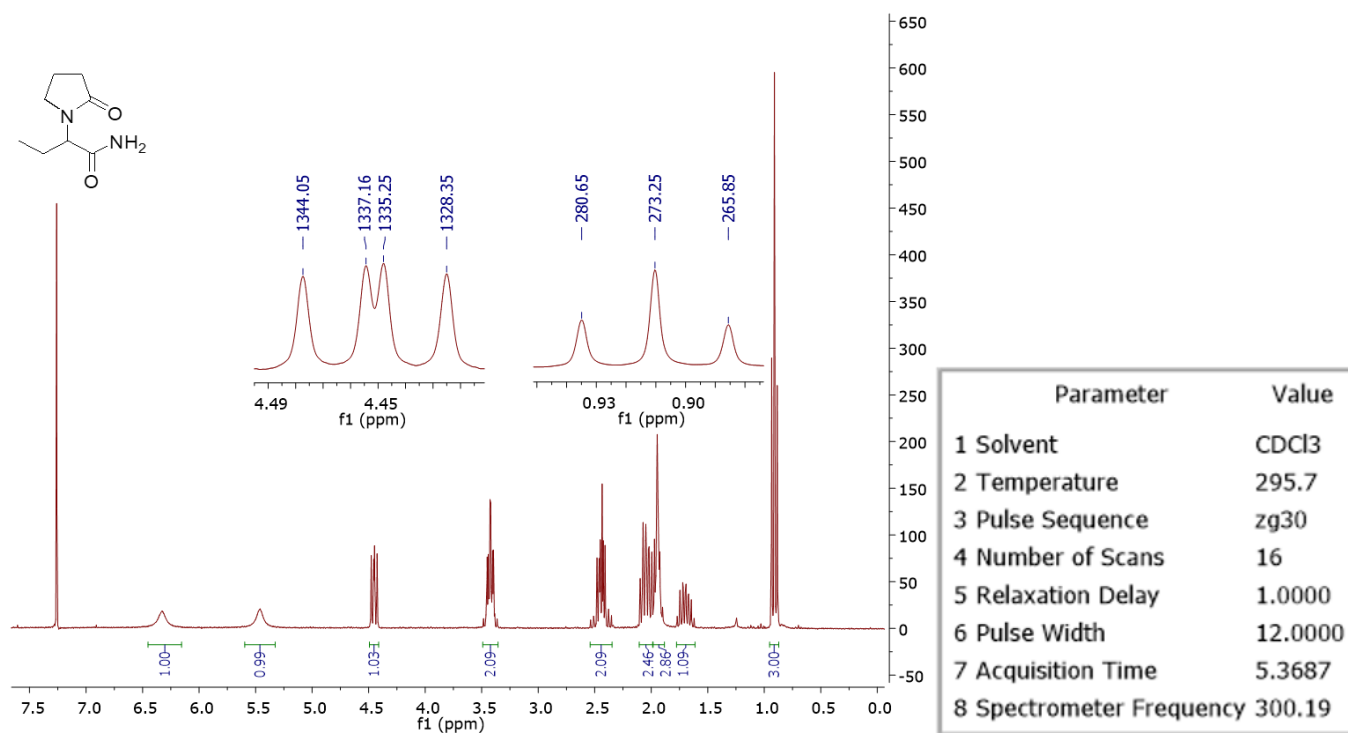


Figure S39. ^1H NMR (300.19 MHz, CDCl_3) spectrum of compound **5a**.

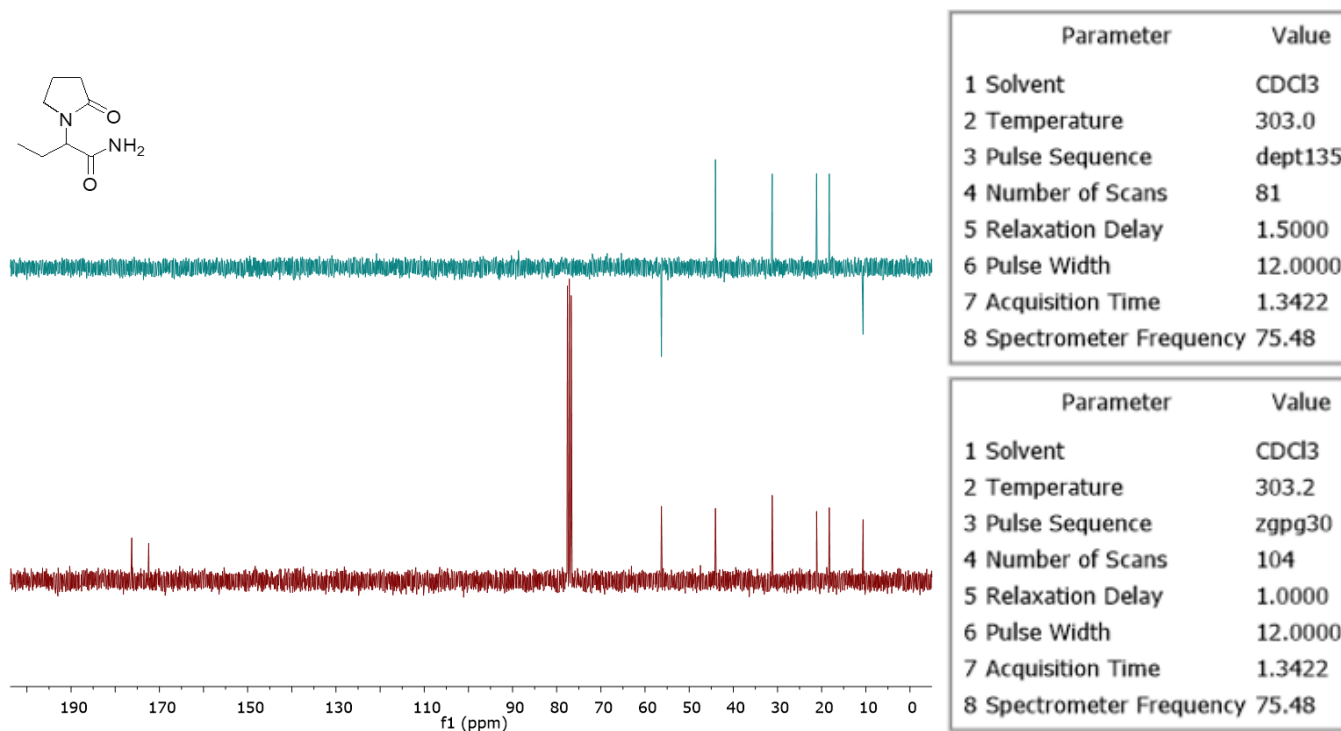


Figure S40. ^{13}C NMR (75.48 MHz, CDCl_3) spectrum and DEPT-135 experiment of compound **5a**.

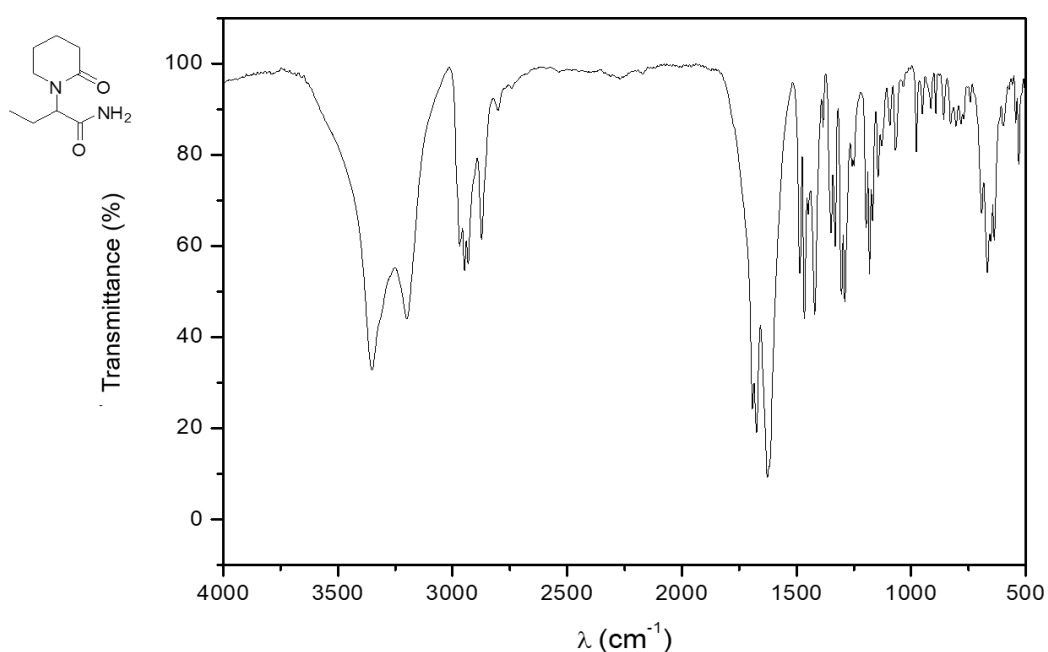
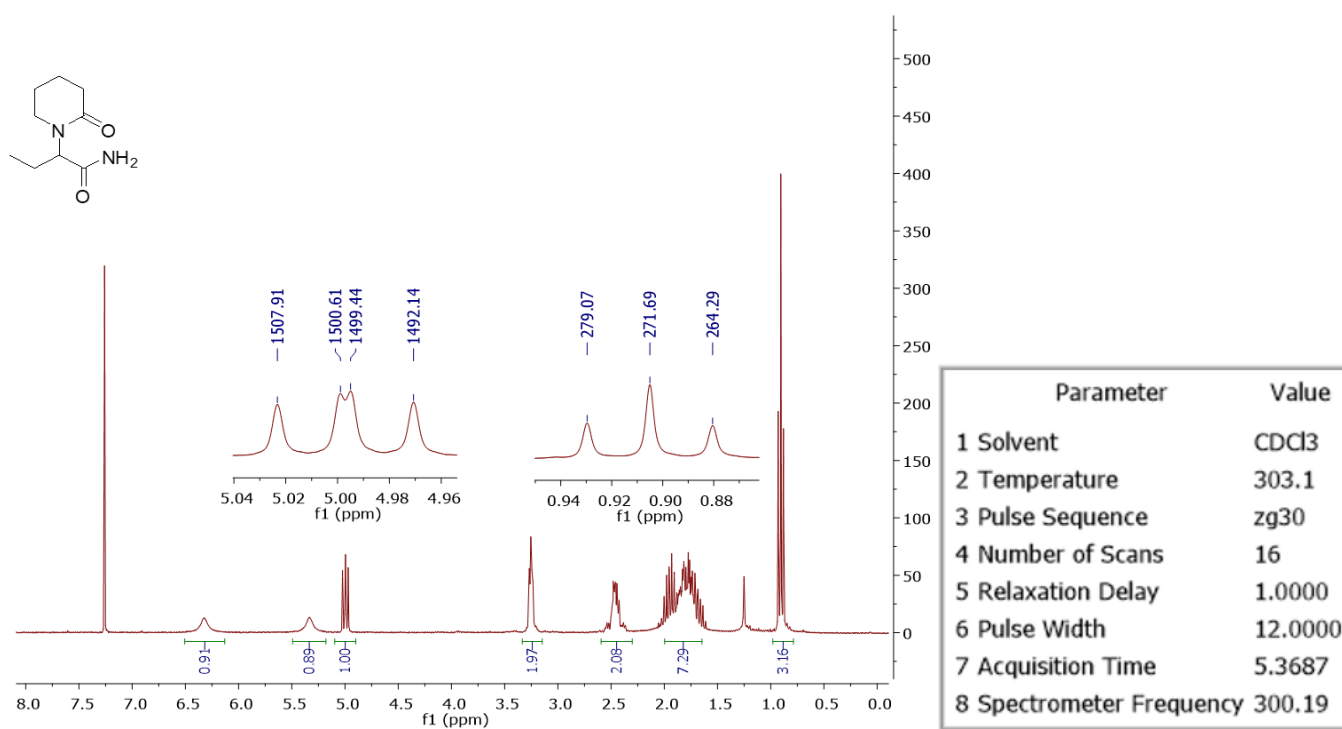
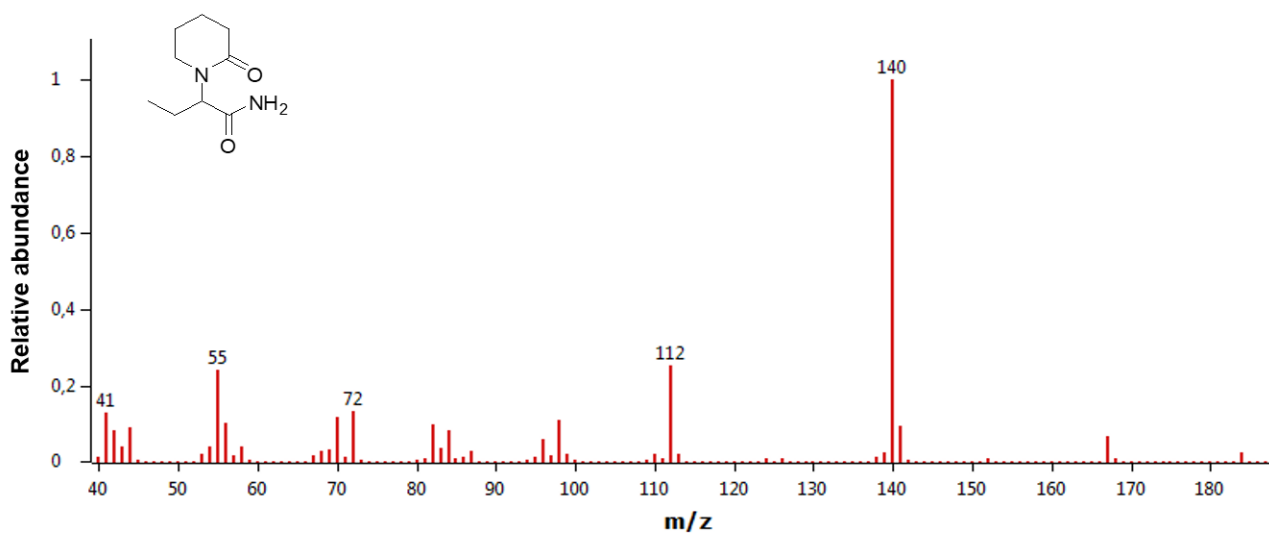


Figure S41. IR spectrum of compound **5b**.



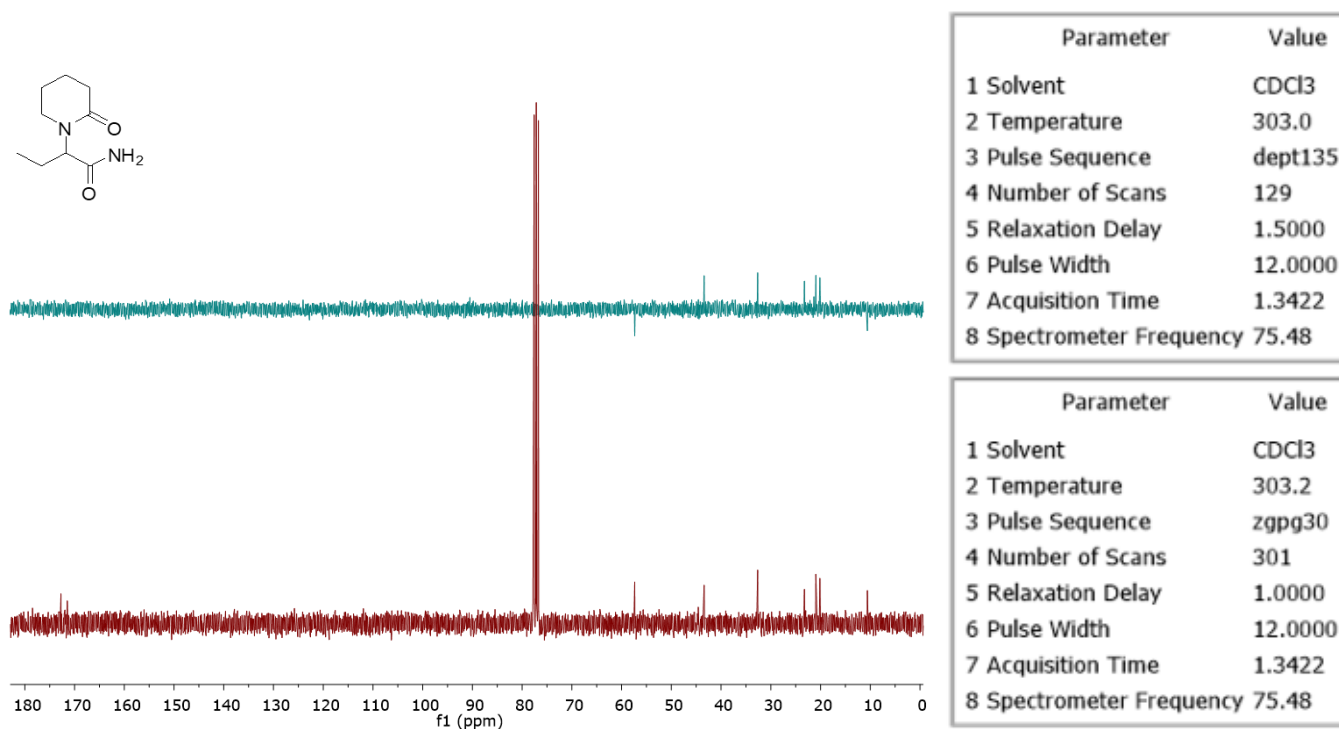


Figure S44. ^{13}C NMR (75.48 MHz, CDCl_3) spectrum and DEPT-135 experiment of compound 5b.

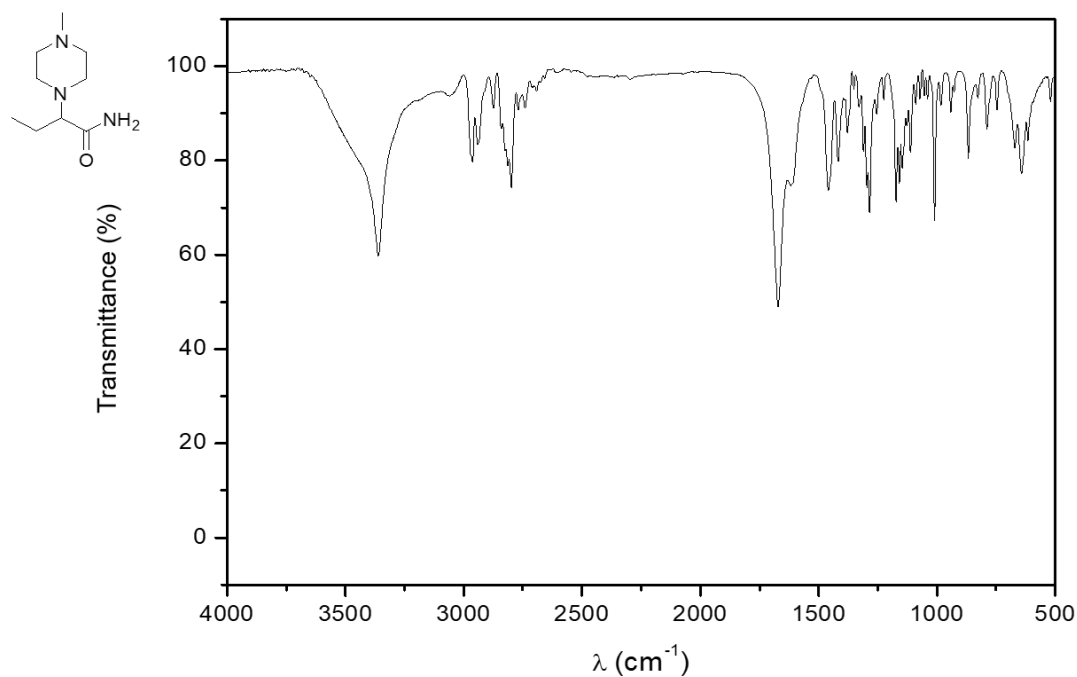
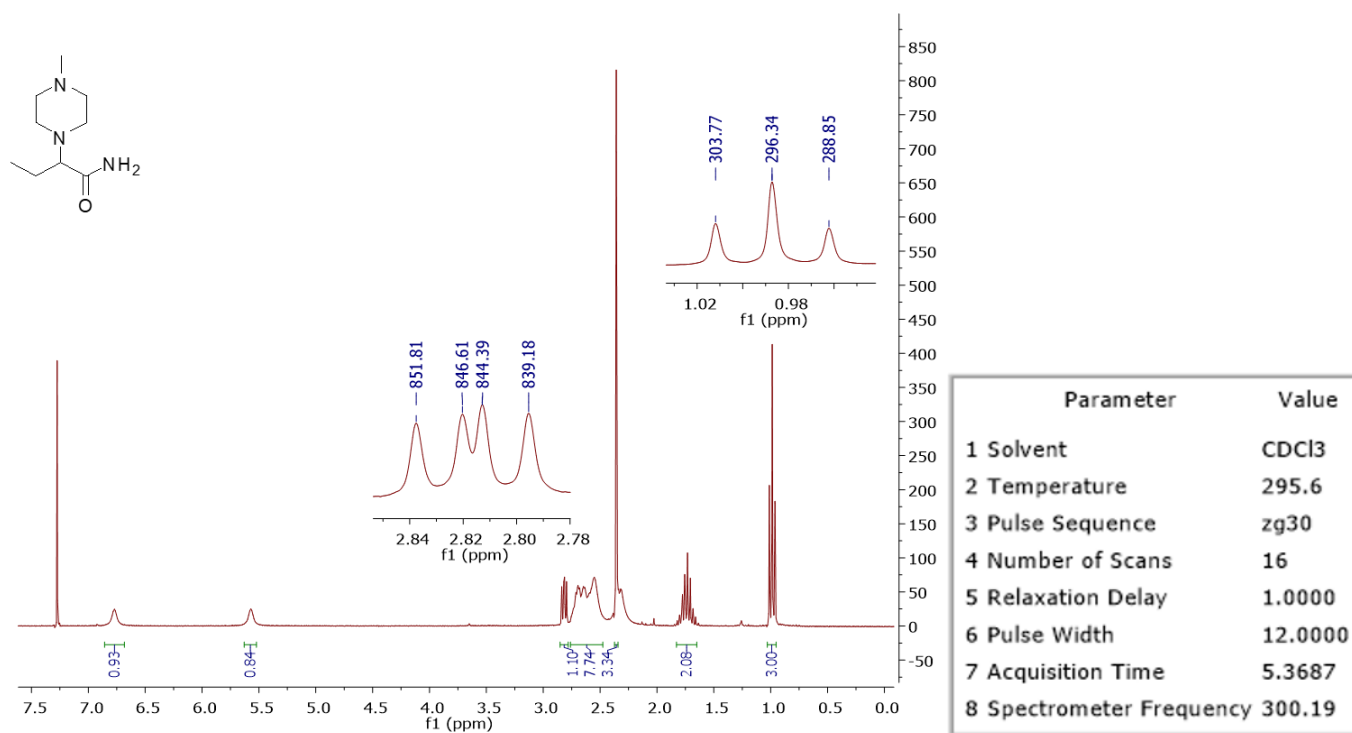
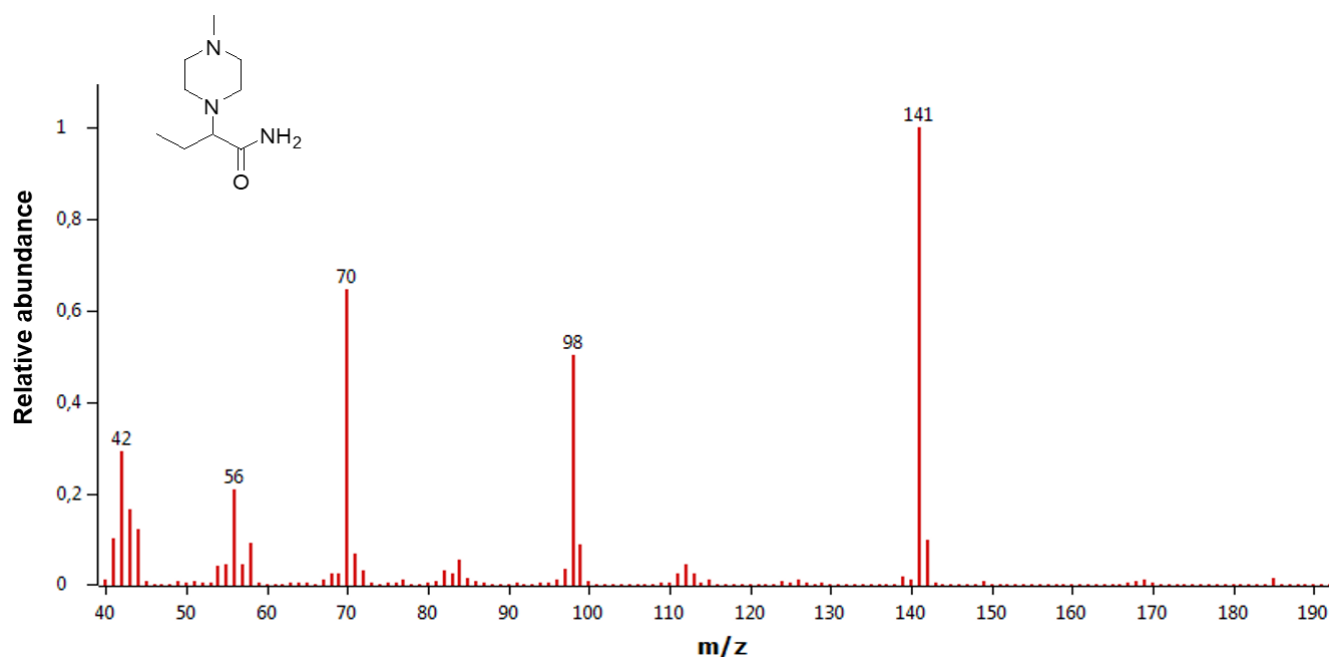


Figure S45. IR spectrum of compound 5d.



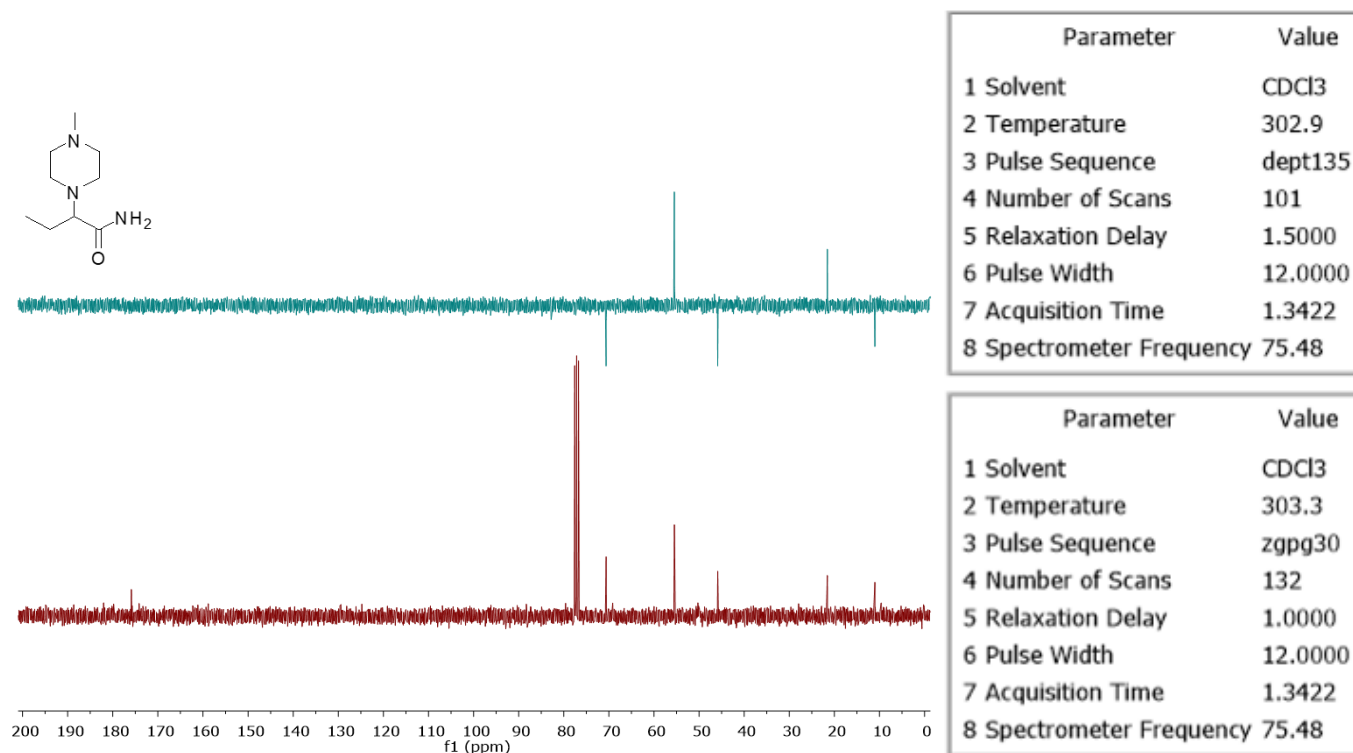


Figure S48. ¹³C NMR (75.48 MHz, CDCl₃) spectrum and DEPT-135 experiment of compound **5d**.

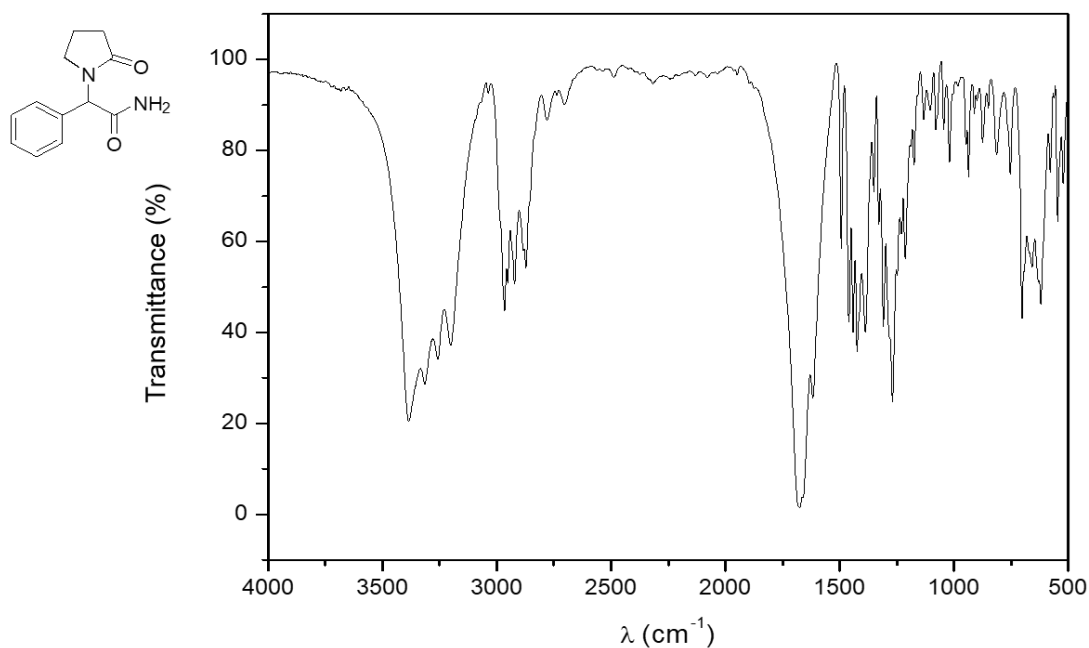


Figure S49. IR spectrum of compound **9a**.

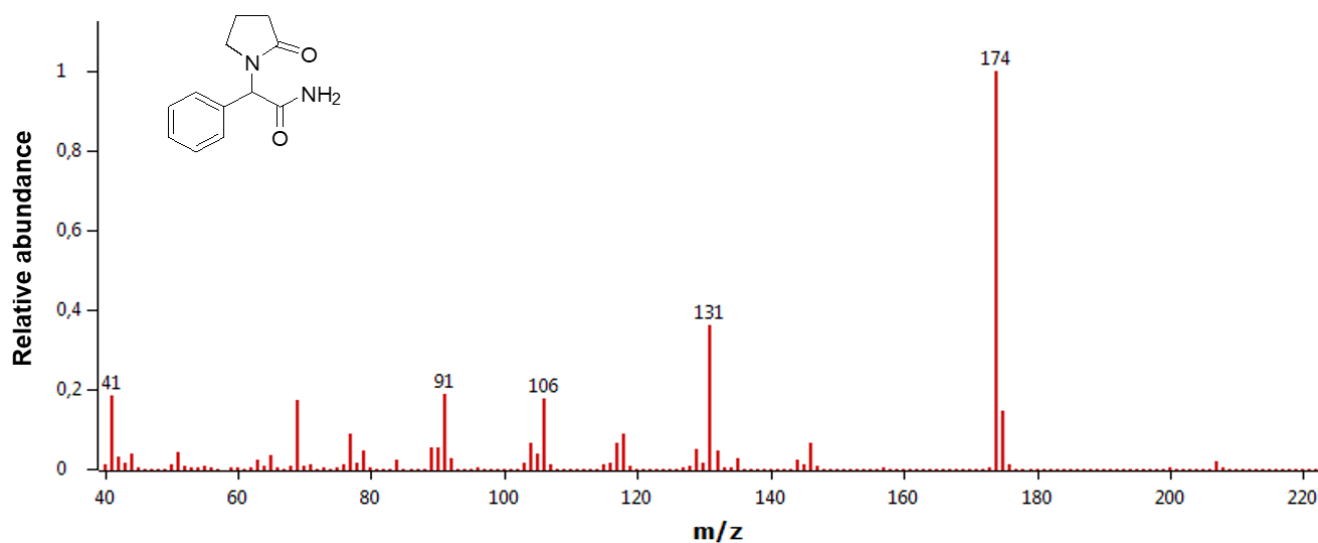


Figure S50. MS (EI, 70 eV) spectrum of compound 9a.

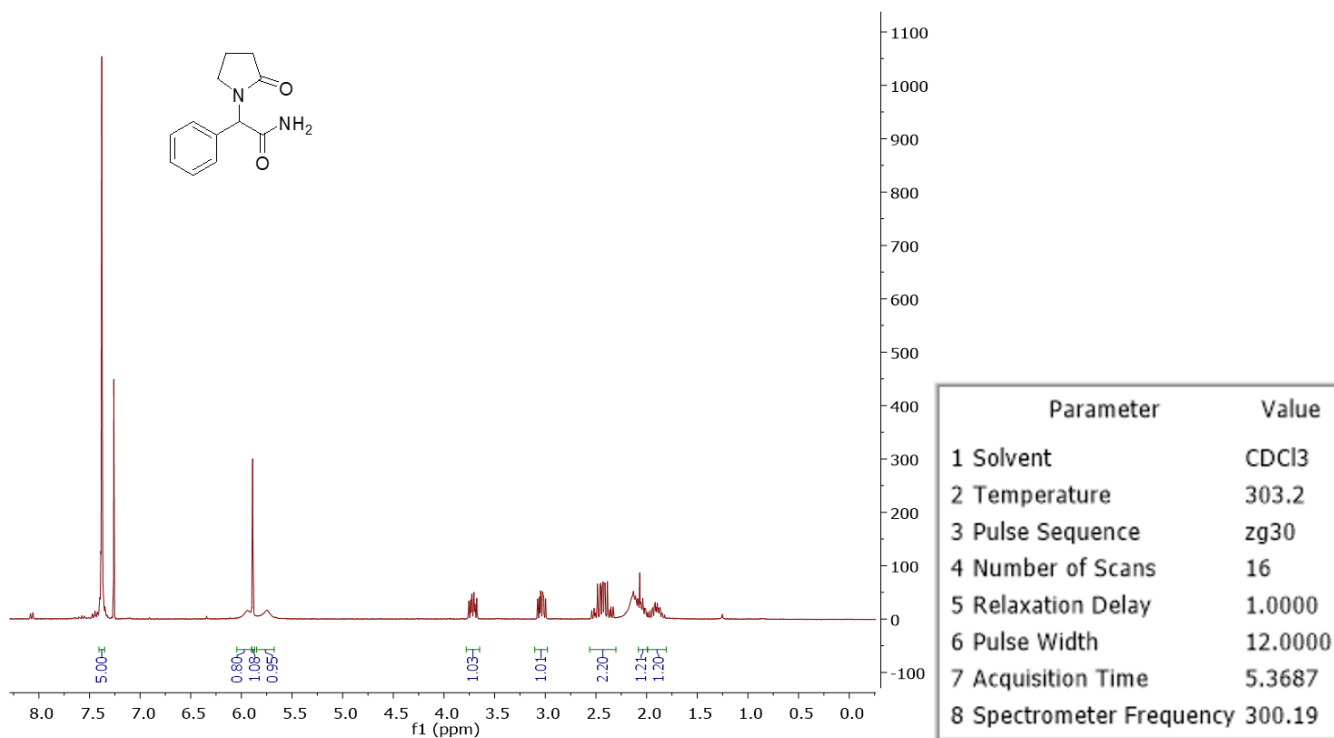


Figure S51. ¹H NMR (300.19 MHz, CDCl₃) spectrum of compound 9a.

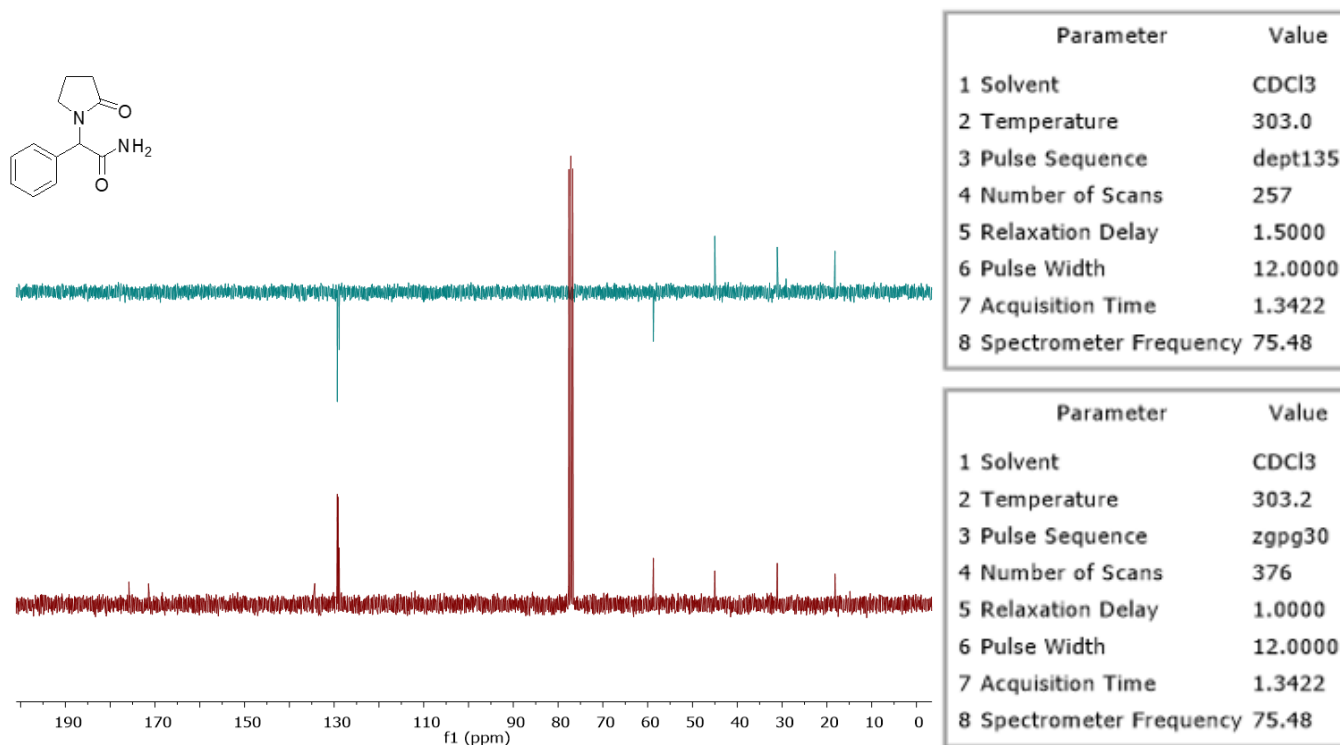


Figure S52. ¹³C NMR (75.48 MHz, CDCl₃) spectrum and DEPT-135 experiment of compound **9a**.

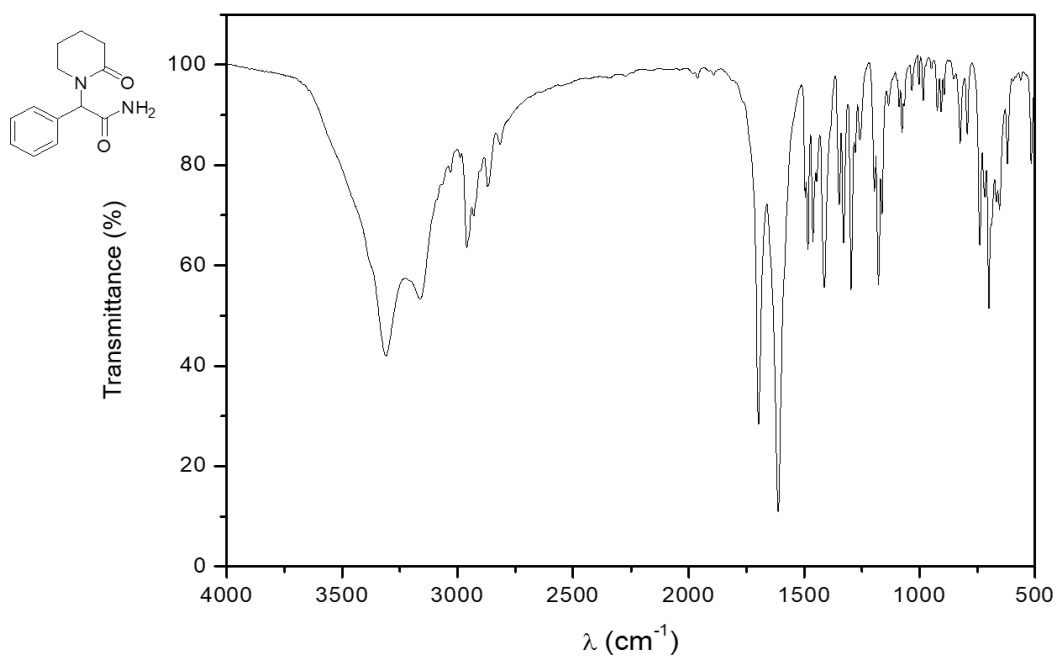


Figure S53. IR spectrum of compound **9b**.

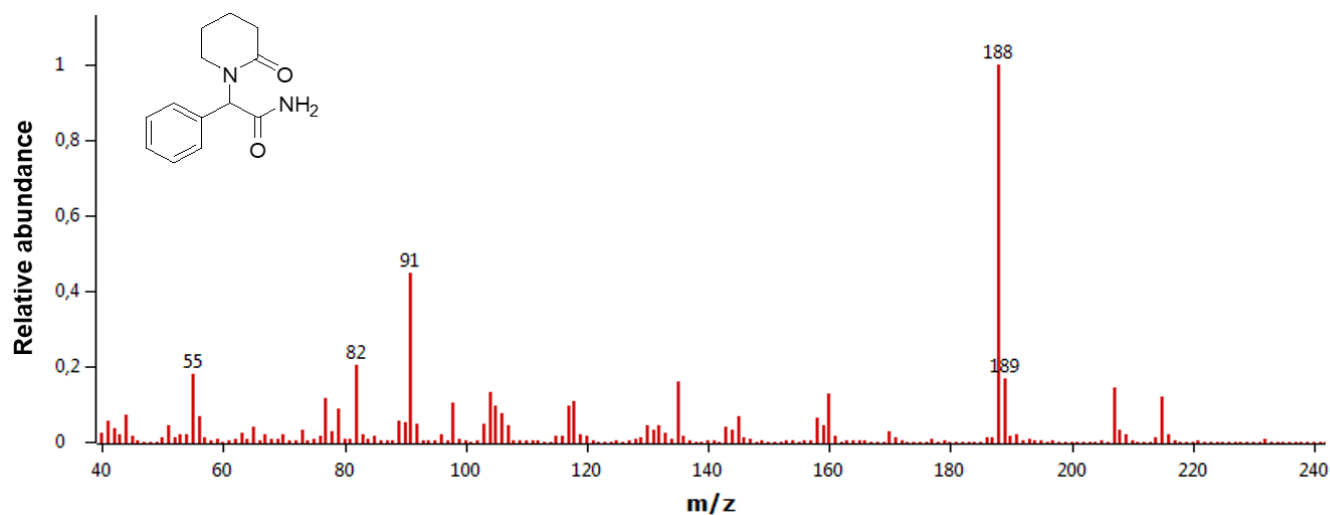


Figure S54. MS (EI, 70 eV) spectrum of compound **9b**.

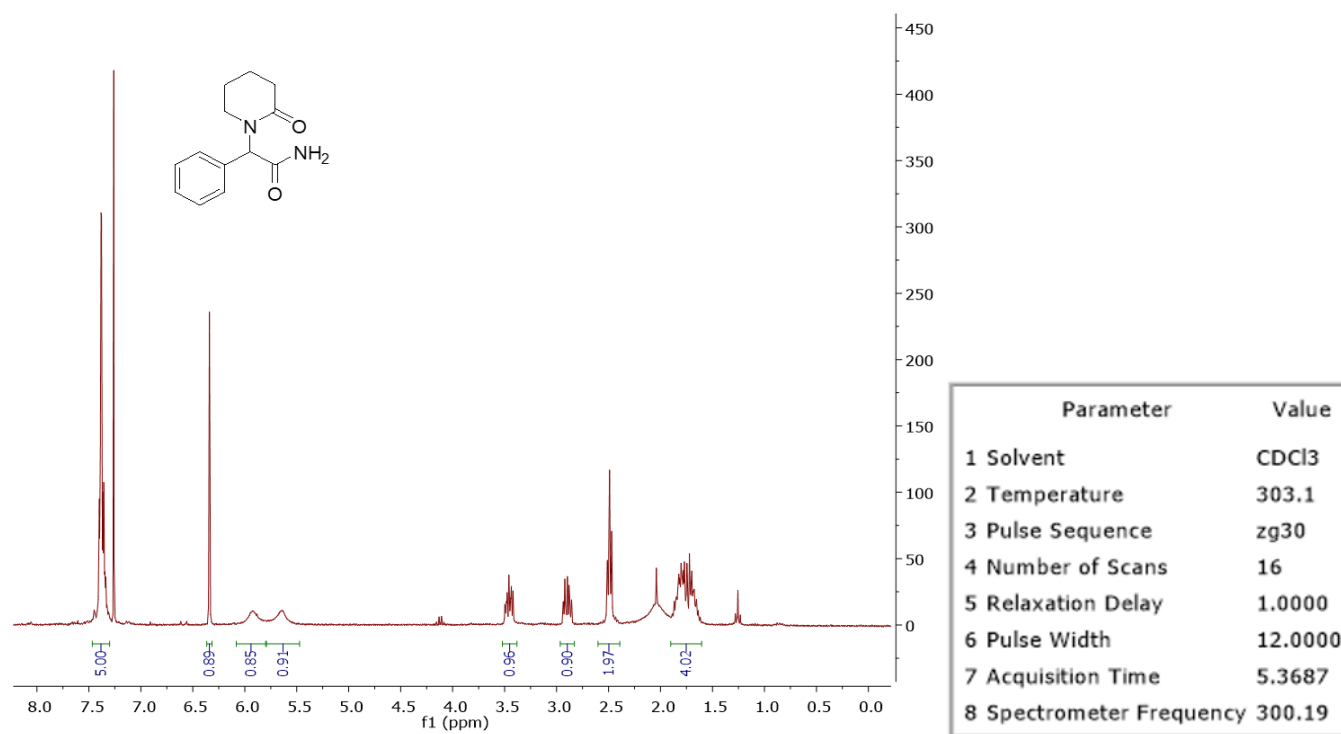


Figure S55. ^1H NMR (300.19 MHz, CDCl_3) spectrum of compound **9b**.

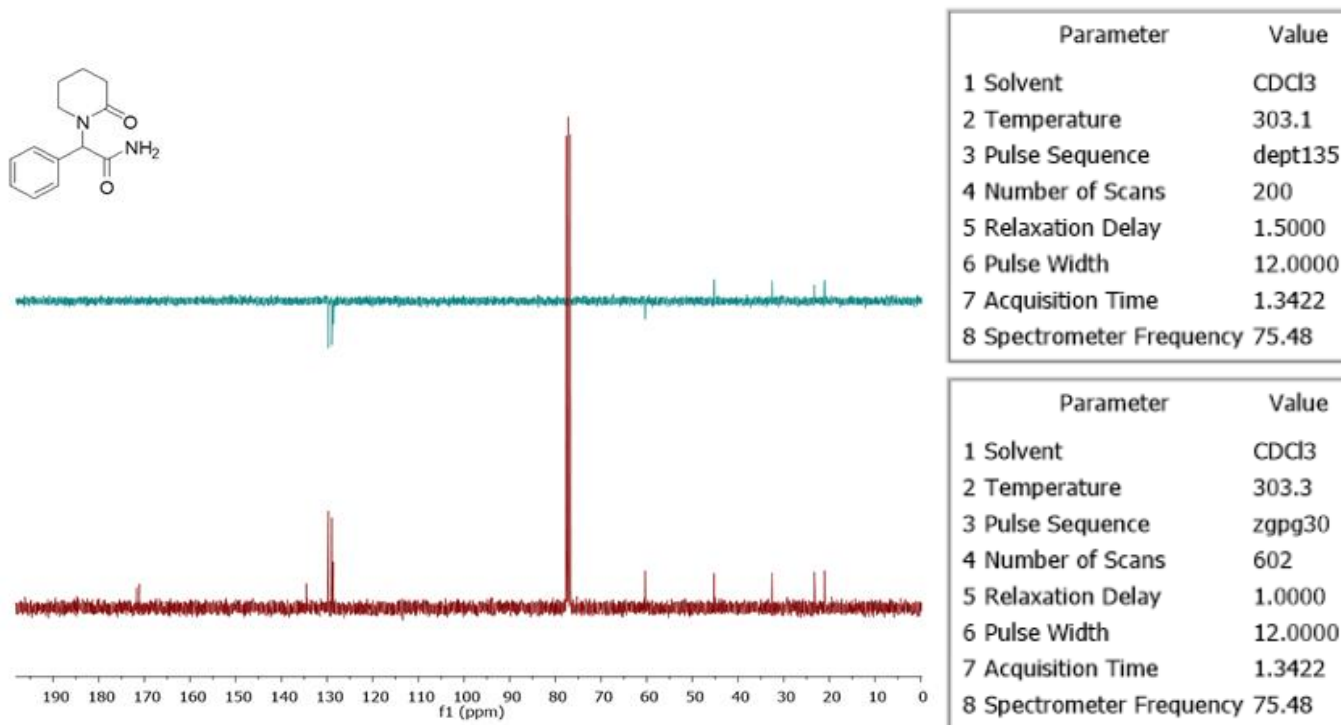


Figure S56. ¹³C NMR (75.48 MHz, CDCl₃) spectrum and DEPT-135 experiment of compound **9b**.

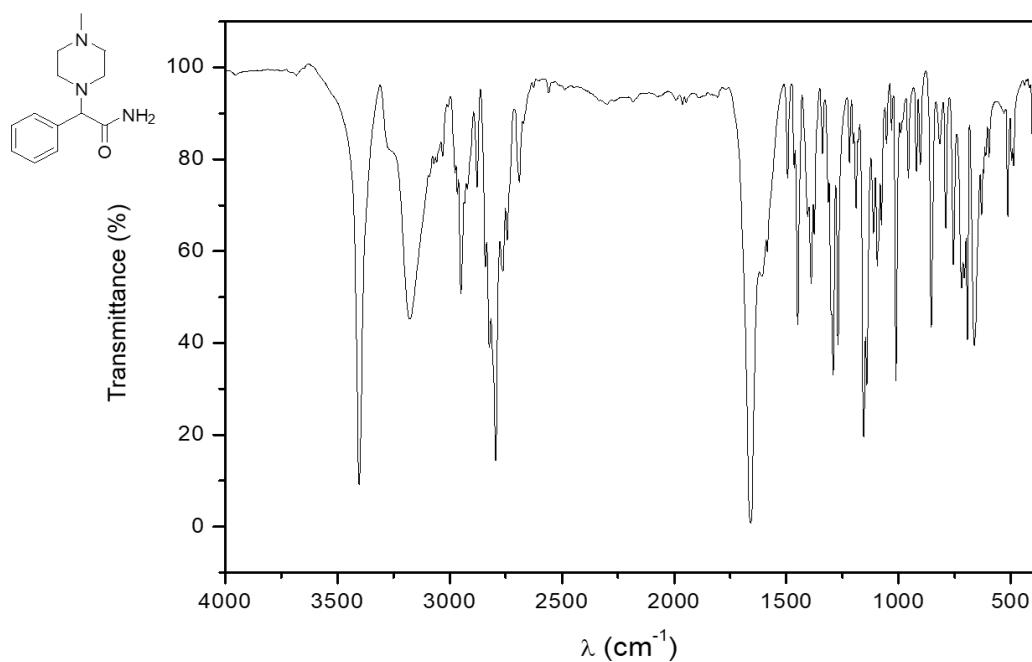


Figure S57. IR spectrum of compound **9d**.

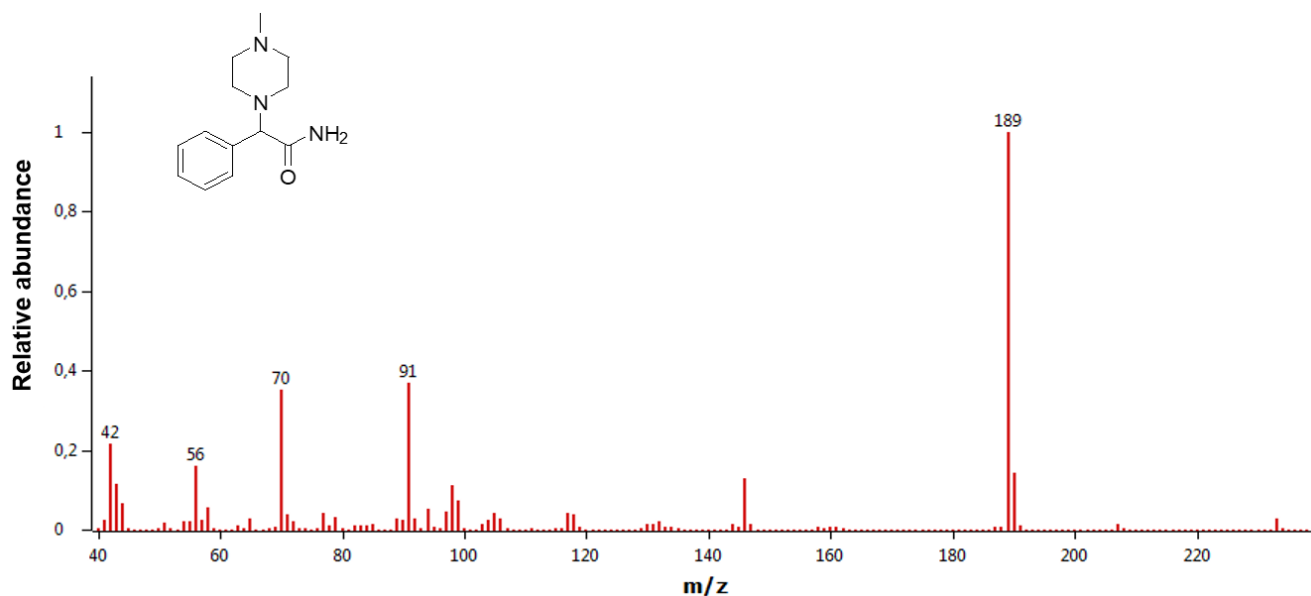


Figure S58. MS (EI, 70 eV) spectrum of compound 9d.

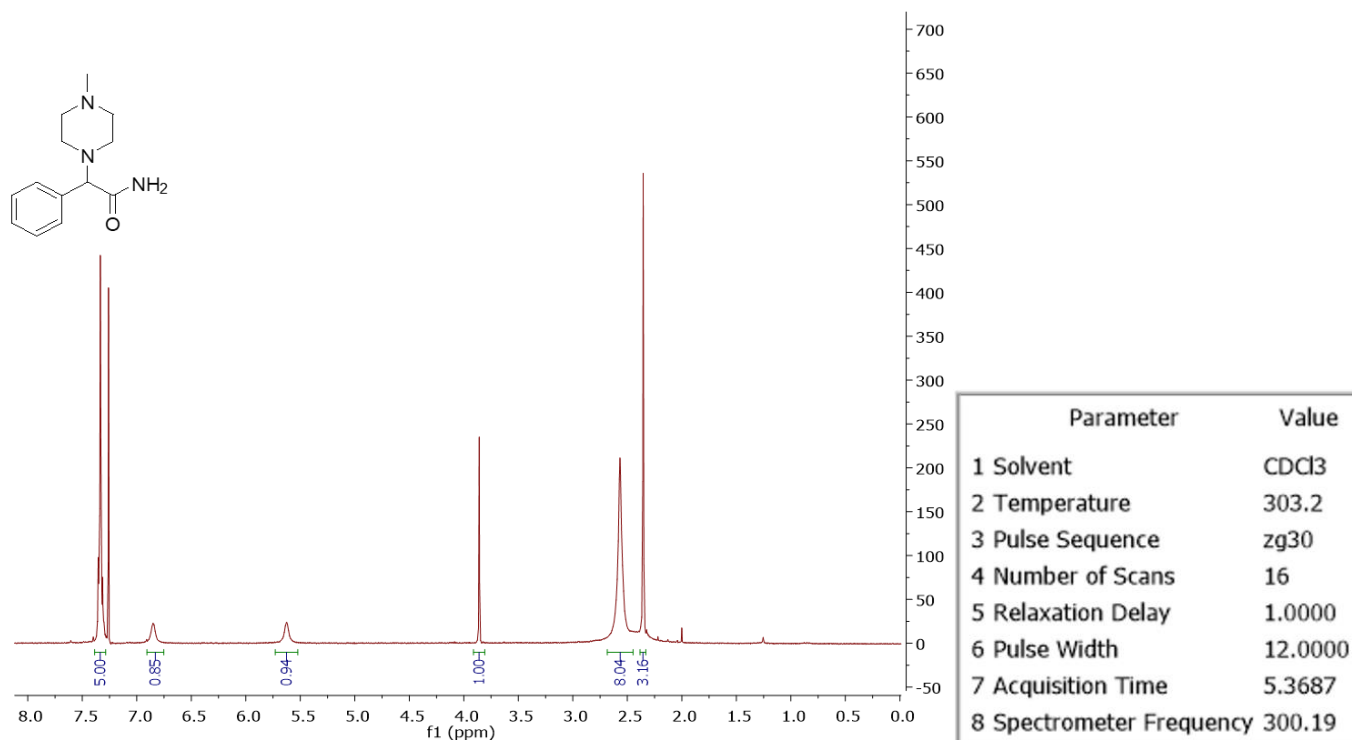
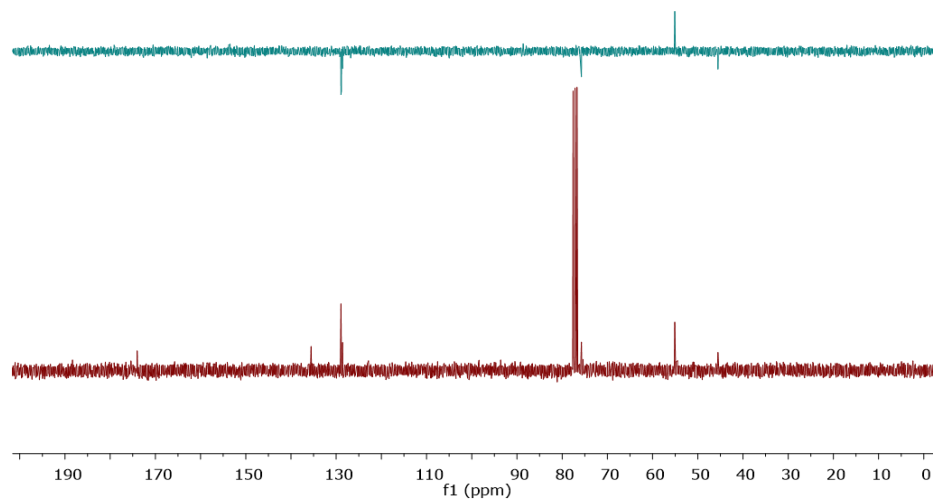
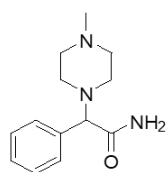


Figure S59. ¹H NMR (300.19 MHz, CDCl₃) spectrum of compound 9d.



Parameter	Value
1 Solvent	CDCl3
2 Temperature	303.0
3 Pulse Sequence	dept135
4 Number of Scans	103
5 Relaxation Delay	1.5000
6 Pulse Width	12.0000
7 Acquisition Time	1.3422
8 Spectrometer Frequency	75.48

Parameter	Value
1 Solvent	CDCl3
2 Temperature	303.2
3 Pulse Sequence	zgpg30
4 Number of Scans	239
5 Relaxation Delay	1.0000
6 Pulse Width	12.0000
7 Acquisition Time	1.3422
8 Spectrometer Frequency	75.48

Figure S60. ^{13}C NMR (75.48 MHz, CDCl_3) spectrum and DEPT-135 experiment of compound **9d**.

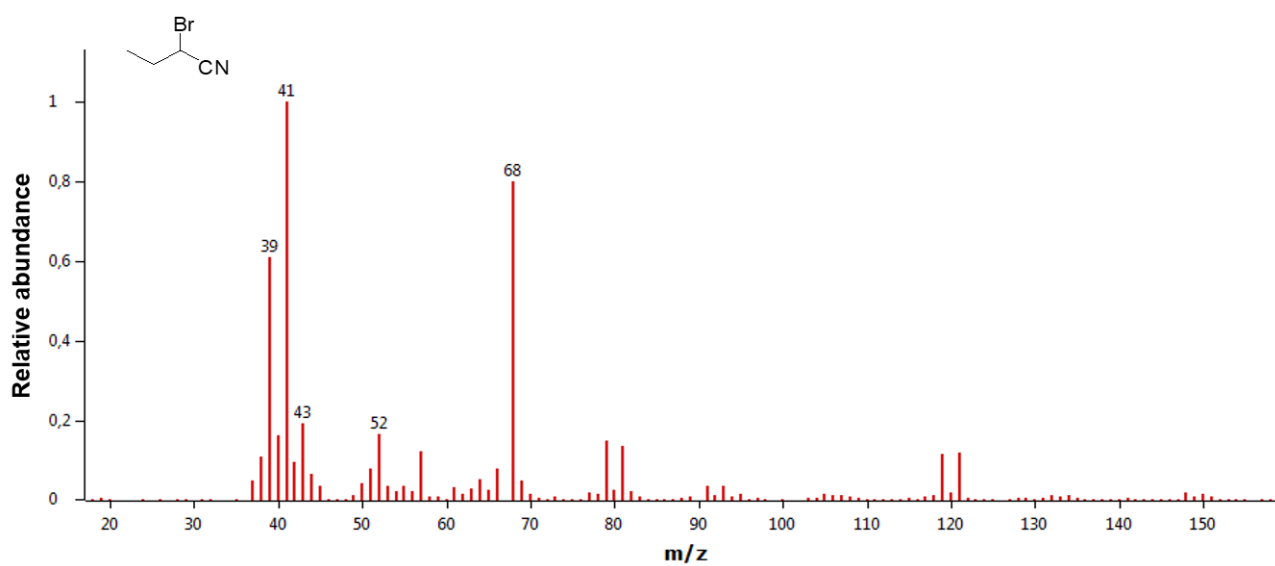


Figure S61. MS (EI, 70 eV) spectrum of compound **3**.

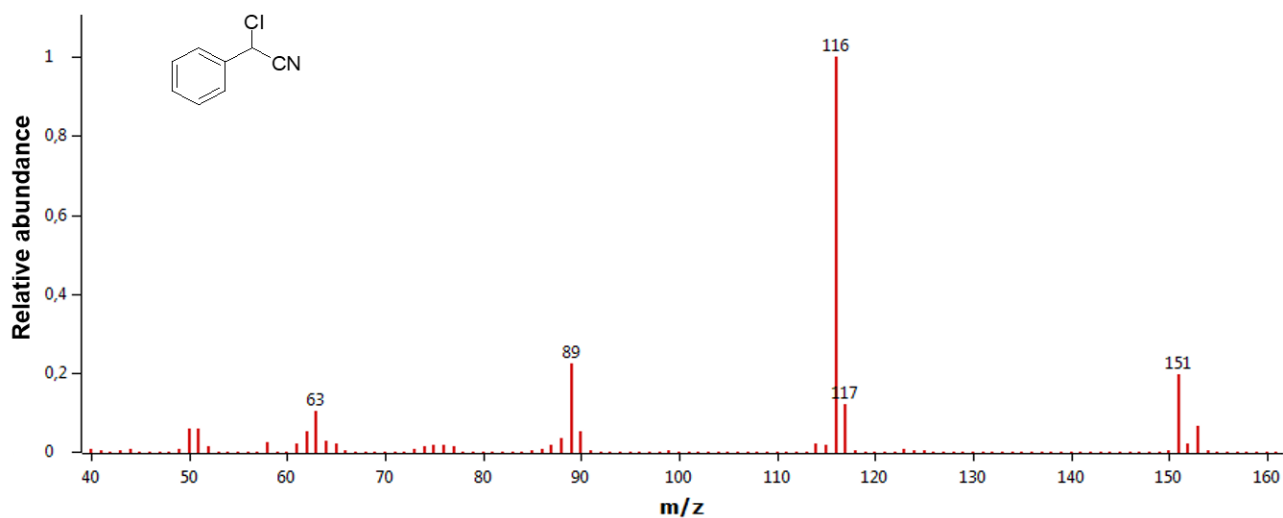


Figure S62. MS (EI, 70 eV) spectrum of compound 7.

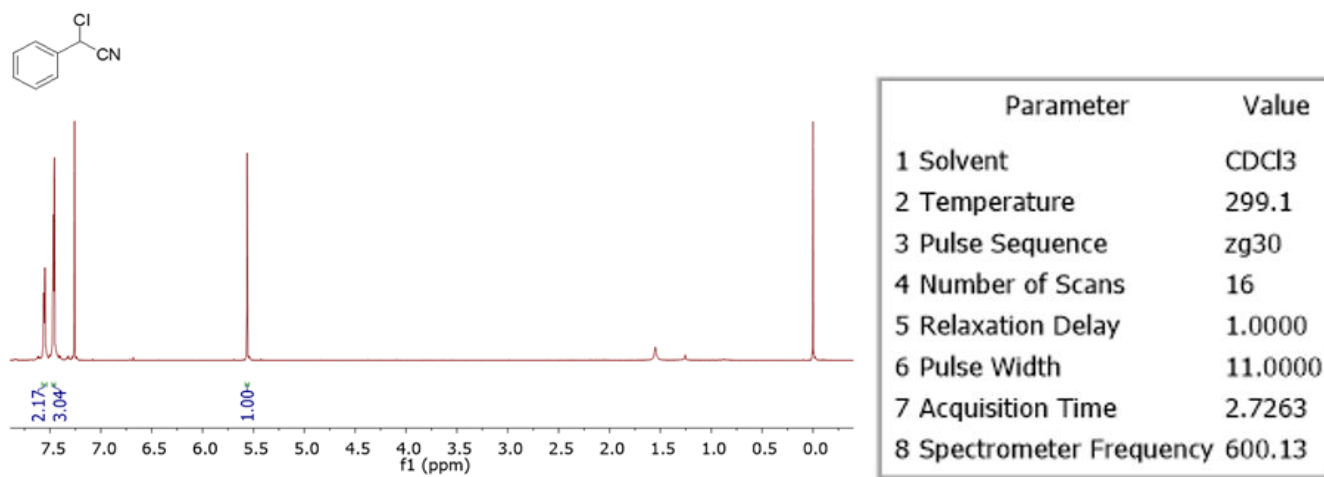


Figure S63. ¹H NMR (300.19 MHz, CDCl₃) spectrum of compound 7.

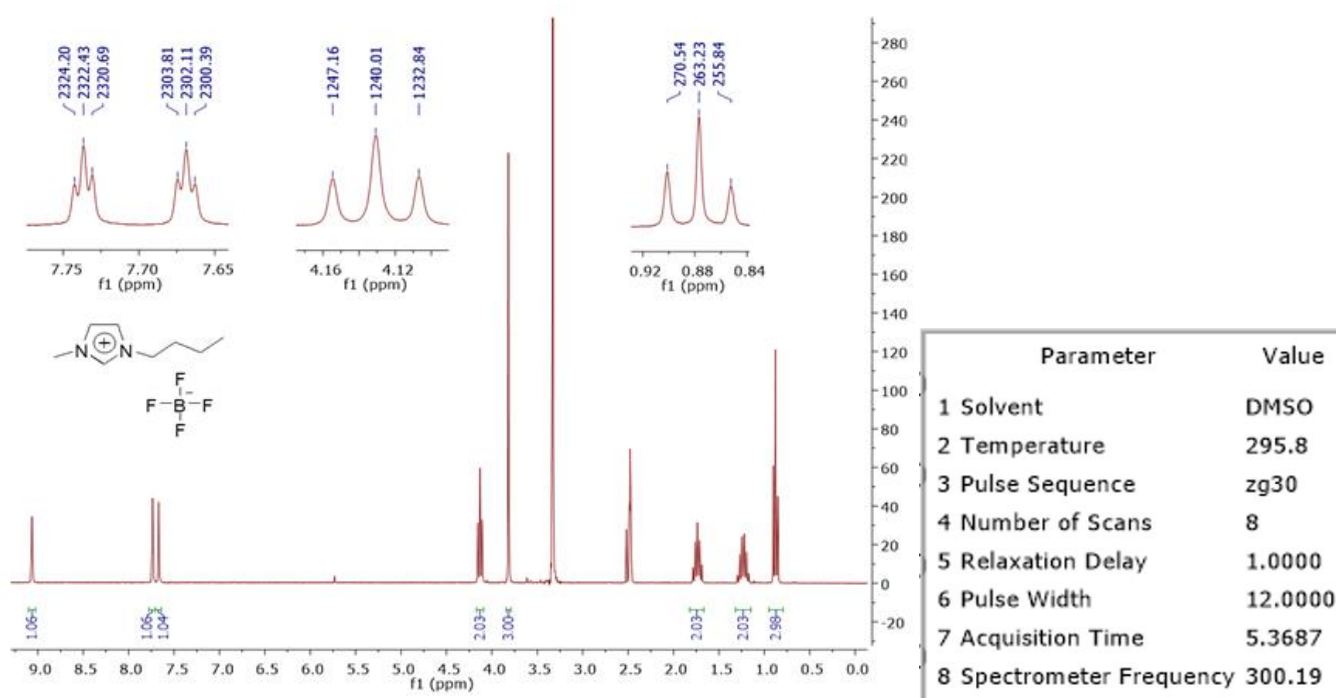


Figure S64. ^1H NMR (300.19 MHz, $\text{DMSO-}d_6$) spectrum of compound **BMIM.BF₄**.

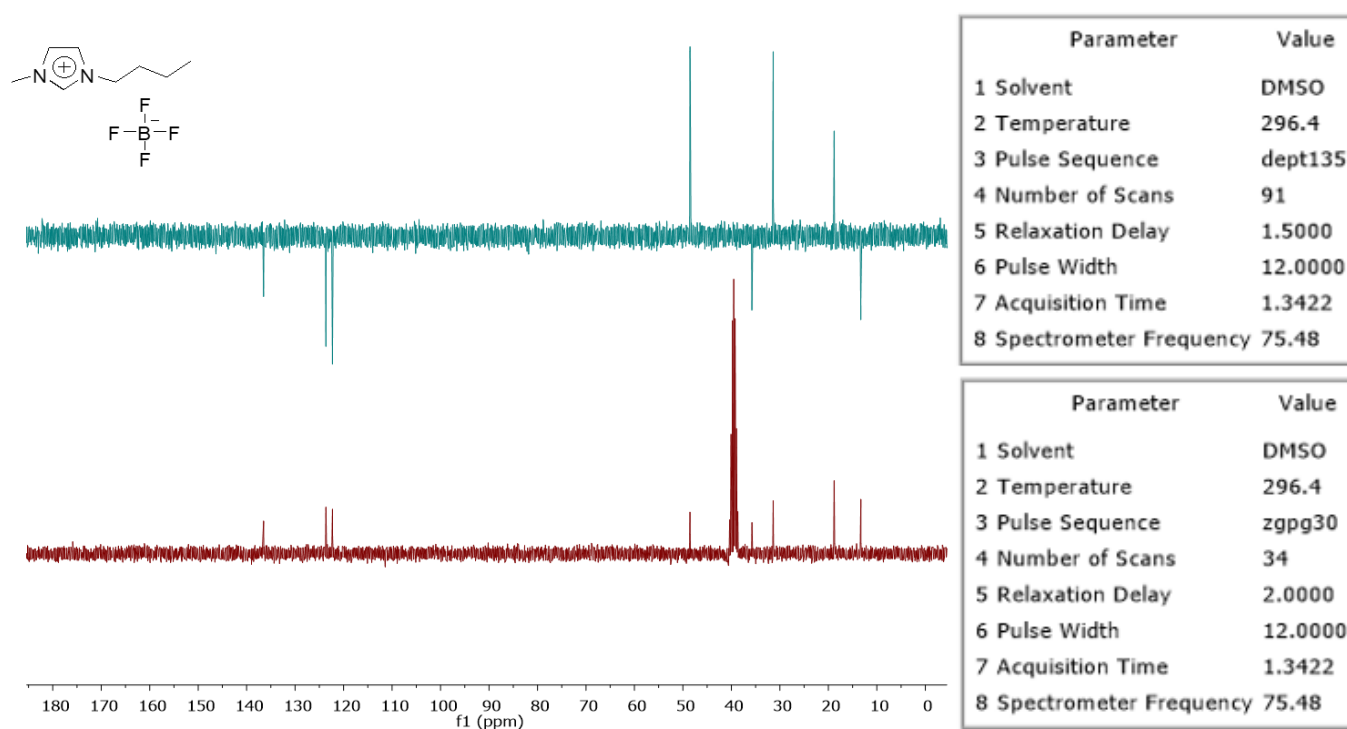


Figure S65. ^{13}C NMR (75.48 MHz, $\text{DMSO-}d_6$) spectrum and DEPT-135 experiment of compound **BMIM.BF₄**.

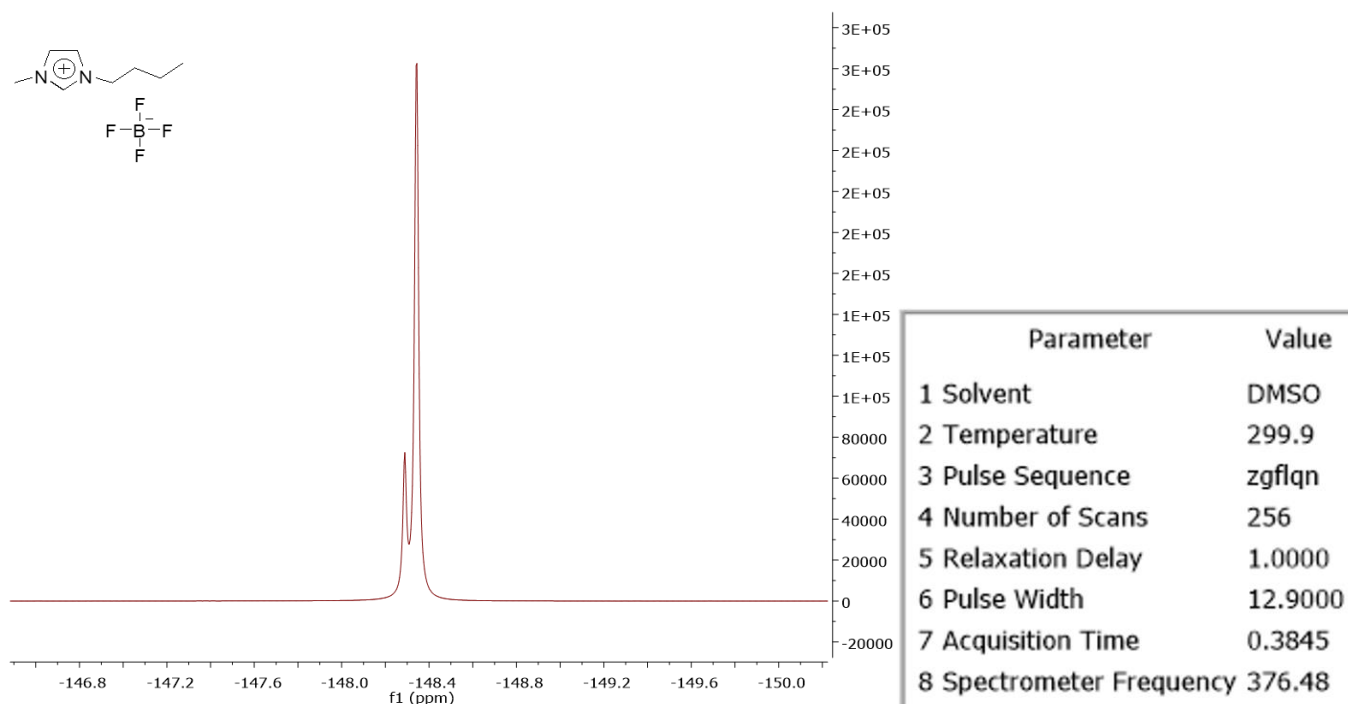


Figure S66. ^{19}F NMR (376.48 MHz, $\text{DMSO-}d_6$) spectrum of compound **BMIM.BF₄**.

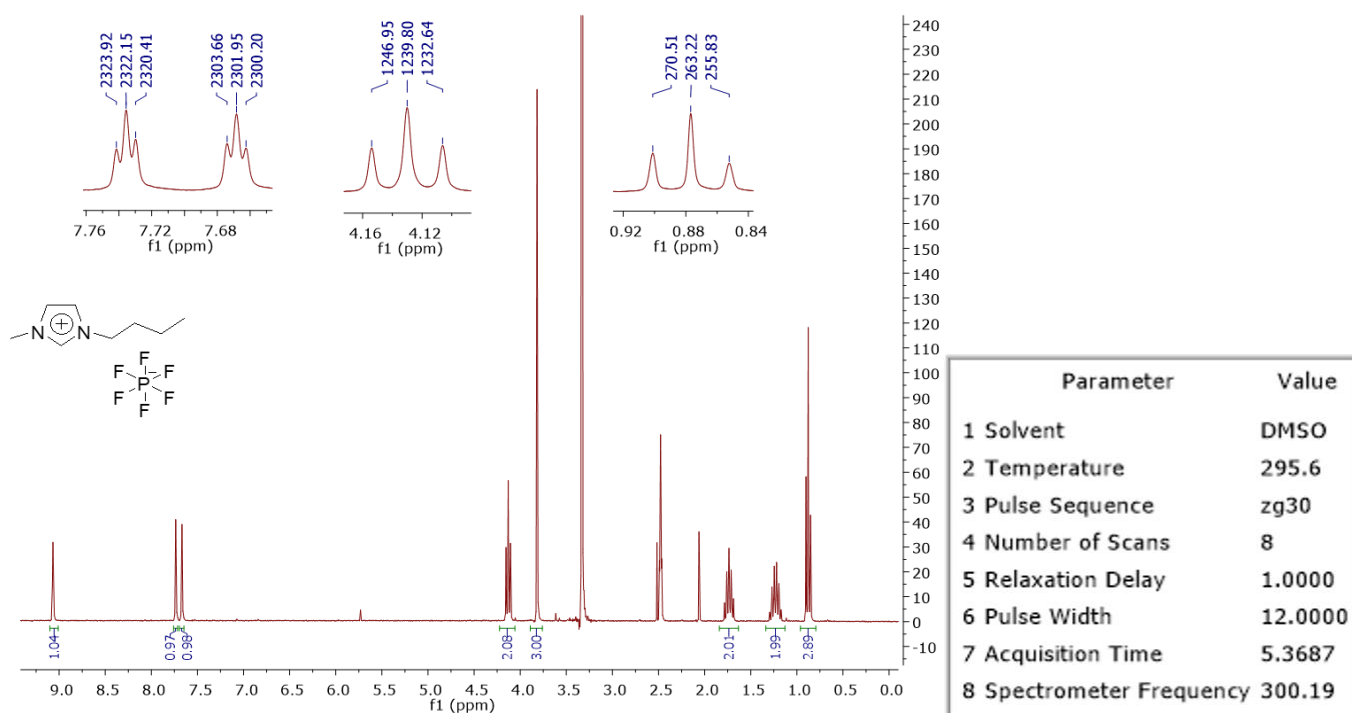


Figure S67. ^1H NMR (300.19 MHz, $\text{DMSO-}d_6$) spectrum of compound **BMIM.PF₆**.

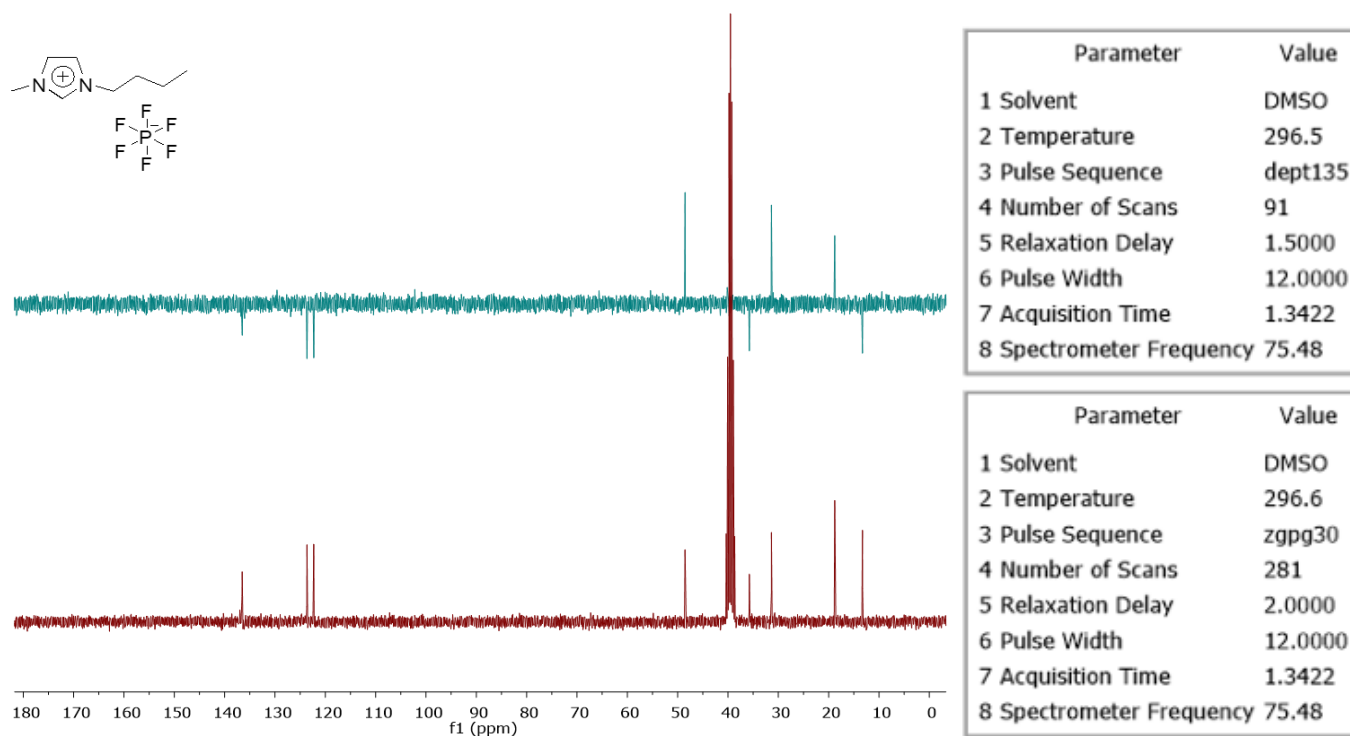


Figure S68. ^{13}C NMR (75.48 MHz, $\text{DMSO-}d_6$) spectrum and DEPT-135 experiment of compound **BMIM.PF₆**.

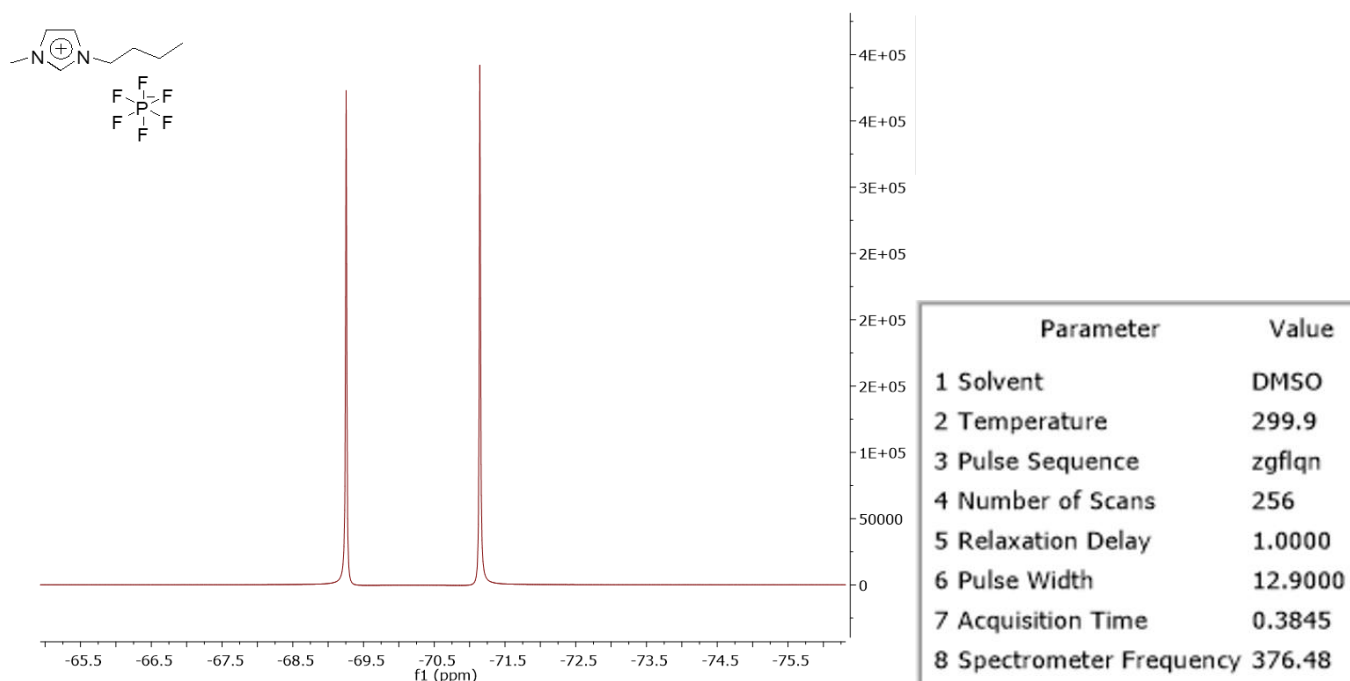


Figure S69. ^{19}F NMR (376.48 MHz, $\text{DMSO-}d_6$) spectrum of compound **BMIM.PF₆**.

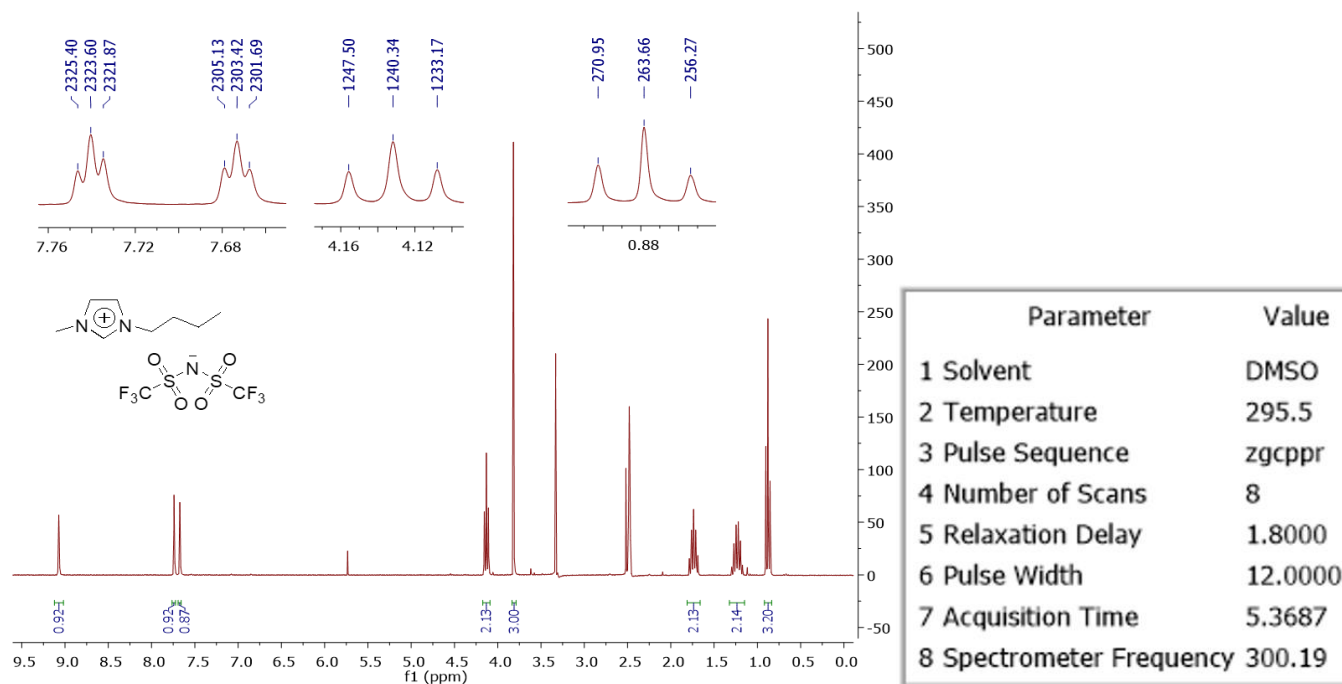


Figure S70. ^1H NMR (300.19 MHz, $\text{DMSO-}d_6$) spectrum of compound **BMIM.NTf₂**.

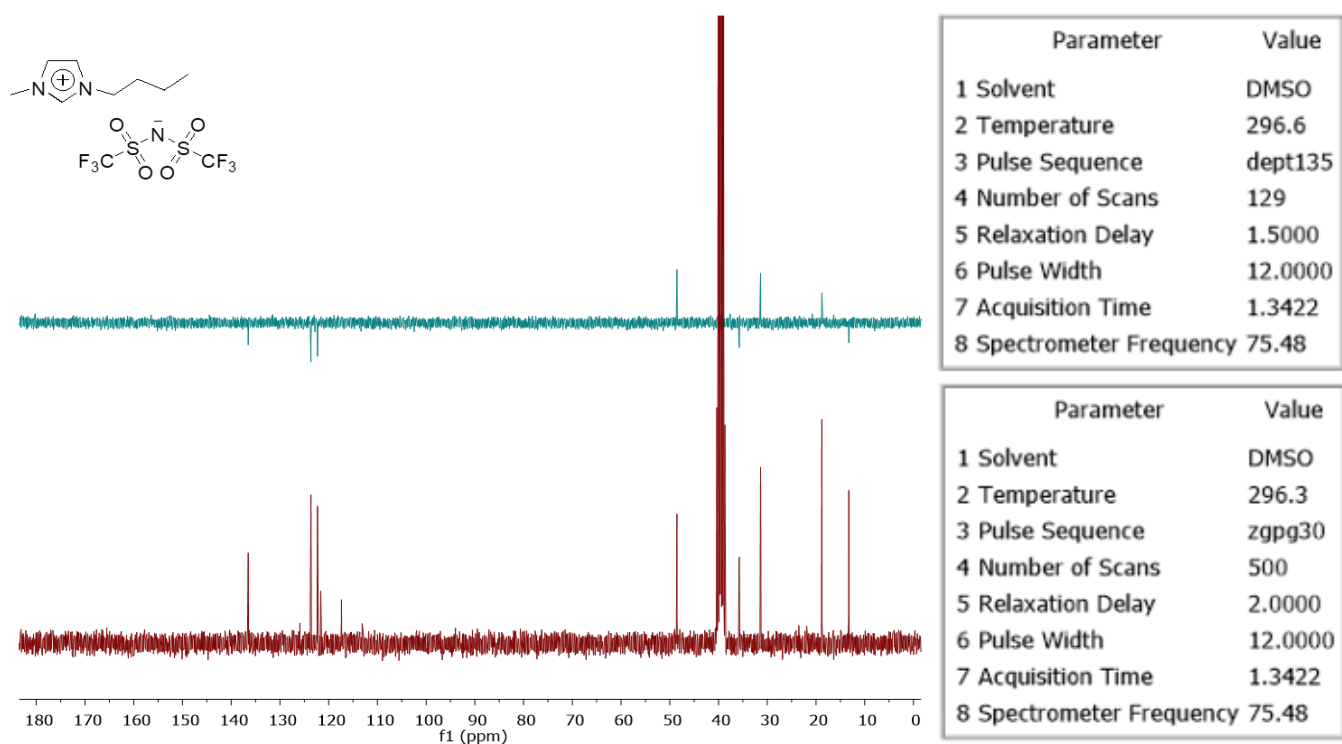


Figure S71. ^{13}C NMR (75.48 MHz, $\text{DMSO-}d_6$) spectrum and DEPT-135 experiment of compound **BMIM.NTf₂**.

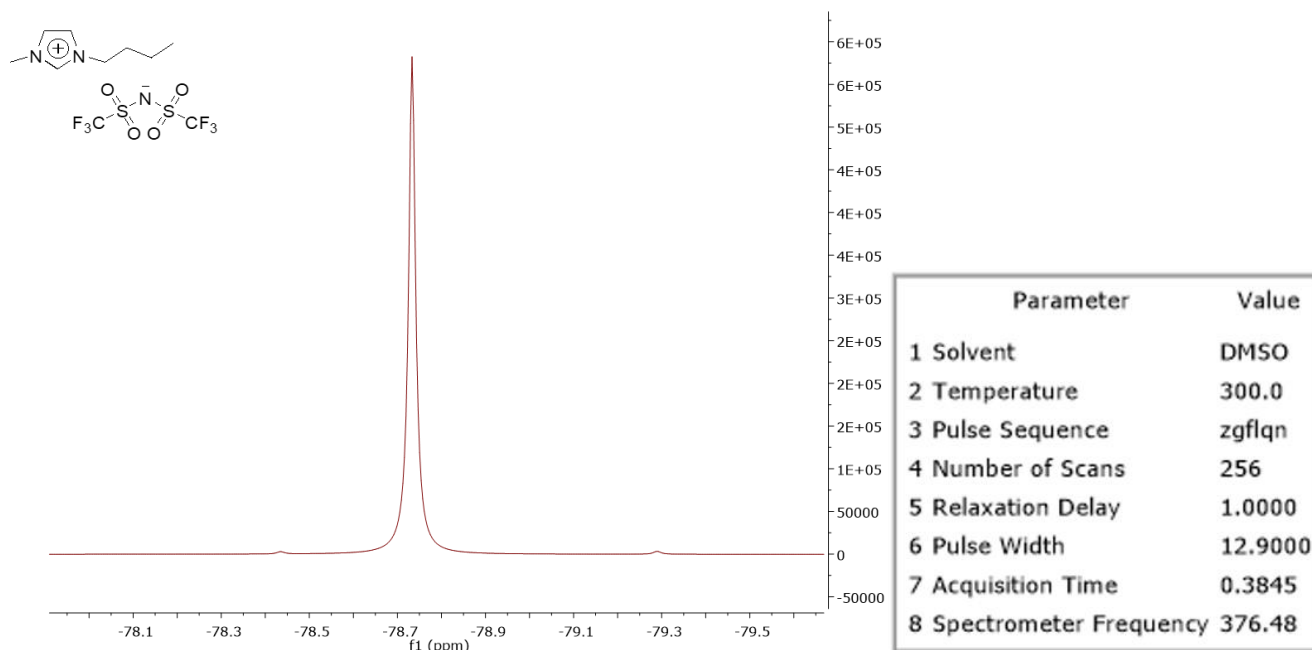


Figure S72. ^{19}F NMR (376.48 MHz, $\text{DMSO-}d_6$) spectrum of compound **BMIM.NTf₂**.

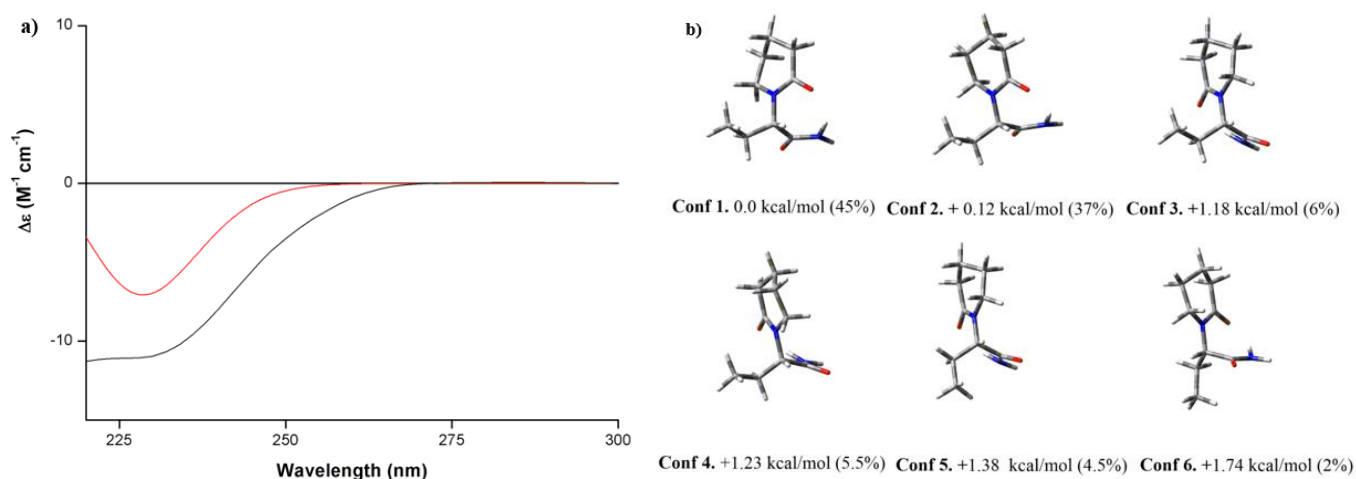


Figure S73. (a) Experimental (black) and calculated (CAM-B3LYP/TZVP, red) ECD spectra of (*S*)-**5b**. (b) Optimized structures, relative energies and Boltzmann populations of the lowest-energy conformers identified for (*S*)-**5b** at the B3LYP/6-31G(d) level.

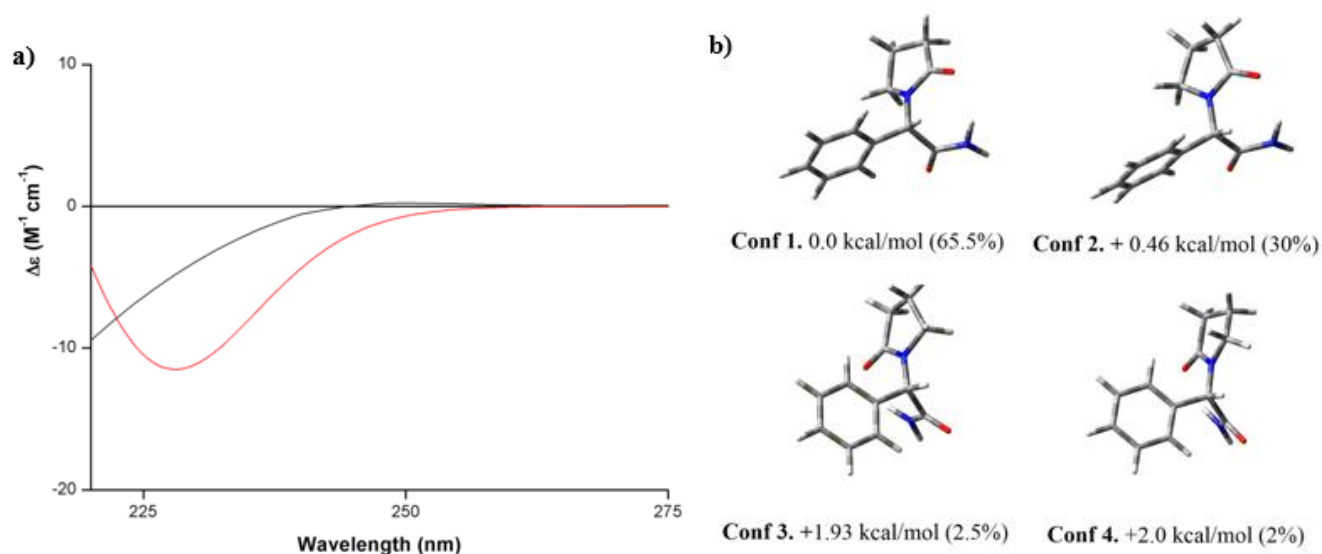


Figure S74. (a) Experimental (black) and calculated (CAM-B3LYP/TZVP, red) ECD spectra of (*S*)-9a. (b) Optimized structures, relative energies and Boltzmann populations of the lowest-energy conformers identified for (*S*)-9a at the B3LYP/6-31G(d) level.

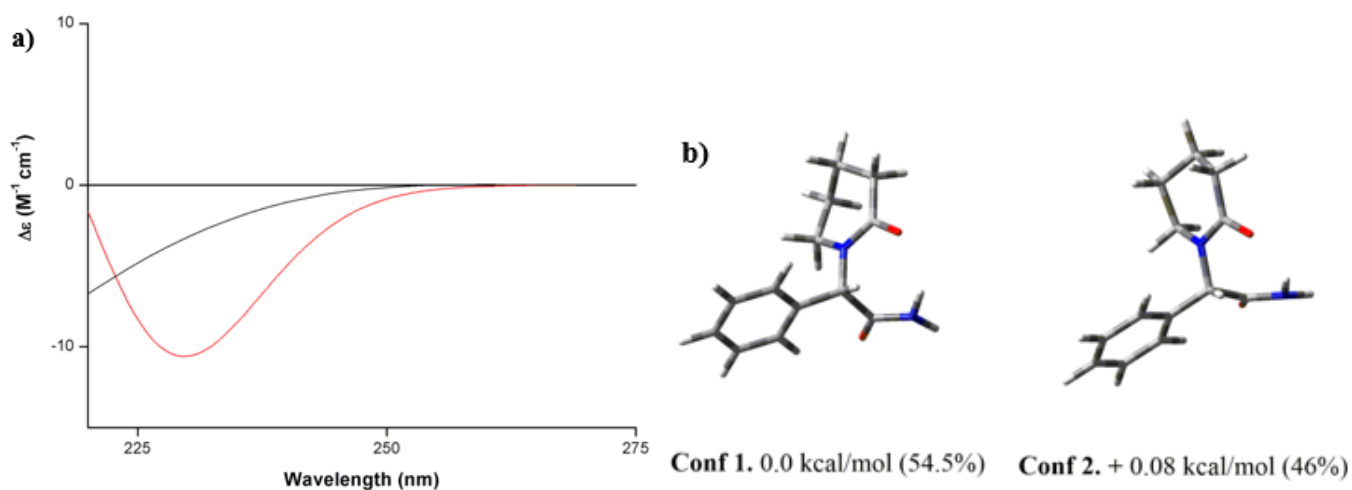






Figure S75. (a) Experimental (black) and calculated (CAM-B3LYP/TZVP, red) ECD spectra of (*S*)-9b. (b) Optimized structures, relative energies and Boltzmann populations of the lowest-energy conformers identified for (*S*)-9b at the B3LYP/6-31G(d) level.

Separation of lactic acid and by-products obtained by catalytic conversion of glycerol using high-performance liquid chromatography

Andreza de Faria Alves Cruz¹⁺, Gabriella Pinho Dias¹, Flávia de Rezende Bittencourt¹, Donato Alexandre Gomes Aranda¹

1. Federal University of Rio de Janeiro, Chemical and Biochemical Process Engineering Program/School of Chemistry, Rio de Janeiro, Brazil.

+Corresponding author: Andreza de Faria Alves Cruz, **Phone:** +31 995581602, **Email address:** andrezafalvesc@gmail.com

ARTICLE INFO

Article history:

Received: August 14, 2021

Accepted: December 09, 2021

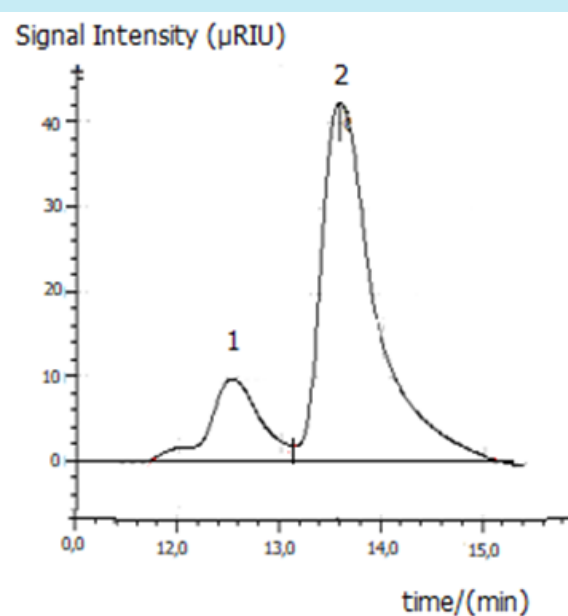
Published: April 01, 2022

Keywords:

1. analytical
2. HPLC
3. lactic acid

Section Editor: Assis Vicente Benedetti

ABSTRACT: Lactic acid is an attractive raw material in synthesizing many products. A new method for quantifying glycerol, lactic acid, and the by-products (pyruvaldehyde) obtained in this reaction was developed using high-performance liquid chromatography (HPLC) with a refractive index detector (HPLC-RI) in a column (300 × 7.7 mm, 8 μm) using H₂SO₄ 0.001 M + 10% ACN (organic modifier) as mobile phase (0.6 mL min⁻¹). This method indicated outstanding linearity for glycerol and lactic acid concentration from 0.6 to 6.6 g L⁻¹ (coefficient of determination (R²) = 0.9912 and 0.9961, respectively) and accuracy between 98.33 and 100.00%. From this, it was possible to conclude that the method is applicable and concise for separating the primordial products in this reaction.



1. Introduction

Biodiesel has significant potential as an alternative diesel due to its biodegradability, renewable energy source, better lubricity, combustion efficiency, and low toxicity compared to other fuels (Tan *et al.*, 2015). Glycerol is produced as a by-product, representing around 10% of the total volume of biodiesel produced (Bilck *et al.*, 2015; Chi *et al.*, 2007).

Studies show that the conversion of glycerol to other chemicals with high added value, such as lactic acid, makes the glycerol industry more profitable (Arcanjo *et al.*, 2017; Manfro and Souza, 2014), making biodiesel production a more suitable option to replace fossil fuels (Huang *et al.*, 2012).

Glycerol can be dehydrogenated to form dihydroxyacetone (Santos *et al.*, 2018). This intermediate went through dehydration to pyruvaldehyde on solid acid catalysts and rearranged via Cannizzaro reaction to lactic acid. Therefore, from the literature, pyruvaldehyde is a crucial intermediate on glycerol valorization in lactic acid (Lari *et al.*, 2016; Santos *et al.*, 2018).

Lactic acid is a raw material to benefit from synthesizing several products, applying in the textile industry and cosmetic industry (Drumright *et al.*, 2000). In the food industry, its main applications are as a pH regulator and food additive (Bruno *et al.*, 2020; Drumright *et al.*, 2000). It has been used as a precursor of solvents in green chemistry, such as ethyl lactate, and used in the synthesis of polylactic acid (PLA), applied in the production of biodegradable packaging (Bruno *et al.*, 2020; Drumright *et al.*, 2000).

Lactic acid is commonly sold as an 88% solution, varying its price according to its application in the market. In general, lactic acid price follows the cost of starch and sugar raw materials used for fermentation (Biddu *et al.*, 2016). With a market growth of 16.2% per year, it is expected that this demand will reach 960.1 kt in 2025, which should represent US\$ 9.8 billion in the global market. As with lactic acid, PLA demand is also expected to grow, reaching \$ 6.5 billion worldwide in 2025. One reason for this would be the Asia-Pacific PLA market growth rate of 22.4% per year due to various beverages and foods and the cosmetics manufacturing units (Oliveira *et al.*, 2018).

The hydrothermal conversion of glycerol to lactic acid has been widely studied recently as an alternative to the fermentation route, with the advantage of using a low-cost raw material. Furthermore, for environmental reasons, there is an increase in demand for lactic acid, as it is the raw material for producing a biodegradable polymer (PLA) (Bruno *et al.*, 2018; Shen *et al.*, 2009).

Some methods described in the literature involve the determination of different organic acids by high-performance liquid chromatography (HPLC). However, these methods cannot efficiently separate glycerol and lactic acid, observing the overlap of peaks. In this context, the present work describes a methodology for separating the lactic acid produced by hydrothermal conversion of glycerol using HPLC.

2. Materials and methods

2.1 Standard samples of glycerol and lactic acid

Glycerol and lactic acid HPLC grade were obtained from Sigma-Aldrich (St. Louis, U.S.A.) and Proquímios (Rio de Janeiro, Brazil). Two calibration curves were obtained using the following concentrations 0.6, 1.8, 3.0, 4.2, 5.4 and 6.6 g L⁻¹ for the composition of the curve points. Standards were diluted in Milli-Q water to 10.0% vol. (Millipore, Bedford, USA) for method analysis. Diluted solutions acted as standards for linearity assessment.

2.2 Design of Experiments

A central composite design (CCD) was proposed to study the influence of experimental variables on glycerolysis reaction. The effect of two variable parameters, time and temperature, requiring nine experiments using face-centered star points was investigated. The low and high values of the variables were chosen based on preliminary investigations. For this purpose, sodium hydroxide and glycerol concentrations, catalyst content, time, and temperature were used as independent variables, and lactic acid concentration was used as the dependent variable, as presented in Tab. 1. The experimental design and optimization were conducted with Statistica 12.0 software.

Table 1. Experimental conditions of central composite design.

Experiment	[NaOH] (g L ⁻¹)	[glycerol] (g L ⁻¹)	Catalyst (%)	t (h)	T (°C)
1	0.6	0.6	5	3	220
2	0.6	0.6	5	3	250
3	0.6	0.6	5	3	280
4	0.6	0.6	5	4.5	220
5	0.6	0.6	5	4.5	250
6	0.6	0.6	5	4.5	280
7	0.6	0.6	5	6	220
8	0.6	0.6	5	6	250
9	0.6	0.6	5	6	280

2.3 Reaction Procedure

A 100 mL 4590 series reactor (Parr Instrument Company, Moline, U.S.A.) was used for hydrothermal conversion of glycerol. The operating conditions were modulated by a 4848 reactor controller (Parr Instrument Company), and the reagents were fed into the reactor in the desired mass ratio of glycerol: NaOH (1:1) and desired temperatures (220, 250 and 280 °C), with the use of 5% of a copper catalyst supported on silica. Then, the reactor contents were stirred at 1000 rpm at a vacuum pressure of 800 psi. The total reaction time was 3, 4.5 and 6 h.

2.4 High-performance liquid chromatography method

Analyses were performed employing the Nexera series UHPLC system (Shimadzu, Japan) equipped with an LC-40 XR binary pump, a RID-20A detector, and a SIL-40XR autosampler. A Hi-Plex H column (Agilent Technologies, Santa Clara, U.S.A.), 300 mm long by 7.7 mm internal diameter and 8 µm particle size was used to separate the products. The mobile phase used was H₂SO₄ 0.001 mol L⁻¹ + 10% ACN (organic modifier), using ultrasound previously to remove bubbles. The conditions used for this method were the temperature of detector and oven at 60 °C, 20 min of running time, and flow rate of 0.6 mL min⁻¹. The flow rate of 0.6 mL min⁻¹, column oven and detector temperature at 60 °C and 20 min for the total execution time. Samples were diluted to 10% vol in ultrapure water (Milli-Q) as a diluent and injected in triplicate. The results were analyzed using the LabSolutions software (Shimadzu).

2.5 Method validation

The developed method was validated according to ICH (2005) guidelines in terms of the following analytical parameters: linearity, limit of detection (LOD), limit of quantification (LOQ), precision, and accuracy (Dias *et al.*, 2020).

2.6 Linearity

Linearity was given by injection in triplicate of the standards of each point used to build the calibration curve (Novaes *et al.*, 2018). Two distinct curves (glycerol and lactic acid) were drawn in the interval of 0.6–6.6 g L⁻¹ (0.6; 1.8; 3.0; 4.2; 5.4 and 6.6 g L⁻¹).

Homogeneity was assessed by the Cochran test (Shen *et al.*, 2009), through Eq. 1.

$$C = \frac{s_{max}^2}{\sum_{k=1}^i s_k^2} \quad (1)$$

where s_{max}^2 is the highest value variance and $\sum_{k=1}^i s_k^2$ is the total of all samples variances.

2.7 Limit of detection and limit of quantification

The LOD and LOQ were calculated using Eqs. 2 and 3, respectively.

$$LOD = \frac{3.3\sigma_{LC}}{S} \quad (2)$$

$$LOQ = \frac{10\sigma_{LC}}{S} \quad (3)$$

where σ_{LC} is the standard deviation of the minor number concentration (LC) tested and S is the slope of the curve obtained.

2.8 Precision

Precision was calculated by repeatability, using three different concentrations (lowest, average, and highest) in triplicate (Rocha and Bacelar Júnior, 2018). Concentrations were 0.6, 3.0 and 6.6 g L⁻¹ for both curves, and the result was expressed as relative standard deviation (RSD, in %), as in Eq. 4.

$$RSD (\%) = \frac{\sigma}{\bar{C}} \times 100 \quad (4)$$

where σ represents the deviation from the lowest standard concentration and \bar{C} is the mean concentration.

2.9 Accuracy

This parameter was represented by the recovery (R, in %) by calculating different concentrations (lowest, average, and highest) in triplicate for the different curves. Concentrations used were 0.6, 3.0 and 6.6 g L⁻¹ for both curves. Accuracy was calculated with Eq. 5.

$$R (\%) = \frac{C_m}{C_e} \times 100 \quad (5)$$

where C_m and C_e are the obtained and theoretical concentrations, respectively.

3. Results and discussion

3.1 Reactions

Table 2 shows the results of conversion and selectivity for lactic acid under the reaction conditions of the experimental design.

Table 2. Selectivity and conversion to lactic acid under the reaction conditions of the experimental design.

Reaction	Conversion (%)	Selectivity for lactic acid (%)
1	33.90	2.42
2	31.40	9.90
3	38.04	35.73
4	32.26	1.80
5	34.60	8.29
6	42.82	34.63
7	29.96	2.04
8	33.81	13.22
9	53.72	58.84

According to Tab. 2, it can be observed that the method proposed by HPLC was efficient in separating

the two compounds, glycerol and lactic acid, allowing the quantification of each one of these compounds and enabling the calculation of the conversion and the selectivity for lactic acid. It is essential to mention that pyruvaldehyde was obtained as a by-product, in smaller amounts, in all reactions, which is expected for catalysis reactions in the primary medium due to the greater predisposition of formation of this intermediate by the Cannizzaro reaction (Lari *et al.*, 2016; Santos *et al.*, 2018).

It can also be noticed that, according to Fig. 1, when comparing the temperatures, increasing this parameter favors the formation of secondary compounds, such as pyruvaldehyde. When the reaction time increases, the appearance of lactic acid is preferred, consequently increasing its selectivity. Therefore, temperature increase combined with the increase in reaction time is favorable to the rise of the conversion and the rise in the selectivity of the lactic acid, which corroborates the results expected in the literature (Evans *et al.*, 2020).

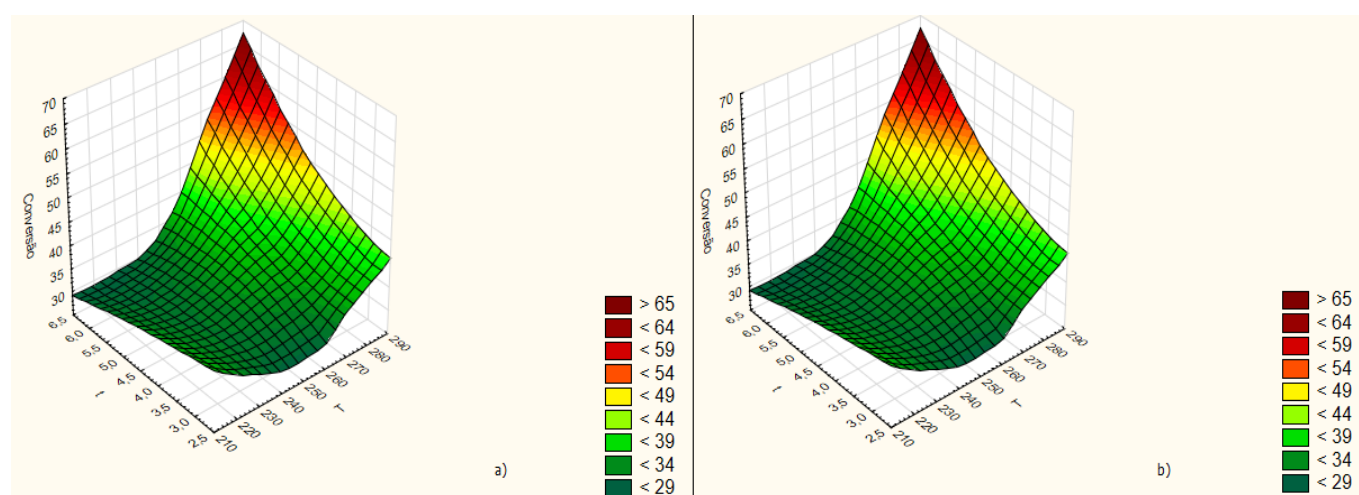


Figure 1. (a) Response surface Selectivity for lactic acid vs. T and t; (b) Response surface conversion vs. T and t.

3.2 Analysis by HPLC

All standards and reaction products were examined by HPLC and showed similar chromatographic appearance, which can be seen in Fig. 2. The overlapping peaks indicate coelution of interference that shares the same transition, with consequences such as inadequate quantification of the compound of interest or even the absence of identification of the combination of interest (Welch *et al.*, 2009). Diluted sulfuric acid as a mobile phase showed this coelution of desired compounds, generating an incorrect quantification.

Beltrán-Pietro *et al.* (2013) validated a chromatographic method using an ionic column at a temperature of 70 °C with a refractive index detector (RID) detector connected to a UV detector, with a phase composed of 3 mmol L⁻¹ of sulfuric acid (H₂SO₄, pH 2.00). with a flow rate of 0.5 mL min⁻¹ in an analysis time of 30 min. With this method, it is possible to identify compounds such as glyceraldehyde, oxalic acid, dihydroxyacetone, among others; however, it presents coelution of other compounds such as glycerol and lactic acid.

Although some methods in the literature report the separation of glycerol and lactic acid in the

chromatographic profile, it is observed that, in fact, there is a co-elution of these compounds, not allowing an efficient quantification of these products, requiring the development of a new method.

As an alternative, using the mobile phase with the organic modifier was essential for separating glycerol and lactic acid compounds, allowing a better chromatographic profile to visualize both peaks. The choice of acetonitrile as an organic modifier was due to its low viscosity (0.4 cP at 25 °C), which generates less pressure and allows a better retention time response (Leite, 2008; Sadek, 1996). Some tests were performed with 5, 10 and 20% vol of acetonitrile to decide the best proportion of acetonitrile in the mobile phase. The best chromatographic separation occurred with the 10% vol of acetonitrile.

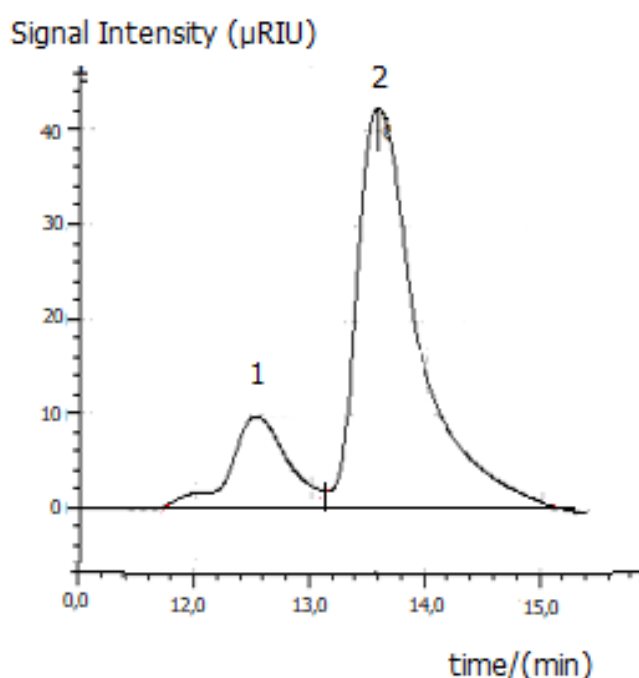


Figure 2. High-performance liquid chromatography chromatogram of the sample obtained through the reaction, using chromatographic conditions. Conditions: dilution of 10% vol, the flow rate at 0.6 mL min⁻¹, and injection volume of 20.0 µL. 1: lactic acid; 2: glycerol.

3.3. Method validation

3.3.1 Linearity

Six standard samples of glycerol and lactic acid were analyzed in triplicate by HPLC for each curve constructed, as seen in Fig. 3. This parameter was evaluated in the interval of 0.6–6.6 g L⁻¹. The

determination coefficient (R^2) was above the acceptance rule values (0.990) (Leite, 2008; Ribani *et al.*, 2004; Sadek, 1996), indicating excellent linearity.

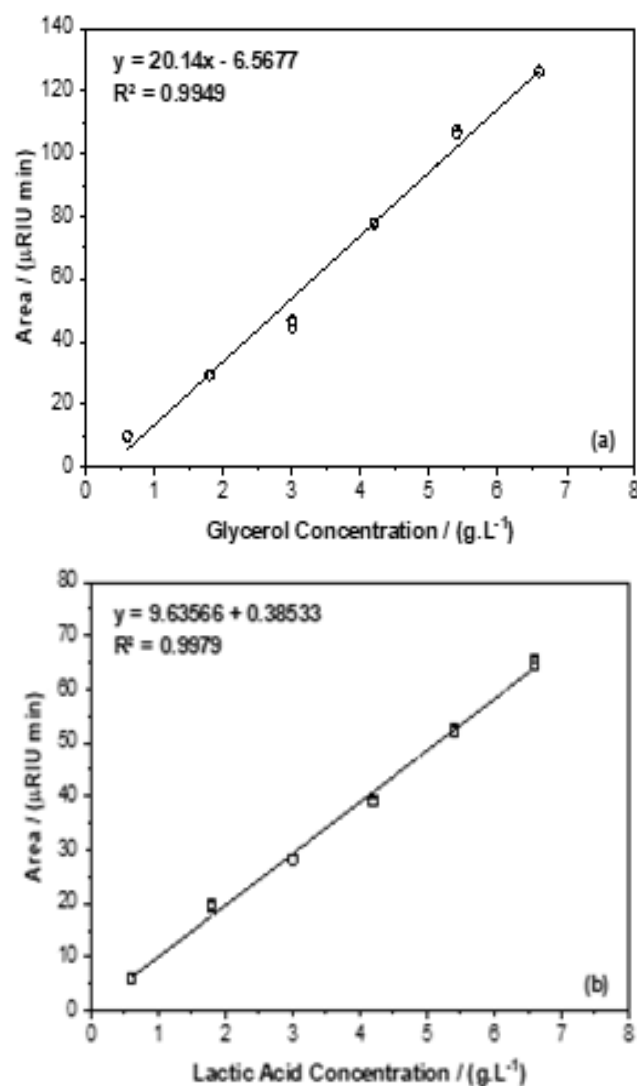


Figure 3. Fitted curves in HPLC analysis for (a) glycerol and (b) lactic acid. Range: 0.6 – 6.6 g L⁻¹.

The Cochran test was used with a 95% confidence level using the number of samples ($n = 6$) in triplicate. The calculated values of C were 0.661 for the glycerol curve and 0.130 for the lactic acid curve, being lower values when compared to the tabulated (0.616), indicating homoscedastic variances (Novaes *et al.*, 2018).

3.3.2 Limit of detection and limit of quantitation

For the glycerol analytical curve, LOD and LOQ values were 0.076 and 0.385 g L⁻¹, respectively, while for lactic acid, the LOD and LOQ values were 0.221

and 1.166 g L⁻¹. The results showed the possibility of differentiation and quantification of the different samples of each curve. The responsible standards require values below 0.5 g L⁻¹, and the present method is applicable (Cassini *et al.*, 2013; Souza and Junqueira, 2005), except only for lactic acid that showed a value above that specified by the standard.

3.3.3 Precision

Through Tab. 3, it is possible to conclude that the values are accurate about repeatability since they are lower than the 5% determined by the standards (Novaes *et al.*, 2018; Ribani *et al.*, 2004; Sadek, 1996).

Table 3. Validation parameters for the HPLC method.

Parameter	Glycerol	Lactic Acid
Linearity range (n = 6) (g.L ⁻¹)	0.6–6.6	0.6–6.6
Regression equation	y = 20.14x – 6.5677	y = 9.63566x + 0.38533
Determination coefficient (R ²)	0.9949	0.9979
LOD (g L ⁻¹)	0.076	0.385
LOQ (g L ⁻¹)	0.231	1.166
Repeatability (RSD, %)		
Lower	1.500	0.751
Middle	0.683	0.568
Higher	0.158	0.889
Recovery (%)		
Lower	100.00 ± 0.01	100.00 ± 0.01
Middle	98.33 ± 0.08	100.00 ± 0.01
Higher	100.00 ± 0.01	100.00 ± 0.05

3.3.4 Accuracy

The values obtained for this parameter are between 98.33 and 100%. Regarding the glycerol curve, the mean recovery was 99.44 ± 0.03%, while for lactic acid, it was 100.00 ± 0.02%, indicating an amicable agreement between experimental and theoretical data. Furthermore, these results are within what is expected by regulatory standards (70–120%) (Goutal *et al.*, 2016; Lanças, 2004).

4. Conclusions

The methodology described in this article allowed the separation of lactic acid and glycerol by HPLC in a quick and straightforward run of 20 min. In addition, it was possible to quantify each one, allowing the calculation of conversion and selectivity for lactic acid for the reactions mentioned in the experimental design.

Authors' contribution

Conceptualization: Cruz, A. F. A.

Data curation: Cruz, A. F. A.

Formal Analysis: Cruz, A. F. A.; Dias, G. P.; Bittencourt, F. R.

Funding acquisition: Not applicable

Investigation: Cruz, A. F. A.

Methodology: Cruz, A. F. A.; Dias, G. P.; Bittencourt, F. R.

Project administration: Aranda, D. A. G.

Resources: Aranda, D. A. G.

Software: Cruz, A. F. A.; Dias, G. P.; Bittencourt, F. R.

Supervision: Aranda, D. A. G.

Validation: Cruz, A. F. A.

Visualization: Cruz, A. F. A.; Aranda, D. A. G.

Writing – original draft: Cruz, A. F. A.; Aranda, D. A. G.

Writing – review & editing: Cruz, A. F. A.; Aranda, D. A. G.

Data availability statement

All data sets were generated or analyzed in the current study.

Funding

Conselho Nacional de Desenvolvimento Científico e Tecnológico (CNPq). Grant No: 167934/2019-8.

Acknowledgments

LIPCAT – Laboratório de Intensificação de Processos e Catálise

References

- Arcanjo, M. R. A.; Silva Júnior, I. J.; Rodríguez-Castellón, E.; Infantes-Molina, A.; Vieira, R. S. Conversion of glycerol into lactic acid using Pd or Pt supported on carbon as catalyst. *Catal. Today*. **2017**, 279 (Part 2). <https://doi.org/10.1016/j.cattod.2016.02.015>
- Beltrán-Prieto, J. C.; Pecha, J.; Kašpárková, V.; Kolomazník, K. Development of an HPLC method for the determination of glycerol oxidation products. *J. Liq. Chromatogr. Relat. Technol.* **2013**, 36 (19), 2758–2773. <https://doi.org/10.1080/10826076.2012.725695>
- Biddy, M. J.; Scarlata, C.; Kinchin, C. *Chemicals from Biomass: a Market assessment of bioproducts with near-term potential*. NREL/TP-5100-65509; National Renewable Energy Laboratory: Golden, CO, 2016. <https://www.nrel.gov/docs/fy16osti/65509.pdf> (Accessed 2021-08-19).
- Bilck, A. P.; Müller, C. M. O.; Olivato, J. B.; Mali, S.; Grossmann, M. V. E.; Yamashita, F. Using glycerol produced from biodiesel as a plasticiser in extruded biodegradable films. *Polímeros*, **2015**, 25 (4), 331–335. <https://doi.org/10.1590/0104-1428.1803>
- Bruno, A. M.; Chagas, C. A.; Souza, M. V. M.; Manfro, R. L. Lactic acid production from glycerol in alkaline medium using Pt-based catalysts in continuous flow reaction system. *Renew. Energ.* **2018**, 118, 160–171. <https://doi.org/10.1016/j.renene.2017.11.014>
- Bruno, A. M.; Simões, T. D. R.; Souza, M. M. V. M.; Manfro, R. L. Cu catalysts supported on CaO/MgO for glycerol conversion to lactic acid in alkaline medium employing a continuous flow reaction system. *RSC Adv.* **2020**, 10 (52), 31123–31138. <https://doi.org/10.1039/D0RA06547A>
- Cassini, S. T.; Antunes, P. W. P.; Keller, R. Validação de método analítico livre de acetonitrila para análise de microcistinas por cromatografia líquida de alta eficiência. *Quim. Nova.* **2013**, 36 (8), 1208–1213. <https://doi.org/10.1590/S0100-40422013000800019>
- Chi, Z.; Pyle, D.; Wen, Z.; Frear, C.; Chen, S. A laboratory study of producing docosahexaenoic acid from biodiesel-waste glycerol by microalgal fermentation. *Process Biochem.* **2007**, 42 (11), 1537–1545. <https://doi.org/10.1016/j.procbio.2007.08.008>
- Dias, G. P.; Santos, R. C.; Carvalho, R. C.; Souza, C. G.; Santos, A. P. F.; Andrade, D. F.; D'Ávila, L. A. Determination of Methanol in Gasoline and Ethanol Fuels by High-Performance Liquid Chromatography. *J. Braz. Chem. Soc.* **2020**, 31 (5), 1055–1063. <https://doi.org/10.21577/0103-5053.20190272>
- Drumright, R. E.; Gruber, P. R.; Henton, D. E. Polylactic Acid Technology. *Adv. Mater.* **2000**, 12 (23), 1841–1846. [https://doi.org/10.1002/1521-4095\(200012\)12:23%3C1841::AID-ADMA1841%3E3.0.CO;2-E](https://doi.org/10.1002/1521-4095(200012)12:23%3C1841::AID-ADMA1841%3E3.0.CO;2-E)
- Evans, C. D.; Douthwaite, M.; Carter, J. H.; Patisson, S.; Kondrat S. A.; Bethell, D.; Knight, D. W.; Taylor, S. H.; Hutchings, G. J. Enhancing the understanding of the glycerol to lactic acid reaction mechanism over AuPt/TiO₂ under alkaline conditions. *J. Chem. Phys.* **2020**, 152 (13), 134705. <https://doi.org/10.1063/1.5128595>
- Goutal, S.; Auvity, S.; Legrand, T.; Hauquier, F.; Cisternino, S.; Chapy, H.; Saba, W.; Tournier, N. Validation of a simple HPLC-UV method for rifampicin determination in plasma: Application to the study of rifampicin arteriovenous concentration gradient. *J. Pharm Biomed. Anal.* **2016**, 123 (1), 173–178. <https://doi.org/10.1016/j.jpba.2016.02.013>
- Huang, D.; Zhou, H.; Lin, L. Biodiesel: an Alternative to Conventional Fuel. *Energy Procedia.* **2012**, 16 (Part C), 1874–1885. <https://doi.org/10.1016/j.egypro.2012.01.287>
- ICH International Conference on Harmonization*. Validation of Analytical Procedures: Text and Methodology – Q2 (R1); Geneva, Switzerland, 2005. https://www.ema.europa.eu/en/documents/scientific-guideline/ich-q-2-r1-validation-analytical-procedures-text-methodology-step-5_en.pdf (Accessed 2021-08-19).
- Lanças, F. M. *Validação de Métodos Cromatográficos de Análise*; Editora RiMA, 2004.
- Lari, G. M.; García-Muelas, R.; Mondelli, C.; López, N.; Pérez-Ramírez, J. Glycerol oxidehydration to pyruvaldehyde over silver-based catalysts for improved lactic acid production. *Green Chem.* **2016**, 18 (17), 4682–4692. <https://doi.org/10.1039/C6GC00894A>
- Leite, F. *Validação em Análise Química*; Átomo, 2008.
- Manfro, R. L.; Souza, M. M. V. M. Production of Renewable Hydrogen by Glycerol Steam Reforming Using Ni–Cu–Mg–Al Mixed Oxides Obtained from Hydrotalcite-like Compounds. *Catal. Lett.* **2014**, 144 (5), 867–877. <https://doi.org/10.1007/s10562-014-1196-6>
- Novaes, C. G.; Yamaki, R. T.; Paula, V. F. Nascimento Júnior, B. B.; Barreto, J. A.; Valasques, G. S.; Bezerra, M. A. Otimização de Métodos Analíticos Usando Metodologia de Superfícies de Resposta – Parte I: Variáveis de Processo. *Rev. Virtual Quim.* **2018**, 9 (3), 1184–1215. <https://doi.org/10.21577/1984-6835.20170070>
- Oliveira, R. A.; Komesu, A.; Rossell C. E. V.; Maciel Filho, R. Challenges and opportunities in lactic acid bioprocess design—From economic to production aspects. *Biochem. Eng. J.* **2018**, 133, 219–239. <https://doi.org/10.1016/j.bej.2018.03.003>
- Ribani, M.; Bottoli, C. B. G.; Collins, C. H.; Jardim, I. C. S. F.; Melo, L. F. C. Validação em métodos cromatográficos e eletroforéticos. *Quim. Nova.* **2004**, 27 (5), 771–780. <https://doi.org/10.1590/S0100-40422004000500017>
- Rocha, K. R.; Bacelar Júnior, A. J. ANOVA Medidas repetidas e seus pressupostos: Análise passo a passo de um

experimento. *Perspect. Cienc. Tec.* **2018**, *10*, 29–51.
<https://doi.org/10.22407/1984-5693.2018.v10.p.29-51>

Sadek, P. C. *The HPLC Solvent Guide*; Wiley, 1996.

Santos, K. M. A.; Albuquerque, E. M.; Borges, L. E. P.; Fraga, M. A. Discussing Lewis and Brønsted acidity on continuous pyruvaldehyde Cannizzaro reaction to lactic acid over solid catalysts. *Mol. Catal.* **2018**, *458* (Part B), 198–205. <https://doi.org/10.1016/j.mcat.2017.12.010>

Shen, Z.; Jin, F.; Zhang, Y.; Wu, B.; Kishita, A.; Tohjj, K.; Kishida, H. Effect of Alkaline Catalysts on the Hydrothermal Conversion of Glycerin into Lactic Acid. *Ind. Eng. Chem. Res.* **2009**, *48* (19), 8920–8925. <https://doi.org/10.1021/ie900937d>

Souza, S. V. C.; Junqueira, R. G. A procedure to assess linearity by ordinary least squares method. *Anal. Chim. Acta.* **2005**, *552* (1–2), 25–35. <https://doi.org/10.1016/j.aca.2005.07.043>

Tan, Y. H.; Abdullah, M.O.; Nolasco-Hipolito, C. The potential of waste cooking oil-based biodiesel using heterogeneous catalyst derived from various calcined eggshells coupled with an emulsification technique: A review on the emission reduction and engine performance. *Renew. Sust. Energ. Rev.* **2015**, *47*, 589–603. <https://doi.org/10.1016/j.rser.2015.03.048>

Welch, C. J.; Brkovic, T.; Schafer, W.; Gong, X. Performance to burn? Re-evaluating the choice of acetonitrile as the platform solvent for analytical HPLC. *Green Chem.* **2009**, *11* (8), 1232–1238. <https://doi.org/10.1039/B906215G>

Sugarcane bagasse biochar pellets for removal of caffeine, norfloxacin, and ciprofloxacin in aqueous samples

Mateus Cottorello Fonsêca¹, César Augusto Marasco Júnior¹, Diógenes dos Santos Dias², João Pedro da Silva¹, Rafaela Silva Lamarca¹, Clóvis Augusto Ribeiro², Lorena Oliveira Pires², Paulo Clairmont Feitosa de Lima Gomes¹⁺

1. São Paulo State University, National Institute for Alternative Technologies of Detection, Toxicological Evaluation and Removal of Micropollutants and Radioactives, Araraquara, Brazil.
2. São Paulo State University, Institute of Chemistry, Araraquara, Brazil.

+Corresponding author: Paulo Clairmont F. de Lima Gomes, **Phone:** +55 16 33019613 **Email address:** paulo.clairmont@unesp.br

ARTICLE INFO

Article history:

Received: September 17, 2021

Accepted: March 04, 2022

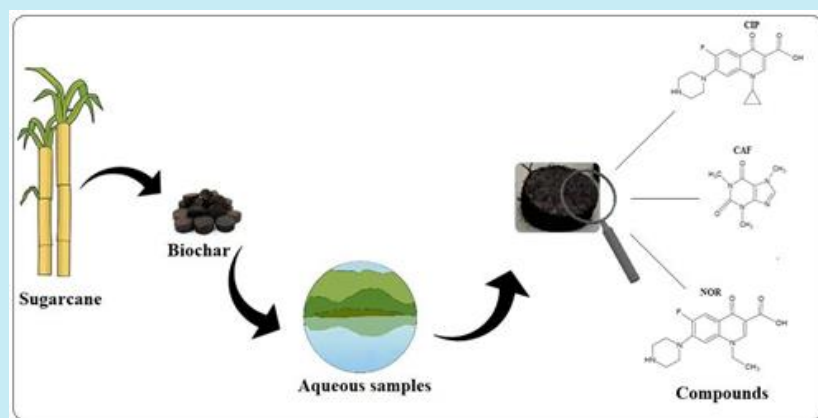
Published: April 01, 2022

Section Editor: Assis Vicente Benedetti

Keywords:

1. torrefaction
2. adsorbent
3. emerging contaminants
4. wastewater
5. removal

ABSTRACT: This work investigates the physicochemical properties of a biochar obtained from sugarcane bagasse by torrefaction at four different temperatures (260, 270, 280, and 290 °C), without chemical or physical activation. The biochar was characterized by thermogravimetric and proximate analysis, Fourier transform infrared spectroscopy (FTIR), scanning electron microscopy, together with measurements of point of zero charge, pH, elemental composition, and surface area. Evaluation regarding the efficiency of the biochar employed as an adsorbent for the removal of caffeine, ciprofloxacin, and norfloxacin in wastewater samples. The assays were performed in batch vessels filled with lab-made sewage spiked with caffeine at 5.00 $\mu\text{g L}^{-1}$ and with ciprofloxacin and norfloxacin at 10.0 $\mu\text{g L}^{-1}$. These compounds were studied separately. The thermogravimetry data demonstrated that increasing the torrefaction temperature led to generation of a greater amount of fixed carbon, as well as loss of volatile materials and removal of non-condensable compounds. This was corroborated by the FTIR analyses, where a higher temperature led to higher intensity of bands corresponding to methyl, methylene, and C=C bonds. The biochar produced at 280 °C presented the best stability, with adsorption efficiencies for removal from the lab-made sewage of 91% (norfloxacin), 81% (ciprofloxacin), and 58% (caffeine).



1. Introduction

Biochar is a solid material obtained by the thermochemical conversion of biomass in an oxygen-restricted environment (International Biochar Initiative, 2015). The characteristics of biochar include porous structure, large specific surface area, mechanical resistance, acid and alkaline corrosion resistance, ion exchange capacity, and diverse chemical functionalities. These properties provide biochar with many different possible uses, including environmental applications such as the removal of organic and inorganic contaminants, water purification, and soil remediation and fertilization (L. Li *et al.*, 2019; Oliveira *et al.*, 2017; Wang *et al.*, 2017).

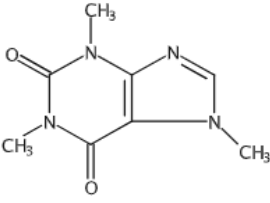
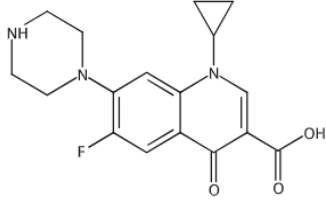
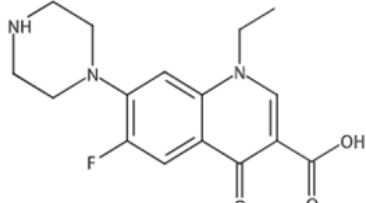
Inyang and Dickenson (2015) reported higher adsorption efficiency of organic contaminants on biochar, compared to activated carbon. The presence of biochar in soil provides benefits such as reduced nutrient leaching, promotion of crop growth, and reduced methane (CH₄) emissions. Biochar can

incorporate fertilizers and nutrients for controlled release, reducing nutrient shortages in the soil (Liu *et al.*, 2019). Another important point to be highlighted is that compared to biochar, the cost of activated carbon is estimated to be 20 times higher, due to high energy consumption and low productivity (Mohanty *et al.*, 2018).

Caffeine (CAF), norfloxacin (NOR), and ciprofloxacin (CIP) are in the class of emerging contaminants. CAF is highlighted because it is a marker of anthropogenic activity and is present in wastewater at concentration levels from $\mu\text{g L}^{-1}$ to ng L^{-1} (Marasco Júnior *et al.*, 2019). CIP and NOR, which are frequently found in wastewater samples at $\mu\text{g L}^{-1}$ concentration level, are broad-spectrum antibiotics of the fluoroquinolone class, widely applied in human and veterinary medicine. In 2019, quinolones were present in more of the 21 million prescriptions in the USA (Buehrle *et al.*, 2021).

Table 1 presents the physicochemical characteristics of the CAF, CIP and NOR.

Table 1. Physicochemical properties of the studied compounds.

Compound	CAF	CIP	NOR
Chemical structure			
Formula	C ₈ H ₁₀ N ₄ O ₂	C ₁₇ H ₁₈ FN ₃ O ₃	C ₁₆ H ₁₈ FN ₃ O ₃
Molecular mass (g mol ⁻¹)	194.19	331.34	319.33
pKa	0.520	6.43; 8.68	0.160; 8.68
Mass solubility (g L) [*]	58.0	0.460 - 1.60	0.350 - 1.40
Log P	0.628	1.625	1.744

* Solubility at the pH range from 7 to 9, at 25 °C; pKa = -logKa; Log P = Octanol-water partition coefficient.

Source: Adapted from SciFinder (2021).

Even at $\mu\text{g L}^{-1}$ concentration level, these compounds inhibit nitrite reductase and polyphosphate kinase, reducing the removal of nitrogen and phosphorus in biological processes applied in wastewater treatment plants (WWTPs) (Yi *et al.*, 2017). Furthermore, the presence of these antibiotics and other pharmaceutical compounds in wastewater samples increases the risk of development of antibiotic resistant genes (ARG) and their transfer through the aquatic environment. Wastewaters containing pharmaceutical compounds,

microbiota, plasmids, transposons, and integrons act as ARG reservoirs that can facilitate the spread of antimicrobial resistance (Osińska *et al.*, 2016).

Biochar, as an adsorbent, can be used for the removal of antibiotics and metals from aqueous solutions, with the advantages of low production costs and environmental sustainability (Liang *et al.*, 2021; Z. Li *et al.*, 2020; Tan *et al.*, 2015). Wang *et al.* (2017) used activated magnetic biochar to remove norfloxacin at concentrations in the range from 1.00 to 10.0 mg L⁻¹

in water solutions, achieving a removal efficiency of 97.62%. Huang *et al.* (2020) prepared biochar from rabbit feces by pyrolysis at four temperatures (400, 500, 600, and 700 °C). The biochar was then used to remove CIP at a concentration of 10 mg L⁻¹ in water solutions, achieving removal efficiencies of 76.41, 96.80, 92.50, and 96.79% after 400 min.

Anastopoulos *et al.* (2020) produced oxidized biochar from pine needles at 650 °C, using boiling nitric acid. The biochar was used for to remove CAF at concentrations from 5 to 50 mg L⁻¹ in water and sewage samples, reaching an adsorption capacity of 1.41 mg g⁻¹ after 150 min, at pH 4.0.

Pyrolysis, torrefaction, and hydrothermal carbonization are the main processes applied for the conversion of biomass to biochar. Pyrolysis is characterized by a high heating rate to temperatures above 300 °C, which produces biochar with high surface area and pore volume. Torrefaction is performed in the temperature range between 200 and 300 °C, so the energy costs are lower and it is possible to use renewable sources, such as solar energy. The reactions during torrefaction involve carbonization, volatilization, and depolymerization of hemicellulose, cellulose, and lignin. In addition, water and lipids are converted to condensable and non-condensable gases that then generate CO₂, CO, and CH₄. Around 70% of the mass is retained as solid material and 30% is lost as condensable and non-condensable compounds (Tumuluru *et al.*, 2011). The hydrothermal carbonization is a thermochemical conversion technique, whose main characteristic is the direct application to biomass with high humidity, for the production of water-soluble organic matter and carbon-rich products at temperatures 150 - 350 °C (Liang *et al.*, 2021).

Lignocellulosic biomasses in the form of natural resources and solid residues generated by anthropic activities worldwide can be used for the production of biochar (Rangabhashiyam and Balasubramanian, 2019), being economically attractive since these raw materials are inexpensive and available in abundance.

The main sources of biochar are lignocellulosic biomasses obtained from solid residues produced in agriculture (such as sugarcane bagasse and straw), forest residues (including branches, foliage, and sawdust), and sludge from wastewater treatment plants.

Among the agricultural lignocellulosic residues, sugarcane bagasse can be highlighted as a raw material for biochar production. Brazil is the world's largest sugarcane producer, with an estimated production of more 654.5 million tons in the 2020/2021 season. São Paulo State was responsible for 354 million tons of

sugarcane, accounting for 54.12% of the sugarcane processed in the country (Brazil, 2021). During sugarcane processing, bagasse is generated as a waste, corresponding to approximately 30% of the planted sugarcane (Jayaraman *et al.*, 2018). Currently, most of this material is burned to produce energy in the boilers in the sugar and ethanol plants.

Sugarcane bagasse is composed, on average, of 40-45% cellulose, 25 - 30% hemicellulose, and 20 - 25% lignin. It has a heterogeneous surface that presents phenolic groups, carboxylic acids, and hydroxyls (Ramos *et al.*, 2016). The use of sugarcane bagasse as raw material for biochar is attractive because it is abundant and inexpensive, with an estimated price of around US\$ 20.00 per ton.

The aim of this work was to evaluate the physicochemical properties of sugarcane bagasse biochars obtained using a torrefaction process at four different temperatures (260, 270, 280, and 290 °C). The biochars were tested as adsorbents for the removal of CAF, CIP, and NOR present in lab-made sewage samples. This study purpose to use this inexpensive and abundant adsorbent material, without need for chemical or physical activation, for the specific removal of these emerging contaminants found at µg L⁻¹ concentration level.

2. Materials and methods

2.1 Chemicals and reagents

The pharmaceutical compounds CAF, CIP, and NOR were acquired from Sigma-Aldrich (Saint Louis, MO, USA). The solvents (HPLC grade) methanol, acetonitrile, and 88% formic acid were purchased from J.T. Baker (Phillipsburg, NJ, USA).

The lab-made sewage composition was as follows: cellulose (47.0 mg L⁻¹), sucrose (98.0 mg L⁻¹), starch (149 mg L⁻¹), NaHCO₃ (370 mg L⁻¹), meat extract (262 mg L⁻¹), NaCl (250 mg L⁻¹), CaCl₂ (7.00 mg L⁻¹), MgCl₂ (4.50 mg L⁻¹), LAS (surfactant, 1.00 mg L⁻¹), K₂HPO₄, and soybean oil (79 mg L⁻¹). These compounds were dissolved in tap water and resulted in a chemical oxygen demand (COD) of 550 mg O₂ L⁻¹ and a pH value of 8.0.

2.2 Biochar preparation

The Santa Cruz sugar and ethanol plant (São Martinho Group) located in Américo Brasiliense (São Paulo State, Brazil; 21°45'09.5"S, 48°04'51.3"W) donated the sugarcane bagasse (from sugarcane variety

RB855156). The bagasse was triturated in an industrial blender, sieved through a 2 mm mesh, and transformed into pellets using a hydraulic press machine at 7 atm. As a way to standardize the size of the pellets produced, a stainless-steel mold was used, in order to obtain pellets with a diameter of 12 mm each.

The samples were torrefied in atmospheric conditions (altitude of 664 meters, atmospheric pressure 1012 hPa). Four different torrefaction temperatures were tested, with evaluation of the resulting biochars in terms of their physicochemical characteristics and mechanical resistance in an aqueous medium. The temperatures used were 260, 270, 280, and 290 °C, producing biochars denoted BG260C, BG270C, BG280C, and BG290C, respectively. The pelleted bagasse samples were placed in porcelain crucibles and torrefied in a muffle furnace (Model 7000, EDG Solutions, São Carlos, SP, Brazil). The oven program started at 40 °C, with a ramp rate of 10 °C min⁻¹ and a residence time of 1 h after reaching the desired temperature (this time was necessary for the pellets not to break easily). After the process, the crucibles were removed and placed in a desiccator. The biochar pellets were washed in water for 2 h, under stirring at 125 rpm, in a shaker-incubator (Model MA830, Marconi, Piracicaba, SP, Brazil) for the removal of ash and impurities derived from the torrefaction process, followed by drying for 24 h at 120 °C. [Figure 1](#) shows the workflow for production of the biochar pellets by torrefaction.

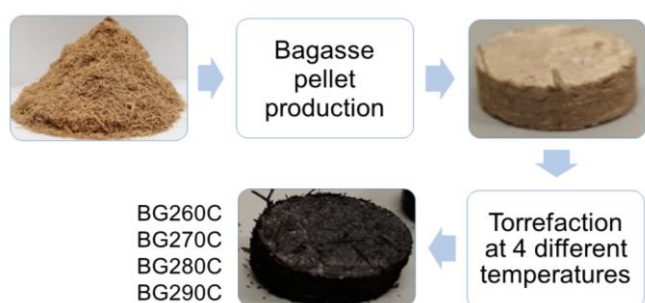


Figure 1. Sugarcane bagasse biochar torrefaction and pellet production processes.

2.3 Characterization of the materials

2.3.1 Thermogravimetry and proximate analysis

Thermogravimetric analysis (TGA) was performed using an SDT-2960 Simultaneous TGA/DTA (differential thermal analysis) Thermal Analyzer (TA Instruments, New Castle, DE, USA). For the characterization by TGA/DTG (derivative

thermogravimetry), the thermal analyzer software was programmed for two evaluation methods: thermal stability and proximate analysis.

For the thermal stability analysis, the biochar sample was macerated and approximately 8 mg were placed in an alumina crucible for weighing using the thermobalance. The sample was heated under an atmosphere of synthetic air at a flow rate of 100 mL min⁻¹, with the temperature increased from 25 to 600 °C at a rate of 10 °C min⁻¹.

For the proximate analysis, about 9 mg of the macerated biochar were weighed out and placed in an alumina crucible, according to the method described previously ([Torquato et al., 2017](#)).

2.3.2 Scanning electron microscope

Topographic contrast micrographs were obtained using a scanning electron microscope (SEM) (Model JSM7500F, JEOL, Kyoto, Japan). The SEM images were acquired at magnifications of 100x and 7000x.

2.3.3 Fourier transform infrared absorption spectroscopy

Fourier transform infrared absorption spectroscopy (FTIR) spectra were acquired in the range from 4000 to 400 cm⁻¹, using a spectrophotometer (Vertex 70, Bruker, Billerica, MA, USA) equipped with an attenuated total reflectance (ATR) accessory.

2.3.4 Elemental analysis

Elemental analysis was performed using a CNHS/O 2400 Series II Elemental Analyzer (Perkin Elmer, Waltham, MA, USA) to determine the sample composition in terms of carbon (C), hydrogen (H), nitrogen (N), sulfur (S), and oxygen (O).

2.3.5 Surface area analysis

The biochar surface area and porosity were measured using the nitrogen adsorption and desorption method. The isotherms were recorded using an ASAP 2000 instrument (Micromeritics, Narcross, GA, USA) operated with ASAP 2010 v. 3.01 software.

2.3.6 Point of zero charge and pH

The pH was measured using a pH meter (Model PG1800, Gehaka, São Paulo, SP, Brazil). The point of zero charge (pH_{PZC}) determination was performed using

the method proposed by Regalbuto and Robles (2004), employing 30 mL of deionized water with 30 mg of crushed biochar. The pH was adjusted with solutions of hydrochloric acid (HCl) and sodium hydroxide (NaOH), both at 0.100 mol L⁻¹, in order to obtain pH values of 2, 3, 4, 5, 6, 7, 8, 9, 10, 11, and 12. After 24 h, the pH was measured again.

The pH analysis was conducted according to the method proposed by Ahmedna *et al.* (1997). The experiments were performed for each biochar sample, which was crushed and added to deionized water (1% w/w). The solution was heated to 90 °C and kept under stirring for 20 min. After this period, the samples were cooled to room temperature and the pH was measured again.

2.4 Adsorption experiments

2.4.1 Selection of torrefaction temperature

The BG260C, BG270C, BG280C, and BG290C biochar pellets were evaluated for the adsorption of CAF at a concentration of 5.00 µg L⁻¹ in ultrapure water. The assays were performed during 24 h, at a controlled temperature of 25 °C, with stirring at 100 rpm, using a shaker-incubator (Model MA830, Marconi, Piracicaba, SP, Brazil). These tests were carried out together with a control experiment using 5.00 µg L⁻¹ CAF solution without the adsorbent material. Aliquots of 500 µL were withdrawn from the solution at different times (0, 0.25, 0.5, 1, 2.5, 5, 10, and 24 h), in order to evaluate the adsorption kinetics.

2.4.2 Kinetics of adsorption of the pharmaceutical compounds onto the biochar in lab-made sewage

Lab-made sewage produced in the laboratory was used, since it enabled simulation of the composition of domestic sewage, in the absence of any preexisting pharmaceutical compounds. The adsorption of CAF, CIP, and NOR was evaluated using the biochar obtained using the best torrefaction temperature. The batch adsorption tests were performed individually for each pharmaceutical compound, in order to avoid possible synergistic interactions and interference in this experiment. For this adsorption kinetics, in 100 mL polypropylene flasks, approximately 6.0 g (equivalent 30 mL) of biochar and 60 mL of lab-made sewage were added.

The lab-made sewage was spiked with each compound, using concentrations of 5.00 µg L⁻¹ for CAF and 10.0 µg L⁻¹ for CIP and NOR. The test was carried

out during 24 h, at a controlled temperature of 25 °C and with stirring at 100 rpm. A control experiment with each individual pharmaceutical compound was performed using only the lab-made sewage, without the adsorbent material.

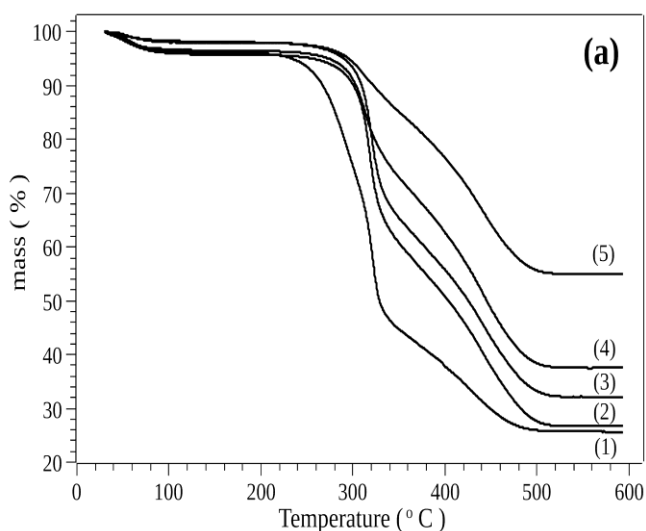
Aliquots of 500 µL were withdrawn from the solution at 10 different times (0, 0.5, 1, 2, 3, 4, 6, 8, 10, and 24 h), for determination of the adsorption kinetics. The samples were filtered through 0.22 µm nylon membranes and analyzed by LC-MS/MS, according to the method developed by Marasco Júnior *et al.* (2021). In this developed method the limits of detection and quantification were, respectively, for CAF 0.001 and 0.5 µg L⁻¹; CIP 0.5 and 3 µg L⁻¹ and for NOR 1 and 3 µg L⁻¹.

3. Results and Discussion

3.1 Thermogravimetric analysis

3.1.1 Thermogravimetry / derivative thermogravimetry

Figure 2 shows the TGA/DTG curves for the in natura bagasse (BG) and the biochars BG260C, BG270C, BG280C, and BG290C, indicating three well-defined thermal events. The first event did not involve decomposition, but was due to the elimination of moisture present in the samples. The curves showed that with increase of the torrefaction temperature, the biochar presented a lower content of hydrophilic components and consequently absorbed a smaller amount of moisture.



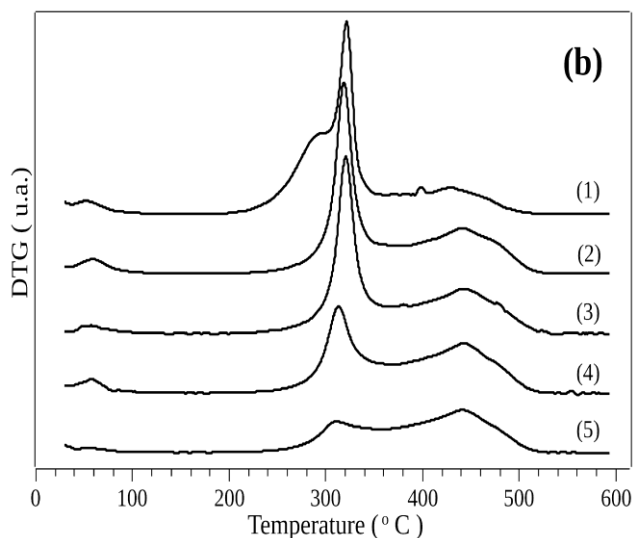


Figure 2. TGA (a) and DTG (b) curves obtained for the in natura bagasse (1), BG260C (2), BG270C (3), BG280C (4), and BG290C (5).

The second thermal event was associated with the decomposition of hemicellulose and cellulose. The

TGA/DTG curves indicated that the in natura bagasse was less stable, with the thermal decomposition temperature being shifted to the left and the presence of two superimposed peaks attributed to hemicellulose and cellulose. The BG290C sample showed greater stability, with the temperature for initiation of decomposition shifted to the right, due to previous elimination of volatile material during the torrefaction.

The third decomposition step could be attributed to lignin, with thermal decomposition between 350 and 530 °C. The TGA curves showed that higher thermal stability was correlated with higher biochar torrefaction temperature.

This increase of stability was related to the amount of residues and metal oxides present in the sugarcane bagasse pellets.

Table 2 shows the mass losses in each temperature range, the mass loss variation in the stages, the residue produced, and the total mass loss for each sample. The moisture losses ranged from 1 to 4% (Fig. 2, Tab. 3), with these low values suggesting that partial degradation of hemicellulose, cellulose, and lignin occurred during pellet torrefaction.

Table 2. Mass loss event temperature ranges (ΔT), mass losses (Δm), sample ash contents, and total mass losses for the in natura bagasse and the biochars.

Sample	ΔT (°C)	Δm (%)	Ash (% , at 591.6 °C)	Total mass loss (%)
Raw BG	1 st) 30.3 – 105	3.68	25.6	74.4
	2 nd) 195 – 376	54.7		
	3 rd) 376 – 518	15.5		
BG260C	1 st) 21.6 – 113	4.06	26.6	73.4
	2 nd) 186 – 360	39.4		
	3 rd) 360 – 517	29.6		
BG270C	1 st) 22.4 – 90.0	1.80	32.2	67.8
	2 nd) 204 – 356	37.2		
	3 rd) 356 – 516	28.6		
BG280C	1 st) 26.6 – 94.4	3.24	37.5	62.5
	2 nd) 208 – 362	27.0		
	3 rd) 362 – 541	31.8		
BG290C	1 st) 41.0 – 106	1.24	54.9	45.1
	2 nd) 163 – 347	12.9		
	3 rd) 361 – 529	27.9		

Table 3. Average compositions of the raw bagasse and the biochars, in terms of moisture, volatile materials, fixed carbon, and ash.

Sample	Composition (%)			
	Moisture	Volatile materials	Fixed carbon	Ash
Raw BG	3.96	51.2	7.67	36.9
BG260C	3.25	48.7	20.3	27.6
BG270C	3.82	31.5	27.8	36.9
BG280C	2.57	27.0	24.5	45.8
BG290C	2.58	40.1	28.2	29.1

In the second step, it could be seen that increase of the torrefaction temperature led to a decrease of the peak related to the mass loss attributed to hemicellulose and volatile compounds, which was greatest for the biochars produced at 280 and 290 °C, since these higher temperatures caused substantial losses of these components.

In the third step, the cellulose and lignin degradation peaks were less intense, compared to the peaks of the second stage. For BG260C and BG270C, the mass loss was higher in the second stage than in the third stage, while the opposite was observed for samples BG280C and BG290C. This suggested that lignin and cellulose were the main components present in BG280C and BG290C. In addition, increase of the torrefaction temperature led to an increase of the ash content, relative to the other fractions (Tab. 2).

Increase of the torrefaction temperature was directly related greater decomposition of the organic content. At high temperatures, the losses affect the mechanical properties, porosity, density, and thermal stability of the material.

3.1.2 Proximate analysis

In the torrefaction temperature range (200-300 °C), increase of the mass loss was directly related to the temperature increase, mainly due to the decomposition of hemicellulose, as shown in Fig. 2 and Tab. 2. When pyrolysis is performed at temperatures above 300 °C, the main mass loss and consequent generation of volatile materials are associated with the decomposition of cellulose and lignin (Dias *et al.*, 2018).

The amounts of water found in the biochars and the in natura bagasse corresponded to the combination of surface humidity and the moisture present within the composition of the material. The moisture contents presented by the biochars and the bagasse did not exceed 4% (Tab. 3).

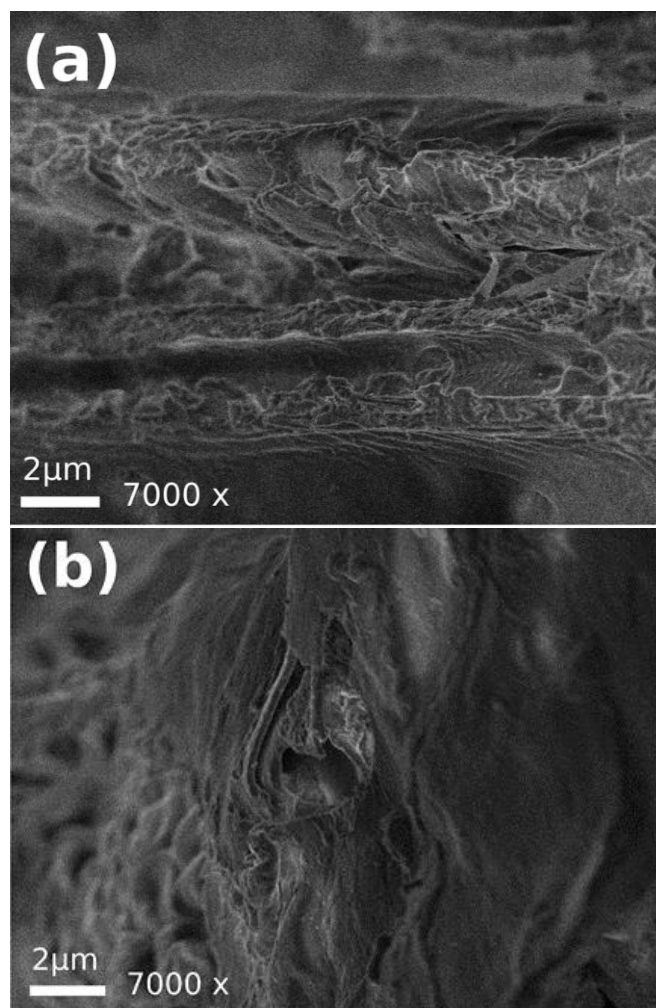
As expected, the in natura bagasse presented the highest mass loss due to volatile materials (51.2%), since the previously torrefied samples had already partially lost these compounds.

3.2 Scanning electron microscopic analyses

The micrographs of the biochars (Fig. 3) obtained at magnifications of 100x and 7000x showed that increase of the torrefaction temperature caused an increase of the amount of carbonized biomass, with small fragments evident. It could also be seen that the biochar surface was not regular, due to partial removal

of the lignocellulosic biomass during the torrefaction process, leaving the biochar with a porous and rough surface. This indicated the suitability of the material for use as an adsorbent, since a high surface area enables efficient interaction with different types of chemical compounds.

The porous structure demonstrated that the thermal conversion process removed the outer fibers, consequently increasing the surface area, which made the cellulose accessible for thermal degradation (Morais *et al.*, 2017). The formation of irregular particles could have been related to the fusion and solidification of oxides formed between silicon, metal elements, and oxygen during combustion. The silicon content in biochar is a favorable aspect for its use as an adsorbent material, since a high silicon content promotes the ionic exchange of metallic species (Rodríguez-Díaz *et al.*, 2015).



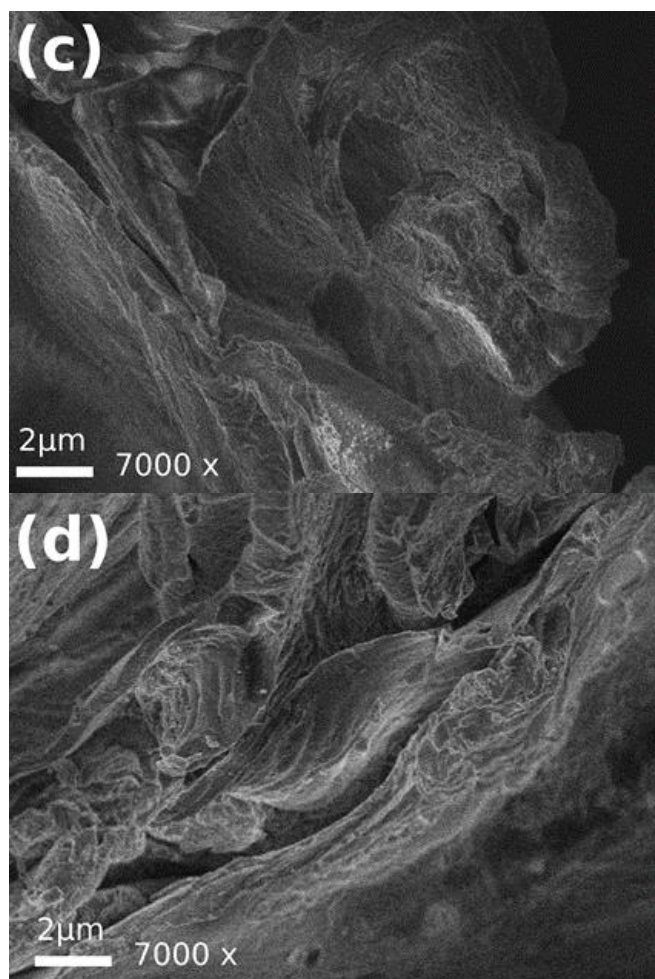


Figure 3. Scanning electron microscopic micrographs of the biochars at magnification of 7000x: BG260C (a), BG270C (b), BG280C (c), and BG290C (d).

3.3 Fourier transform infrared analysis of the biochars

Figure 4 shows the FTIR spectra obtained in the range from 4000 to 400 cm^{-1} .

Bands in the region between 3700 and 3100 cm^{-1} could be attributed to O–H bond stretching, due to the presence of alcoholic, phenolic, and hydroxyl groups in the lignocellulosic biomass. Bands in the range 3000–2700 cm^{-1} corresponded to asymmetric and symmetric stretching of methyl and methylene groups, respectively (Becker *et al.*, 2013; Granados *et al.*, 2017). Bands in the region between 1800 and 1650 cm^{-1} were due to carbonyl group stretching, indicating the presence of conjugated and unconjugated

C=O of carboxylic acids from hemicellulose and from cellulose after oxidation.

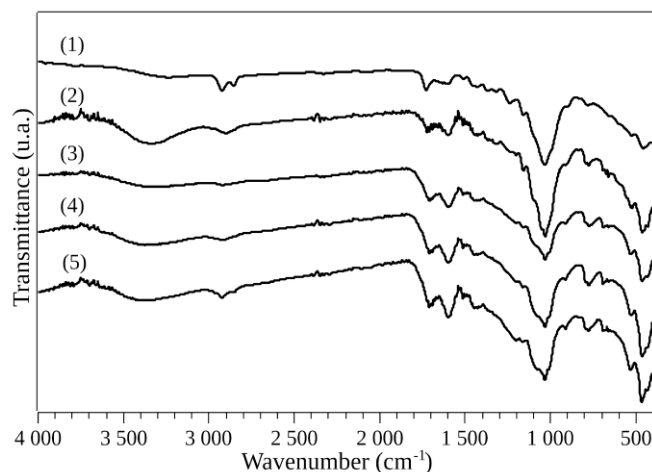


Figure 4. Infrared spectra of the in natura bagasse (1), BG260C (2), BG270C (3), BG280C (4), and BG290C (5) in the 4000–400 cm^{-1} region.

The torrefaction process led to decreased intensity of this peak, reflecting a decrease of carboxylic acid groups, leading to the formation of new products, as shown by signals at around 1700 cm^{-1} .

Signals in the range 1600–1500 cm^{-1} could be attributed to vibrations of C=C in the lignin aromatic skeleton, which increased as the torrefaction temperature increased. Bands between 1500 and 1350 cm^{-1} corresponded to deflections and deformations of C–H bonds of amorphous lignin and cellulose polysaccharides. Bands in the range 1300–1150 cm^{-1} were due to stretching vibrations of C–O of the lignin guaiacyl aromatic rings and antisymmetric stretching of the C–OH and C–O–C bonds of cellulose and hemicellulose. The intensity of the bands in this region tended to decrease with increase of the torrefaction temperature. Bands in the range 1050–1000 cm^{-1} corresponded to C–O, C=C, and C–C vibrations of cellulose, hemicellulose, and lignin. A small band at around 900 cm^{-1} could be attributed to the beta-glycosidic bonds in cellulose and hemicellulose, while bands in the range 800–600 cm^{-1} were due to the vibrations of O–H connections (Granados *et al.*, 2017; Ibrahim *et al.*, 2013; Mubarik *et al.*, 2015; Rodríguez-Díaz *et al.*, 2015). The FTIR data is presented in Tab. 4.

Table 4. Possible functional groups and compounds found in the samples by FTIR.

Wavenumber (cm ⁻¹)	Type of vibration	Chemical functionalities and/or possible components	References
3700-3100	O-H	Alcoholic, phenolic, and hydroxyl groups	Granados <i>et al.</i> (2017); Mubarik <i>et al.</i> (2015); Rodríguez-Díaz <i>et al.</i> (2015)
3000-2700	C-H	Methyl and methylene	Granados <i>et al.</i> (2017)
1800-1650	C=O	Carboxylic acid	Granados <i>et al.</i> (2017); Mubarik <i>et al.</i> (2015); Rodríguez-Díaz <i>et al.</i> (2015)
1600-1500	C=C	Aromatics	Mubarik <i>et al.</i> (2015)
1500-1350	C-H	Amorphous polysaccharides	Granados <i>et al.</i> (2017)
1300-1150	C-O, C-OH, C-O-C	Aromatics, lignin, cellulose, and hemicellulose	Granados <i>et al.</i> (2017); Mubarik <i>et al.</i> (2015)
1050-1000	C-O, C=C, C-C-O	Cellulose, hemicellulose, and lignin	Granados <i>et al.</i> (2017)
900	β-glycoside	Hemicellulose and cellulose	Granados <i>et al.</i> (2017)
800-600	O-H	Alcoholic, phenolic, and hydroxyl groups	Granados <i>et al.</i> (2017)

3.4 Biochar elemental composition

The elemental compositions of the biochars are shown in Tab. 5. As expected, there was an increase of the carbon content as the temperature increased, while the hydrogen, oxygen, and sulfur contents decreased. Higher nitrogen contents were found for the biochars produced at 280 and 290 °C, compared to those produced at 260 and 270 °C.

In general, as the torrefaction temperature and residence time increase, there are increases of the amount of carbon and decreases of the amounts of hydrogen and oxygen. Therefore, the values of the H/C

and O/C atomic ratios tend to decrease with increase of the torrefaction temperature (Tumuluru *et al.*, 2011).

Slight decreases of the H/C and O/C ratios values were observed as the torrefaction temperature increased, which could be explained by the loss of hydroxyl and carboxylic functional groups, respectively (Rangabhashiyam and Balasubramanian, 2019). Lower O/C values were observed according to increase of the temperature, indicating a more aromatic biochar and a less hydrophilic structure, due to dehydration reactions and the higher degree of carbonization.

Table 5. Elemental compositions and atomic ratios of the biochars.

Elements and ratios	Composition (%)			
	BG260C	BG270C	BG280C	BG290C
Carbon (C)	49.5	50.7	52.2	54.1
Hydrogen (H)	4.19	3.91	2.54	2.33
Nitrogen (N)	0.15	0.14	0.35	0.27
Sulfur (S)	1.02	0.96	0.64	0.66
Oxygen (O)	30.9	30.0	29.3	20.4
Ratio H/C	0.08	0.08	0.05	0.04
Ratio O/C	0.62	0.59	0.56	0.38
Ratio (O+N)/C	0.63	0.60	0.57	0.38

The low H/C values indicated that the biomass was carbonized, suggesting an increase of aromaticity as the torrefaction temperature increased. However, the biochar produced was not totally hydrophobic and aromatic, since the FTIR spectra showed the presence of bands corresponding to hydrophilic groups. This was also observed by Al-Wabel *et al.* (2013), who found

that the H/C ratio decreased using temperatures in the range from 200 to 800 °C. Hafshejani *et al.* (2016) compared a sample of in natura sugarcane bagasse with bagasse pyrolyzed at 300 °C and observed an increase from 0.3 to 4.1%.

3.5 Surface area

The results obtained for the BET surface area, pore total volume, and pore size of the biochars are presented in [Tab. 6](#).

The use of torrefaction temperatures from 260 to 290 °C, with heating rates of 10 °C min⁻¹ and short residence times (1 h), resulted in BET surface areas ranging from 1.83 to 3.24 m² g⁻¹. The small variation in the torrefaction temperature did not significantly alter the surface areas. The BG280C sample presented the highest values for the surface area and the pore volume. This biochar also showed the highest release of volatile materials, as shown by the proximate analysis.

[Sun et al. \(2018\)](#) pyrolyzed sugarcane bagasse at temperatures ranging from 300 to 600 °C, with a residence time of 2 h and heating rate of 5 °C min⁻¹, obtaining a surface area and total pore volume of 1.05 m² g⁻¹ and 0.68 cm³ g⁻¹, respectively, for the sample produced at 300 °C. In other work, peanut shells were used for biochar production, with specific surface areas of 1.83 and 7.11 m² g⁻¹ obtained at temperatures of 200 and 300 °C, respectively ([J. Chen et al., 2017](#); [W.-H. Chen et al., 2017](#)).

Table 6. BET surface areas, pore total volumes, and pore sizes of the biochars.

Sample	BET surface area (m ² g ⁻¹)	Pore total volume (cm ³ g ⁻¹)	Pore size (Å)
BG260C	1.83	5.1 x 10 ⁻³	112
BG270C	2.08	5.5 x 10 ⁻³	126
BG280C	3.24	6.2 x 10 ⁻³	108
BG290C	2.04	6.1 x 10 ⁻³	121

3.6 Determination of pH and pHPZC

The values obtained for the point of zero charge and pH are provided in [Tab. 7](#).

Table 7. pHPZC and pH values of the biochars.

Sample	pHPZC	pH
BG260C	4.61 ± 0.52	4.38 ± 0.08
BG270C	5.01 ± 0.73	4.43 ± 0.08
BG280C	5.64 ± 0.06	4.60 ± 0.03
BG290C	5.53 ± 0.56	4.58 ± 0.09

The pHPZC ranged from 4.61 to 5.53, while the pH ranged from 4.38 to 4.60. The solution pH was lower than the pHPZC, indicating that the sugarcane bagasse biochar presented a positive surface charge, related to an excess of H⁺ ions capable of adsorbing anionic species ([Binh and Nguyen, 2020](#)). These results were in agreement with the findings of

[Hafshejani et al. \(2016\)](#), which obtained a pHPZC of 5.35 for torrefied biochar produced from modified sugarcane bagasse.

As the torrefaction temperature increased, there was a small increase of the pH, which could be explained by the separation of alkaline salts from organic materials ([Al-Wabel et al., 2013](#); [Tag et al., 2016](#)). The alkalinity and carbonate content of biochars tend to increase as the temperature increases, while the contribution of organic anions to biochar alkalinity decreases ([Yuan et al., 2011](#)).

3.7 Adsorption kinetics

3.7.1 Selection of torrefaction temperature

The choice to prepare pellets by torrefaction was based on lower energy costs, in addition to the possibility of using renewable sources, such as solar energy ([Quéno et al., 2019](#)). In order to identify the best biochar torrefaction temperature, preliminary experiments were performed using 5.00 µg L⁻¹ CAF in aqueous solution. The CAF removal efficiencies are shown in [Tab. 8](#). CAF was selected since it is an important emerging contaminant, considered as a biomarker of anthropogenic contamination of wastewater and surface waters ([Buerge et al., 2003](#)).

The biochar samples showed similar behaviors, with removal efficiencies higher than 88% and attainment of equilibrium in approximately 10 h, with the exception of BG270C, for which equilibrium was reached after 24 h. After 24 h of the experiment, the BG260C pellets underwent disintegration, with the solution presenting a yellow color (data not shown). The BG270C and BG290C samples showed partial disintegration of some biochar pellets, but no color change of the solution. The BG280C sample presented the best stability in the aqueous medium, without disintegration or solution color change. Therefore, the BG280C sample was selected for use as an adsorbent, since it presented the best stability in solution and showed a CAF adsorption efficiency of 92.8% after 10 h, in comparison to the control.

Table 8. Removal efficiencies obtained for CAF at 5.00 µg L⁻¹ in aqueous solution, using the BG260C, BG270C, BG280C, and BG290C biochars.

t (h)	CAF removal efficiency (%)			
	Biochar sample			
	BG260C	BG270C	BG280C	BG290C
10	89.61	92.50	92.84	90.29
24	88.25	93.53	91.82	89.95

3.7.2 Adsorption of the pharmaceutical compounds on biochar pellets in lab-made sewage

The BG280C biochar was chosen as the adsorbent material. Contact time experiments were carried out for CAF, CIP, and NOR in three separate assays employing the lab-made sewage pH 8.0 (COD of 550 mg O₂ L⁻¹) simulating the composition of domestic sewage. Figure 5 presents the removal efficiencies obtained for these three compounds.

In this study the main objective was to remove the CAF, CIP and NOR using the biochar in complex samples, such as lab-made sewage which mimics the soluble components of domestic sewage and present pH equal to 8. Therefore, the pH tests were not carried out to investigate possible effects of this parameter in the removal process. All batch studies were performed at pH equal to 8.

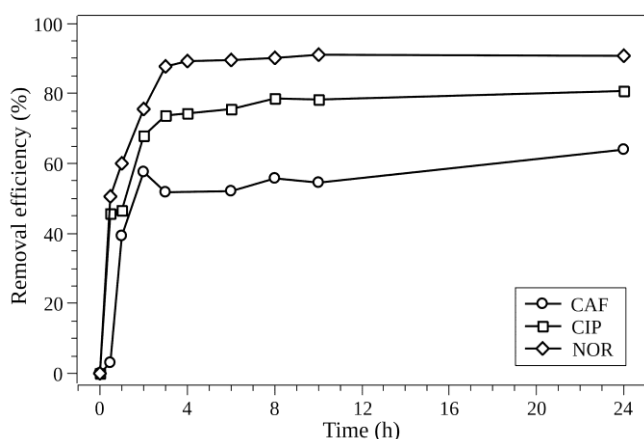


Figure 5. Removal efficiencies obtained for CAF at 5.00 µg L⁻¹, CIP at 10.0 µg L⁻¹, and NOR at 10.0 µg L⁻¹, using the BG280C biochar in lab-made sewage.

NOR and CIP presented similar adsorption behaviors, with removal efficiencies of 91.0 and 81.0%, respectively and attainment of equilibrium after around 4 and 8 h, respectively. This removal could be attributed to the positive charges present on the surface of the biochar pellets, which attracted the negative parts of the CIP and NOR molecules in the lab-made sewage with pH 8.0. These molecules exist in zwitterionic forms in solutions with pH from 6.0 to 8.8 (Osonwa *et al.*, 2017; Sun *et al.*, 2002).

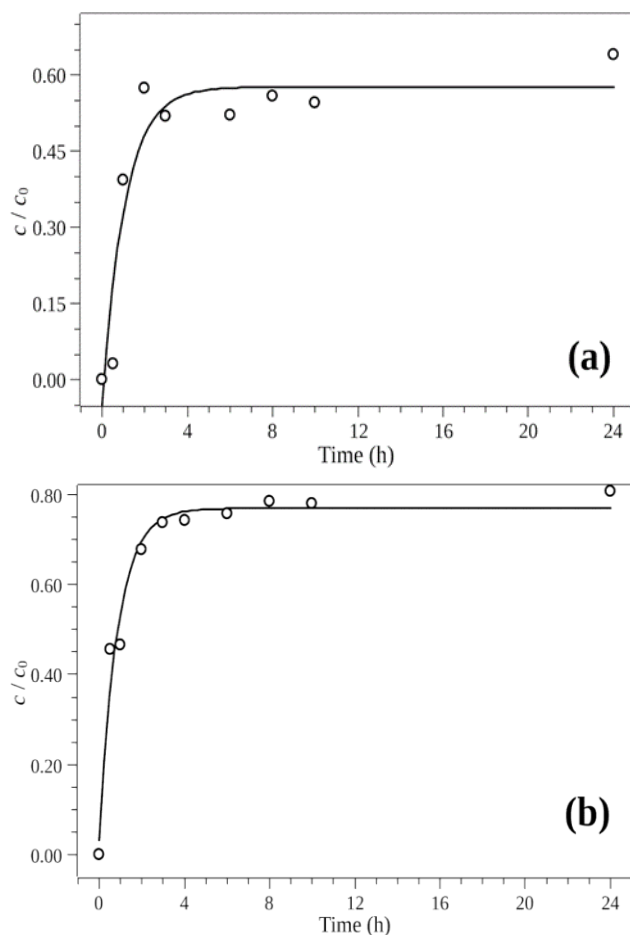
In the case of CAF, there was a decrease of the adsorption between 3 and 4 h, with equilibrium being reached after 6 h. A total of 58.0% of CAF was removed from the lab-made sewage, which was lower

than the value of 92.8% obtained in the earlier experiment using the compound in ultrapure water.

The observed difference in the CAF removal efficiency could be explained by the compositional complexity of the lab-made sewage, compared to ultrapure water. In particular, the presence of chloride ions and soybean oil can interfere in the adsorption efficiency.

As mentioned previously, the π - π interactions of the biochar with the aromatic rings of the compounds could have contributed to the adsorption. As indicated by the results of the FTIR and elemental composition analyses, the presence on BG280C of groups containing electronegative elements such as oxygen and nitrogen provided abundant sites for adsorption (Tran *et al.*, 2017).

The keyhole pore filling mechanism could have contributed to the adsorption of the compounds. CIP presents dimensions of 13.5 × 3 × 7.4 Å, so it (as well as CAF) could be adsorbed by this mechanism, since the dimensions of the molecules were smaller than those of the biochar pores (Ma *et al.*, 2017). Figure 6 shows the removal efficiencies obtained using the BG280C biochar in the lab-made sewage.



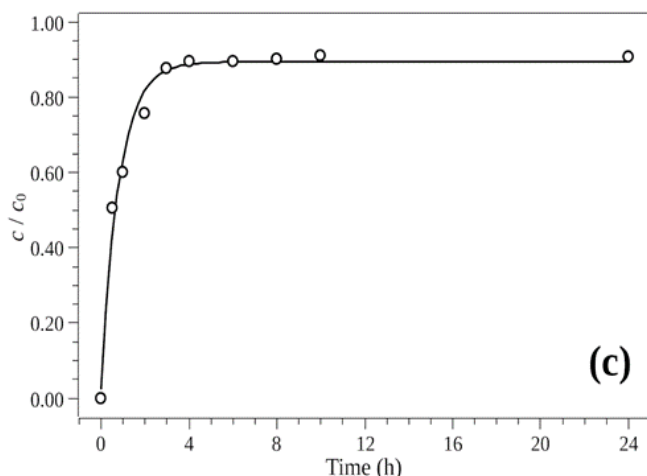


Figure 6. Removal efficiencies obtained for CAF at $5.00 \mu\text{g L}^{-1}$ (a), CIP at $10.0 \mu\text{g L}^{-1}$ (b), and NOR at $10.0 \mu\text{g L}^{-1}$ (c), using the BG280C biochar in lab-made sewage.

The compounds NOR, CAF, and CIP reached equilibrium after periods of 4, 6, and 8 h, respectively. As shown from the pH/pH_{PCZ} results, the sugarcane bagasse biochar samples had positive charges on their surfaces, due to the excess of H⁺ ions. Therefore, the adsorption of a cationic species such as CAF occurred due to other interaction mechanisms.

The presence of functional groups rich in oxygen on the adsorbent surface can contribute to the adsorption of contaminants. In addition, π - π interactions of electron donors and acceptors are important in removal by adsorption. The FTIR and elemental analyses of the biochars demonstrated the presence of carboxylic acids and nitrogenous groups. Therefore, π - π interactions could have contributed to the adsorption of CAF on the torrefied sugarcane bagasse. As reported previously, carboxylic acids and carbonyls tend to be electron acceptors in the formation of π - π interactions with aromatic molecules, contributing to CAF adsorption (Ahmed *et al.*, 2018; Keiluweit and Kleber, 2009).

The adsorption of CAF could also have been favored by the biochar pore size, which varied from 108 to 126 Å, since the caffeine molecule has dimensions of $7.8 \times 6.1 \times 2.1$ Å, enabling its penetration into the biochar pores (Pendolino, 2014). Correa-Navarro *et al.* (2020) produced a biochar from fique bagasse, using pyrolysis at 850 °C and a residence time of 3 h, which was used for the removal of caffeine and diclofenac.

4. Conclusions

In this paper, torrefaction was used as a carbonization strategy, as a way to prepare sugarcane bagasse biochar which presented a high performance in the adsorption of pharmaceutical compounds. Characterization of sugarcane bagasse biochar samples using thermogravimetric and proximate analyses demonstrated the presence of lignin and cellulose as the main constituents after the thermochemical conversion. The biochars could be considered mesoporous adsorbents, with irregular and positively charged surfaces. The FTIR spectra showed the presence of hydrophilic and hydrophobic groups. Samples of the BG260C, BG270C, BG280C, and BG290C biochars were evaluated for the adsorption of CAF in aqueous media. The BG280C material presented the best adsorption efficiency (up to 93%) and stability in the aqueous media. High adsorption efficiency was achieved even at low concentrations of contaminants (at the $\mu\text{g L}^{-1}$ concentration level) in a complex matrix such as lab-made sewage, where adsorptions of 91, 81, and 58% were achieved for NOR, CIP, and CAF, respectively. In addition, the low cost per ton (around US\$ 20.00) of the raw material provides to sugarcane bagasse biochar a promising adsorbent and economic alternative to be used as technology to mitigate the presence of emerging contaminants in wastewater treatment plants and water supply units.

Authors' contribution

Conceptualization: Fonsêca, M. C.; Lima Gomes, P. C. F.; Pires, L. O.; Ribeiro, C. A.

Data curation: Fonsêca, M. C.; Lima Gomes, P. C. F.

Formal Analysis: Fonsêca, M. C.; Marasco Júnior, C. A.; Lima Gomes, P. C. F.

Funding acquisition: Lima Gomes, P. C. F.

Investigation: Fonsêca, M. C.; Lima Gomes, P. C. F.; Dias, D. S.

Methodology: Lima Gomes, P. C. F.; Pires, L. O.; Ribeiro, C. A.

Project administration: Lima Gomes, P. C. F.

Resources: Lima Gomes, P. C. F.

Software: Fonsêca, M. C.; Lima Gomes, P. C. F.; Pires, L. O.

Supervision: Lima Gomes, P. C. F.; Pires, L. O.

Validation: da Silva, J. P.; Marasco Júnior, C. A.

Visualization: Lima Gomes, P. C. F.; Pires, L. O.; Lamarca, R. S.

Writing – original draft: Fonsêca, M. C.; Lima Gomes, P. C. F.; Pires, L. O.; Lamarca, R. S.

Writing – review & editing: Fonsêca, M. C.; Lima Gomes, P. C. F.; Pires, L. O.; Lamarca, R. S.; Ribeiro, C. A.

Data availability statement

The data are available in the UNESP repository. The data that support the findings of this study are available from the corresponding author, Paulo C. F. Lima Gomes, upon reasonable request.

Funding

Fundação de Amparo à Pesquisa do Estado de São Paulo (FAPESP). Grant No: 2016/03369-3; 2018/22393-8; 2018/11700-7.

INCT-DATREM. Grant No: 2014/50945-4.

Conselho Nacional de Desenvolvimento Científico e Tecnológico (CNPq). Grant No: 465571/2014-0.

Coordenação de Aperfeiçoamento de Pessoal de Nível Superior (CAPES). Grant No: 88887136426/2017/00.

Acknowledgments

The authors are grateful for the support provided by Institute of Chemistry (Araraquara, São Paulo State University).

References

Ahmed, M. B.; Zhou, J. L.; Ngo, H. H.; Johir, Md. A. H.; Sun, L.; Asadullah, M.; Belhaj, D. Sorption of hydrophobic organic contaminants on functionalized biochar: Protagonist role of π - π electron-donor-acceptor interactions and hydrogen bonds. *J. Hazard. Mater.* **2018**, *360*, 270–278. <https://doi.org/10.1016/j.jhazmat.2018.08.005>

Ahmedna, M.; Johns, M. M.; Clarke, S. J.; Marshall, W. E.; Rao, R. M. Potential of agricultural by-product-based activated carbons for use in raw sugar decolourisation. *J. Sci. Food Agric.* **1997**, *75* (1), 117–124. [https://doi.org/10.1002/\(SICI\)1097-0010\(199709\)75:1<117::AID-JSFA850>3.0.CO;2-M](https://doi.org/10.1002/(SICI)1097-0010(199709)75:1<117::AID-JSFA850>3.0.CO;2-M)

Al-Wabel, M. I.; Al-Omran, A.; El-Naggar, A. H.; Nadeem, M.; Usman, A. R. A. Pyrolysis temperature induced changes in characteristics and chemical composition of biochar produced from conocarpus wastes. *Bioresour. Technol.* **2013**, *131*, 374–379. <https://doi.org/10.1016/j.biortech.2012.12.165>

Anastopoulos, I.; Katsouromalli, A.; Pashalidis, I. Oxidized biochar obtained from pine needles as novel adsorbent to remove caffeine from aqueous solutions. *J. Mol. Liq.* **2020**, *304*, 112661. <https://doi.org/10.1016/j.molliq.2020.112661>

Becker, H.; Matos, R. F.; Souza, J. A.; Lima D. A.; Souza, T. C.; Longhinotti, E. Pseudo-stem banana fibers: Characterization and chromium removal. *Orbital: Electon. J. Chem.* **2013**, *5* (3), 164–170.

Binh, Q. A.; Nguyen, H.-H. Investigation the isotherm and kinetics of adsorption mechanism of herbicide 2,4-dichlorophenoxyacetic acid (2,4-D) on corn cob biochar. *Bioresour. Technol. Rep.* **2020**, *11*, 100520. <https://doi.org/10.1016/j.biteb.2020.100520>

Buehrle, D. J.; Wagener, M. M.; Clancy, C. J. Outpatient Fluoroquinolone Prescription Fills in the United States, 2014 to 2020: Assessing the Impact of Food and Drug Administration Safety Warnings. *Antimicrob. Agents Chemotherapy* **2021**, *65* (7), e00151-21. <https://doi.org/10.1128/AAC.00151-21>

Buerge, I. J.; Poiger, T.; Müller, M. D.; Buser, H.-R. Caffeine, an Anthropogenic Marker for Wastewater Contamination of Surface Waters. *Environ. Sci. Technol.* **2003**, *37* (4), 691–700. <https://doi.org/10.1021/es020125z>

Brazil. Ministry of Agriculture, Livestock and Supply. National Supply Company – CONAB. Acompanhamento da safra brasileira de cana-de-açúcar: v.7 - Safra 2020/21 n.4 - Quarto levantamento, 2021; pp 15. Available in: <http://www.conab.gov.br> (accessed 2021-07-04).

Chen, J.; Zhang, D.; Zhang, H.; Ghosh, S.; Pan, B. Fast and slow adsorption of carbamazepine on biochar as affected by carbon structure and mineral composition. *Sci. Total Environ.* **2017**, *579*, 598–605. <https://doi.org/10.1016/j.scitotenv.2016.11.052>

Chen, W.-H.; Hsu, H.-J.; Kumar, G.; Budzianowski, W. M.; Ong, H. C. Predictions of biochar production and torrefaction performance from sugarcane bagasse using interpolation and regression analysis. *Bioresour. Technol.* **2017**, *246*, 12–19. <https://doi.org/10.1016/j.biortech.2017.07.184>

Correa-Navarro, Y. M.; Giraldo, L.; Moreno-Piraján, J. C. Biochar from fique bagasse for remotion of caffeine and diclofenac from aqueous solution. *Molecules* **2020**, *25* (8), 1849. <https://doi.org/10.3390/molecules25081849>

Dias, D. S.; Crespi, M. S.; Torquato, L. D. M.; Kobelnik, M.; Ribeiro, C. A. Torrefied banana tree fiber pellets having embedded urea for agricultural use. *J. Therm. Anal. Calorim.* **2018**, *131*, 705–712. <https://doi.org/10.1007/s10973-016-6049-7>

Granados, D. A.; Ruiz, R. A.; Vega, L. Y.; Chejne, F. Study of reactivity reduction in sugarcane bagasse as consequence

- of a torrefaction process. *Energy* **2017**, *139*, 818–827. <https://doi.org/10.1016/j.energy.2017.08.013>
- Hafshejani, L. D.; Hooshmand, A.; Naseri, A. A.; Mohammadi, A. S.; Abbasi, F.; Bhatnagar, A. Removal of nitrate from aqueous solution by modified sugarcane bagasse biochar. *Ecol. Eng.* **2016**, *95*, 101–111. <https://doi.org/10.1016/j.ecoleng.2016.06.035>
- Huang, W.; Chen, J.; Zhang, J. Removal of ciprofloxacin from aqueous solution by rabbit manure biochar. *Environ. Technol.* **2020**, *41* (11), 1380–1390. <https://doi.org/10.1080/09593330.2018.1535628>
- Ibrahim, R. H. H.; Darvell, L. I.; Jones, J. M.; Williams, A. Physicochemical characterization of torrefied biomass. *J. Anal. Appl. Pyrolysis* **2013**, *103*, 21–30. <https://doi.org/10.1016/j.jaap.2012.10.004>
- International Biochar Initiative. *Standardized Product Definition and Product Testing Guidelines for Biochar That Is Used in Soil* 2.1, 2015; 61. https://www.biochar-international.org/wp-content/uploads/2018/04/IBI_Biochar_Standards_V2.1_Final.pdf (accessed 2022-03-23).
- Inyang, M.; Dickenson, E. The potential role of biochar in the removal of organic and microbial contaminants from potable and reuse water: A review. *Chemosphere* **2015**, *134*, 232–240. <https://doi.org/10.1016/j.chemosphere.2015.03.072>
- Jayaraman, K.; Gokalp, I.; Petrus, S.; Belandria, V.; Bostyn, S. Energy recovery analysis from sugar cane bagasse pyrolysis and gasification using thermogravimetry, mass spectrometry and kinetic models. *J. Anal. Appl. Pyrolysis* **2018**, *132*, 225–236. <https://doi.org/10.1016/j.jaap.2018.02.003>
- Keiluweit, M.; Kleber, M. Molecular-Level Interactions in Soils and Sediments: The Role of Aromatic π -Systems. *Environ. Sci. Technol.* **2009**, *43* (10), 3421–3429. <https://doi.org/10.1021/es8033044>
- Li, L.; Yang, M.; Lu, Q.; Zhu, W.; Ma, H.; Dai, L. Oxygen-rich biochar from torrefaction: A versatile adsorbent for water pollution control. *Bioresour. Technol.* **2019**, *294*, 122142. <https://doi.org/10.1016/j.biortech.2019.122142>
- Li, Z.; Wang, Z.; Wu, X.; Li, M.; Liu, X. Competitive adsorption of tylosin, sulfamethoxazole and Cu(II) on nano-hydroxyapatitemodified biochar in water. *Chemosphere* **2020**, *240*, 124884. <https://doi.org/10.1016/j.chemosphere.2019.124884>
- Liang, L.; Xi, F.; Tan, W.; Meng, X.; Hu, B.; Wang, X. Review of organic and inorganic pollutants removal by biochar and biochar-based composites. *Biochar* **2021**, *3*, 255–281. <https://doi.org/10.1007/s42773-021-00101-6>
- Liu, X.; Liao, J.; Song, H.; Yang, Y.; Guan, C.; Zhang, Z. A Biochar-Based Route for Environmentally Friendly Controlled Release of Nitrogen: Urea-Loaded Biochar and Bentonite Composite. *Sci. Rep.* **2019**, *9*, 9548. <https://doi.org/10.1038/s41598-019-46065-3>
- Ma, S.; Si, Y.; Wang, F.; Su, L.; Xia, C.; Yao, J.; Chen, H.; Liu, X. Interaction processes of ciprofloxacin with graphene oxide and reduced graphene oxide in the presence of montmorillonite in simulated gastrointestinal fluids. *Sci. Rep.* **2017**, *7*, 2588. <https://doi.org/10.1038/s41598-017-02620-4>
- Marasco Júnior, C. A.; Luchiari, N. C.; Lima Gomes, P. C. F. Occurrence of caffeine in wastewater and sewage and applied techniques for analysis: a review. *Eclética Quím. J.* **2019**, *44* (4), 11–26. <https://doi.org/10.26850/1678-4618eqj.v44.4.2019.p11-26>
- Marasco Júnior, C. A.; Silva, B. F.; Lamarca, R. S.; Lima Gomes, P. C. F. Automated method to determine pharmaceutical compounds in wastewater using on-line solid-phase extraction coupled to LC-MS/MS. *Anal. Bional. Chem.* **2021**, *413*, 5147–5160. <https://doi.org/10.1007/s00216-021-03481-7>
- Mohanty, S. K.; Valenca, R.; Berger, A. W.; Yu, I. K. M.; Xiong, X.; Saunders, T. M.; Tsang, D. C. W. Plenty of room for carbon on the ground: Potential applications of biochar for stormwater treatment. *Sci. Total Environ.* **2018**, *625*, 1644–1658. <https://doi.org/10.1016/j.scitotenv.2018.01.037>
- Morais, L. C.; Maia, A. A. D.; Guandique, M. E. G.; Rosa, A. H. Pyrolysis and combustion of sugarcane bagasse. *J. Therm. Anal. Calorim.* **2017**, *129*, 1813–1822. <https://doi.org/10.1007/s10973-017-6329-x>
- Mubarik, S.; Saeed, A.; Athar, M. M.; Iqbal, M. Characterization and mechanism of the adsorptive removal of 2,4,6-trichlorophenol by biochar prepared from sugarcane bagasse. *J. Ind. Eng. Chem.* **2015**, *33*, 115–121. <https://doi.org/10.1016/j.jiec.2015.09.029>
- Oliveira, F. R.; Patel, A. K.; Jaisi, D. P.; Adhikari, S.; Lu, H.; Khanal, S. K. Environmental application of biochar: Current status and perspectives. *Bioresour. Technol.* **2017**, *246*, 110–122. <https://doi.org/10.1016/j.biortech.2017.08.122>
- Osińska, A.; Harnisz, M.; Korzeniewska, E. Prevalence of plasmid-mediated multidrug resistance determinants in fluoroquinolone-resistant bacteria isolated from sewage and surface water. *Environ. Sci. Pollut. Res.* **2016**, *23*, 10818–10831. <https://doi.org/10.1007/s11356-016-6221-4>
- Osonwa, U. E.; Ugochukwu, J. I.; Ajaegbu, E. E.; Chukwu, K. I.; Azevedo, R. B.; Esimone, C. O. Enhancement of antibacterial activity of ciprofloxacin hydrochloride by complexation with sodium cholate. *Bull. Fac. Pharm. Cairo Univ.* **2017**, *55* (2), 233–237. <https://doi.org/10.1016/j.bfopcu.2017.09.006>

- Pendolino, F. Self-assembly of molecules on nanostructured graphene. Ph.D. Dissertation, Universidad Autónoma de Madrid, Madrid, Spain, 2014.
- Quéno, L. R. M.; Souza, A. N.; Costa, A. F.; Valle, A. T.; Joaquim, M. S. Aspectos técnicos da produção de *pellets* de madeira. *Ciênc. Florest.* **2019**, *29* (3), 1478–1489. <https://doi.org/10.5902/1980509820606>
- Ramos, S. N. C.; Xavier, A. L. P.; Teodoro, F. S.; Gil, L. F.; Gurgel, L. V. A. Removal of cobalt(II), copper(II), and nickel(II) ions from aqueous solutions using phthalate-functionalized sugarcane bagasse: Mono- and multicomponent adsorption in batch mode. *Ind. Crops Prod.* **2016**, *79*, 116–130. <https://doi.org/10.1016/j.indcrop.2015.10.035>
- Rangabhashiyam, S.; Balasubramanian, P. The potential of lignocellulosic biomass precursors for biochar production: Performance, mechanism and wastewater application—A review. *Ind. Crops Prod.* **2019**, *128*, 405–423. <https://doi.org/10.1016/j.indcrop.2018.11.041>
- Regalbuto, J. R.; Robles, J. O. The engineering of Pt/Carbon catalyst preparation: for application on Proton Exchange Fuel Cell Membrane (PEFCM). Progress Report, University of Illinois, Chicago, USA, 2004. https://amrel.bioe.uic.edu/NSFREU2004/Reports2004/Jaime%20Robles_Final%20Report.pdf (accessed 2022-03-23)
- Rodríguez-Díaz, J. M.; García, J. O. P.; Sánchez, L. R. B.; Silva, M. G. C.; Silva, V. L.; Arteaga-Pérez, L. E. Comprehensive Characterization of Sugarcane Bagasse Ash for Its Use as an Adsorbent. *BioEnergy Res.* **2015**, *8*, 1885–1895. <https://doi.org/10.1007/s12155-015-9646-6>
- SciFinder – ACS Solutions. Available in: <https://scifinder.cas.org> (accessed 2021-06-18).
- Sun, J.; Sakai, S.; Tauchi, Y.; Deguchi, Y.; Chen, J.; Zhang, R.; Morimoto, K. Determination of lipophilicity of two quinolone antibacterials, ciprofloxacin and grepafloxacin, in the protonation equilibrium. *Eur. J. Pharm. Biopharm.* **2002**, *54* (1), 51–58. [https://doi.org/10.1016/S0939-6411\(02\)00018-8](https://doi.org/10.1016/S0939-6411(02)00018-8)
- Sun, L.; Chen, D.; Wan, S.; Yu, Z. Adsorption studies of dimetridazole and metronidazole onto biochar derived from sugarcane bagasse: Kinetic, equilibrium, and mechanisms. *J. Polym. Environ.* **2018**, *26*, 765–777. <https://doi.org/10.1007/s10924-017-0986-5>
- Tag, A. T.; Duman, G.; Uçar, S.; Yanik, J. Effects of feedstock type and pyrolysis temperature on potential applications of biochar. *J. Anal. Appl. Pyrolysis.* **2016**, *120*, 200–206. <https://doi.org/10.1016/j.jaap.2016.05.006>
- Tan, X.; Liu, Y.; Zeng, G.; Wang, X.; Hu, X.; Gu, Y.; Yang, Z. Application of biochar for the removal of pollutants from aqueous solutions. *Chemosphere* **2015**, *125*, 70–85. <https://doi.org/10.1016/j.chemosphere.2014.12.058>
- Torquato, L. D. M.; Crnkovic, P. M.; Ribeiro, C. A.; Crespi, M. S. New approach for proximate analysis by thermogravimetry using CO₂ atmosphere: Validation and application to different biomasses. *J. Therm. Anal. Calorim.* **2017**, *128*, 1–14. <https://doi.org/10.1007/s10973-016-5882-z>
- Tran, H. N.; You, S.-J.; Hosseini-Bandegharai, A.; Chao, H.-P. Mistakes and inconsistencies regarding adsorption of contaminants from aqueous solutions: A critical review. *Water Res.* **2017**, *120*, 88–116. <https://doi.org/10.1016/j.watres.2017.04.014>
- Tumuluru, J. S.; Sokhansanj, S.; Hess, J. R.; Wright, C. T.; Boardman, R. D. A review on biomass torrefaction process and product properties for energy applications. *Ind. Biotechnol.* **2011**, *7* (5), 384–401. <https://doi.org/10.1089/ind.2011.7.384>
- Wang, B.; Jiang, Y.; Li, F.; Yang, D. Preparation of biochar by simultaneous carbonization, magnetization and activation for norfloxacin removal in water. *Bioresour. Technol.* **2017**, *233*, 159–165. <https://doi.org/10.1016/j.biortech.2017.02.103>
- Yi, K.; Wang, D.; QiYang, Li, X.; Chen, H.; Sun, J.; An, H.; Wang, L.; Deng, Y.; Liu, J.; Zeng, G. Effect of ciprofloxacin on biological nitrogen and phosphorus removal from wastewater. *Sci. Total Environ.* **2017**, *605–606*, 368–375. <https://doi.org/10.1016/j.scitotenv.2017.06.215>
- Yuan, J.-H.; Xu, R.-K.; Zhan, H. The forms of alkalis in the biochar produced from crop residues at different temperatures. *Bioresour. Technol.* **2011**, *102* (3), 3488–3497. <https://doi.org/10.1016/j.biortech.2010.11.018>

Ni-Nb-Zr metastable phases formation, a thermodynamic and chemical approach

Leonardo Pratavieira Deo¹⁺ 

1. Federal University of Lavras, Engineering Department, Lavras, Brazil.

+Corresponding author: Leonardo Pratavieira Deo, Phone: +55 (35) 3829-1860, Email address: leonardo.deo@ufla.br

ARTICLE INFO

Article history:

Received: October 22, 2021

Accepted: February 10, 2022

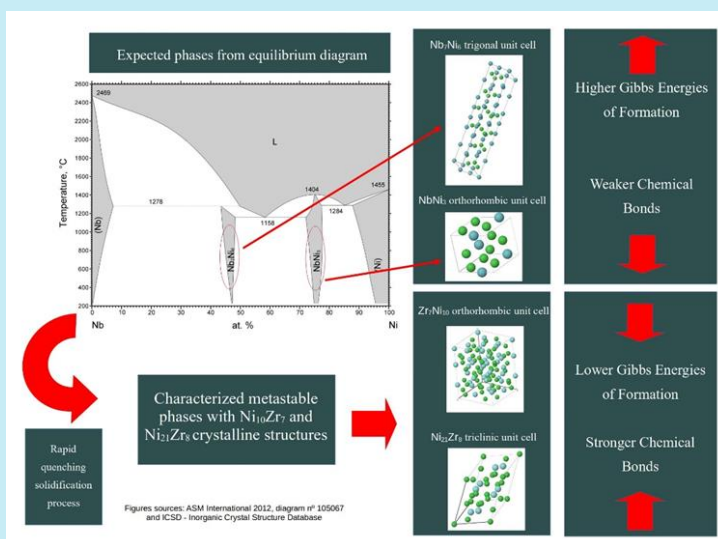
Published: April 01, 2022

Section Editor: Assis Vicente Benedetti

Keywords:

1. Ni-Nb-Zr alloy
2. no equilibrium phases
3. remnant stability

ABSTRACT: Gibbs' free energy of formation is considered a good guidance in order to describe or predict the phases formation within the standard state; however, many materials are produced out of their equilibrium conditions, and consequently, metastable phases are formed. There is no universal knowledge related to metastable phases formation; therefore, this paper presents considerations in order to elucidate some understanding about two metastable phases found in a rapid quenched alloy from Ni-Nb-Zr system during the solidification process. The analyzed alloy, namely Ni_{61.6}Nb_{33.1}Zr_{5.3} (at.%) was previously synthesized and characterized in two previous works. The hypotheses presented here consider free energies of formation among phases which compete to nucleate, stability of crystalline phases at nanoscale and atomic pair preferences during the nucleation. The understanding related to metastable phases formation may produce and improve promising technological materials.



1. Introduction

Since the formulation of materials thermodynamics by Josiah Willard Gibbs in 1878 (Gibbs, 1878), one of the biggest paradigms in materials science and engineering has been the understanding about metastable materials and their phases (Sun *et al.*, 2016). According to Gibbs' theory, the constituent phases of materials have Gibbs free energy of formation (ΔfG°) values, which describes the quantity of energy necessary when a phase is formed from its constituent elements in their standard state. With changes in chemical composition, temperature and pressure, the ΔfG° of a phase varies and the most stable position is that one with the lowest value. The Gibbs free energy of formation also depends on other thermodynamics parameters, such as enthalpy and entropy of formation (Olivotos and Economou-Eliopoulos, 2016).

In contrast with stable phases, which are well described by Gibbs free energy of formation, in some especial manufacturing cases, metastable phases can be formed and they do not present the lowest free energy values. In other words, the metastable phases kinetically trap the stable phases with lower free energy values within the equilibrium state (Sun *et al.*, 2016). For numerous alloys, metastable phases can exhibit superior properties than their corresponding stable phases; examples can be found for metallic glasses, high entropy alloys and quenched steels (Hidalgo *et al.*, 2019; Kube and Schroers, 2020; Li *et al.*, 2016). Some mechanical properties of these alloys are their superior strength and hardness, excellent

corrosion and wear resistance, as well as their general inability to undergo homogeneous plastic deformation (Trexler and Thadhani, 2010).

In this context, the present work presents a thermodynamics explanation about the crystallization of two metastable phases that developed in a rapid quenched alloy, namely $Ni_{61.6}Nb_{33.1}Zr_{5.3}$ (at.%), produced and characterized in previous works (Deo and Oliveira, 2014; 2017). According to the *liquidus* projection diagram of the Nb–Ni–Zr system calculated by Tokunaga *et al.* (2007), the expected equilibrium solidification crystalline phases for the analyzed alloy are the $NbNi_3$ and Nb_7Ni_6 , both with some minor zirconium solubility; however, the previous characterization indicated a different crystallization behavior with non-equilibrium crystalline structures. The found structures were the same of the equilibrium $Ni_{10}Zr_7$ and $Ni_{21}Zr_8$ phases, in addition, with a large solubility of niobium in both structures, around 40 and 25 at.%, respectively (Deo and Oliveira, 2017).

In order to obtain some understanding about the non-equilibrium behavior of the analyzed alloy, some approach of the Gibbs energy of formation for each above-mentioned phase were calculated. The thermodynamic functions of formation expressed by Eqs. 1 and 2 for the Ni–Zr system were determined through reduction reactions examined with a Knudsen-cell mass spectrometer (Zaitsev *et al.*, 2002). Equations 3 and 4 were performed on the basis of the calculation of phase diagrams (CALPHAD) method for the Nb–Ni system (Tokunaga *et al.*, 2007). The Gibbs energy of formation of each phase per mole of formula unit are expressed by:

$$\Delta fG(Ni_{21}Zr_8) = -47028 + 5.99T, 1201 \leq T \leq 1438K \quad (1)$$

$$\Delta fG(Ni_{10}Zr_7) = -50075 + 5.16T, 1058 \leq T \leq 1339K \quad (2)$$

$$\Delta fG(NbNi_3) = -35300.6 + 4.83322T, 298 \leq T \leq 6000K \quad (3)$$

$$\Delta fG(Nb_6Ni_7) = -22770 + 0.305T, 298 \leq T \leq 6000K \quad (4)$$

Gibbs free energies of formation are relative values, not absolute, therefore this thermodynamic parameter allows to compare energies of different phases and only the individual values do not have physical significance. In addition, with the free energies of formation values, considerations were done about the stability of crystalline phases at nanoscale, as well as the atomic pair preferences during the nucleation. Therefore, the present paper presents some understanding about two metastable phases, which can be formed in the Ni–Nb–Zr system under a rapid

solidification condition. The literature presents a lack of fundamental understanding related to metastable phases formation, even that metastable phases may yield promising new technological materials (Sun *et al.*, 2016).

2. Alloy confection and characterization and Gibbs energies of formation calculation

A rapid quenched wedge shape sample with maximum amorphous thickness of 3 mm was produced

by injection casting according to a procedure described in the previous work (Deo and Oliveira, 2014). The estimated cooling rate during the solidification process was around 250 K s^{-1} , therefore out of the equilibrium condition. In addition to the amorphous phase and metastable crystalline phases previously mentioned, the analyzed alloy shown the presence of unknown crystalline compounds not indexed by X-ray diffraction technique.

From transmission electron microscopy (TEM), the metastable phases present in the alloy microstructure were characterized by selected area electron diffraction (SAED), bright field (BF) images and energy dispersive X-ray (EDS) analysis. A transmission electron microscope with a tungsten source and an acceleration voltage of 120 kV coupled with an EDS detector was used to operate the TEM analysis. In addition, the X-ray diffraction (XRD) analysis was used as a complementary technique in order to confirm the phases previously identified by TEM. The diffraction analysis was carried out in a diffractometer with Cu $K\alpha$ (1.5418 \AA) radiation and the 2-theta varying from 20 to 70° .

In order to calculate the Gibbs energies of formation relative to each phase as presented by Eqs. 1–4, from

another previous work (Deo and Oliveira, 2014), a differential scanning calorimetry (DSC) curve data was used to estimate the solidification temperature (1393 K) of the analyzed alloy. This DSC data is relative to an alloy chemical composition close to that analyzed in this paper. During the DSC experiment, the sample with weight around 40 mg was heated at a rate of 20 K min^{-1} from room temperature up to $1400 \text{ }^\circ\text{C}$. DSC experiments are typically used to determine the characteristic temperatures of phase transformations, such as the solidification temperature. All detailed steps of sample characterization are described in previous works (Deo and Oliveira, 2014; 2017).

3. Thermodynamic hypothesis for metastable formation

The Gibbs energies of formation were calculated according to Eqs. 1–4 for the $\text{Ni}_{21}\text{Zr}_8$, $\text{Ni}_{10}\text{Zr}_7$, NbNi_3 and Nb_7Ni_6 phases, respectively, in the solidification temperature, 1393 K . Structural formulas, crystal systems and Gibbs energies values associated to each phase are shown in Tab. 1.

Table 1. Chemical, crystallographic and calculated thermodynamic parameters of phases.

Phase structural formula	Crystal system	Gibbs energy of formation calculated from solidification temperature (kJ mol^{-1})
$\text{Ni}_{21}\text{Zr}_8$ (Okamoto, 2007)	Triclinic (Joubert <i>et al.</i> , 1998)	-38.683
$\text{Ni}_{10}\text{Zr}_7$ (Okamoto, 2007)	Orthorhombic (Joubert <i>et al.</i> , 1997)	-42.887
NbNi_3 (Tokunaga <i>et al.</i> , 2007)	Orthorhombic (Fang <i>et al.</i> , 1992)	-28.567
Nb_7Ni_6 (Tokunaga <i>et al.</i> , 2007)	Trigonal (P. Nash and A. Nash, 1986)	-22.345

The Gibbs energy of formation values presented in Tab. 1 clearly show that $\text{Ni}_{21}\text{Zr}_8$ and $\text{Ni}_{10}\text{Zr}_7$ crystalline phases are thermodynamically preferred to be formed in the analyzed alloy when compared to NbNi_3 and Nb_7Ni_6 crystalline phases, once the first phases present lower values of Gibbs energy of formation. However, in contrast with this expectation, as reported by Matsumoto *et al.* (2005) in their calculated *liquidus* projection diagram of the Nb–Ni–Zr system, the NbNi_3 and Nb_7Ni_6 phases should be expected in the analyzed alloy, under equilibrium conditions during the solidification process.

The solidification always starts from a high-energy precursor, i.e., liquid phase, and there has not been a clear and detailed understanding of the effects causing the formation of the metastable structures from the viewpoint of thermodynamics, neither clear insight related to chemical and physical origins in order to lead to a tendency of metastable phases formation (C. Wang

and Yang, 2005). Here, how surface energies and chemical composition may be related to the stabilization of metastable phases with $\text{Ni}_{21}\text{Zr}_8$ and $\text{Ni}_{10}\text{Zr}_7$ crystalline structures in the analyzed alloy is discussed.

First, the discussion is grouped around the influence of surface energies in order to form metastable phases. Before becoming a bulk crystalline material, all crystals first nucleate and grow in the nanoscale, where the contribution of surface energy is very significant. Small spherical crystalline particles with sizes larger or equal than $1/R$ (where R is the radius) can stabilize metastable crystalline polymorphic phases with low surface energies. Indeed, calorimetry experiments have demonstrated that metastable polymorphs can be stabilized at the nanoscale if they have lower surface energy than the stable phase (Navrotsky, 2004; 2011). These metastable phases can have the preferential nucleation instead of the equilibrium phases, once they

are thermodynamically stable at nanoscale because their lower surface energy can surpass the steady-state nucleation rate of the stable phase and consequently they have a lower nucleation barrier. This steady-state nucleation rate depends exponentially on this nucleation barrier, so minor differences in surface energy between polymorphs can correspond to orders of magnitude differences in nucleation rates, which can potentially result in bulk metastability (Sun *et al.*, 2015).

Thus, under the announced solidification experimental conditions in the analyzed alloy, the hypothesis is that, at nanoscale, the structures $\text{Ni}_{10}\text{Zr}_7$ and $\text{Ni}_{21}\text{Zr}_8$ from crystal systems orthorhombic and triclinic, respectively, must present lower nucleation barriers or surface energies than NbNi_3 and Nb_7Ni_6 structures from crystal systems orthorhombic and trigonal, respectively. In addition, with nucleation barrier concept, the stabilization of metastable phases also is intimately related to structure selection during nucleation (Sun *et al.*, 2015); however, the absolute values of these intermetallic compounds surface energies is not reported in literature yet. In a complementary way, the lower nucleation barrier concept associated to the metastable phases with structures $\text{Ni}_{10}\text{Zr}_7$ and $\text{Ni}_{21}\text{Zr}_8$ found in the analyzed alloy can be considered a remnant thermodynamic stability as evidenced by the Gibbs energy of formation values presented in Tab. 1.

The solidification always starts from the liquid, i.e., a supersaturated solution and metastable phases may nucleate with the lowest free energy at small sizes and low surface energies. After nucleation, the metastable nuclei may reduce their free energy by crystal growth, consuming the solute elements from liquid by atomic diffusion, in this case the niobium atoms, in order to form metastable solid solutions in $\text{Ni}_{10}\text{Zr}_7$ and $\text{Ni}_{21}\text{Zr}_8$ crystalline structures. As reported in a previous work (Deo and Oliveira, 2017), the niobium atomic radius is around 7% smaller than zirconium atomic radius, as well as; the mixing enthalpy for the Nb–Zr atomic pair has a positive value (4 kJ mol⁻¹). In this way, the Hume-Rothery rules provide some support for the solid solution formation. When the component atomic-size differences are less than 15%, in addition to positive or small negative values of enthalpy of mixing between elements, the formation of a substitutional solid solution is more feasible (Zhang *et al.*, 2008). This previous work also shows other experimental evidences about solid solution formations, such as EDS chemical compositions, peak shift in the XRD patterns and decrease in unit cell volumes and lattice parameters calculated from TEM data (Deo and

Oliveira, 2017). Once the barrier to crystal growth is smaller than the barrier to nucleation of a new phase, the metastable phases may grow to a stabilized size. At this point, there is a thermodynamic driving force for a phase transformation from metastable to stable phases; however, the rapid quenching during the solidification process suppressed this transformation (Chen *et al.*, 2018). Thus, under thermodynamic equilibrium, it should be expected the formation of NbNi_3 and Nb_7Ni_6 crystalline phases with minor solid solubility of zirconium; however, due to the solidification condition, the metastable phases with $\text{Ni}_{10}\text{Zr}_7$ and $\text{Ni}_{21}\text{Zr}_8$ crystalline structures and large solubility of niobium were found.

4. Chemical hypothesis for metastable formation

Another complementary point of view about metastable phases formation is concerned to alloy chemical composition. The analyzed alloy has a higher amount of niobium than zirconium; however, the crystallized phases presented the crystalline structures like $\text{Ni}_{10}\text{Zr}_7$ and $\text{Ni}_{21}\text{Zr}_8$. This hypothesis about these unexpected crystalline structures is related to the larger negative value of mixing enthalpy between Ni–Zr and Ni–Nb atomic pairs than it is between Nb–Zr atomic pair. The mixing enthalpies for these atomic pairs are -49 (Ni–Zr), -30 (Ni–Nb) and 4 (Nb–Zr) kJ mol⁻¹ (Yamaura *et al.*, 2005). When nucleation starts from the liquid, despite the large amount of niobium, the atomic pair Ni–Zr is preferred, conducting to $\text{Ni}_{10}\text{Zr}_7$ and $\text{Ni}_{21}\text{Zr}_8$ formation instead of NbNi_3 and Nb_7Ni_6 .

According to J. Wang *et al.* (2021), the mixing enthalpy can be approximately the cohesive energy when the samples are exposed to an oscillation of external pressure during the solidification process. In addition, Sun *et al.* (2016) affirm that when the average cohesive energy for a given chemistry is stronger, greater is the possibility for crystalline metastability. In other words, when cohesive energy and consequently chemical bonds are stronger, it is possible to stabilize higher-energy atomic arrangements, allowing thermodynamically that metastable compounds resist the transformations to equilibrium states.

In addition, a liquid below solidus temperature is considered to be in a metastable/unstable equilibrium, and the strongest attractive interactions between specific atomic pairs are preferred in order to make up short-range order domains (as quenched-in embryos) (Fan *et al.*, 2000). If nucleation is suppressed, the amorphous phase may be formed; however, if cooling

rate during the solidification process is not high enough to lead to the glassy phase, metastable crystalline phases with the strongest attractive interactions between specific atomic pairs can be nucleated and after growing up in the material, as evidenced in the analyzed alloy in a previous work (Deo and Oliveira, 2017).

4. Conclusions

The discussion above presents two complementary hypotheses in order to understand the reasons why two metastable phases were formed in an alloy from Ni–Nb–Zr system during a rapid quenching solidification process instead of the thermodynamic equilibrium phases. The first hypothesis is concerned about the stability of Ni₁₀Zr₇ and Ni₂₁Zr₈ crystalline phases at nanoscale, once they must present lower surface energies than other polymorphs, so these crystalline phases have a lower nucleation barrier. Metastable phases may present the nucleation rates with orders of magnitude higher than stable phases due their lower surface energies, conducting to bulk metastability, as observed in the analyzed alloy. In addition, the barrier to crystal growth is smaller than the barrier to nucleation, so the metastable solid solutions with large amount of niobium in Ni₁₀Zr₇ and Ni₂₁Zr₈ crystalline structures might grow to a stabilized size. The presence of these reported phases is in good agreement with Gibbs energy of formation values, once these phases presented lower values compared to that presented to the expected phases according to the *liquidus* projection diagram. The second hypothesis is related to stabilization of atomic arrangements due the highest bonding energy between their constituent elements, i.e., during crystalline phases nucleation, the atomic pair Ni–Zr was preferred, despite the large amount of niobium in the alloy composition, leading to Ni₁₀Zr₇ and Ni₂₁Zr₈ structures formation.

From the viewpoint of thermodynamics, there is no universal understanding why some metastable phases can be nucleated and grown; however, in this present analysis, the metastable nucleation happens under instantaneous local thermodynamic conditions (nuclei with low surface energies and low Gibbs energy of formation) and the growth happens through the reduction of free energy related to the phase transformation in the solidification process. Therefore, it is possible to suppose that metastability can be considered as a “kind of remnant stability”, so if the remnant stability can be understood, the metastability also can be better understood as well. In addition, the metastable nucleation can also be associated with

atomic chemical preferences in order to make preferential bonds in a system with several elements.

Authors' contribution

Conceptualization: Deo, L. P.
Data curation: Deo, L. P.
Formal Analysis: Deo, L. P.
Funding acquisition: Not applicable.
Investigation: Deo, L. P.
Methodology: Deo, L. P.
Project administration: Deo, L. P.
Resources: Deo, L. P.
Software: Not applicable.
Supervision: Deo, L. P.
Validation: Deo, L. P.
Visualization: Deo, L. P.
Writing – original draft: Deo, L. P.
Writing – review & editing: Deo, L. P.

Data availability statement

Data sharing is not applicable.

Funding

Not applicable.

Acknowledgments

Not applicable.

References

- Chen, B.-R.; Sun, W.; Kitchaev, D. A.; Mangum, J. S.; Thampy, V.; Garten, L. M.; Ginley, D. S.; Gorman, B. P.; Stone, K. H.; Ceder, G.; Toney, M. F.; Schelhas, L. T. Understanding crystallization pathways leading to manganese oxide polymorph formation. *Nat. Commun.* **2018**, *9*, 2553. <https://doi.org/10.1038/s41467-018-04917-y>
- Deo, L. P.; Oliveira, M. F. Accuracy of a selection criterion for glass forming ability in the Ni–Nb–Zr system. *J. Alloys. Compd.* **2014**, *615* (Suppl. 1), S23–S28. <https://doi.org/10.1016/J.JALLCOM.2013.11.194>
- Deo, L. P.; Oliveira, M. F. Metastable Phases Found in the Ni–Nb–Zr System. *Mater. Charact.* **2017**, *127*, 60–63. <https://doi.org/10.1016/j.matchar.2017.03.001>
- Fan, C.; Li, C.; Inoue, A. Nanocrystal composites in Zr–Nb–Cu–Al metallic glasses. *J. Non-Cryst. Solids.* **2000**, *270* (1–3), 28–33. [https://doi.org/10.1016/S0022-3093\(00\)00078-8](https://doi.org/10.1016/S0022-3093(00)00078-8)

- Fang, T.; Kennedy, S. J.; Quan, L.; Hicks, T. J. The structure and paramagnetism of Ni₃Nb. *J. Phys. Condens. Matter.* **1992**, *4*, 2405. <https://doi.org/10.1088/0953-8984/4/10/007>
- Gibbs, J. W. On the Equilibrium of Heterogeneous Substances. *Am. J. Sci.* **1878**, *96*, 3. <https://doi.org/10.11588/heidok.00013220>
- Hidalgo, J.; Huizenga, R. M.; Findley, K. O.; Santofimia, M. J. Interplay between metastable phases controls strength and ductility in steels. *Mat Sci Eng A.* **2019**, *745*, 185–194. <https://doi.org/10.1016/J.MSEA.2018.12.096>
- Joubert, J.-M.; Černý, R.; Yvon, K.; Lacroche, M.; Percheron-Guégan, A. Zirconium-Nickel, Zr₇Ni₁₀: Space Group Revision for the Stoichiometric Phase. *Acta Crystallogr C.* **1997**, *C53*, 1536–1538. <https://doi.org/10.1107/S0108270197007142>
- Joubert, J.-M.; R. Černý; Yvon, K.; Lacroche, M.; Percheron-Guegan, A. Refinement of the Crystal Structure of Zirconium Nickel, Zr₈Ni₂₁. *Z. Krist-New Cryst. St.* **1998**, *213*, 227–228. <https://doi.org/10.1524/NCRS.1998.213.14.227>
- Kube, S. A.; Schroers, J. Metastability in high entropy alloys. *Scr. Mater.* **2020**, *186*, 392–400. <https://doi.org/10.1016/J.SCRIPTAMAT.2020.05.049>
- Li, Z., Pradeep, K. G.; Deng, Y.; Raabe, D.; Tasan, C. C. Metastable high-entropy dual-phase alloys overcome the strength–ductility trade-off. *Nature.* **2016**, *534*, 227–230. <https://doi.org/10.1038/nature17981>
- Matsumoto, S.; Tokunaga, T.; Ohtani, H.; Hasebe, M. Thermodynamic Analysis of the Phase Equilibria of the Nb–Ni–Ti System. *Mater Trans.* **2005**, *46* (12), 2920–2930. <https://doi.org/10.2320/MATERTRANS.46.2920>
- Nash, P.; Nash, A. The Nb–Ni (Niobium-Nickel) system. *Bull. Alloy. Phase Diagr.* **1986**, *7*, 124–130. <https://doi.org/10.1007/BF02881547>
- Navrotsky, A. Energetic clues to pathways to biomineralization: Precursors, clusters, and nanoparticles. *Proc. Natl. Acad. Sci. U.S.A.* **2004**, *101* (33), 12096. <https://doi.org/10.1073/PNAS.0404778101>
- Navrotsky, A. Nanoscale Effects on Thermodynamics and Phase Equilibria in Oxide Systems. *ChemPhysChem.* **2011**, *12* (12), 2207–2215. <https://doi.org/10.1002/CPHC.201100129>
- Okamoto, H. Ni–Zr (Nickel–Zirconium). *J. Phase Equilib. Diffus.* **2007**, *28*, 409. <https://doi.org/10.1007/S11669-007-9120-Z>
- Olivotos, S.; Economou-Eliopoulos M. Gibbs Free Energy of Formation for Selected Platinum Group Minerals (PGM). *Geosci.* **2016**, *6* (1), 2. <https://doi.org/10.3390/GEOSCIENCES6010002>
- Sun, W.; Jayaraman, S.; Chen, W.; Persson, K. A.; Ceder, G. Nucleation of metastable aragonite CaCO₃ in seawater. *Proc. Natl. Acad. Sci. U.S.A.* **2015**, *112* (11), 3199–3204. <https://doi.org/10.1073/PNAS.1423898112>
- Sun, W.; Dacek, S. T.; Ong, S. P.; Hautier, G.; Jain, A.; Richards W. D.; Gamst A. C.; Persson K. A.; Ceder, G. The thermodynamic scale of inorganic crystalline metastability. *Sci. Adv.* **2016**, *2* (11), e1600225. <https://doi.org/10.1126/SCIADV.1600225>
- Tokunaga, T.; Matsumoto, S.; Ohtani, H.; Hasebe, M. Thermodynamic Analysis of the Phase Equilibria in the Nb–Ni–Zr System. *Mater. Trans.* **2007**, *48* (9), 2263–2271. <https://doi.org/10.2320/matertrans.MB200713>
- Trexler, M. M.; Thadhani N. N. Mechanical properties of bulk metallic glasses. *Prog. Mater. Sci.* **2010**, *55* (8), 759–839. <https://doi.org/10.1016/J.PMATSCI.2010.04.002>
- Wang, C. X.; Yang, G. W. Thermodynamics of metastable phase nucleation at the nanoscale. *Mater. Sci. Eng. R Rep.* **2005**, *49* (6), 157–202. <https://doi.org/10.1016/J.MSER.2005.06.002>
- Wang, J.; Qin, J.; Zhou, J.; Cheng, K., Zhan, C.; Zhang, S.; Zhao, G.; Li, X.; Shen, K.; Zhou, Y. Correlation between mixing enthalpy and structural order in liquid Mg–Si system. *T. Nonferr. Metal. Soc.* **2021**, *31* (3), 853–864. [https://doi.org/10.1016/S1003-6326\(21\)65544-9](https://doi.org/10.1016/S1003-6326(21)65544-9)
- Yamaura, S.; Sakurai, M.; Hasegawa, M.; Wakoh, K.; Shimpo, Y.; Nishida, M.; Kimura, H.; Matsubara, E.; Inoue, A. Hydrogen permeation and structural features of melt-spun Ni–Nb–Zr amorphous alloys. *Acta Mater.* **2005**, *53* (13), 3703–3711. <https://doi.org/10.1016/j.actamat.2005.04.023>
- Zaitsev, A. I.; Zaitseva, N. E.; Shakhpazov E. K.; Kodentsov, A. A. Thermodynamic Properties and Phase Equilibria in the Nickel–Zirconium System. The Liquid to Amorphous State Transition. *Phys. Chem. Chem. Phys.* **2002**, *4* (24), 6047–6058. <https://doi.org/10.1039/B201036B>
- Zhang, Y.; Zhou, Y. J.; Lin, J. P.; Chen, G. L.; Liaw, P. K. Solid-Solution Phase Formation Rules for Multi-Component Alloys. *Adv. Eng. Mater.* **2008**, *10* (6), 534–538. <https://doi.org/10.1002/adem.200700240>